TECHNISCHE UNIVERSITÄT MÜNCHEN

Lehrstuhl für Biologische Bildgebung

Robust Methods and Algorithms for Fluorescence Imaging and Tomography

Pouyan Mohajerani

Vollständiger Abdruck der von der Fakultät für Elektrotechnik und Informationstechnik der Technischen Universität München zur Erlangung des akademischen Grades eines

Doktor-Ingenieurs

genehmigten Dissertation.

Vorsitzender: Univ.-Prof. Dr.-Ing. habil., Dr.h.c. Alexander W. Koch

Prüfer der Dissertation:

1. Univ.-Prof. Vasilis Ntziachristos, Ph.D.
2. Univ.-Prof. Gordon Cheng, Ph.D.
3. Priv.-Doz. Dr. med. Reinhard Meier

Die Dissertation wurde am 07.08.2013 bei der Technischen Universität München eingereicht und durch die Fakultät für Elektrotechnik und Informationstechnik am 03.07.2014 angenommen.

Dedicated to my best teacher
My father, Mr. Ahmad Mohajerani

Abstract

Molecular imaging involves extracting information about biological activities at cellular and molecular levels within tissue by relying on extrinsic or intrinsic probes or tracers to target processes. Optical imaging often enhanced using contrast induced by fluorescent probes, is in particular an attractive approach for non-invasive, non-ionizing imaging of physiological as well as molecular functions in tissue *in vivo*.

The purpose of this work was the development of robust algorithms, methods and processing frameworks for novel applications of fluorescence planar and tomographic imaging in preclinical and clinical environments. Opportunities afforded as well as challenges posed by the wealth of information made available by the hybrid modalities as well as the prospects of emerging preclinical and clinical applications have motivated this work. We focused on development of accurate, fast and robust methods and algorithmic approaches and processing framework for modeling and processing of data extracted using various planar and tomographic systems. We developed a framework for modeling and processing of the hybrid fluorescence molecular tomography-X-ray computed tomography (FMT-XCT) system, relying on a finite element method (FEM)-based model for light propagation in tissue, as an efficient and optimized tool for accurately processing FMT-XCT datasets with a versatile graphical interface. The system was geometrically calibrated using a two-step process for accurate mapping between CT and optical domains.

A new algorithm for compression of large amounts of information gathered by the FMT-XCT was developed. This method takes advantage of inter-source data redundancy to compress the Born data in optimally grouped spatial detector clusters. Besides the novelty of the algorithm itself, the compression results constitute the first demonstration of any compression method for *in vivo* imaging using fluorescence tomography.

Robust FMT-XCT inversion, driven by data and anatomical priors, was achieved using a novel method based on weighted least squares. The

residual weights were optimized using a fuzzy inference system, where the rules were designed based on an information-theoretic analysis of system behavior. The developed algorithmic framework was verified using several preclinical applications and the results are presented - some of which for the first time. The flexibility and accuracy of the code also afforded synergy of FMT and phase-contrast X-ray CT, called FMT-PCCT, which has been demonstrated in this work for the first time for small animal imaging.

The algorithmic and processing frameworks proposed in this work were further expanded and applied to clinical applications. We develop a method for processing fluorescence images supplied by a real-time planar system, designed for imaging rheumatoid arthritis in human hands. The proposed spatiotemporal analysis decouples signal components of different spatial and temporal characteristics emanating from local concentration of intravenously injected Indocyanine Green (ICG). We furthermore proposed and demonstrated for the first time tomographic imaging of synovitis in human finger joints, post injection of ICG. Several acquisition and algorithmic modifications and developments were carried out toward quantitative three-dimensional imaging of ICG accumulation in inflamed synovial tissue in finger joints (many of the clinical results herein were validated and co-registered with MRI findings).

The methods developed in this work made robust and efficient processing and inversion of FMT-XCT measurements using anatomical priors possible. The developed processing framework also enabled clinical applications toward more accurate diagnosis of joint inflammation using planar and tomographic techniques. The methods and results presented in this work are expected to enhance the roll of fluorescence imaging and tomography in preclinical and clinical environments as well as initiate avenues for further theoretical development.

Zusammenfassung

Molekulare bildgebende Methoden für biologische und medizinische Anwendungen umfassen präklinische und klinische Messverfahren, wodurch gewisse biologische Aktivitäten des tiefliegenden Gewebes sich auf molekularen Ebenen messen lassen. Solche Informationen über die molekulare Funktion des Gewebes, wie beispielsweise Enzymaktivitäten, sind ansonsten durch konventionelle anatomische Modalitäten nicht zu charakterisieren. Molekulare Bildgebung mithilfe optischer Methoden ist aufgrund ihres niedrigen Kostens, Abwesenheit der schädlichen Strahlungen und der Fähigkeit molekulare Aktivitäten tief im Gewebe quantitativ zu erfassen insbesondere interessant. Optische molekulare Bildgebung ist in Zusammenhang mit Kontrastmitteln besonders effektiv. Fluoreszente Kontrastmittel und Proben ermöglichen nichtinvasive Darstellung molekularer Aktivitäten durch bildgebende optische Verfahren *in vivo*. Durch Fluoreszenzmittel verstärkte optische Bildgebung existiert in planaren und tomografischen Geometries und Varianten, die einer Reihe präklinischenr und klinischer Anwendungen entgegenkommen. Bezeichnende Anwendungsgebiete sind unter anderem Arzneimittelforschung- und Entwicklung, Krebstherapie und Therapieüberwachung.

Der Zweck dieser Arbeit war Entwicklung von Algorithmen, numerischen Verarbeitungsmethoden und Rahmenwerken für neue und aufkommende präklinische und klinische Anwendungen anhand planarer und tomografischer Fluoreszenzbildgebung. Numerische und algorithmische Herausforderungen die durch große Menge von Informationen hervorgerufen sind, zusammen mit neu entstehenden präklinischen sowie klinischen Anwendungen, haben diesen Forschungsaufwand motiviert. Wir zielten die Entwicklung von präzisen und schnellen numerischen und algorithmischen Ansätzen an, um verschiedene planare und tomografische Modalitäten zu modellieren und verarbeiten. Ein umfassendes Rahmenwerk zur Modellierung und Verarbeitung der hybriden molekularen Fluoreszenztomografie/Röntgen Computertomografie, FMT-XCT genannt, wurde en-

twickelt, das auf Finite-Elemente-Methode (FEM) setzt, um die Lichtausbreitung in biologischem Gewebe zu modellieren. Das FMT-XCT System ist zusätzlich durch ein Zweistufenverfahren geometrisch kalibriert. Wir präsentieren weiter einen neuen Algorithmus um die durch FMT-XCT aufgenommen Datensätze zu komprimieren und dadurch die rechnerische Belastung zu mildern. Die vorgeschlagene Methode nutzt die Datenredundanz zwischen benachbarten Gantry-winkeln aus. Die Detektor sind in räumliche Cluster gruppiert und jedes Cluster ist durch Hauptkomponentenanalyse komprimiert. Eine neue Methode wurde zusätzlich zu robuster Inversion der FMT-XCT Daten durch ein gewichtetes Kleinste-Quadrate-Modell entwickelt. Das Modell setzt auf ein Fuzzy-Inferenzsystem um die Gewichte zu optimieren und ist von Messungen sowie anatomischen Informationen getrieben. Das Fuzzy-Inferenzsystem wurde mithilfe einer Informationstheoritischen Analyse entworfen. Aufgrund ihrer Genauigkeit und Flexibilität, die hierin entwickelten Methoden haben mehrere präklinische Anwendung ermöglicht - manche zum ersten Mal. Wir präsentieren zum ersten Mal hybride Bildgebung von Kleintieren durch eine Kombination von der FMT und Phasenkontrast-Röntgentomografie; FMT-PCCT genannt.

Die numerischen und algorithmischen Rahmenwerke wurden weiterentwickelt um aufkommenden klinischen Interessen entgegenzukommen. Wir entwarfen einen Algorithmus zur verbesserten Lokalisierung von gezielten Signals in einem durch Indocyaningrün (ICG) verstärkten planaren Messverfahren zur verbesserten Charakterisierung und Diagnose von Rheumatoidarthritis in menschlichen Handgelenken. Außerdem präsentieren wir einen neuen Ansatz zur quantitativen und tomografischen Erfassung der ICG-Anlagerung in Synovialgewebe der menschlichen Fingergelenke. Die klinischen Ergebnisse wurden mithilfe kontrastversärkter Kernspintomografie ausgewertet.

Die hierin entwickelten Methoden und Algorithmen ermöglichten robuste und effiziente Verarbeitung und Inversion der FMT-XCT Messungen anhand der anatomischen Informationen sowie klinische Anwendungen mithilfe planarer und tomografischer Verfahren. Es wird erwartet, dass die Methoden und Ergebnisse dieser Arbeit den Stellenwert der Fluoreszenztomografie in präklinischen sowie klinischen Umfeldern fördern und Entwickelung weiterer theoretischen Ansätze motivieren.

Acknowledgements

It would be impossible to fulfill justice if I were to try to fully appreciate or even name all individuals who have helped me with their words, support, advice or sheer presence along the path of my doctoral studies.

Foremost, I wish to thank my adviser Professor Vasilis Ntziachristos for the excellent academic mentorship and for having provided me with the opportunity to work under his supervision. I appreciate all the intriguing research ideas and accurate scientific judgements, as well as to have allowed and trusted me to also follow my intuition during the research.

I further thank the chairman of the thesis committee, Professor Alexander Koch, as well as the committee members Professor Gordon Cheng and Priv.-Doz. Dr. Reinhard Meier for the great discussions and the precious times spend toward examination of my work.

My humble gratitude goes to my dear parents Parvindokht Shayanfar and Ahmad Mohajerani, my awesome siblings Mehrdokht Mohajerani and Dr. Amirhossein Mohajerani well as my dear aunt Gagali and my late grandmother for their unconditional love. Kamal Mohajerani, Hassan Mehdinia and Parvaneh Mohajerani have been excellent role models and friends. The gratitude owed to Dr. Ehsan Mohajerani I shall fulfill by a simple “thank you”.

Dr. Ali Mohajerani was there when I needed him the most. Thank you my dear uncle for being the best trainer and life coach ever.

I cannot imagine having been able to get here without the support of many. I wish to thank my friends and former colleagues back in U.S., Professor Ali Adibi, Professor Salman Mohagheghi, Dr. Kambiz Nayebi, Dr. Farhad Farzbod, Dr. Ali Behrooz, Dr. Ali A. Eftekhar, Sarah Gleaton, Marilou Mycko and Dr. Marmar Mehrabadi. Very special thanks to Dr. Wael Yared at PerkinElmer Inc. USA for all the support and encouragement.

Deepest appreciations for my dear friends Navid Shams, Farzad Khalilimehr, Nima Shams, Behzad Khalilimehr, Milad Masoudi, Dr. Mohammad Nazari, Farzaneh Ebrahimi, Mostafa Ebrahimi and Reza Naghinasab for their support.

I would also like to thank my friends and colleagues in Munich, at the institute for biological and medical imaging (IBMI), iThera Medical, Helmholtz Zentrum München (HMGU), Helmholtz Graduate School Environmental Health (HELENA), Klinikum rechts der Isar and Garching Forschungszentrum. Foremost, I thank Zsuzsanna Öszi and Susanne Stern at IBMI for going the extra mile on a regular basis and their amazing attitude and efficiency. Many thanks to Frau Silvia Weinzierl for her stellar resourcefulness. I further thank Maximilian Koch, Dr. Vladimir Ermolayev, Dr. Marija Trajkovic-Arsic, Dr. Andreas Brandstätter, Dr. Julia Niefnecker, Dr. Angelique Ale, Dr. Peter B. Noël, Dr. Neal C. Burton, Dr. Andreas Oancea, Stratis Tzoumas, Panagiotis Symvoulidis, Andrei Chekkoury, Dr. Mojgan Mohajer, Karin Radrich, Alexander Dima, Dmitry Bozhko, Dr. Amir Rosenthal, Jürgen Glatz, Dr. Beatriz Garcia, Dr. Stephan Kellnberger, Christen Lutzweiler, Xiaopeng Ma and Dr. Jing Shi for the excellent discussions. I further appreciate Professor Franz Pfeiffer, Dr. Martin Bech, Alexander Hipp and Marian Willner in the physics department of TUM at Garching for their helps with the phase-contrast imaging. I am also grateful to Professor Ernst J. Rummeny and Dr. Klaus Thürmel at Klinikum rechts der Isar for having supported the clinical developments. Special thanks to Priv.-Doz. Dr. Reinhard Meier at the radiology department of Klinikum rechts der Isar for great discussions as well as clarifications on biomedical topics. I appreciate Uwe Klemm, Sarah Glasl and Florian Jurgeleit for their exemplary assistance in the lab. I further thank Frau Hanife Kara at the Personalabteilung of HMGU for her help with the visa process and orientation.

Several of the topics presented in this work are presented in published papers and submitted or, otherwise, in preparation manuscripts. As indicated in the body of this work, the reproductions of the materials (text, formulas, figures and tables) in this dissertation were performed with permission from respective journals, wherever applicable, and the corresponding papers, manuscripts or drafts were cited according to the latest status of the peer-review process. Furthermore, the field of medical imaging is highly interdisciplinary and is, hence, often advanced through

collaborative effort between several groups or researchers of different backgrounds. All technical or intellectual contributions from the coauthor, colleagues and collaborators have been explicitly clarified and acknowledged throughout this dissertation. In addition, I appreciate all the coauthors as well as the collaboration partners I have worked with during my doctoral studies in Munich for their comments, discussions or corrections to the material presented here, in the papers or in the manuscripts.

Außerdem, ein noch herzlicheres Dankeschön für meine Freunde im IBMI, immer dabei und hilfsbereit gewesen zu sein, mir die verwirrenden, doch zugeleich faszinierenden Raffinessen der deutschen Grammatik aufzuklären. Ihr habt meine Leidenschaft für Fremdsprachen begrüßt und mit großzügiger Geduld gefördert. Ohne euch wäre es nie so weit gekommen. Ich weiß alles aufrichtig zu schätzen. Wozu immer es auch gut sein mag, wenn ihr eines Tages Persisch lernen wollt, könnt ihr euch auf mich sicherlich verlassen!

My most heartfelt appreciations are for my lovely and beautiful wife Farzaneh Najafian for all her love, wisdom and support along this path. She is the light that makes everything else shine. I would have not made it without her; of this, I am very sure.

Contents

1 Introduction

1.1 Fluorescence-based optical imaging

Medical and biological imaging is a vast and highly interdisciplinary field with several imaging modalities existing with applications in preclinical and clinical scenarios ranging from diagnosis to drug development and therapy monitoring. Imaging methods often rely on the physical descriptions of wave-tissue or photon-tissue interactions to extract information about tissue anatomy or molecular and physiological function, while operating *in vivo* or *ex vivo* and with or without invasion of the underlying tissue. Each of current the medical imaging modalities have their specific applications, advantages and disadvantages. Examples of common metrics for characterization of imaging systems include their spatial and temporal resolution, penetration depth, signal to noise ratio, sensitivity to underlying physical quantity or contrast, hardware cost, operator dependency and diagnostic sensitivity and specificity. Different segments of almost the entire electromagnetic spectrum are employed to probe biological tissues of various sizes and compositions to deliver one or multidimensional images of one or more physical quantities of the underlying tissue.

Application of optical techniques to medical and biological imaging, called optical imaging, has been an actively researched field of medical imaging [1–9]. Recent technological advances in optical components and sensors and computing power as well as the expansion of biological marker and probe technology have in particular have been conducive to rapid expansion of optical technologies for biomedical imaging in recent decades [2, 6, 7, 10–13]. While optical microscopy offers powerful techniques for characterization of surface structures, the application of optical techniques for imaging tissue several millimeters deep under the skin is hindered by the presence of various chromophores and scatterers

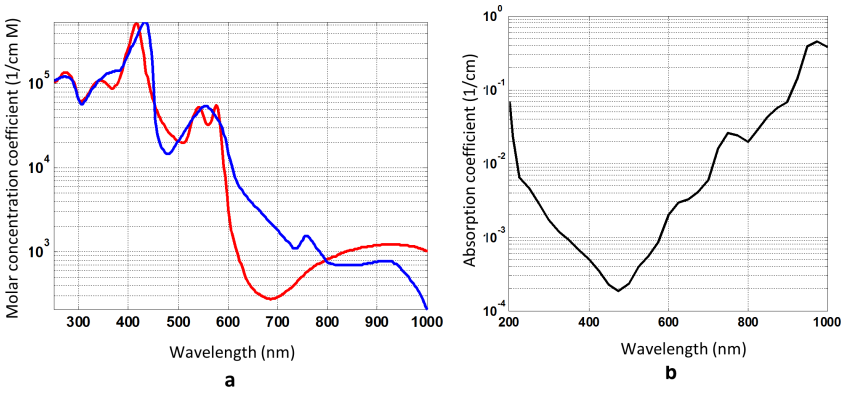

Figure 1.1: Near-infrared (NIR) optical window in tissue; (a) absorption spectra of oxygenated hemoglobin (HbO2, red curve) and deoxygenated hemoglobin (Hb, blue curve) in tissue, (b) absorption spectrum of water vs. wavelength (plots in (a) and (b) were generated using data compiled by Scatt Prahl from Oregon Medical Laser Center, presented in `http://omlc.ogi.edu/spectra/`, from sources [14–16]).

in tissue. In particular water, deoxyhemoglobin and oxyhemoglobin are known to significantly absorb optical photons in tissue. Furthermore, several molecules and in particular lipids tend to randomly change the course of photons traveling throughout the tissue; hence, causing diffusive light propagation due to scattering effects. While hemoglobin and water cause severe absorption of photons in most of the visible and infrared spectra as shown in Figure 1.1, there exists a window of opportunity in the optical spectrum, called the near-infrared (NIR) region, where the tissue has a relatively low optical absorption [8]. The biological tissue has the least optical absorption in NIR, as shown in Figure 1.1(a), where it is observed that hemoglobin and deoxyhemoglobin dominate the absorption for wavelengths shorter than 650 nm and water has higher absorption beyond 900 nm. The tissue scattering is roughly uniform over the NIR bandwidth, but is much stronger than the absorption. The propagation of NIR light in tissue is mainly characterized with absorption and elastic scattering. The NIR window, often considered to range from 650 nm to 850 nm [8], offers a unique opportunity to optically probe biological tissue up to tens of millimeters under the skin non-invasively.

Local contrast in optical properties and characteristics of underlying tissue make imaging possible. As an example, high optical absorption of tissue can be indicative of higher local blood concentration in tissue. As

many other imaging modalities, the performance of optical imaging techniques can be significantly improved via application of contrast agents. The contrast agents are often administered prior to imaging and create a higher level of contrast between the optical characteristics of the target tissue with respect to surrounding tissue [8].

The application of fluorescence to create contrast between target and background tissue is in particular a very powerful technique [10]. The technology of fluorescent probe design has vastly advanced in recent years and has provided a myriad of probes with the ability to bind to specific macromolecules in tissue, hence biologically marking specific molecular processes [2,12]. For instance, fluorescent probes have been designed with the ability to specifically target integrin $\alpha_v\beta_3$ receptors which are often expressed in tumor cells and during angiogenesis [9, 17]. Such probes especially afford imaging potential by creating highly fluorescent lesions in otherwise non-fluorescent tissue. The fluorescence phenomenon can be briefly, mathematically described as follows. An electron can be excited to a higher energy state upon absorbing an "excitation" photon. The excited electron subsequently relaxes to its initial energy state, thereby releasing heat as well as energy as a photon with a lower frequency level (than the excitation photon) - which is called the fluorescence photon. Materials capable of fluorescence often absorb photons within a specific excitation bandwidth and release photons in a group of wavelengths. The development of activatable and targeted fluorescent molecular probes has facilitated *in vivo* study and monitoring of certain molecular processes several millimeters under the skin [2,12,18]. The capability of fluorescent probes to target or be activated by specific molecules has been conducive to their wide deployment in cancer and drug development research [19, 20].

Fluorescence-based optical imaging exist in different measurement geometries and imaging domains. Planar or photographic approach obtain two-dimensional (2-D) fluorescence images of the sample under planar illumination. These images carry information regarding fluorophore concentration within the tissue. The illumination is often performed in trans-illumination geometry, where the excitation and measurements are carried out on the two sides of the sample or in epi-illumination form where both excitation and measurement are carried on the same side. While potentially a powerful technique with many preclinical and clinical applications [21–24], planar imaging lacks depth resolution as the

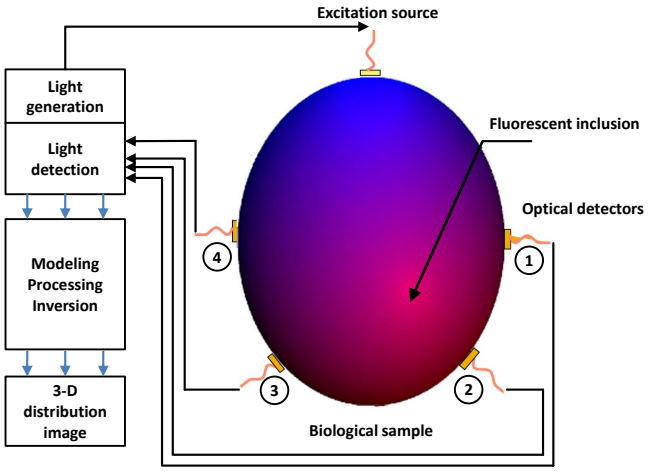

Figure 1.2: Principles of fluorescence molecular tomography (FMT); the excitation light (blue color) from the source excites the fluorophores in the tissue to generate the emission photons (red color), which are sensed by the optical probes located on the surface.

final image is a weighted sum of components at different depths [7]. Instead, optical tomography has been developed as a non-invasive modality for quantitative and three-dimensional (3-D) molecular imaging of tissue deep ($>$ 1-2 mm) under the skin [1, 6, 8, 25]. Different variations of optical tomography aim at quantification of chromophore and fluorophore molecule concentrations. Optical tomography generally involves excitation of tissue at several source locations using collimated or diffusive light sources and measurement of light which reaches the skin at one or more wavelengths using several detection technologies. Optical tomography is usually conducted within near infra-red (NIR) regime covering 650-850 nm. The light propagation models in diffusive tissue can be used to image various quantities of biological interest inside the tissue up to several millimeters. Diffuse optical tomography (DOT) techniques seek quantification of chromophores such a hemoglobin and deoxyhemoglobin, which disclose information about blood concentration and oxygenation using their characteristic absorption spectra as shown in Figure 1.1, by solving for scattering and absorption coefficients given light measurements on the skin. Other molecules of imaging interest, in addition to chromophores, are the fluorophores. These molecules fluoresce upon excitation at the proper wavelength and exist either in endogenous form in the tissue or are administered exogenously. The concentration and lifetime of fluorophores

carry plenty of information regarding the local biological processes and activities of specific enzymes. It is possible to non-invasively quantify the concentration and lifetime of fluorophores at a given location in tissue drawing upon the diffusive light propagation model in tissue, using a method called fluorescence molecular tomography (FMT) [2].

The methodology of FMT is schematically described in Figure 1.2. The oval shape in this figure depicts a hypothetical tissue containing a packet of fluorophores in the location pointed to with the arrow. The tissue is excited at a given source location at the excitation wavelength of the targeted fluorophores. The excitation light photons propagate diffusively throughout the tissue; as shown by the blue color in Figure 1.2. The fluorophores emit photons at the emission wavelength upon interaction with the excitation photons that reach them. The emission light originating at the fluorophore inclusion is depicted by the red color in Figure 1.2. The amount of the light that reaches the skin is detected by some sort of optical detection on the surface. The optical detector is used to measure light fluence at both excitation and emission wavelengths on the skin. These measurements are then used to trace back the source of the emissions and, thus, yielding a 3-D image of the fluorophore distribution in tissue.

Fluorescence tomography has applications in both preclinical and clinical stages. In the preclinical stage FMT is extensively used in small animal studies for imaging biological processes by quantification of exogenous or indigenous fluorophores targeting specific marcomolecules associated with these biological processes with applications in drug discovery and development processes and subsequent therapy monitoring [7, 11]. In the clinical stage the application of fluorescence imaging is limited due to the toxicity concerns about the fluorescent probes. However, the FDA (U.S. food and drug administration) approved Indocyanine Green (ICG) has been used as a fluorescent agent for imaging applications such as breast tumors detection in humans [26] or inflammation detection in human hands [27].

The resolution and accuracy of FMT is limited by several factors such as imperfect knowledge about the optical properties of the tissue sample and the inherent ill-posed nature of the linear model. Hybrid modalities aim to improve the quality of the molecular imaging component by incorporating anatomical information [28–31]. In particular, combination

of FMT and X-ray CT, called FMT-XCT, has been proposed to mitigate the effect of the aforementioned problems on image quality by using anatomical information as *a priori* knowledge in the forward and inverse problems [25, 32].

Full realization of the potential of fluorescence-enhanced molecular imaging in planar or tomographic variations, for biomedical applications poses several numerical and algorithmic challenges. Efficient processing and extraction of desirable biological information from the measurement requires accurate system and light propagation modeling. The large amount of information and data gathered by these imaging systems does not just create processing and numerical challenges - it also affords novel and interesting diagnostic and imaging applications for both preclinical and clinical scenarios.

1.2 Objectives and outline

The goal of this work was the development of algorithmic and processing frameworks and methods to accommodate recent applications of fluorescence-enhanced planar and tomographic imaging of tissue in preclinical and clinical environments. Numerical and algorithmic challenges posed by the large quantity of information afforded by the hybrid molecular and anatomical modalities as well as the prospects of emerging preclinical and clinical applications motivated this work. We focus on development of accurate, fast and memory-efficient numerical methods and algorithmic approaches and processing frameworks for modeling, processing, compression and inversion of information extracted using planar and tomographic systems. Optimization of hardware calibration and acquisition protocols were also carried out as indispensable steps toward improvement of imaging performance.

This thesis is structured as follows. In Chapter 2 we present the mathematical modeling of the FMT system based on finite element modeling (FEM) of light propagation in tissue. An efficient implementation of FEM is presented and optimizations are discussed using analytical and phantom measurements. Chapter 3 discusses and presents geometrical calibration of the FMT-XCT system using a two-step approach as well as the acquisition protocol. The optimized processing framework developed

in this work is presented in Chapter 4. In Chapter 5 we present a new method for compression of the Born data by exploiting the inter-source correlation between adjacent projections based on principal component analysis. A novel weighted least squares approach for inversion of FMT-XCT is presented in Chapter 6. The method uses a fuzzy-inference system for residual weight optimization and is driven by data and anatomical priors. The developed methods and algorithms are verified and demonstrated using *in vivo* animal studies in Chapter 7, where we demonstrate hybrid FMT—phase contrast X-ray CT, FMT-PCCT for the first time. Chapter 8 presents a novel method for spatiotemporal treatment and FEM-based analysis of fluorescence-aided imaging of rheumatoid arthritis in hand joints in epi-illumination planar geometry. The results are presented for several patients and compared and verified with MR findings. In Chapter 9 we present the first tomographic imaging of synovitis in human finger joints using the FMT system and the XFMT code expanded with several acquisition as well as algorithmic modifications and developments. The results are presented for 5 patients and 4 healthy volunteers and compared and coregistered with magnetic resonance imaging (MRI) results. Chapter 10 concludes the work and presents ideas for future development and research. Supporting materials are provided in Appendices A-D.

2 FEM-based modeling of fluorescence tomography

2.1 Introduction

Imaging the underlying physical parameters of tissue using an imaging system often consists of two steps; the forward modeling and the inversion. Simply put, the forward modeling seeks to construct a mathematical model which predicts measurements given knowledge about the (otherwise unknown) underlying physical quantities. For instance, in conventional X-ray computed tomography, the forward problem consists of predicting the measured X-ray photon counts given the complete X-ray absorption map of the sample. This is achieved using the well-known Radon transform which models the total attenuation of the X-ray beam as a line integral of the absorption caused by infinitesimal volume elements. The forward modeling is a vast field which overlaps applied mathematics and physics. The physical description of the system is often achieved using partial differential equations, which dictate local tissue-wave or tissue-particles interactions. Once a forward model of the system is established, it is used in the inversion process to reconstruct the underlying image using the acquired measurements. The inversion can be envisioned as the process of finding the image that would predict (using the forward model) the acquired measurements, as accurately as possible. Forward modeling and inversion can be briefly described as follows. Suppose x and y are vectors representing the input and output of a system which want to model. The system is parameterized using a set of variables θ. The forward modeling can be expressed as finding a forward operator $\mathfrak{F}$ such that $y = \mathfrak{F}(x, \theta)$. Given the forward operator $\mathfrak{F}$, the inversion then consists of estimating θ such that a measure of the prediction error (defined as the measurements minus $\mathfrak{F}(x, \theta)$) is minimized.

The forward modeling necessitates understanding and modeling the light propagation in biological tissue. The biological tissue can have a diverse range of optical properties; from highly absorptive to highly scattering or ballistic propagation in air-filled body cavities [11]. The interaction of various types of tissue with near-infrared (NIR) photons are subject to various differential equations, such the diffusion equation or the more general radiative transfer equation (RTE) and result in several physical phenomena such as absorption, scattering or reflection and diffraction of photons. While a thorough analysis of light propagation in tissue and photon-tissue interaction is an extensive topic and not the purpose of this work, we aim to develop a numerical model for propagation of light photons in tissue in diffusive regime for our imaging purposes. The diffusive light propagation, shortly explained, occurs when a photon undergoes a significantly larger number of scattering events than absorption events in a given length. Such a modeling is a critical tool in optical imaging applications where a large (several millimeters in diameter) tissue sample is optically probed, such as in several variations of optical tomography. In many types of biological tissue the diffusive regime holds, as NIR photons experience on average several tens of scattering and an order of magnitude less number of absorption events in a centimeter of propagation.

The main objective of this chapter is to derive a mathematical model of fluorescence molecular tomography (FMT) describing a relationship between the fluorescence measurements and the unknown fluorophore distribution in tissue. FMT can be described using a linear system, where the system matrix is derived in terms of the tissue optical properties and the measurement geometry. Toward this goal, we develop a finite element method (FEM) based numerical framework of light propagation in diffusive medium. The FEM model is optimized for our tomographic imaging purposes and verified using numerical and physical phantom studies. The developed FEM-based framework is not only helpful in modeling tomographic imaging systems, but it also helps with understanding the planar imaging tools, as discussed later in this work.

2.2 Diffusive propagation of light in tissue

Imaging the concentration of different molecules at depth inside the tissue requires a realistic model describing the propagation of photons inside

tissue. A comprehensive description of light propagation in tissue can be achieved using the radiative transfer equation (RTE), which essentially states that the number of photons in a point in time and space is given by the addition of all factors increasing it minus those which reduce it and is in this way a conservation equation. The RTE in the time-domain is given as [33]

$$\begin{aligned}\left(\frac{\delta}{\delta t} + \hat{s}.\nabla + \mu_s(r) + \mu_a(r)\right)\phi(r,\hat{s},t) = \\ \mu_s(r)\int_{4\pi}\Theta(\hat{s},\hat{s}')\phi(r,\hat{s},t)\,d^2\hat{s}' + q(r,\hat{s},t),\end{aligned} \tag{2.1}$$

where $\phi(r,\hat{s},t)$, called photon density or radiance and expressed in m^{-3} st^{-1}, is the number of photons traveling in the direction $\hat{s}$ from the point r in time t and is the quantity we are eventually interested in to find. The source photons are shown by $q(r,\hat{s},t)$ and are defined in the same manner. The term $\Theta(\hat{s},\hat{s}')$, called the scattering phase function, characterizes anisotropic scattering and equals (when multiplied by $d\hat{s}'$) the probability of a photon scattering from "the direction $\hat{s}$ into the direction $\hat{s}'$" [33](the notations follow those used in [33]). The optical scattering and absorption coefficients are recognized as, respectively, $\mu_s(r)$ and $\mu_a(r)$ in Equation 2.1. These quantities have both units of m^{-1} and denote the probability of a photon being scattered or absorbed at the point r in unit length. The RTE can be used to describe light propagation for arbitrary values of the absorption and scattering coefficients and can, therefore, be used to model light propagation in diffusive and non-diffusive regions of tissue. However, RTE is usually solved using Monte Carlo methods and is relative computationally complex to solve for large tissue volumes [33]. Therefore, simpler approximations ro RTE are sought and employed in different variations of optical tomography including FMT, whereby angle dependent radiance is expanded by spherical harmonics or other approximations [34–36].

The most commonly used approximation in optical tomography is the P_1 approximation, also called the diffusion equation (DE) obtained from the diffusion approximation (DA), and is given in the time domain as [33]

$$-\nabla.D(r)\nabla\,\phi(r,t) + \mu_a\phi(r,t) + \frac{1}{c}\frac{\delta\phi(r,t)}{\delta t} = q_0(r,t), \tag{2.2}$$

where c is the speed of light in the medium and $D(r)$ is the diffusion

coefficient given by

$$D(r) = \frac{1}{3(\mu_a(r) + \mu_s'(r))}, \tag{2.3}$$

and

$$\phi(r,t) = \int_{4\pi} \phi(\hat{s}, \hat{s}', t)\, d\hat{s}'. \tag{2.4}$$

The μ_s' in Equation 2.3 is called the reduced scattering coefficient and defined as $\mu_s' = (1-g)\mu_s$, where g is the anisotropy coefficient (≈ 0.9 in biological tissue) and is a function of $\Theta(\hat{s}, \hat{s}')$. For convenience, throughout the rest of this work reduced scattering coefficient is simply referred to as scattering coefficient and is denoted by μ_s instead of μ_s'. Equation 2.2 in the frequency-domain is given by

$$-\nabla.D(r)\nabla\phi(r,\omega) + \mu_a\phi(r,\omega) + \frac{i\omega}{c}\phi(r,\omega) = q_0(r,\omega), \tag{2.5}$$

where ω is the source modulation frequency. For $\omega = 0$ the DE in the continuous wave (CW) domain as

$$-\nabla.D(r)\nabla\phi(r) + \mu_a\phi(r) = q_0(r). \tag{2.6}$$

The quantity measured on the skin is some function of the photon flux given by

$$\Gamma(r) = -D(r)\,\hat{n}.\nabla\,\phi(r). \tag{2.7}$$

An extensive study for modeling different boundary conditions and also optical sources is presented in [37]. There are two commonly used boundary conditions; tissue adjacent to air and tissue adjacent to perfectly absorbing medium. In the tissue-air situation, the Robin boundary condition is used to model the boundary while in the tissue-dark medium situation the fluence on the surface is forced to zero. Robin condition places the fluence in immediate vicinity of the surface in a specific proportionality to the surface optical flux [37] and can be implemented by taking the fluence-flux relationship into accounting during the modeling using extrapolated boundary condition, where the fluence is forced to zero instead on a imaginary boundary one scattering length above the tissue-air surface. The Robin boundary condition can be expressed as

$$\phi(r) + 2\,D\,A\hat{n}.\nabla\phi(r) = 0, \tag{2.8}$$

where A is a real number (≈ 2.74) which accounts for mismatch between refractive indices of tissue and air [37].

For our applications in this work, the excitation source is modeled as a diffusive source inducing a diffusive photon current into the sample in the illumination area. The diffusive source is modeled by assigning different weights to the mesh boundary nodes illuminated by the source. The weights are determined by the illumination pattern as well as the location of the surface nodes with respect to the source, as shown later in Equation 2.13.

2.3 Propagation modeling using FEM

The forward problem consists of solving for $\phi(r)$ in Equation 2.6, given the measurement geometry and tissue optical properties. Approaches for solving this problem can be divided into analytical, statistical and numerical techniques [8]. The analytical solutions involve applications of Green's function to simple geometries with homogeneous optical properties [38]. Extensions to arbitrary geometries have been proposed based on Kirchhoff approximation [39]. Statistical techniques and Monte Carlo methods in particular, trace the trajectories of individual photons from a large pool and are especially helpful in modeling light transport in arbitrary regions of tissue and are often applicable for solving the RTE [33,40]. Numerical methods are best suited for efficiently modeling complex geometries with arbitrarily heterogeneous optical properties. A common numerical approach to the forward problem in diffusive tomography is based on the finite element method (FEM) [33].

The first step in deriving the mathematical model of FEM involves solving for the propagation of the excitation photons. In other words, we are interested in calculating the photon fluence that reaches any given location in tissue from a given source placed at a given location in tissue. The same formulation is applied to solving for the spatial distribution of photons emanating from a hypothetical packet of fluorophores inside the tissue.

A tetrahedral mesh is used discretizing the volume of tissue into T tetrahedral elements consisting of a total of N nodes. By discretizing the

DE over this mesh using the Galerkin formulation [33], a linear equation for the unknown fluence vector is achieved as (using notations and formulations from [33])

$$[\mathbf{K} + \mathbf{C}]\,\Phi = Q + \beta, \tag{2.9}$$

where

$$\mathbf{K}_{ij} = \int_{\Omega} D(\mathbf{r})\nabla\psi_i(\mathbf{r}).\nabla\psi_j(\mathbf{r})d\Omega \tag{2.10}$$

$$\mathbf{C}_{ij} = \int_{\Omega} \mu_a(\mathbf{r})\psi_i(\mathbf{r})\psi_j(\mathbf{r})d\Omega \tag{2.11}$$

$$\beta_j = \int_{\delta\Omega} \psi_j(\mathbf{r})\Gamma(\mathbf{r})d\delta\Omega \tag{2.12}$$

$$Q_j = \int_{\Omega} \psi_j(\mathbf{r})q_0(\mathbf{r})d\Omega. \tag{2.13}$$

The matrices $\mathbf{K}$ and $\mathbf{C}$ are symmetric sparse matrices of size $N \times N$ and Ω and $\delta\,\Omega$ denote tissue volume and surface, respectively. Equation 2.9 can be rearranged as

$$\mathbf{H}\,\Phi = Q, \tag{2.14}$$

where

$$\mathbf{H} = \mathbf{K} + \mathbf{C} + \mathbf{B}, \tag{2.15}$$

and

$$\mathbf{B}(i,j) = \frac{1}{2\,c\,A}\int_{\delta\Omega} D(r)\,\psi_i(r)\,\psi_j(r)\;d\delta\Omega. \tag{2.16}$$

We assume the diffusion coefficient is constant within each voxel (but can change between different voxels). The matrix $\mathbf{H}$ is also referred to in the literature as the stiffness matrix. The term $\mathbf{K} + \mathbf{C}$ is a positive-definite[1], symmetric matrix [33]. The matrix $\mathbf{B}$ is also symmetric and positive-definite. The positive-definiteness of $\mathbf{B}$ can be shown by decomposing it as a summation of matrices, where each matrix has 9 non-zero elements for a given surface triangle. In other words,

$$\mathbf{B} = \sum_{\sigma\in\delta\Omega} B_\sigma, \tag{2.17}$$

where B_σ is calculated for only the 3 vertices of the triangle σ. There-

[1] Matrix A is called positive-definite if and only if for every non-zero vector x, $x^\top Ax > 0$.

fore,

$$x^\top \mathbf{B}\, x = \sum_{\sigma \in \delta\Omega} x_\sigma^\top B_\sigma x_\sigma, \tag{2.18}$$

where x_σ is non-zero only on the 3 vertices of the surface triangle σ, denoted by v_σ, u_σ and w_σ. The notation $^\top$ denotes throughout this work the transpose operator. It is shown in Appendix A that for a given triangle $\int_{\delta\Omega} \psi_i(r)\, \psi_i(r)\; d\,\delta\Omega = S/6$ and $\int_{\delta\Omega} \psi_i(r)\, \psi_j(r)\; d\,\delta\Omega = S/12$, if $i \neq j$ (with S being the area of the respective triangle). Hence,

$$x^\top \mathbf{B}\, x = \sum_{\sigma \in \delta\Omega} D_\sigma S_\sigma \left(\frac{(v_\sigma + u_\sigma + w_\sigma)^2 + v_\sigma^2 + u_\sigma^2 + w_\sigma^2}{12} \right). \tag{2.19}$$

Therefore, $x^\top \mathbf{B}\, x \geq 0$ and the FEM matrix $\mathbf{H}$ is positive-definite.

We briefly review the method of conjugate gradient (CG) for solving the FEM linear system of Equation 2.9.[2] CG is an iterative method for solving large linear systems, where the model matrix is symmetric and positive-definite [41] - as is the case in the FEM problem shown above. The method is in particular effective when the matrix is large and sparse; a situation where direct inversion and Cholesky decomposition become computationally prohibitive. The method of CG is based on the idea of conjugate vectors (different from concept of complex conjugate). Specifically, for a $K \times K$ matrix W, two vector x and y are called conjugate (with respect to W) if and only if $x^\top W\, y = 0$. CG uses an iterative algorithm to find K mutually conjugate vectors to span the solution space. CG seeks to minimize the following cost function

$$f(x) = \frac{1}{2} \| W\, x - M \|_2^2 = \frac{1}{2} x^\top W\, x - x^\top M + \frac{1}{2} M^\top M. \tag{2.20}$$

Minimization of $f(x)$ is achieved in the first step by moving in the direction of steepest descent, that is $- \bigtriangledown f(x)$. Therefore, the first conjugate direction (or vector) p_0 is given as

$$p_0 = - \bigtriangledown f(x) = \underbrace{M - W\, x_0}_{r_0}, \tag{2.21}$$

where x_0 is the initial guess for the solution and r_0 is the residual vector. The k^{th} direction is found similarly using the k^{th} residual, after project-

[2] Treatment here follows the one used by D. N. Arnold "A concise introduction to numerical analysis" Lecture Notes, Penn State, MATH 597I Num. Anal. (2001).

ing the k^{th} residual vector over all previous conjugate directions. This projection is made to ensure the k^{th} direction is conjugate to the previous $k-1$ directions. Specifically,

$$p_k = r_k - \sum_{j=1}^{k-1} \lambda_j p_j, \tag{2.22}$$

where λ_j is the normalized projection of r_k over p_j given as $\frac{p_j^\top W r_k}{p_j^\top W p_j}$ [42]. The k^{th} direction is then used to update the solution from x_k to x_{k+1} by optimally moving along p_k. That is, $x_{k+1} = x_k + \alpha_k\, p_k$ such that

$$\alpha_k = \arg\min_{\alpha} \left\{ f(x_k + \alpha\, p_k) \right\}. \tag{2.23}$$

Through derivation it is found

$$\alpha_k = \frac{p_k^\top M}{p_k^\top W p_k}. \tag{2.24}$$

The review presented here, briefly touches upon the guiding principles of CG; full details and specific implementations can be found in literature, including [41, 42].

2.4 Efficient implementation of FEM

An efficient implementation of Equations 2.10-2.13 is performed in this work in MATLAB (MathWorks, Natick, MA, USA). A description of the MATLAB code is presented here and integral calculations are presented in Appendix A. The code assumes optical scattering and absorptions assigned to each individual tetrahedral voxel. The final stiffness matrix $\mathbf{H}$ is a sparse $N_n \times N_n$ matrix, N_n being the number of mesh nodes, where non-zero values are determined by voxel-node associations. First, a `for` loop runs over all voxels, and for each voxel the integrals of Equation 2.10 and Equation 2.11 are calculated. As shown in Appendix A, these integrals turn out to have a simple closed-form solution up to a scaling factor of the voxel volume. A second `for` is used to solve for the integral of Equation 2.12 and is executed for all surface elements. Likewise, the integrals have a simple form scaled by the surface triangle areas. Efficient

implementation of this code is also made by possible by proper indexing and assignment of the final sparse matrix $\mathbf{H}$. Normally within each `for` loop iteration, an addition would be necessary, as the value of $\mathbf{H}(i,j)$ between the i^{th} and j^{th} nodes is determined by all the voxels which have the $(i-j)$ segment as an edge. However, such addition if repeated in each loop operation would significantly hinder the execution and slow down the operation. Instead, we stack all the values and the corresponding indices of the matrix where the local additions would be performed in two pre-allocated arrays `Value` and `Index`. Filling these arrays does not entail addition within each loop and is very fast. We exploit MATLAB spare-matrix handling functionality to add all the values stacked in the array `Value` in to the locations pointed by the array `Index` without iterations. Note that an arbitrarily number of entries in `Value` with different values might be added to the same index designated by the array `Index`. The calculation of the stiffness matrix for a typical animal study consisting of around 40000 nodes and 230000 elements takes approximately 8 seconds on a computer with an Intel Core$^{\text{TM}}$ i7 CPU @ 3.4 GHz and 16 GB RAM.

2.5 Numerical aspects of FEM modeling

In Section 2.3 we reviewed the formal framework for modeling the light propagation in turbid media using the finite element method for discretization of the diffusion equation. It was shown that the forward problem can be represented by a linear equation in the discretized domain, where the optical fluence is represented by a vector, whose each entry represents the fluence on a given mesh node. In this section we analyze several numerical aspects of the FEM modeling using numerical phantom studies and draw conclusions with applications in processing of FMT data. The meshing is performing in this work using a module from the `CGAL` library, as employed in the `ISO2Mesh` framework [43, 44]. The code is capable of generating tetrahedral meshes for multi-region spatial volumes, where each pixel in space is assigned an integer number representing the region it belongs to. The method further is capable of efficiently modeling irregular geometries. An important issue to address when solving the forward problem is the mesh design. Several issues such

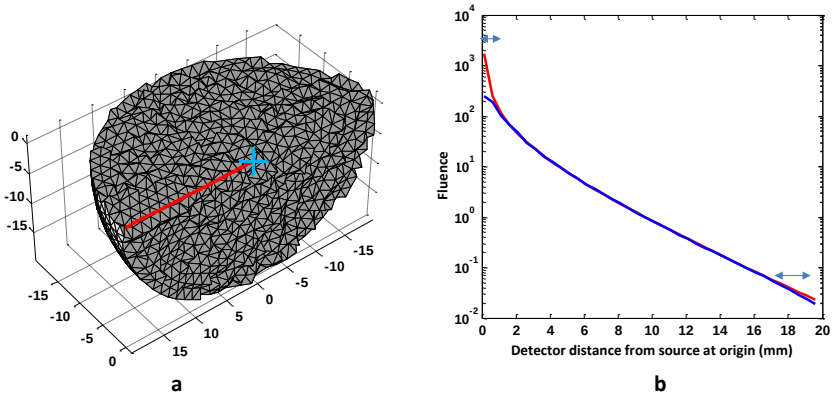

Figure 2.1: Modeling light propagation in infinite medium with a uniform mesh; (a) the tetrahedral mesh with uniform resolution, where the source at origin and detectors points are shown by red and cyan markers, (b) FEM simulations (blue) and analytical Green's function solution (red) vs. source-detector distance. All distances are in millimeters.

as the relative node density as well as spatial resolution need to be resolved toward an adequately accurate modeling performance. We address these issues in this section using numerical phantoms.

In the first step, we investigate modeling light propagation in an infinite homogenous medium. The Green's function for the diffusion equation for the infinite medium is given as:

$$\phi(r) = \frac{S_0}{4\pi D\, r} e^{-\sqrt{\frac{\mu_a}{D}}r}, \tag{2.25}$$

where D denotes the diffusion coefficient and S_0 is the point source intensity [45].

For modeling the infinite medium, a sphere with a radius of 20 mm with $\mu_a = 0.03$ mm^{-1} and $\mu_s = 1$ mm^{-1} was used, as shown in Figure 2.1(a). A tetrahedral mesh of uniform resolution was used to discretize the phantom volume.[3] The fluence was calculated on a row of detectors placed inside on the phantom along the red line in Figure 2.1(a), for an isotropic point source located at the center. The simulated fluence versus source-detector distance is shown in Figure 2.1(b). The blue and red curves in

[3] The spherical meshes were generated using the MATLAB-based toolbox `DistMesh` by P.-O. Persson available from `http://persson.berkeley.edu/distmesh/` [46]. The mesh renderings were performed using the function `simpplot.m` from the same toolbox.

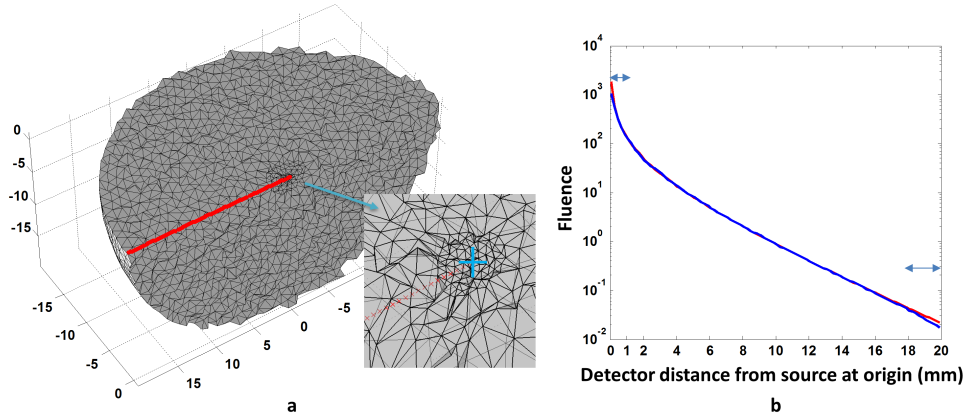

Figure 2.2: Modeling photon propagation in infinite medium with non-uniform meshing; (a) the mesh with finer resolution around the source located at the origin and (b) conformance between the simulated FEM fluence (blue) and the Green's function (red). The FEM results very accurately predict the GF values at a large distance span - there is divergence close to boundaries of the sphere, where the infinite medium condition does not hold.

the logarithmic plot of Figure 2.1(b) represent the simulated fluence and the analytical solution of Equation 2.25, respectively.

Three regions can be recognized in Figure 2.1(b); the area is vicinity of the source, the area in vicinity of the boundary and the area in between these two regions. The first two regions are delineated using double-headed arrows in Figure 2.1(b). The mismatch in the first region is large as the FEM model fails in close vicinity of the source (distance < 1 mm) to closely model the DE. This is due to the relatively large gradient of the fluence in this region (as gradient grows with $\frac{1}{r^2}$). Also, the FEM-modeling error (in comparison with the analytical solution) is relatively large in the third region as well. This is clearly due to the fact that the sphere fails to mimic the infinite medium condition close to the boundary. However, the FEM-based solution very closely matches the analytical solution in between these two extremities, where the sphere fairly well mimics the infinite-medium.

It is expected that the error can be reduced in source vicinity using a finer mesh resolution which can capture the larger fluence change in that region. To test this hypothesis, the spherical phantom was meshed using a tetrahedral mesh with higher resolution at the origin, as shown in Figure 2.2(a). The simulated fluence vs. the analytical solution are shown in Figure 2.2(b) using blue and red curves, respectively. As seen, using

the higher resolution the FEM-based solution does match the analytical solution with a higher accuracy close to the source than the uniform mesh. It should be noted that in this discussion we are mainly interested in FEM-based modeling of DE, rather than the accuracy of DA itself in modeling the physical fluence. The results presented in Figure 2.2(b) substantiate the accuracy of the FEM code in modeling the DE.

So far we have demonstrated accurate modeling of light propagation in infinite medium using the FEM code. It was observed that high degree of modeling accuracy in very close vicinity of the source can be achieved with a non-uniform mesh with higher resolution around the source. A uniform mesh results in accurate modeling in distances larger than around 1 mm from the source. It should be further noted that in the practice of tomographic imaging (and in particular for transillumination geometries, such as in FMT-XCT), we are not necessarily interested in the exact fluence value in immediate vicinity of the source, as long as the forward model is capable of accurately predicting the fluence in other parts of the tissue.

An adequately fine mesh will result in desirably accurate matching between the fluence predicted by the FEM model and the actual fluence (either obtained from the Green's function or from a physical phantom or tissue). For a typical animal study, an average edge length of 0.5 mm for the tetrahedral edge lengths could possibly result in over 200,000 mesh nodes and around 1 million voxels. Such sizes are numerically and memory-wise prohibitive for conventional computing power. Therefore, it is critical to investigate different mesh sizes and determine the average size adequate for our purposes. To this end, we use an optically homogeneous cylindrical numerical phantom. The geometry is illustrated in Figure 2.3(a), where the source and detectors positions are shown on the cylinder boundary. As we are not necessarily interested in immediate vicinity of the source, uniform meshes of various resolution were used to assess model accuracy of FEM, as compared with Green's function solution for a cylindrical mesh. The Green's function for a finite cylinder of radius a and length l is given as

$$\begin{aligned} g(r) &= \frac{1}{\pi\sqrt{2\pi}a\,l} \sum_{m=1,\ \text{odd}}^{+\infty} \sum_{n=-\infty}^{+\infty} \cos(n\,\theta)\,\frac{I_n(\alpha_m\,r')}{I_n(\alpha_m\,a)} \\ \alpha_m &= \sqrt{3\mu_a(\mu_a+\mu_s)+\frac{m^2\,\pi^2}{l^2}}, \end{aligned} \tag{2.26}$$

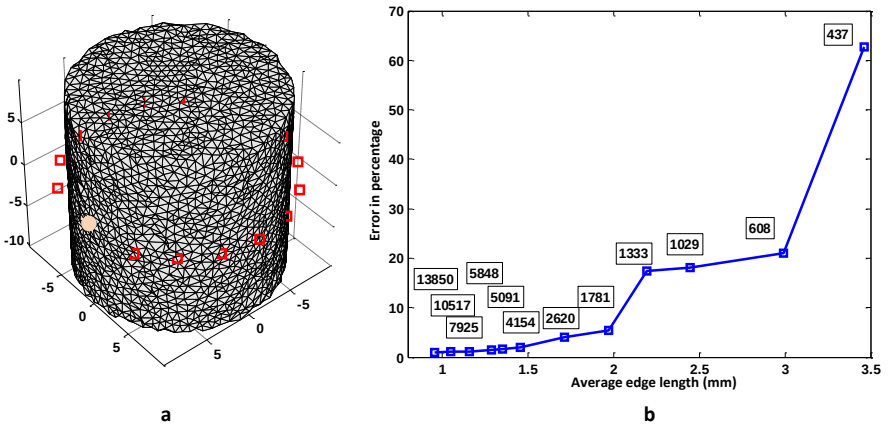

Figure 2.3: Modeling light propagation in a homogenous cylinder; (a) uniform cylindrical mesh with source and detectors denoted by orange and red markers, (b) accuracy of forward model vs. average edge sizes. The labels show the corresponding number of nodes for each given average edge size.

where I_n's are modified Bessel functions of the first kind [38]. This analytical solution holds for the dark boundary condition, where the fluence on the boundary is 0. This condition was taken into account in the FEM modeling for this specific phantom.

Figure 2.3(b) shows the accuracy of FEM modeling as relative error with respect to the Green's function solution for different mesh resolutions, represented by the average edge size of the mesh. The average error was calculate in percentage between normalized numeric and analytical solutions. It can be seen that meshes with average edge size of $\sim$1.3 mm or less result in adequately small modeling error (less than 5%). This level of accuracy attainable using a uniform mesh in modeling the light propagation is well suited for our purposes, as the other sources of modeling error due to, for instance, incomplete knowledge of tissue optical properties, cause a much larger (a few hundred percents) modeling error.

It was observed that meshing with average edge length of 2 mm or more results in unacceptable error in the modeling and degradation of the performance of the FEM-based forward solver. These observations were further confirmed using a physical agar-based phantom in the next section.

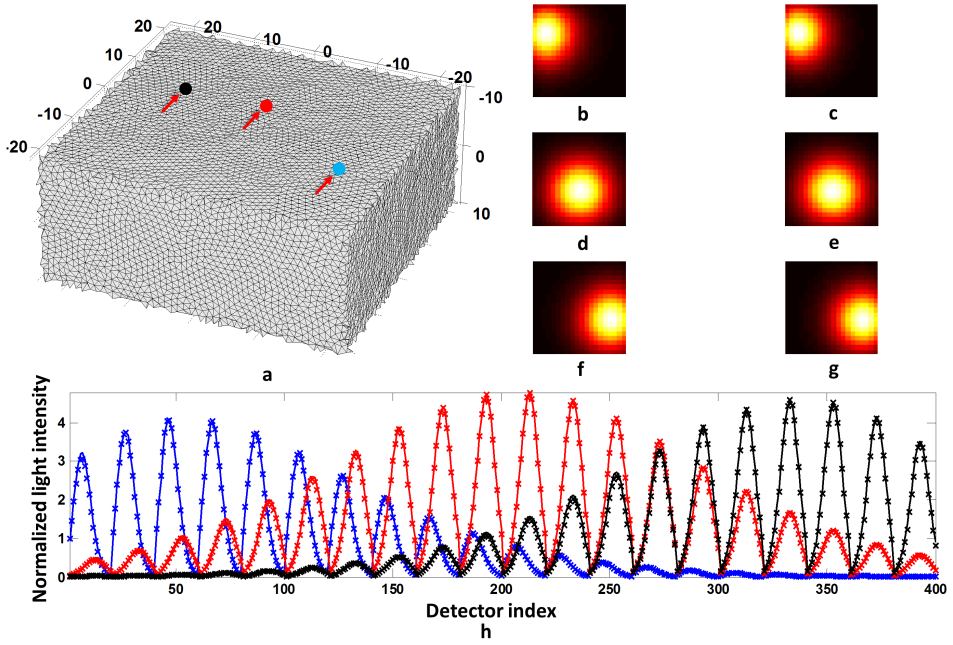

Figure 2.4: Verification of FEM code using phantom measurements; (a) the FEM mesh for the slab phantom, where the red, blue and green markers show the location of the 1st, 2nd and 3rd sources respectively. (b, c), (d, e) and (f, g) Binned measured intrinsic images for the 1st, 2nd and 3rd source positions, respectively. The measured (solid) and simulated (marked with x) signal profiles are shown in (h), where 1st, 2nd and 3rd source positions are designated using blue, red and black curves, respectively.

2.6 Physical validation

The FEM-based forward modeling code developed above was verified using phantom measurements. A slab phantom was made for this purpose.[4] The phantoms were positioned in front of a 750 nm laser and imaged with a cooled CCD camera, using the BBQ system (a planar, photographic trans-illumination imaging system) at IBMI. The positions of the laser and the phantom with respect to each other and the camera were carefully calibrated using a checkerboard. The FEM verification process was as follows. For a given source location, the optical parameters were optimized to achieve maximum similarity between the simulated and the measured signals (both normalized to their respective maxima). The same set of optical parameters and measurement were used across other

[4] Xiaopeng Ma at IBMI made this phantom and assisted with the data acquisition and measurement setup using the BBQ system.

source locations. The results for are shown in Figure 2.4 for three source positions, as depicted on Figure 2.4(a) using different makers on a mesh with 69984 nodes and 357255 elements and an average edge length of 1 mm. The signal profiles shown in Figure 2.4(h) are normalized to their maxima. The normalization factors, defined as the maximum of the measured signal to the maximum of the respective simulated signal for three source positions were 2.6367, 2.5694 and 2.6249. The slight differences between the normalization factors is likely due to the variability of the laser power between the measurement sets and other physical factors, such as calibration error or imperfect positioning of the phantoms. Otherwise, as seen in Figure 2.4(h), the FEM predictions almost perfectly match the measured signal and the normalization factors are almost the same across the 3 source positions.

Experimental phantom results were also employed to confirm conclusions of Section 2.5 regarding the required mesh resolution. The above physical phantom measurements were examined against FEM-based simulations for various edge sizes. The optical properties of the phantom were found using a trial and error based approach to minimize fluence prediction error. Then FEM modeling was performed for various mesh resolutions (quantified by average edge size) and for each resolution the modeling error was calculated. The results are demonstrated in Figure 2.5, where edge sizes of around 1.3 mm or less were observed to provide an acceptable modeling error, as also predicted by numerical simulations above.

2.7 System model of FMT

The goal of this section is to derive the relationship between the X and the optical measurements collected on the tissue surface. It is known that the relationship is described by a linear model [47,48]. The discretization of the tissue volume using a tetrahedral mesh of N nodes also presents a framework for representation the fluorophore distribution as a represented by a $N \times 1$ vector X. Each entry of X represents the fluorophore concentration on a given mesh node. The concentration is defined as the product of the absorption cross-section of fluorophores and their quantum yield. The process of modeling FMT is schematically shown in Figure 2.6. We make use of the FEM formulation describing the propagation of the excitation and emission photons in tissue, as described in Section 2.3.

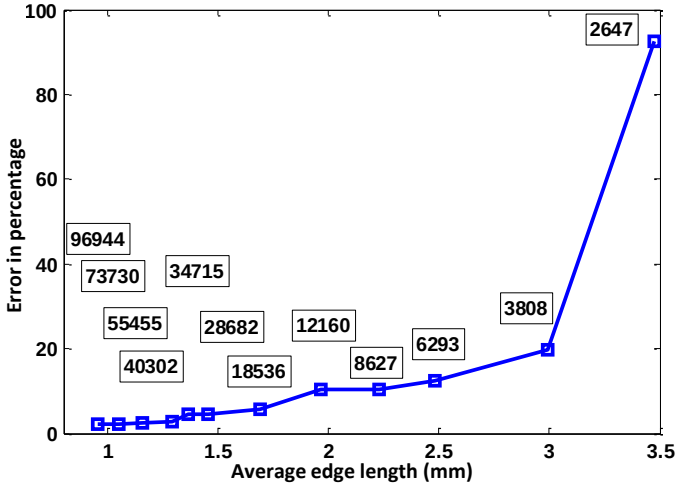

Figure 2.5: FEM modeling error versus edge size for experimental data. The labels show the corresponding number of nodes for each given average edge size.

The stiffness matrices obtained from the FEM formulation at the emission and excitation wavelengths are denoted by $N \times N$ real matrices $\mathbf{H}_m$ and $\mathbf{H}_e$, respectively (note that for the CW case the matrices are real while in the frequency domain, they are complex [48]). For the excitation and emission wavelengths, denoted by subscripts e and m, assuming the i^{th} source is illuminated we have (using author's methodology in [47])

$$\mathbf{H}_m \Phi_m^i = S_m^i \tag{2.27}$$

$$S_m^i = \text{diag}\left(\Phi_e^i\right) X \tag{2.28}$$

$$\mathbf{H}_e \Phi_e^i = S_e^i, \tag{2.29}$$

where S_e^i (S_m^i) and Φ_e^i (Φ_m^i) are column vectors denoting source intensity and light fluence for respectively the excitation (emission) wavelength. The excitation source vector S_e^i is non-zero only on the mesh nodes that are in the illumination spot of the i^{th} diffusive source. For the emission wavelength, each mesh node can be regarded as an optical source whose intensity is determined by the local fluorophore concentration on that node and the local excitation fluence. As a result, Equation 2.28 holds, where the operation "diag" converts a vector to a diagonal matrix. Furthermore, assuming the measurements are obtained at the emission wavelength, denoted for the i^{th} source by a column vector M^i consisting

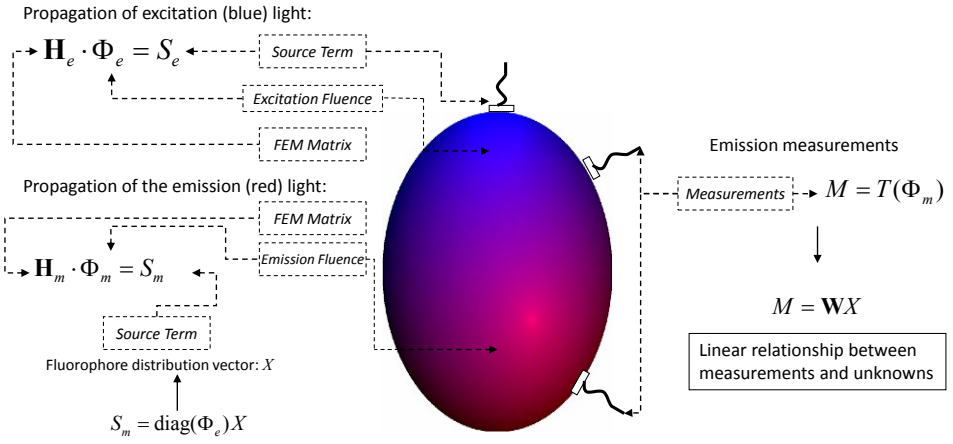

Figure 2.6: Diagrammatic description of FMT modeling steps.

of Q (number of detectors) entries, we have

$$M^i = \mathcal{T}\left(\Phi_m^i\right), \tag{2.30}$$

where $\mathcal{T}$ is an operator relating the fluences to the measurements, such as a $Q \times N$ real matrix describing measurement obtained on each detector as a linear combination of the fluences of its neighboring nodes. By combining Equation 2.27- 2.30, we can establish a linear relationship between measurements and the solution vector X. The entire measurement vector is given by a $PQ \times 1$ column vector M defined as

$$M = \left[M^{1^\top} \quad \dots \quad M^{P^\top}\right]^\top. \tag{2.31}$$

The linear FMT system model is then given as

$$M = \underbrace{\begin{bmatrix} \mathcal{T}\left(\mathbf{H}_m^{-1}\mathrm{diag}\left(\mathbf{H}_e^{-1}S_e^1\right)\right) \\ \vdots \\ \mathcal{T}\left(\mathbf{H}_m^{-1}\mathrm{diag}\left(\mathbf{H}_e^{-1}S_e^P\right)\right) \end{bmatrix}}_{\mathbf{W}} X + \upsilon, \tag{2.32}$$

where υ denotes the measurement noise. The inverse problem of FMT consists of solving Equation 2.32 for X given M and $\mathbf{W}$. In derivation of the system model, it was assumed that the optical properties of the tissue are known. In practice, same sets of homogenous or organ-specific optical scattering and absorption are used for the forward modeling at both

excitation and emission wavelengths [25, 49]. The fluorescence measurements are oftentimes normalized using the measurements obtained at the intrinsic (or excitation) wavelength. The so-called normalized Born ratio consists of dividing the fluorescence measurement by the intrinsic [50]. This normalization removes the uncertainty associated with such physical factors as the laser or detector coupling. Moreover, the impact of modeling error introduced by incomplete knowledge about tissue optical properties is largely mitigated by Born normalization [51].

The linear system model of FMT with regard to the Born normalization can be alternatively derived using the following equation

$$b_{s,d} := \frac{f_{sd}}{i_{sd}} = \int_{\Omega} \frac{g(s,r)\, g(r,d)}{g(s,d)} X(r) d\Omega, \tag{2.33}$$

where $i_{s,d}$, $f_{s,d}$ and $b_{s,d}$ denote the intrinsic and fluorescence measurements and the Born ratio for source s and detector d, respectively. $g(p,q)$ denotes the Green's function between points p and q and the integral is taken over the tissue volume Ω and $X(r)$ denotes the fluorophore concentration on point r. Using volumetric discretization, Equation 2.33 can be written as

$$b_{s,d} = \sum_{i} \frac{g(s,v_i) g(v_i,d)}{g(s,d)} X(v_i), \tag{2.34}$$

where the summation is taken over all the voxels. The GF values g are found using the FEM formulation presented above.

2.8 Conclusion

In this chapter a modeling approach for FMT based on finite-element based discretization of the diffusion equation was developed. The proposed method was efficiently implemented in MATLAB and is capable of handling large tissue samples several centimeters in diameter. It was shown that the developed FEM code is capable of accurately modeling light propagation in numerical as well as physical phantoms. The effect of the mesh resolution was examined on the modeling accuracy and it was concluded that a uniform tetrahedral mesh with an average edge size of 1.3 mm or less is capable of modeling light propagation with an accuracy adequate for practical purposes. We further presented the derivation of

the mathematical model of the FMT as a linear system based on the FEM formulation. The practical problems encountered in development of the MATLAB-based FEM code were discussed. Efficient utilization of the developed light propagation framework toward processing FMT-XCT measurements requires an accurate geometrical description of the various optical and CT components - an issue addressed in the next chapter.

3 FMT-XCT calibration and acquisition methodology

3.1 Introduction

Hybrid modalities and in particular the combination of FMT and XCT, called FMT-XCT and recently developed at the Institute for Biological and Medical Imaging (IBMI) in Helmholtz Zentrum München (HMGU) [32], provide a wealth of information across time and space regarding molecular function as well as anatomy of tissue. FMT-XCT is a hybrid modality, where three-dimensional (3-D) entities of two separate origins are combined toward improved performance. The anatomical information from the CT component is rendered as a 3-D image, where every element represents the local absorption of X-ray photons in a given volumetric voxel. The raw FMT data is acquired on the other hand as two-dimensional (2-D) fluorescence and intrinsic images. The FMT-XCT system and its components are shown in Figure 3.1. The system is comprised of a cooled-CCD and two laser sources, in an axis perpendicular to the X-ray tube and the X-ray camera axis [32]. There is also the provision of obtaining front-illumination images using electroluminescent foils. The animal is placed on a bed (comprised of two parallel carbon rods, often connected through threads in a zigzag formation) and slid into the imaging chamber. The animal is kept under anesthesia during the whole imaging period. The optical images are obtained using a set of optical filters in 360 degree rotation geometry. The imaging system is controlled using LabView (National Instruments, Austin, TX, USA). The FMT also supplies metadata; specifically, the location of the translation stage which moves the fiber tip as well as respective laser powers and exposure times for both wavelengths and gantry angles are saved as metadata by the system. Imaging using FMT-XCT involves the solution to

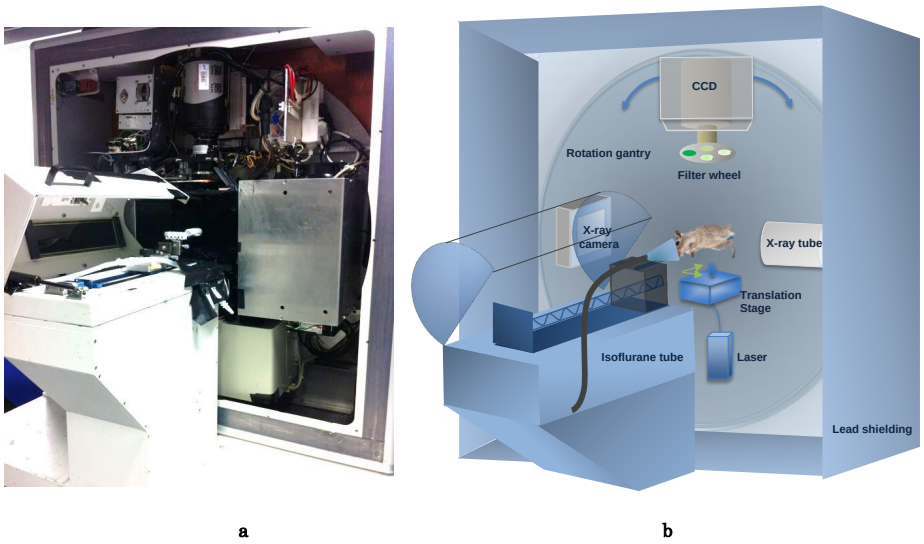

Figure 3.1: The FMT-XCT hybrid imaging system; (a) photograph of the system with front lead cover removed, (b) the optical and X-ray components shown on perpendicular axes, mounted on a rotating gantry.[1]

the forward and the inverse problems. Furthermore, the end result of the FMT-XCT is a 3-D matrix, representing the volumetric reconstruction of the fluorophore concentration. This solution matrix is often rendered two or three-dimensionally along with the underlying CT data. Examples include isosurfaces or transparency maps imposed over the CT slices. All the steps during the process of imaging, including solving the forward and inverse problems as well as final coregistration and demonstration, require an accurate geometrical mapping between various volumetric and planar entities arising in optical and CT domains. The issue of finding this spatial mapping is referred to herein as geometrical calibration or simply calibration. In this chapter we analyze the different components of the FMT-XCT that require geometrical calibration and the challenges involved and present a calibration framework. The proposed framework consists mainly of two intertwined steps; the camera calibration and the source calibration. The former involves a mathematical description between the CT domain and the optical domain using a pinhole model at several equispaced gantry angles and the later addresses laser beam position in space. The calibration is performed using a resin-based cylindrical calibration phantom with a diameter of 19 mm. Although inherently a

[1] Xiaopeng Ma at IBMI contributed to the graphic design.

tedious task, the entire procedure has been mostly automatized, so that minimal user interference is required. The FMT-XCT systems located at the HMGU and the Klinikum rechts der Isar have been both accurately calibrated using this framework.

3.2 Camera calibration

A calibration phantom is needed to find the geometrical mapping between the CT domain and the optical domain. Camera calibration, defined as derivation of a mathematical model describing the geometrical relationship between the image plane and the real world, is conventionally accomplished using a checkerboard [52]. The checkerboard is imaged using the camera at several positions and the square corners are then extracted. Such an approach is difficult to use for our calibration purposes. The reason is that the limited field and depth of view of the camera necessitate imaging the checkerboard using the CT and the camera at many orientations and positions. The fact that the camera should be calibrated at many gantry angles due to imperfect circular motion of the gantry and unaccounted-for mechanical movements between different gantry angles, made this process very cumbersome from a practical point of view.

Instead, we developed a cylindrical silicon phantom with a diameter of 19 mm, as depicted in Figure 3.2.[2] The phantom has special fiducial surface features that make the calibration feasible. The surface of the cylinder was covered with white paper and then marked with stripes of black electric tape. The tapes are clearly visible in the optical images and also have pronounced absorption of X-ray photons; therefore clearly seen in the CT. To be able to correctly index the corners of the stripe intersections (to be used later during the calibration), four squares were marked with 1, 2, 3 or 4 pieces of black electric tape; also visible in both CT and optical domains. Due its surface curvature the cylindrical object covers a relatively large depth of view, hence yielding a proper estimate of the camera calibration matrix using few object positions.

Let (x, y) designate a pixel in the image domain for a given gantry angle θ. Using the concept of homogenous coordinates and the pinhole camera

[2] Maximilian Koch at IBMI contributed to the idea of using this calibration phantom.

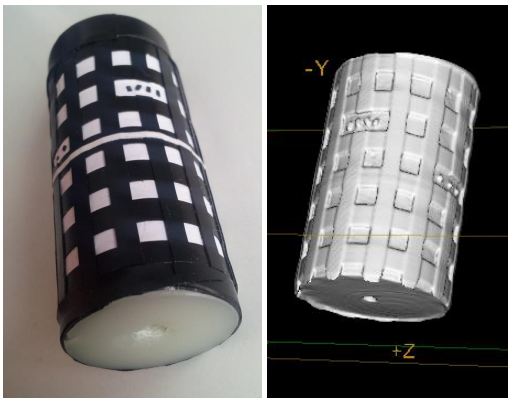

Figure 3.2: FMT-XCT calibration phantom; (a) the photograph of the silicon cylinder marked with stripes of black electric tape (b) isosurface of the CT. The features are designed so as to be visible in both optical and CT domains. Small black dots in (a) made automatic indexing of the stripes possible.

model,[3] the set of points (X, Y, Z) in the 3-D coordinate system which are projected onto this pixel through the camera satisfy the following equation

$$\begin{pmatrix} xw \\ yw \\ w \end{pmatrix} = K^{\theta} \left(X, Y, Z, 1\right)^{\top}, \tag{3.1}$$

where $w > 0$ and K^{θ} is a 3×4 matrix, called the camera matrix [52]. The variation over w allows for a set of 3-D points projected onto (x, y) which all fall on a 3-D line in space. Let θ_1 through θ_N designate the set of gantry angles for which the camera matrices K^{θ} have been calculated. For any other angle, θ then matrix K^{θ} is then estimated as a linear combination of the camera matrices of the adjacent 2 angles. That is

$$K^{\theta} \simeq \frac{\theta_{i+1} - \theta}{\theta_{i+1} - \theta_i} K^{\theta_i} + \frac{\theta - \theta_i}{\theta_{i+1} - \theta_i} K^{\theta_{i+1}}, \tag{3.2}$$

where $\theta_i \leq \theta \leq \theta_{i+1}$.

To find the camera matrix at several projection angles simultaneously, the calibration cylinder of Figure 3.2 was placed on the animal bed and front-illumination images were obtained at several gantry locations, followed

[3] The previous processing framework described in [32] used parallel projection model which was found to be not as accurate as the pinhole model. A methodologically different calibration approach has been described in [53] - however, the method proposed in here was developed independently.

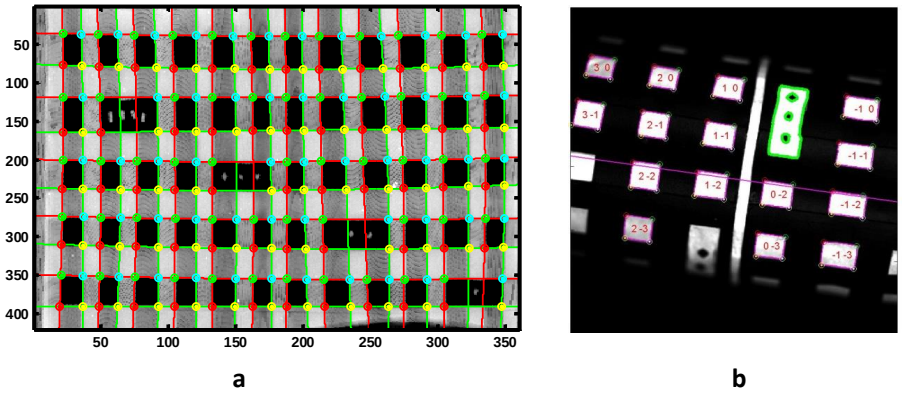

Figure 3.3: Automatic corner detection and indexing of the calibration phantom; (a) the rolled out surface of the CT scan with the automatically detected white stripes (black tape) marked by vertical and horizontal green and red lines and four corners around each black square (white paper) marked with red, yellow, cyan and green dots, (b) the indexing of the white squares on the photograph of the cylinder. The numbers within each square show vertical and horizontal distances from the marked rectangle (here the rectangle with 3 spots).

by acquisition of the CT scan. The process is repeated for the cylindrical phantom with different geometrical orientations (nominally 4-5 orientations deliver a satisfactory level of calibration accuracy). For a given orientation and gantry angle, the cylinder surface from reconstructed CT volume is automatically extracted and "rolled out" in a rectangle, as shown in Figure 3.3(a).

The corners of the black rectangles in the rolled-out image, corresponding to the areas covered with white paper, are detected using a corner detection approach for accurately locating the actual corner in the vicinity of line intersections. The corners are then indexed according to the vertical and horizontal distance from the nearest of the 4 larger rectangles (marked with 1 to 4 small black tape spots). The corresponding locations of the extracted corners are then found in the CT coordinate system. The corners of the front-illumination image are found and indexed accordingly, as shown in Figure 3.3(b). These corners are found based on segmentation of the thresholded binary image where the curved-quadrilaterals are recognized according to the object properties (such as area, orientation and convex hull). The sets of corresponding 2-D corners (extracted from the optical images) and 3-D corners (extracted from the CT volume) extracted at several phantom orientations for a given gantry

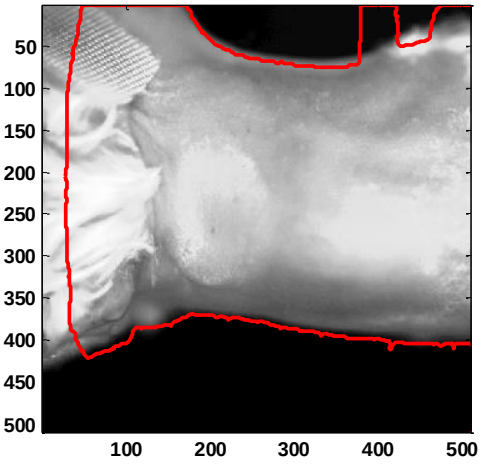

Figure 3.4: Calibration accuracy between CT and optical domains; the red curve shows the outline of the projection of the CT volume over the mouse photograph. The non-matching locations on the top right corner are due to objects in the back side, visible in CT but in the photograph. The left-most part of the photograph falls outside of the FOV of the X-ray detector.

angle are processed using `CVX`, a MATLAB-based toolbox package for specifying and solving convex programs [54, 55]. The result of the optimization is the 3×4 camera matrix for that particular gantry angle. The FMT-XCT systems were calibration for 68-72 such gantry angles. The performance of the camera calibration is shown in Figure 3.4 for an animal study, demonstrating a very accurate matching between the projected volume and the boundary of the animal in the front-illumination photograph.

3.3 Laser calibration

The laser calibration consists of finding the 3-D line corresponding to the laser beam, given a gantry angle and 2-D laser stage position (available from the FMT-XCT metadata as a pair of numbers in millimeters). The laser stage is mounted on a 2-D translation stage. For a given (r, s) location of this stage, let $L(r, s)$ denote the 3-D laser beam line. The laser beam illuminates the calibration plate (consisting of a glass slab cover with a white plate for optical marking) at the first and second positions at locations P_1 and P_2. These points are seen on the camera at

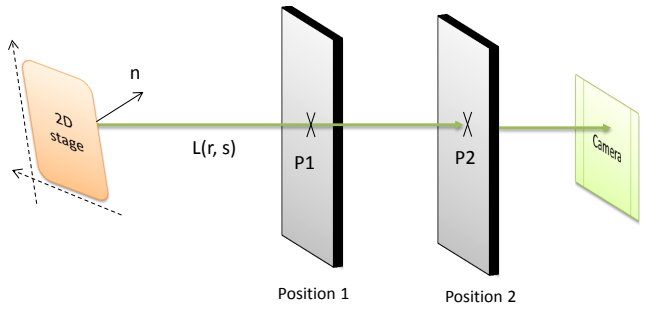

Figure 3.5: Geometrical laser calibration; the location of the laser beam in the 3-D coordinate system is found using a glass plate at two different locations, where the incidence points, P_1 and P_2 are found using the camera calibration results.

pixels p_1 and p_2. We use this information to find $L(r, s)$ and the normal vector n.

Given the gantry angle, we have the camera matrix from the previous calibration stage. Also using the CT reconstructions of the plates, we have the 3-D planar description of the calibration plate at positions 1 and 2. Let $A_1 = (a_1, b_1, c_1, d_1)$ and $A_2 = (a_2, b_2, c_2, d_2)$ denote these 3-D planes, where $a_i\, x + b_i\, y + c_i\, z + d_i = 0$.

For say the first plate position we have

$$\begin{pmatrix} x_1 w \\ y_1 w \\ w \end{pmatrix} = K^{\theta} \begin{pmatrix} P_1 \\ 1 \end{pmatrix} \tag{3.3}$$

$$A_1 \begin{pmatrix} P_1 \\ 1 \end{pmatrix} = 0. \tag{3.4}$$

This system of equations contains 4 unknowns (P_1 and ω) and 4 equations. The solution yields the 3-D location of the intersection of the laser beam and the calibration plate, i.e. P_1. The same approach yields P_2 for the second position. These two points yield the 3-D laser line for the translation stage location (r, s). The set of the line equations for at least 3 translation stage positions (forming a triangle with a non-zero area), give the normal vector n and the laser beam location for any stage position.

For a given gantry angle θ, a subset of 3-D points on the imaging sample surface, are seen on the camera. Here we also analyse the mapping between these 3-D points and the corresponding pixels. Let us assume that the points $P = (X, Y, Z)$ is located on the surface of the sample and is visible by the camera for the angle θ, at pixel (x, y). Then (x, y) is found using Equation 3.1. That is, the mapping from 3-D to 2-D is straightforward, given the correct camera matrix K^θ. The inverse mapping, i.e. from image to volume is computationally more involved. This problem arises in mapping detector points from the images to the sample surface. The mapping from pixel to volume is achieved using a ray-tracing approach by finding the intersecting the 3-D line (representing all 3-D points mapped to the given pixel) and the volume. The ray tracing operation makes use of the geometrical description of the CCD camera, as modeled in Section 3.2. To reduce the numerical complexity of the ray tracing operation, an initial estimate of the 3-D intersection point of the volume surface and the spatial ray associated with the 2-D pixel is found using a parallel projection simplification of the camera model matrix. This initial estimation is then refined in its neighborhood using the accurate camera matrix.

3.4 Optimizing the acquisition protocol

FMT-XCT imaging comprises optical and CT acquisitions. The CT imaging part lasts around 20 minute for the system at HMGU and less than 3 minutes for the newer system at Klinikum rechts der Isar and can be performed before or after optical imaging. The quality and length of the optical imaging heavily depends on the acquisition protocol. The previously used imaging protocol is presented as a flowchart in Figure 3.6(a). This method involves moving turning the laser off and on as well as several filtering flips (as many as source positions) in each gantry location. This method results in a large mechanical overhead. Furthermore, the output power of the laser was observed to fluctuate significantly (up to 40%) in a non-negligible time interval (up to several tens of seconds) every time the laser is switch from the “off” state to the “on” state; again, carried out as many times as the number of sources in every gantry location. These laser power fluctuations cannot be accounted for and result in error. A typical FMT acquisition using this approach lasts 40-50 minutes.

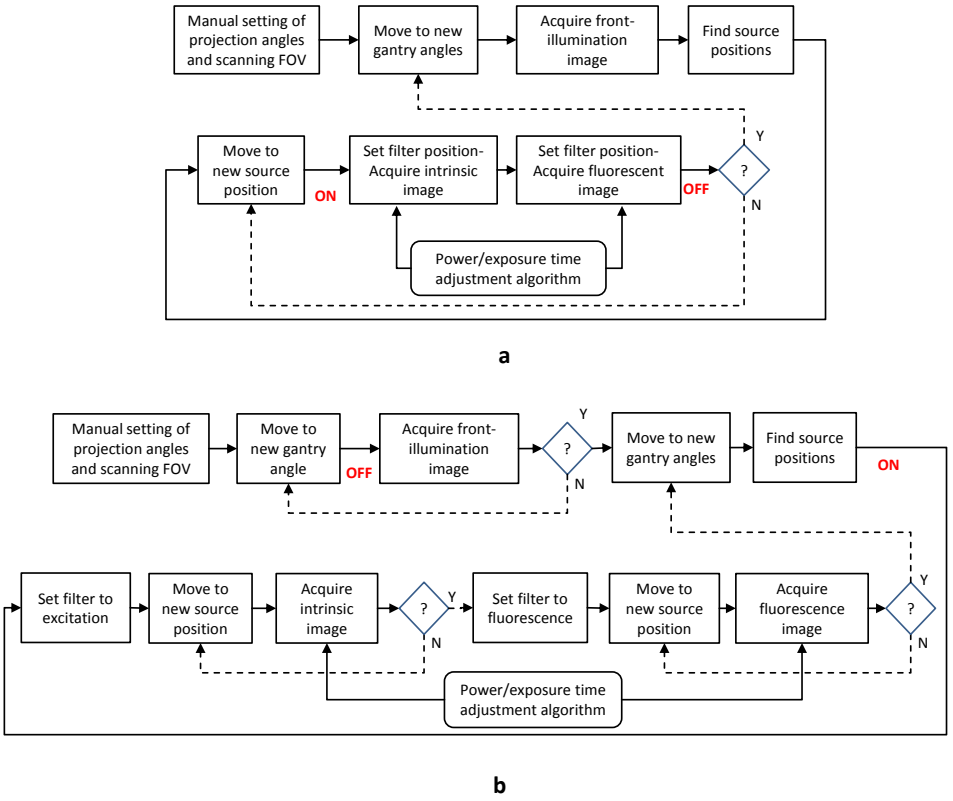

Figure 3.6: Previous and improved FMT acquisition methodologies; (a) the flowchart of the previous protocol, (b) the flowchart of the improved and current approach. The rhombi denote conditional units, where the "Y" port is valid upon completion of the preceding operation. Red ON and OFF labels denote activity status of the laser.

The improved and currently used method, presented in Figure 3.6(b), overcomes some of these limitations. The set of all front-illumination images is obtained before the fluorescence measurements. This set is stored and later retrieved for automatic source positioning. During the acquisition of the front-illumination images, the eletrolumiscent panels are turned on and the laser is turned off. As seen, all the intrinsic and all the fluorescence images are acquired then in one setting. The laser is kept on during the entire imaging. While turning the laser on from the off state was observed to result in large power fluctuations, changing the laser power in the "on" state resulted in reasonably small fluctuations. This approach results in significantly lower mechanical overhead and more accurate imaging; a full *in vivo* mouse measurement set lasts around 20-25 minutes to acquire, indicating a two-fold improvement in

the acquisition speed. Several modes with different degrees of adaptation are available for adjustment of laser power and exposure time. Adaptive methods start with a given laser power (intrinsic wavelength) or exposure time (fluorescence wavelength) and increase it until a preset maximum signal intensity is achieved [32]. We observed in several animal experiments that fixed settings of laser power often result is reasonable dynamic range of images at both wavelengths; a fact which can be used to lower the imaging time. The actual optical measurement time is fairly small. Assuming 20 gantry angles, 300 source positions and exposure times of 100, 100 and 500 ms for front-illumination, intrinsic and fluorescence images respectively, the physically minimum imaging time is around 3 minutes. The rest of the 20-25 minute acquisition time is owed then to mechanical movements of the gantry, filter wheel and laser stage as well as CCD readout time, laser power/exposure time adjustment and LabView (National Instruments, Austin, TX, USA) overhead. Further optimization of acquisition protocol and power/exposure time adjustment methods are possible and potential topic of future work (Section 10.2). This acquisition approach also enabled us to further expand FMT to clinical applications, as presented in Chapter 9, where a clinical acquisition was optimized to last around 12 minutes.

3.5 Conclusion

In this chapter we described a two-step procedure for geometrical calibration of the FMT-XCT system. In the first step, 3×4 camera matrices based on the pinhole camera model were extracted for several gantry angles using a cylindrical calibration phantom. The phantom was carefully marked so that the fiducial features were visible in both optical and CT domains. The reconstructed CT scan was automatically rolled out and the corners were picked and indexed. The camera matrix for arbitrary angles was then found as a spatial interpolation of the calibrated angles. The results of the camera calibration were used in a second step to calibrate the location of the laser beam, as 3-D line, in the camera coordinate system. The camera calibration was shown to have a high accuracy in mapping the CT domain to the optical domain. Both FMT systems located at the IBMI and Klinikum were calibrated using this approach. We further analyzed the LabView acquisition approach and

proposed a method with approximately two-fold improvement of the acquisition speed. We build upon the forward modeling presented in the previous chapter along with the accurate system calibration results of this chapter, to develop in the next chapter a comprehensive framework for processing of datasets acquired by the FMT-XCT systems.

4 Optimized processing for FMT-XCT

4.1 Introduction

Development of hybrid modalities which utilize the sensitivity as well as molecular and functional information afforded by optical imaging and the anatomical information of another modality, such as magnetic resonance imaging (MRI) or computed tomography (CT), help improve imaging quality and accuracy [25, 32, 56, 57]. In particular, X-ray CT has been used to mitigate the low spatial resolution and ill-posed nature of the FMT through provision of high-resolution anatomical images, as discussed in Section 3.1. The 3-D CT images are used in conjunction with FMT toward more accurate molecular imaging. The anatomical data are employed in the reconstruction as *a priori* information in the inversion as well as for geometrical characterization of the tissue and improving light propagation modeling accuracy.

The efficient synergy of these datasets is only possible through careful development of data processing, forward modelling and inversion algorithms as well as robust user interface and display frameworks. Furthermore, in processing FMT-XCT measurements one has to deal with huge datasets which place particular limitations on the memory and computational units of the computer. The processing code should be optimized to handle such issues efficiently and also optimally extract the desired biological information embedded in the datasets. The challenges one faces during code development for FMT-XCT processing can be divided into two categories. The first category includes the necessity of accurate forward modeling of light propagation in tissue and the inverse problem. The second category includes computational and memory issues which can become quickly prohibitive if not properly handled, due to the sheer

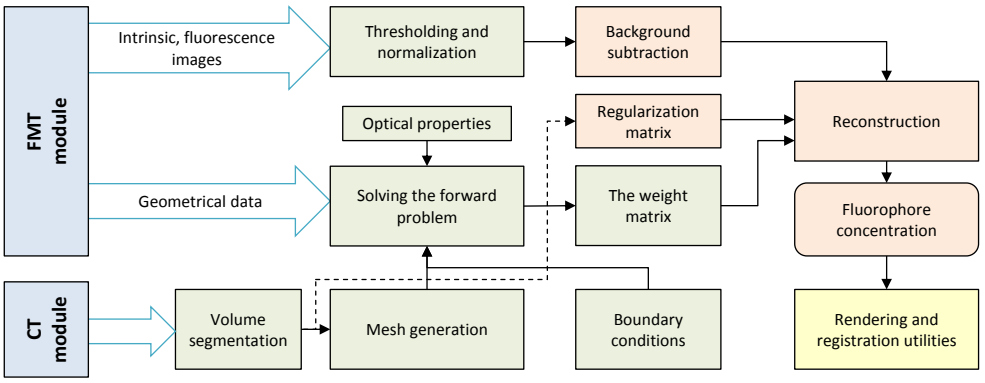

Figure 4.1: Flowchart of the XFMT code; hardware units are shown with blue boxes, data preprocessing and conditioning and forward processing units are shown with green boxes and inversion units are depicted with orange boxes.

size of the datasets involved. In this chapter we present a processing framework (also called in this work the XFMT code) that was developed during this research for efficient processing of FMT-XCT datasets and the code architecture as well as numerical issues involved and addressed toward optimized processing.[1] The development here was performed in the MATLAB environment. While it is not possible to elaborate all programming challenges herein, we do describe few important tissues in detail.

4.2 Code development and structure

The general flow of the different hardware and processing blocks of the FMT-XCT system are given in Figure 4.1. For conciseness, the hardware are denoted simply as FMT and CT modules. More details regarding the hardware can be found in [32].

4.2.1 Data processing and forward problem

The processing blocks in Figure 4.1 which relate to importing data to the code, preconditioning of the data and setting up and solving the for-

[1] Few modules (mainly the LSQR solver and raw data file readers) are shared between the framework developed and presented here and the code previously used at IBMI and reported in [32, 57, 58]. The author appreciates Maximilian Koch and Dr. Angelique Ale at IBMI for the discussions during the evolvement of the code developed by the author and presented here.

ward problem are marked with green color. The FMT-XCT hardware generates optical measurements and metadata, stored in `SPE` (image saving format from Princeton Instruments, Trenton, NJ, USA) and `FMT` files respectively, as well as CT `DICOM` (abbreviation of Digital Imaging and Communications in Medicine) files. The CT data is processed using GE's proprietary software, which reconstructs a 3-D `uint16` (16-bit unsigned integer format) matrix. The metadata consist of positions of the laser translation stage as well as the laser powers and exposure times for each position and wavelength. The code reads all the `FMT` files in the corresponding folder and combines files into a single dataset - it is assumed that the different `FMT` files corresponding to separate gantry angles, as the imaging operation might have been interrupted and resumed. The code automatically determines if the gantry has mechanically jittered during the imaging, resulting in gantry angles and images in between the preset equispaced angles. Such outliers are discarded. The front-illumination images are extracted either from the `EPI` file (for the new acquisition LabView code) or from the `SPE` file (for the older versions, see Section 3.4). The CT dataset is read from the `VFF` file (SUN™ TAAC file format) and cropped around non-zero volume. The entire combined dataset is then normalized for laser power and exposure times. Next, "CT preview" images are generated, which are defined as maximum intensity projection (MIP) images of the CT volume seen through the CCD camera. These images, when viewed with fluorescence, intrinsic or Born images superimposed as transparency overlays, help with settings of several regions of interest (ROIs) (an example of a CT preview can be seen in Figure B.1).

Prior to further processing, several regions of interest (ROIs) should be adjusted. Specifically, 3 ROIs can be distinguished; the reconstruction, detector and meshing ROI, corresponding to the regions within which, respectively, the inversion is performed, the optical measurements are used and the light propagation is modeled. While the code makes automatic suggestions for these regions, the user is given the possibility to manually adjust them as well (further explained in Appendix B). The initially suggested reconstruction and detector ROIs are set to the scanning region of the laser and the meshing ROI is set to a 2-3 mm expansion of the scanning ROI in the axial direction. We assume air-to-tissue boundary condition for the entire volume. It was found that the 2-3 mm expansion results in an adequately accurate modeling of tomography purposes.

As shown in Section 2.5, a uniform mesh with an average edge size of

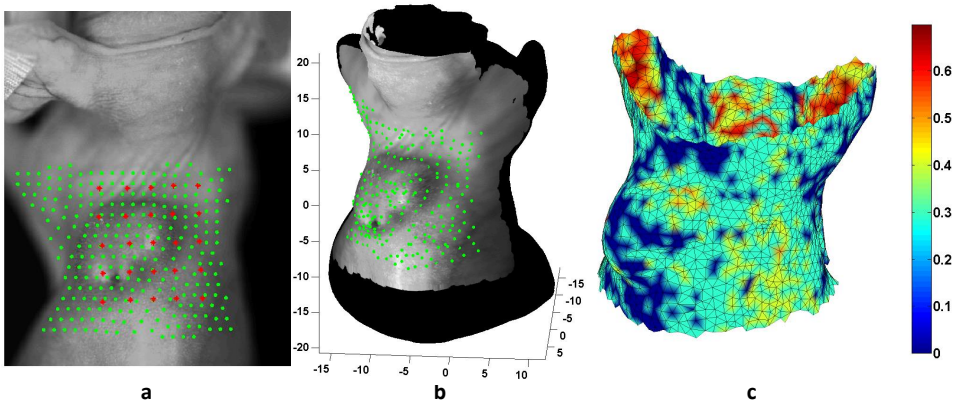

Figure 4.2: Meshing and ray tracing demonstration; (a) a front-illumination image along with the 2-D detectors (green dots) and the 2-D source locations (red starts), (b) the isosurface of the animal volume with the front-illumination image wrapped on the surface along with the 3-D detector points projected on the skin via ray tracing and (c) distances between the surface mesh nodes and the actual skin in mm, representative of meshing accuracy. All numbers are in millimeters.

1.3 mm or less results in a fairly accurate solution of the forward problem. Particularly, the meshing is achieved by starting with a coarse mesh with a given maximum surface element size (denoted by `radbound` in the `ISO2Mesh` framework and set to 10). A tetrahedral mesh is then generated from the labeled volume tensor (achieved through segmentation of the CT volume) for the given surface element size and then the average edge length is calculated. If the average edge size is smaller than the preset value (typically 1.3mm), the `radbound` is arithmetically reduced and the process is repeated until the desirable average edge size is achieved. This process typically results in a tetrahedral mesh of $\sim$ 10000-15000 nodes and around 50000-75000 elements for a typical animal study. Further segmentation of the CT volume is possible and accomplished through semi-automatic and automatic methods [59]. Semi-automatic tracing-based segmentation, for instance possible using Amira (Visage Imaging, Richmond, Australia), is an approach which was found to be especially efficient for segmentation purposes.

4.2.2 Measurement vector generation

The 2-D detector points are determined in the optical image domain, using the projections of the CT volume through the CCD camera (i.e.

CT preview images, defined above in Section 4.2.1). The 3-D detector positions are then found by tracing the 2-D points in space back to volume surface (e.g. animal skin). The source positions are initially given as real 2-tuple metadata denoting the corresponding positions of the laser translation stage. These values are converted 3-D laser beam lines in space, using the laser calibration results of Section 3.3, and intersected with the volume surface using the aforementioned ray tracing approach. An example of a meshed volume along with the 3-D source and detector positions and their 2-D projections are shown in Figure 4.2.

For every detector point, the corresponding intrinsic and fluorescence measurements are calculated and the Born ratio is found as the ratio of the two measurements [50]. The data with saturated fluorescence or intrinsic values or with intrinsic values smaller than a threshold (typically 100 counts, which is justified as a typical dark CCD image ranges between 580-700 counts and all images are thresholded at 620 before the processing) are excluded. A typical *in vivo* study can result in up to half a million measurement points.

4.2.3 Solving the forward problem

Forming the weight matrix requires knowledge about the Green's function values between sources and detectors, sources and voxels and voxels and detectors, as explained in Section 2.7. Each source or detector point is modeled using the spatial FEM basis functions of the surface element that encompasses the corresponding 3-D point (estimated using the laser calibration information and the ray tracing approach, as explained in Section 3.3. Given a source or detector point, the element containing that spatial 3-D point if found. The search algorithm first finds a group of elements with centroids in the vicinity of the given 3-D point. Then, the surface element containing the point is found from within this group. The same approach is applied where the source or detector points are modeled using diffusive patterns (such as using Gaussian-shape filters). For every source or detector, the forward solution is then found by solving Equation 2.14. The forward problem is used solved gradient method, described above, using a preconditioning matrix derived as incomplete Cholesky factorization of the weight matrix [60].

In a typical animal study with 20 projections and 20-30 source positions and 200-400 detectors points for each projection, the forward problem

should be solved on average $20 \times (25 + 300) = 6500$ times. Many of these individual source or detector locations share the same boundary nodes; a fact which can be employed to reduce the computation burden of the forward solution. Specifically, it is computationally favorable to solve the forward problem for all of the boundary nodes of the tetrahedral mesh, which fall in the field of view. For an average animal volume, mesh edge size of ≈ 1.3 mm and axial field of view of ≈ 15 mm, there exist less than 2500 surface mesh nodes within the axial FOV. Once the forward problem has been solved for all surface nodes in the field of view, the desirable Green's functions can be easily found as linear combinations of forward solutions of corresponding surface nodes.

4.2.4 Mitigating the effect of non-specific fluorescence

The impact of the fluorescence emanating from general, non-targeted tissue due to unspecific uptake or distribution of the fluorescent probe is further reduced using methods described in [61,62] (the method described [61] in has been shown to improve imaging performance for FMT-XCT [63]). These methods consists of modeling the Born ratio associated with the fairly homogenous background fluorescence of the injected probe using a 1^{st} degree [61] or 3^{rd} degree [62] polynomial function of the source-detector Euclidean distance. We have implemented these estimations in the XFMT code allowing manual or automatic determination of the approximating linear or cubic functions. The polynomials are fit using constrained optimization to the following function

$$f(r) = P_\alpha \left\{ m_{s,d} | r - \delta < r_{s,d} < r + \delta \right\}, \tag{4.1}$$

where for a given set S, $P_\alpha(S)$ denotes the α-percentile of S defined as a real value which is larger than α percent of all the elements of S. The parameter α is typically set to a very small value (e.g. 0.1) and δ is set to 0.5 mm. The operation and rationale of the background subtraction method is demonstrated in Figure 4.3 for a mouse-shaped numerical phantom with uniform and heterogeneous distributions of background fluorescence. The linear approximation often delivers reasonably good results; however, depending on the specific study, other methods such as using cubic polynomials might be more suitable.

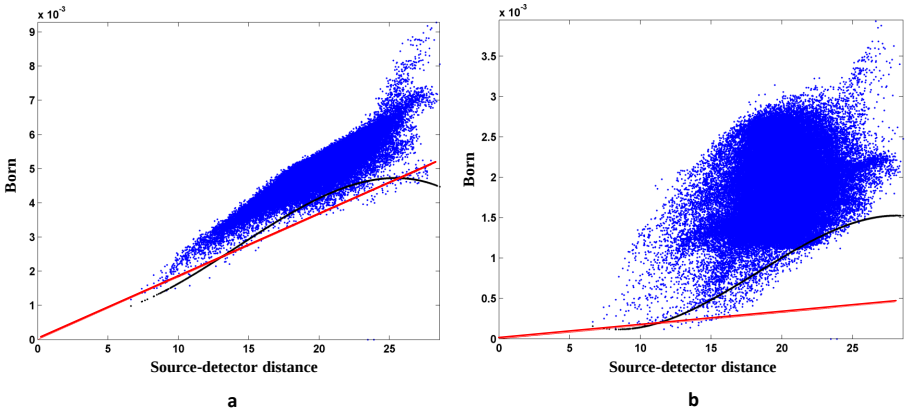

Figure 4.3: Approximation of background fluorescence using polynomials; linear (red) and cubic (black) approximations of the simulated Born signal vs. source-detector distances for (a) a mouse-shaped phantom with uniform background fluorescence and (b) the same phantom, but with heterogeneous, yet smooth background distribution.

4.3 Regularization and inversion approaches

Although the number of measurements in the FMT is typically much higher the number of unknown variables, the FMT linear system model is highly ill-posed as other optical tomography methods such as DOT [64, 65]. Hence, unconstrained inversion of the linear system results in highly irregular solutions, with an unrealistically large dynamic range. Constrained or regularized optimization can, however, result in fairly accurate reconstructions of the underlying distribution. Although the fluorescence distribution is not known in advance, it is assumed to have certain deterministic and statistical properties. For instance, the unknown vector X is bounded as non-negativity of the distribution sets a lower bound of 0 on X and the total injected probe quantity determines an upper bound. Furthermore, the vector X is often not arbitrary irregular as the distribution is often composed of a specific accumulation of the probe in the target lesion and a generally smooth background fluorescence. Depending on the specific application and probe or target properties, other signal characteristics such as sparseness can be assumed as well [66, 67].

Optimization constrains rely on such known deterministic or statistical descriptions of the unknown vector to reduce the size of the reconstruction space. A particularly important property is the limited energy of the solution. The linear FEM problem of Equation 2.32 can be solved using the least squares (LS) approach as

$$X_{LS} = \arg\min \|\mathbf{W}\, X - M\|_2. \tag{4.2}$$

To constraint the solution, the signal energy can be limited as follow

$$X_\delta = \arg\min \|\mathbf{W}\, X - M\|_2 \ \texttt{subject to}\ \|X\|_2^2 \leq \delta^2, \tag{4.3}$$

where δ^2 is the energy bound. Using the method of Lagrangian multipliers and dropping the constant δ^2 term, Equation 4.3 can be written as

$$X_\lambda = \arg\min \left(\|\mathbf{W}\, X - M\|_2^2 + \lambda^2 \left(\|X\|_2^2 \right) \right). \tag{4.4}$$

It can be shown that under certain conditions, for appropriately chosen λ the solutions X_λ and X_δ are equivalent [68].

The approach of Equation 4.4 is referred to as Tikhonov regularization and poses a quadratic problem which has a closed-form solution given as

$$X_0 = \left(\mathbf{W}^T \mathbf{W} + \lambda^2\, I_N \right)^{-1} \mathbf{W}^T M, \tag{4.5}$$

or equivalently

$$X_0 = \mathbf{W}^T \left(\mathbf{W}\mathbf{W}^T + \lambda^2\, I_m \right)^{-1} M, \tag{4.6}$$

where N is the number of unknowns (voxels in our case), m is number of measurements and I_N is the identity matrix of size $N \times N$. The inversion in Equation 4.5 is limited by the number of rows or the number of columns of the weight matrix. Either way, the inversion is likely to take a large amount of time. Instead, this equation is often minimized using iterative approaches such a the conjugate gradient methods (discussed in Section 2.3) or the least squares methods (LSQR), as is the case in this work as well. LSQR is a method based on conjugate gradient approach for solving linear or least-square problems involving large sparse matrices [69] and is used for tomographic inversion [32, 70].

It can be readily shown that the solution to the Tikhonov-regularized

problem is equivalent to

$$X_{svd} = \sum_{i=1}^{N} \frac{s_i}{s_i^2 + \lambda^2} \left(v_i^\top \, u_i \, M \right), \tag{4.7}$$

where s_i's are singular values of $\mathbf{W}$ and v_i and u_i are, respectively, i^{th} rows of the unitary matrices of the singular value decomposition (SVD) of the weight matrix $\mathbf{W}$ given as

$$\mathbf{W} = U \, \text{diag}(s_1 \dots s_N) V. \tag{4.8}$$

In this way, the Tikhonov-solution can be regarded as the SVD-based direction inversion solution, where singular values are lower-bounded through addition of a constant λ term.

A more general form of the regularization solution can be written as

$$\begin{aligned} X_0 = &\arg\min \left(\|\mathbf{W}X - M\|_2^2 + \lambda^2 \, \|\Gamma(X)\|_p^p \right) \\ &\texttt{subject to } X \geq 0, \end{aligned} \tag{4.9}$$

where the regularization term $\Gamma(X)$ is chosen to enforce *a priori* known signal properties. For instance, the sparseness of the distribution can be enforced for $p = 1$ by penalizing the L_1 or total variation norm of the solution [47, 67] or for general $1 \leq p \leq 2$ [71]. Tikhonov-type regularization is achieved by for $p = 2$. In particular, the anatomical information available from the X-ray CT can be used to enforce different penalization for different tissue regions [32, 72, 73]. For instance, prior knowledge about absence or presence of fluorophores or uniformity of distribution in a given organ have been employed to define the regularization term as $\Gamma(X) = L\,X$, where L is an invertible square matrix determining penalization terms for different regions.

Two main types of structured regularization are particularly employed in fluorescence tomography. The first method, called weighted-segments, penalizes the energy of the solution in different anatomical segments differently using preset (or data-driven) weights [32, 72, 73]. For this method the structured regularization matrix L is a $N \times N$ diagonal matrix where each entry on the main diagonal has a value equivalent to the weight assigned to its respective segment. The second category, consists of Laplace-type methods where the uniformity of solution within each segment is re-

warded [32, 58, 73, 74]. The matrix L for the basic Laplace-based method is given as

$$L(i,j) = \begin{cases} -\frac{1}{N_k} & i,j \in k^{\text{th}} \text{ segment} \\ 0 & \text{else,} \end{cases} \tag{4.10}$$

where N_k is the number of solution elements in the k^{th} segment. Given the regularization matrix, the inverse problem is then solved as

$$\begin{aligned} X_0 = &\arg\min \left(\|\mathbf{W}\mathbf{L}^{-1}Y - M\|_2^2 + \lambda^2 \|Y\|_2^2 \right) \\ &\texttt{subject to } X = \mathbf{L}^{-1}Y \geq 0. \end{aligned} \tag{4.11}$$

The regularization parameter λ dictates a balance between minimization of the two norms in Equation 4.11; very small values result in highly irregular solutions with high dynamic range which minimize the residue and large λ's result in smooth solutions concentrated around tissue center and almost independent of the measurements. This tradeoff can be well observed using the L-curve, which shows the relation between solution norm and residue norm. The corner of the L-curve, offering an optimal tradeoff between modeling accuracy and solution dynamic range, is often selected as the point with maximum curvature [75]. A more thorough analysis of the behavior of structured regularization methods is presented in Chapter 6 prior to introducing a new inversion approach.

4.4 XFMT graphical user interface (GUI)

The code is equipped with a versatile GUI capable of several functionalities. A snapshot of the GUI for an *ex vivo* study is demonstrated in Figure B.1. This graphical interface is critical for full utilization of the developed processing framework and it allows efficient customization and combination of available options and algorithms for different studies or applications through. Segmentation of the CT volume using automatic and semi-automatic routines (some of which described in [76]) are incorporated. The GUI offers several tools for L-curve analysis and background subtraction, as well as rendering FMT-XCT processing results in 2-D and 3-D modes. Furthermore, the GUI makes partial processing of the results possible; that is, upon changing a parameter only the minimum required processing is performed to update the results. Accuracy of geometrical calibration can be examined to spot possible calibration errors

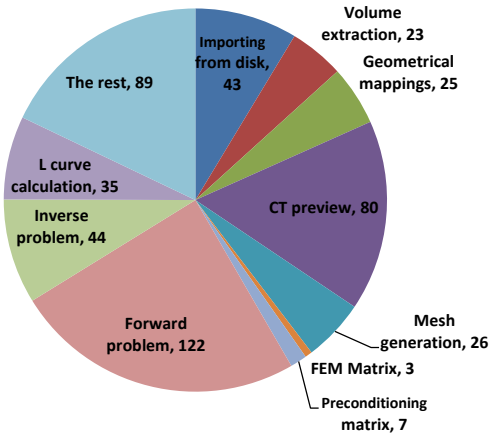

Figure 4.4: Processing time analysis showing the computation times in seconds for various functional modules for an *ex vivo* experiment with 17 mm FOV in the axial direction and 28 mm in the coronal plane. The tetrahedral mesh had 14821 nodes and 80499 elements and the total number of measurements were 216091. Total processing time was around 500 seconds on a computer with an Intel Core^{TM} i7 CPU @ 3.4 GHz and 16 GB RAM.

which might arise with time. The processing results for a given study can be saved and retrieved in various formats at any stage of the processing. Note that, although the actual reconstruction resolution of FMT is around 1 mm, it is the most commonly used approach to render the results graphically in a spatially interpolated form, such as through interpolating the reconstructed values on a finer demonstration mesh which can be twice as fine as the reconstruction mesh. Applications of interpolated-based rendering approach are abound in literature as in [13,25,32,77–80], to name a few. This practice is followed for almost all of the demonstrations presented in this work by interpolating the results twice in the transverse plane. Among other popular volume rendering approaches for demonstrating FMT results is the use of isosurfaces (3-D surfaces representing points of common values).

The processing of a typical animal study using this GUI lasts less than 10 minutes. An analysis of the total processing time is given in Figure 4.4. The code is capable of processing FMT measurements from both of the currently available FMT-XCT systems located at HMGU and Klinikum as well as datasets acquired by single-view geometry FMT 2500 machine (PerkinElmer, Waltham, MA, USA). The processing of the single-view ge-

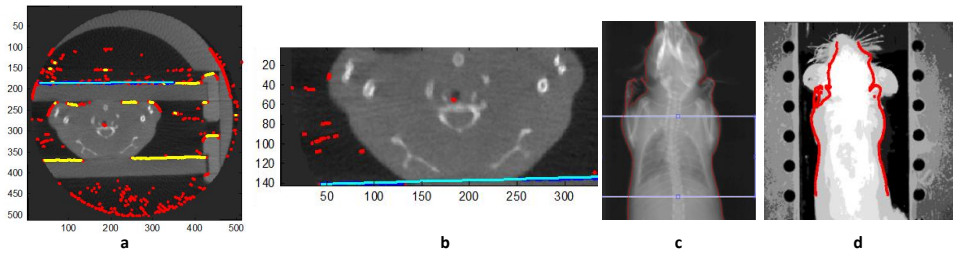

Figure 4.5: XFMT preprocessing and coregistration of single-geometry data from the FMT 2500 system; (a) and (b) extraction of the animal holder from the CT images and carving of the mouse volume using line detection, (c) the red boundary of the extracted mouse volume on the CT projection and (d) the superimposition of the CT volume boundary over the optical image using correlation-based mapping between optical and CT domain.

ometry datasets required further preprocessing and coregistrations steps, explained next. A short operational manual of the `XFMT_GUI` is presented in Appendix B.

4.4.1 Single-view geometries

The FMT machine from PerkinElmer (Waltham, MA, USA) (previously VisEn Medical), called FMT 2500 operates in single-view transillumination geometry. The animal is placed in an animal holder and imaged in micro-CT as well. We have adapted our code to processing of these hybrid datasets as well. In particular, the holder is first automatically recognized, using line detection-based methods, and the animal volume is carved out. Then, the animal volume is optimally rotated spatially to compensate for rotations between FMT and CT acquisitions and is then optimally coregistered with the FMT front-illumination image using 2-D correlation. As example of these preprocessing steps is demonstrated in Figure 4.5.[2]

4.5 Conclusion

The unique hardware of the FMT-XCT system sets forth unique algorithmic and numerical development challenges and requirements toward

[2] The data was provided by Karin Radrich at IBMI and the automatic method presented here is conceptually similar to a manual method previously used by her [81].

optimal exploitation of the hybrid data afforded by this system. We have herein presented the development of such processing framework in the MATLAB environment. Special care was given to the problem of solving the forward problem which accounts for modeling propagation of the excitation and fluorescence photons in tissue. Various forward and inverse modules as well as data-condition units were discussed and a flexible graphical interface, critical to successful deployment, was presented. Complete processing of an animal study using this framework last less than 10 minutes for conventional computing power. The large size of measurements acquired by poses numerical problems for the reconstruction and limit range of applicable inversion methods; an issue addressed in the next chapter.

5 Compression of Born data

5.1 Introduction[1]

The full-rotation geometry and CCD acquisition at several excitation locations can result in up to millions of measurement points in FMT-XCT. It has been shown that best results are obtained when 18 or more gantry angles are used during the acquisition [82]. By scanning an axial view of 2 cm and assuming a width of 2 cm - typical in preclinical applications - a source scan pitch of 2 mm will result in 2000 source positions for 20 projections. In practice the number is slightly less, due to geometrical irregularities. Each fluorescence-intrinsic image pair has 512×512 pixels. One way to calculate the total number of measurement is counting all the pixels across all source positions (around 500 million in our hypothetical example). However, compression of the acquired images by means of binning on square or Gaussian shaped virtual detectors has a very minimal impact on the information content. Nevertheless, assuming a 1 mm $\times$ 1 mm virtual detector grid, still results in 1 million data points.

The huge size of measurement space poses numerical limitations on the inversion method and increase complexity. These limitations include large number of forward problems to be solved, restrictive memory requirements and long reconstruction times. Another limitation is from the algorithmic point of view; such large numbers of source-detector data points can only be handled with implicit representation of the weight matrix which in turn limits the reconstruction algorithm to methods which require only matrix-vector multiplications in the inversion process, such

[1] Some of the materials of this chapter are also presented (at places with minimal or no changes) in P. Mohajerani and V. Ntziachristos, "Compression of Born ratio for fluorescence molecular tomography/x-ray computed tomography hybrid imaging: methodology and *in vivo* validation", Optics Letters vol. 38, issue 13, pp. 2324-2326 (2013) `http://dx.doi.org/10.1364/OL.38.002324`. Materials reproduced with permission from the Optical Society of America (OSA).

as conjugate gradient (CG) type methods. Other inversion techniques based on singular value decomposition (SVD), for instance, are not possible with such matrix sizes in reasonable time (as the complexity grows with n^3 or $(m\,n\,\min(m,n))$, for a $m \times n$ matrix [83]).

Measurement compression and compressive sensing are approaches which are often utilized to reduce the size of the linear problem. These methods often rely on removing correlation between measurements toward achieving a smaller set of relatively less correlated data points. It is also known that FMT measurements contain significant redundancy; a fact which has been employed to optimize the acquisition protocol [82]. Several efforts have been previously made to reduce the size of the optical tomography problems, both in non-fluorescence DOT methods as well as FMT systems [84–86]. These methods achieve compression on a per source basis by taking advantage of the redundancy in the measurement or image domain for a given source location.

As we will show later in this chapter, there exists a different dimension across which FMT signal shows significant redundancy. Specifically, the Born data is found to be highly correlated between sources in a given projections or across adjacent gantry angles. Here we propose a compression framework that makes use of inter-source signal dependencies to reduce the size of the FMT-XCT reconstruction problem. Our approach relies on the principal component analysis (PCA) [87] to remove the correlation among optical measurements across Born images obtained at different sources between adjacent gantry angles. The method has been validated using phantom experiments as well as *ex vivo* and *in vivo* small animal experiments. Besides the novelty of the proposed compression method itself, to our knowledge the results here constitute the first demonstration of a compression method applied to *in vivo* FMT data.

5.2 Previous approaches

Several compression approaches have been previously proposed for FMT. [84, 86, 88–91]. These methods can be generally divided into two categories. The first category apply a preconditioning matrix to the weight matrix or to its sub-matrices [88, 91]. Other methods have also based proposed for removing temporal correlation of the FMT signal across different acquisition time points toward dynamic imaging [92]. The second

group of compression methods rely on 2-D transformations, such Fourier or wavelet transforms, applied to the fluorescence or Born-normalized images [84–86, 89, 90]. Significant transformation coefficients are then retained which are used later as the detection patterns. Every retained transformation coefficient corresponds to a 2-D basis function in the image domain. The weight matrix can be directly calculated for this spatial function, instead of for all individual pixels. The wavelet-based approaches are often employed in conjunction with patterned source illumination to achieve a smaller measurement size. The compression rates reported by these methods usually pertain to the ratio between the number of retained components and the original number of image pixels; although, binning the original pixels significantly reduces the detectors number while retaining the information content. It should be noted that all of the above methods have been demonstrated for simulated or physical phantoms of regular geometrical shapes or simulated mouse data with artificial fluorescence distributions (spherical or tubular inclusions).

The transformation-based approach can be expressed as follows. Suppose I_i and F_i for $i = 1 \dots N$ are square matrices denoting, respectively, intrinsic and fluorescence images measured at the i^{th} source position. Also, $\mathcal{T}$ denotes a 2-D transformation in the image domain. The normalized Born images are defined as $B_i = \frac{F_i}{I_i}$. The compression can be achieved by application of the transformation to the fluorescence images or the Born images. The transformation can be applied to the fluorescence images as well; however, due to robust properties of the Born normalization, we assume here the Born images are transformed. The transformed images C_i are given as

$$\vec{C_i} = \mathcal{T}\vec{B_i}, \tag{5.1}$$

where for a matrix A, $\vec{A}$ denotes the vectorization operator, consisting of column-wise stacking of elements of A into a column vector $\vec{A}$. The transformation $\mathcal{T}$ is supposed here to be a $K \times K$ matrix where K is the number of elements of $\vec{B_i}$, i.e. the number of all pixels. Equation 5.1 is the general form of two-dimensional transformation. In practice, such representation is numerical prohibitive as for a typical image size of 512×512, the matrix $\mathcal{T}$ takes approximately 500 GB in memory (using double-precision format). Many conventional 2-D transformations are, however, orthogonal separable transforms. The orthogonality and separability make the

following representation possible

$$C_i = \mathbf{T}\, B_i\, \mathbf{T}^\top, \tag{5.2}$$

where $\mathbf{T}$ in this case represents the transformation matrix of size $L \times L$, with L being the number of rows of squares matrices B_i (typically 512). The transformation of Equation 5.2 can be applied in the forward modeling of FMT. Specifically, the elements of B_s are given as

$$B_s(m,n) = \sum_v \frac{g(\delta_{\mathfrak{S}}(m,n), v)\, g(v,s)}{g(\delta_{\mathfrak{S}}(m,n), s)} X(v), \tag{5.3}$$

where (m,n) are pixel coordinates in the image domain, $g(p,q)$ is the Green's function between points p and q (located either on the surface $\mathfrak{S}$ or in the tissue volume $\mathcal{V}$), $X(v)$ is concentration on voxel v and s is the source. Furthermore, $\delta_{\mathfrak{S}}(m,n)$ denotes mapping between the pixel (m,n) and the tissue surface $\mathfrak{S}$.

By combining Equations 5.2 and 5.3, the transformed measurement can be expressed as

$$C_s(m,n) = \sum_{i=1}^{L}\sum_{j=1}^{L}\sum_{v\in\mathcal{V}} \frac{g(\delta_{\mathfrak{S}}(j,i), v)\, g(v,s)}{g(\delta_{\mathfrak{S}}(j,i), s)}\, X(v)\, \mathbf{T}(m,j)\, \mathbf{T}(n,i). \tag{5.4}$$

Equation 5.4 can be rewritten as

$$C_s(m,n) = \sum_{v\in\mathcal{V}} H\, g(v,s)\, X(v) \tag{5.5}$$

$$H = \sum_{i=1}^{L}\sum_{j=1}^{L} \frac{g(\delta_{\mathfrak{S}}(j,i), v)}{g(\delta_{\mathfrak{S}}(j,i), s)}\, \mathbf{T}(m,j)\, \mathbf{T}(n,i). \tag{5.6}$$

The variable H in Equation 5.5 and defined in Equation 5.6 can be rewritten as

$$H = \sum_{i=1}^{L}\sum_{j=1}^{L} g(\delta_{\mathfrak{S}}(j,i), v) Q(i,j) \tag{5.7}$$

$$Q(i,j) = \frac{\mathbf{T}(m,j)\, \mathbf{T}(n,i)}{g(\delta_{\mathfrak{S}}(j,i), s)}. \tag{5.8}$$

It can be shown that quantity H is in fact the Green's function between the source s and the detection pattern defined for a given pixel (m,n) by

the image $Q(i,j)$. The variable $Q(i,j)$ can be considered as a the 2-D basis image consisting of multiplication of the m^{th} row and n^{th} column of $\mathbf{T}$ weighted by the reciprocal of the modeled intrinsic image $g(\delta_{\mathfrak{S}}(j,i),s)$. Therefore, the forward problem can be solved in the transformation-based method by solving for the Green's functions of all the source as well as the weighted detection patterns $Q(i,j)$.

Due to spatial regularity of measured Born images, application of conventional transformations, such as the wavelet transform [84] or the Fourier transform [86], will result in transformed images C_i with fewer non-negligible entries than the original images B_i. Hence, retention of significant transformation coefficients will result in large compression without losing much of the signal energy.

5.3 Principal component analysis

We briefly review the method of principal component analysis (PCA), which is employed in the next section to develop a method for compression of Born data in the inter-source domain (as opposed to intra-source, transformation-based techniques presented in the previous section).

PCA is a transformation for converting a group of random variable realizations to set a of numbers, which can be considered as realizations of uncorrelated random variables [87]. In this sense, PCA is an adaptive transformation for optimal decorrelation and has wide applications in signal and image processing for biomedical applications. The operation of PCA as an orthogonal transformation can be qualitatively expressed as follows. Consider a group of vectors, where each vector represents a set of measured variables or parameters. For simplicity, we consider the $\mathfrak{R}^2$ space where each vector is a 2-tuple. Therefore, the group of vectors can be considered as a set of points in the Cartesian plane. An orthogonal transform consists of two orthogonal "basis" vectors where the projection of each point on these vectors yields the transformed point. The first basis vector is found then by finding the direction of the "largest span" in the set of data points. For instance, if all the data points lie on the $x = y$ line, then the first PCA direction would be naturally this line. The projection of each data point on the first basis, is the part of that point that can be predicted by the first basis. The direction along which the unpredictable (using the first basis) data has the largest variance, is then the

second basis vector. The basis vectors are also called "components" and since each consecutive estimation is performed only on residual values from the previous steps, all the estimated components are orthogonal.

Specifically, let us assume V is a N-dimensional random vector, consisting of N random variables v_i, $i = 1 \dots N$. For an orthonormal transformation matrix $\mathbf{T}$, the transformed random vector is given as $U = \mathbf{T}\,V$. Assuming the random vector V has zero mean ($\mathbb{E}[V] = \mathbf{0}$, with $\mathbb{E}$ denoting mathematical expectation), the first basis vector T_1 as a $1 \times N$ row vector, can be found by solving the following optimization problem

$$T_1 = \arg\max_{w} \left\{ \mathbb{E}\left[\|wV\|_2^2 \right] \right\} \ \texttt{subject to} \ \|w\|_2 = 1. \tag{5.9}$$

The solution to this optimization problem is readily found using the method of Lagrange multipliers, where the Lagrangian is given as

$$\Lambda(w, \lambda) = w\,\texttt{cov}(V)\,w^\top - \lambda(w\,w^\top - 1), \tag{5.10}$$

where for a random vector X, its covariance matrix $\texttt{cov}(X)$ is defined as $\texttt{cov}(X) = \mathbb{E}\left[X\,X^\top\right]$. Derivation with respect to w results in $w(\texttt{cov}(V) - \lambda I_N) = 0$. Since $\|w\|_2 = 1$, this can be achieved only if $\det(\texttt{cov}(V) - \lambda I_N) = 0$, which is the characteristic polynomial of matrix V. In other words, λ and w should be then, respectively, a corresponding eigenvalue and eigenvector pair of the covariance matrix of V. Moreover, the maximized quantity in Equation 5.9 is equal to λ. Hence, optimization is achieved when λ is the largest eigenvalue of the covariance matrix.

The next component T_2 is found similarly for the residual random vector V_1 defined as $V_1 = V - (T_1\,V)T_1^\top$. It can be easily shown that the second component T_2 is in fact the eigenvector of the covariance matrix $\texttt{cov}(V)$ corresponding to the second largest eigenvalue. As a symmetric and positive-definite matrix, $\texttt{cov}(V)$ has N positive and real eigenvalues and eigenvectors. The N eigenvectors then yield then N principal directions.

Furthermore, if $\texttt{cov}(V) = \Lambda\,S\,\Omega$ is the singular value decomposition of $\texttt{cov}(V)$, then Λ is equal to Ω (due to positive-definiteness and symmetry of $\texttt{cov}(V)$) and the rows of the unitary matrix Λ represent the principal components and then covariance of the transformed vector U is given

as

$$\mathtt{cov}(U) = \Lambda\, \mathtt{cov}(V)\, \Lambda^\top = S. \tag{5.11}$$

The PCA, as shown, can be applied to a group of vectors v_i, $i = 1 \dots K$ as realizations of the random vector V. In this case, the covariance matrix is estimated empirically as

$$\mathtt{cov}(V) := \mathbb{E}\left[V\, V^\top\right] \approx \frac{\sum_{i=1}^{K} v_i\, v_i^\top}{K}. \tag{5.12}$$

Similarly, PCA can be applied in the 2-D domain to a set of images, as realizations of an underlying 2-D random vector. Specifically, for a group of $L \times L$ images A_i, $i = 1 \dots K$, the PCA is performed on the vectorized images $\vec{A_i}$ using a $K \times K$ matrix $\mathbf{T}$ is achieved using SVD of $\mathbf{A}\,\mathbf{A}^\top$ where

$$\mathbf{A} = \begin{bmatrix} \vec{A_1} \\ \vdots \\ \vec{A_K} \end{bmatrix}. \tag{5.13}$$

This way, the transformed vectorized images are given as $\mathbf{B} = \mathbf{T}\,\mathbf{A}$ where every row of $\mathbf{B}$, when reshaped into the original image size gives the transformed image. The transformed images are uncorrelated with each other and their energies (square of L_2 norm) are given by the corresponding singular values.

5.4 The proposed compression algorithm

While it is straight-forward to verify inter-source correlation using cumulative sum of singular values associated with a group of images, we confirm the presence of information redundancy among Born normalized images obtained between different source locations using a visual, more intuitive approach. For this purpose an experiment was performed on an *ex vivo* CD1 mouse with a fluorescent tube inserted through the esophagus (refer to Appendix C). We visualized then the Born data between 3-tuples of adjacent sources in the 3$^{\text{rd}}$ projection as presented in Figure 5.1. Figure 5.1(a) shows the 3-tuples of Born data, each 3-D point corresponding to a virtual detector point in the given projection image. For each source 3-tuple, a plane (P_1 through P_4) is fitted through the points. The fact that for a 3-D dataset (corresponding to 3 sources) a

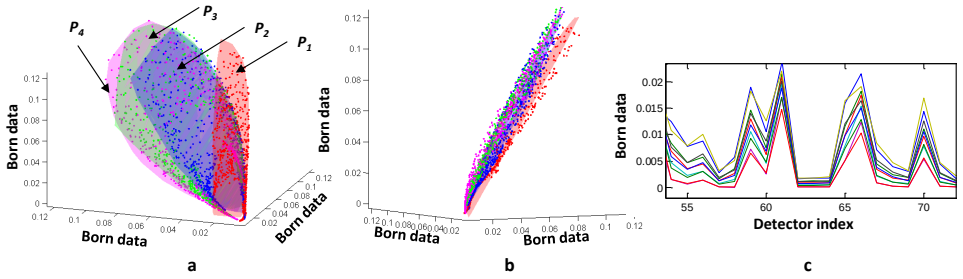

Figure 5.1: Analysis of inter-source correlation of Born data for an *ex vivo* mouse dataset, (a) and (b) show from different angles 4 planes (P_1 through P_4) fitted to 3-tuples of Born data, where the three elements are measured Born values on different detectors for 3 adjacent sources. The plane P_1 is fitted to these 3-tuples for sources (n, n+1, n+2), P_2 is fitted to sources (n+1, n+2, n+3) and so on. The fact that a 2-D plane is a good fit of the 3-D data 3-tuples and that the planes are close to each other for adjacent source 3-tuples, signifies data correlation. (c) Born data over different detectors for sources in a given projection.

2-D plane represents the data to a high degree of accuracy, signifies inter-source correlation. The representation accuracy is also seen from the side view of Figure 5.1(b) as the 4 planes are located very close to each other. This suggests that a hyper-plane in the $\mathfrak{R}^6$ space can be good approximation for all 6 sources of this example. This dependency can also been seen in Figure 5.1(c) where different Born signals across different sources are shown versus different detectors.

As discussed in Chapter 2, the forward modeling of the FMT is achieved here by finite element method (FEM) based discretization of the diffusion equation. The volume of the tissue is discretized using a tetrahedral mesh P with N_p nodes and elements T. The unknown fluorophore distribution is denoted by a $N_p \times 1$ vector X representing the fluorophore concentrations on the nodes. Although the method presented here is constructed with the framework of a tetrahedral mesh, it is easily expandable to other implementations.

Through out this chapter we use the following notations. For a vector X and matrices $\mathbf{M}$ and $\mathbf{N}$, the notations $|X|$, $\|\mathbf{M}\|$, $\mathbf{M}^\top$, mean($\mathbf{M}$) and $\mathbf{M} \odot \mathbf{N}$ denote, respectively, the number of elements of X, the Frobenius norm of $\mathbf{M}$, the transpose of $\mathbf{M}$, a column vector consisting of the average values of the rows of $\mathbf{M}$ and the element-wise multiplication between $\mathbf{M}$ and $\mathbf{N}$. Also, $\mathbf{1}_k$ is a row vector consisting of k 1's and $\{a_i\}$ is a set consisting of elements a_i, $i = 1 \ldots L$ where L is implied in context.

As a reminder, assuming a set of source and boundary conditions and optical absorption and scattering values for the tissue, the FMT reconstruction problem can be written as

$$\mathbf{W}X = M, \tag{5.14}$$

where $\mathbf{W}$ is the weight matrix and M is the measurement vector consisting of the ratio between the measurements at the fluorescence and excitation wavelengths (i.e. the Born ratio). This linear problem is then solved using regularization as

$$X_0 = \arg\min \left(\|\mathbf{W}X - M\|_2^2 + \lambda^2 \|\Gamma X\|_2^2 \right), \tag{5.15}$$

where Γ represents the regularization matrix, which can be determined using the *a priori* anatomical information from CT and λ is set to a fraction of $\|\mathbf{W}\|$. $\mathbf{W}$ is formed from the Green's function (GF) $g(r, v)$ between surface points r and mesh nodes v (for notation simplicity, we assume the same optical properties for excitation and emission wavelengths).

For any r and v the GF can be calculated as a linear combination of the GF's of vertices of the surface triangle containing r. Hence, the forward problem needs to be solved only for all surface nodes, as discussed in Section 4.2.3. This suggests that the number of forward equations in the FMT-XCT problem is not likely to be affected by any compression approach, as discussed later. The proposed compression method is demonstrated using a flowchart in Figure 5.2. The first step of the compression consists of defining a set of indexed detector points. This is achieved by defining the detector points directly on the sample 3-D surface, rather than in the CCD image domain. Specifically, let d_i, $i = 1 \dots K$ and s_i, $i = 1 \dots L$ be 3-D points denoting K virtual detectors and L sources on the sample surface. In practice, this is achieved by generating a surface triangular mesh with the desirable detector pitch (usually around 1 mm). It is also possible to set the virtual detector points directly to the mesh surface nodes. The next step consists of forming a "source-detector association" binary matrix. This matrix specifies which detector is "seen" by which sources. An example is demonstrated in Figure 5.3. Figure 5.3(a) shows a group of detector points (red dots) which are seen by a subset of sources. The sources are shown by circles of different colors, where each color corresponds to a given projection angle to which the respective source belongs. This specific group of detector points are seen by

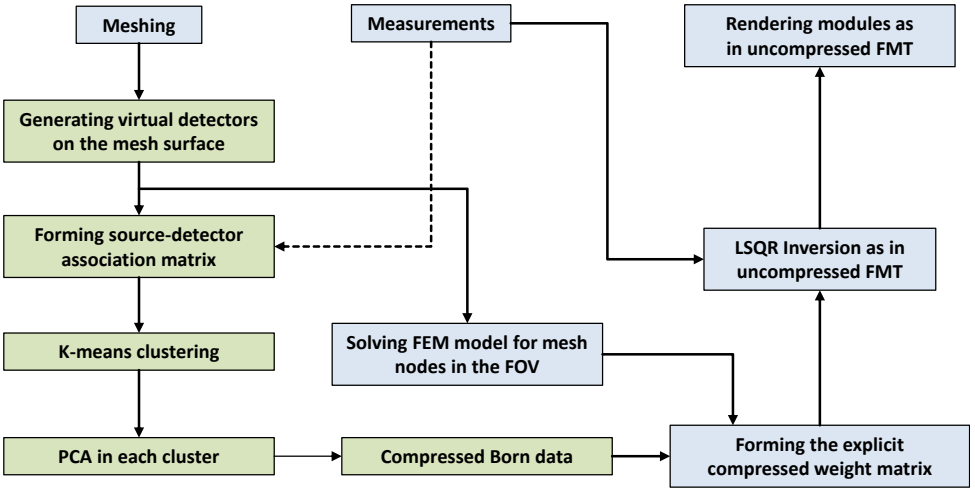

Figure 5.2: Flowchart of the compression algorithm showing the operational components which differ from the conventional FMT-XCT in green. The indexed virtual detectors are clustered based on the respective source-detector association binary matrix and PCA is performed within each cluster. The PCA components then form the compressed measurements, for which the weight matrix is calculated from the solution to the forward problem.

sources across 8 projection. A binary matrix is depicted as a binary image in Figure 5.3(b), which shows if a detector (columns) is observed when the sample is illuminated by a given source (rows). There can be several reasons that some locations are black within the white stripe of Figure 5.3(b); either geometrical irregularities or the mouse holder block the vision at a specific location or the corresponding source-detector pair does not pass the thresholding criteria.

Specifically, a subset of $\{s_i\}$ is used during acquisition at each of the projection angles. A $L \times K$ source-detector association binary matrix $\mathbf{F}$ is defined as $\mathbf{F}(i,j) = 1$ if and only if (1) the detector d_i is seen by the camera when the source s_j is illuminated and (2) the signal measured on the pixel corresponding to d_i during excitation by s_j passes the thresholding requirements. The number of 1's in the matrix $\mathbf{F}$ designates the total number of measurements.

The columns of the matrix $\mathbf{F}$ are divided into a group of clusters $\mathcal{C}_k$, so as to form a partitioning of the set $\{d_i\}$ such that

$$\forall\ \mathcal{C}_k\ \exists \text{ a set } \mathcal{S}_k \text{ s.t. } \frac{\mathbf{F}(\mathcal{S}_k, \mathcal{C}_k)}{|\mathcal{S}_k| \times |\mathcal{C}_k|} \approx 1. \tag{5.16}$$

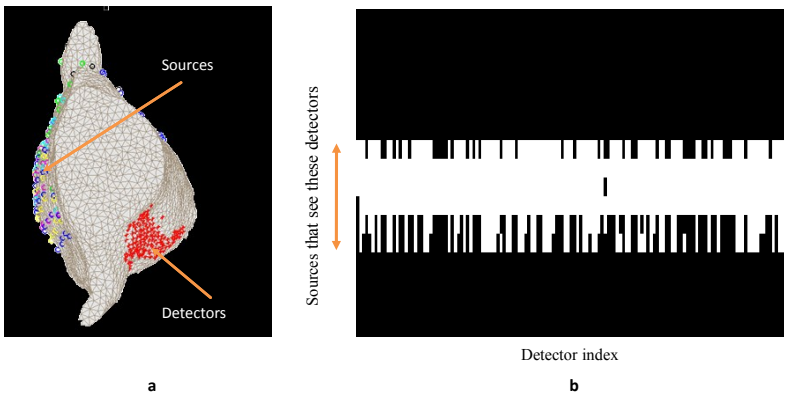

Figure 5.3: Source-detector association across adjacent gantry locations; (a) the detector points shown with red dots on the animal surface all seen by a subset of the source, shown with circles of different colors - each color corresponding to a different projection. (b) The source-detector association as a binary image; each detector on the x-axis is visible in by the corresponding sources on the y-axis. A detector is not seen by all the sources because of geometrical irregularities and applied signal thresholds.

In other words, a clustering is performed on columns of $\mathbf{F}$ so as to group the detector points such that within each group the detectors almost all see the same group of sources. The clustering is done to maximize the right side ratio of above equation; however, achieving a maximum ratio of 1 might not be possible, due to geometrical irregularities and below-threshold measurements. This partitioning is performed through k-means clustering of the binary columns of $\mathbf{F}$ with the Hamming distance [93]. The sets $\mathcal{S}_k$ are not disjoint, meaning some sources can be seen by different detectors in different spatial clusters.

The k-means clustering can be briefly explained as follows. For a group of N vectors $v_i \in \mathfrak{R}^m$, $i = 1 \dots N$, K vectors are selected which represent the centroids of K respective clusters. The selection method operates using the following iterative method:

1. *Initialization*: for $p = 0$, set K cluster centroids $c_i^{(p)} \in \mathfrak{R}^m$, $i = 1 \dots K$ using, for instance, random partitioning.

2. *Update*:

$$c_i^{(p+1)} = \frac{\sum_{j \in I_i^p} v_j}{|I_i^p|},$$

where I_i^p consists of indices of vectors which are closest to c_i^p and $|I_i^p|$ is the number of elements in I_i^p.

3. *Termination*: upon $\max_i \left(\|c_i^{(p)} - c_i^{(p-1)}\| \right) < \epsilon$, for a preset threshold ϵ.

For every cluster $\mathcal{C}_k$ a $|\mathcal{S}_k| \times |\mathcal{C}_k|$ matrix $\mathbf{B}_k$ is formed such that

$$\mathbf{B}_k(i,j) = \begin{cases} b(\mathcal{S}_k(i), \mathcal{C}_k(j)) & \mathbf{F}(\mathcal{S}_k(i), \mathcal{C}_k(j)) = 1 \\ 0 & \text{else,} \end{cases} \tag{5.17}$$

where $b(s,d)$ denotes the Born ratio between source s and detector d.

The rows of $\mathbf{B}_k$ are decorrelated using PCA after subtraction of the mean value as

$$\mathbf{U}_k \Lambda \mathbf{U}_k = Q_k \, Q_k^\top, \tag{5.18}$$

where

$$Q_k = \left(\mathbf{B}_k - \text{mean}(\mathbf{B}_k) \mathbf{1}_{|\mathcal{C}_k|} \right) \odot \mathbf{F}(\mathcal{S}_k, \mathcal{C}_k). \tag{5.19}$$

The main diagonal of Λ is sorted in descending order. The singular values contained in Λ fall rapidly, due to the higher correlation of the measurements within one cluster. The compression is achieved by maintaining only a few components with significant singular values.

Specifically, for cluster $\mathcal{C}_k$ the first $N_k(\beta)$ components are maintained using a threshold β, between 0 and 100, applied to the normalized cumulative energy vector E_i defined as

$$E_i = \sum_{l=1}^{i} \Lambda(l,l) - \Lambda(1,1), \tag{5.20}$$

using

$$N_k(\beta) = \min \left\{ i | \frac{E_i}{E_{|\mathcal{C}_k|}} \leq \frac{\beta}{100} \right\}. \tag{5.21}$$

The compressed measurement matrix for $\mathcal{C}_k$ is a $N_k(\beta) \times |\mathcal{C}_k|$ matrix $\mathbf{M}_k$ given as

$$\mathbf{M}_k = \mathbf{U}_k(1 : N_k(\beta), :) \mathbf{B}_k. \tag{5.22}$$

The values in matrices $\mathbf{M}_k$ are the transformations of the Born data $\mathbf{B}_k$ using the first $N_k(\beta)$ rows of the PCA unitary matrix $\mathbf{U}_k$.

In the next step, we construct the weight matrix corresponding to each of these values. Specifically, for $\mathbf{M}_k(i,j)$ the weight matrix is defined as

$$\mathbf{W}_k(i,j,v) = \sum_{s \in \mathcal{S}_k} \mathbf{U}_k(i,s)\mathbf{F}(s,j)\frac{\mathcal{G}(s,v)\mathcal{G}(j,v)}{\mathcal{G}(s,j)}. \tag{5.23}$$

The tensor $\mathbf{W}_k$ is a 3-D matrix relating the value of the i^{th} row, j^{th} column value of $\mathbf{M}_k$ to the concentration on the voxel v. Vectorizing and assembling the $\mathbf{M}_k$ matrices and $\mathbf{W}_k$ tensors for all clusters, the compressed FMT-XCT problem can be written as

$$\mathbf{W}^p X = M^p, \tag{5.24}$$

where the total number of measurements is

$$\sum_{clusters} N_k(\beta) \times |\mathcal{C}_k|, \tag{5.25}$$

and the compression rate is defined as $|M^p|/|M|$.

The reconstructed solution X_β is compared to the original, uncompressed solution X_0 using two measures. One measure $h_t(X)$ quantifies the fidelity of the reconstructed target and another one $h_b(X)$ quantifying the relative amount of background signal.

Given I as a set of indices of X_0, where $X_0(I) > \alpha \max(X_0)$ and I^c as the set complement of I (I and I^c denote target and background, respectively),

$$h_t(X) = 100 \times \left(\frac{\|X(I) - X_0(I)\|}{\|X_0(I)\|} \right), \tag{5.26}$$

and

$$h_b(X) = 100 \times \left(\frac{\|X(I^c)\|\|X_0\|}{\|X_0(I^c)\|\|X\|} - 1 \right). \tag{5.27}$$

Positive $h_t(X)$ and $h_b(X)$ signify distortion in the desired signal and increased background signal, respectively. The target-background threshold parameter α was set to 0.3. Equation 5.14 and Equation 5.22 are solved then using the LSQR method [69] with 50 iterations.

5.5 Results

The proposed compression method is validated using a phantom dataset as well as *ex vivo* and *in vivo* experiments. For the *ex vivo* experiment, a glass tube with an inner diameter of 1 mm was filled 10 mm with 390 picomoles of Alexa 750. The dye was mixed with Intralipid to mimic tissue scattering and the upper tube was filled with diluted Intralipid 20% and small oil layer separated the two sections (see Appendix C for description). The animal preparation was as follows. An 89 day old CD1 mouse was sacrificed and shaved and the tube was inserted 25 mm through the esophagus.

For *in vivo* validation, a 96 day old nude mouse was injected with 1 million 4T1 breast cancer cells subcutaneously on the back, 10 days before imaging. 2 nanomoles of IntegriSense 750 was injected in the tail vein 24 hours before the imaging. The samples were imaged at 24 equispaced gantry angles, with the CT measurements following the optical acquisitions, using the FMT-XCT system at HMGU. In the *in vivo* case the animal was kept under anesthesia using Isoflurane while imaging and was sacrificed and frozen later at -80 degrees Celsius for cryoslicing-based validation.

5.5.1 Compression of phantom measurements

The proposed compression method was validated using the phantom dataset containing one tube filled with fluorescent liquid. The results are presented in Figure 5.4.[2] Specifically, Figure 5.4(a) shows a sample axial FMT-XCT slice of the reconstructed tube without (the "original" reconstruction) and with compression, with specified values of the PCA threshold parameter $\beta = 0$, 20, 60, 80, 90, 95 and 98. The compression rate ranges from 28 to 193 for this case. Figure 5.4(b) shows the values of the metrics designed in Equation 5.26 for the reconstruction signal at the different β values. The value of the artifact level metric $h_b(X)$ was less than 5% and was not shown. Figure 5.4(c) shows the regions of the clusters on the animal surface marked with different colors. The black edges in this figure correspond to the surface mesh edges.

[2] As a reminder, the FMT demonstrations presented in this work are interpolated for rendering, as explained in Section 4.4.

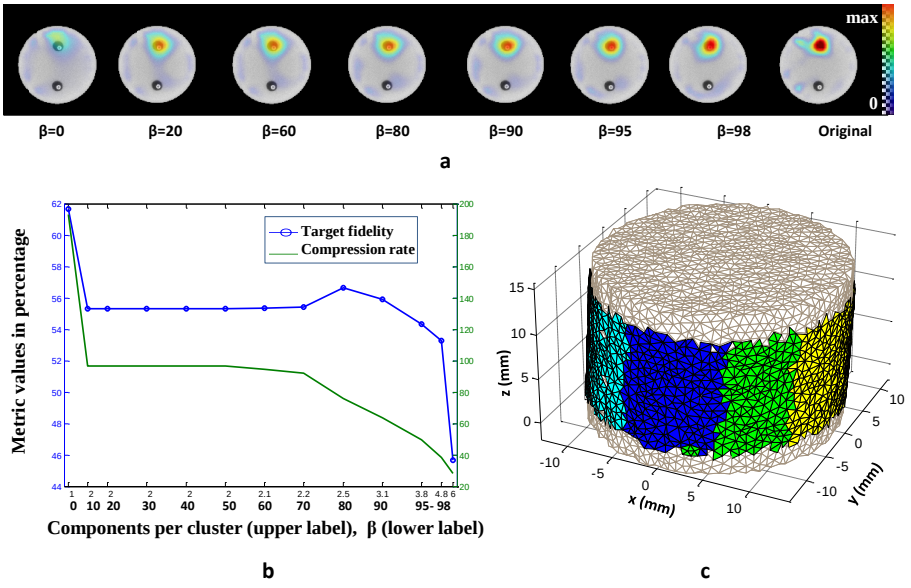

Figure 5.4: Compression results for an agar phantom with a fluorescence tube. The tube was inserted through one of the holes with the other hole left empty; (a) the same FMT-XCT slices for β coefficients of (0, 20, 60, 80, 90, 95, 98) corresponding to compression rate of (193, 97, 92, 64, 50, 39, 28), (b) the object fidelity curve and the compression rate for different β's (upper labels in the x-axis are number of retained components per cluster). The relative artifact level was less than 5% (and is not shown). (c) The cluster regions shown over the phantom surface with different colors.

5.5.2 Compression of *ex vivo* data

Figure 5.5 shows the reconstruction results with and without compression for the *ex vivo* experiment described above. Figure 5.5(a-f) show an FMT-XCT sample axial slice through the thorax of the animal for the original reconstruction and the values of the PCA threshold parameter $\beta = 95$, 80, 60, 20 and 0, respectively. Note that $\beta = 0$ signifies only one PCA component per cluster. These values of β correspond to compression rates of 16, 58, 86, 136 and 270. The red allow in Figure 5.5(b) shows the location of the actual tube. Figure 5.5(g) shows the object fidelity and relative background metrics defined in Equation 5.26 for this experiment. Both the object error and the background signal level have a decreasing trend with decreasing compression rate. Figure 5.5(h) shows the 8 cluster regions with different colors on the animal surface.

The performance of the compression method is specially impacted by quality and nature of the clustering. This effect is shown in Figure 5.6, where

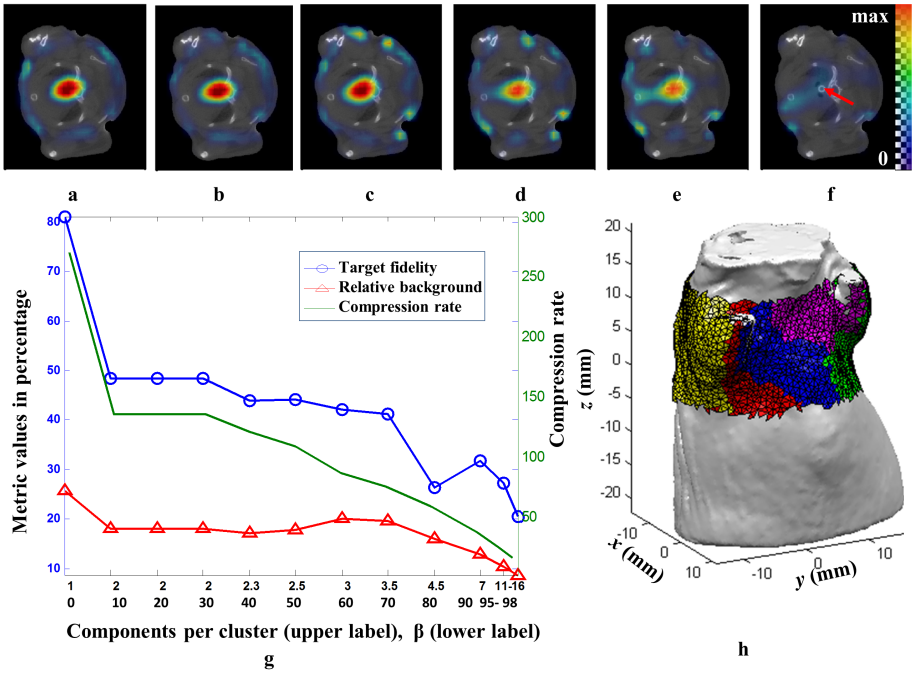

Figure 5.5: Compression results for the *ex vivo* case; (a) an axial slice of the original reconstruction, (b-f) slices for compression parameter β of 95, 80, 60, 20 and 0 (compression rates of 16, 58, 86, 136 and 270), (g) $h_t(X)$, $h_b(X)$ and the compression rate vs. average number of retained components per cluster and vs. β, (h) clusters shown on the animal surface. Arrow in (f) points to the tube.

the results are presented and compared for 1, 2 and 8 clusters, applied to the same *ex vivo* experiment as in this section. The three rows of axial FMT-XCT slices in Figure 5.6(a) show the results for 1, 2 and 8 clusters (top, middle and bottom row), for different values of β. It can be easily seen, that for 1, 2 and 8 clusters, reasonably localized reconstructions are achievable for β's of 90, 80 and 20. The 2 clusters are demonstrated in Figure 5.6(b). Therefore, it is important to achieve around 10, relatively homogenous clusters (with the ratio in Equation 5.16 as close to 1) for high compression rates with minimal loss of information.

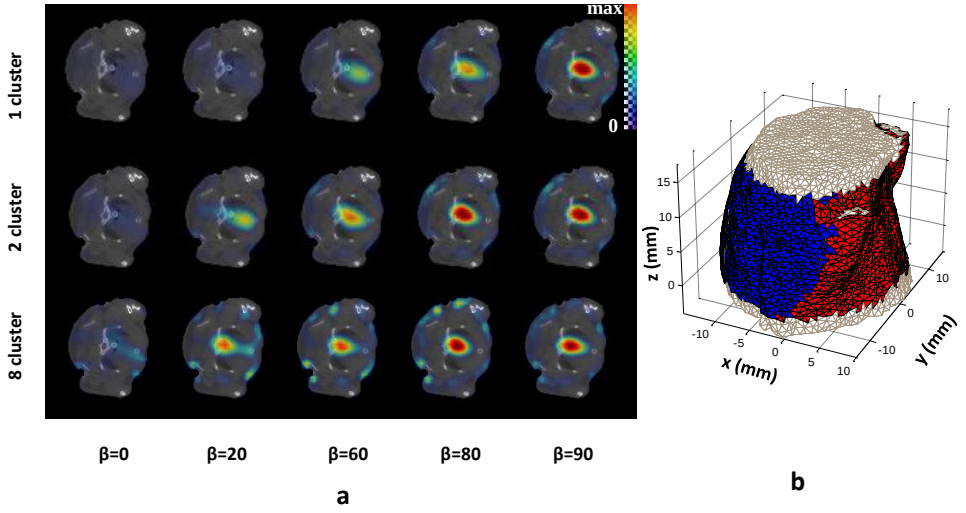

Figure 5.6: The impact of clustering on the reconstruction quality for the *ex vivo* experiment; (a) reconstruction slices for different β coefficients for 1, 2 and 8 clusters, (b) the 2 clusters on the animal surface. As seen the reconstruction quality improves significantly with increasing number of (optimized) clusters - however, significant compression is possible with one and 2 clusters as well.

5.5.3 PCA-based compression verified using *in vivo* data

The *in vivo* reconstructions were performed for a nude mouse with subcutaneously injected 4T1 cells, as described above. The proposed compression method is in fact not dependent on the regularization scheme and is applicable to reconstructions with use of anatomical *a priori* information. To demonstrate this fact, reconstruction were performed without and with using the anatomical information of CT. A weighted-Laplace based regularization approach [58] was used in the latter case after manually segmenting the tumor from the CT data. Figure 5.7 shows the reconstruction results with and without compression for the *in vivo* experiment and also with and without use of *a priori* information about the tumor location. Figure 5.7(a-e) show an FMT-XCT sample axial slice through the tumor for the original reconstruction and the values of the PCA threshold parameter $\beta = 90$, 80, 20 and 0, respectively; corresponding to compression rates of 25, 41, 104 and 209. Similarly, Figure 5.7(f-j) show the slices for the same parameters with the use of *a priori* information. Figure 5.7(m) shows the object fidelity and relative

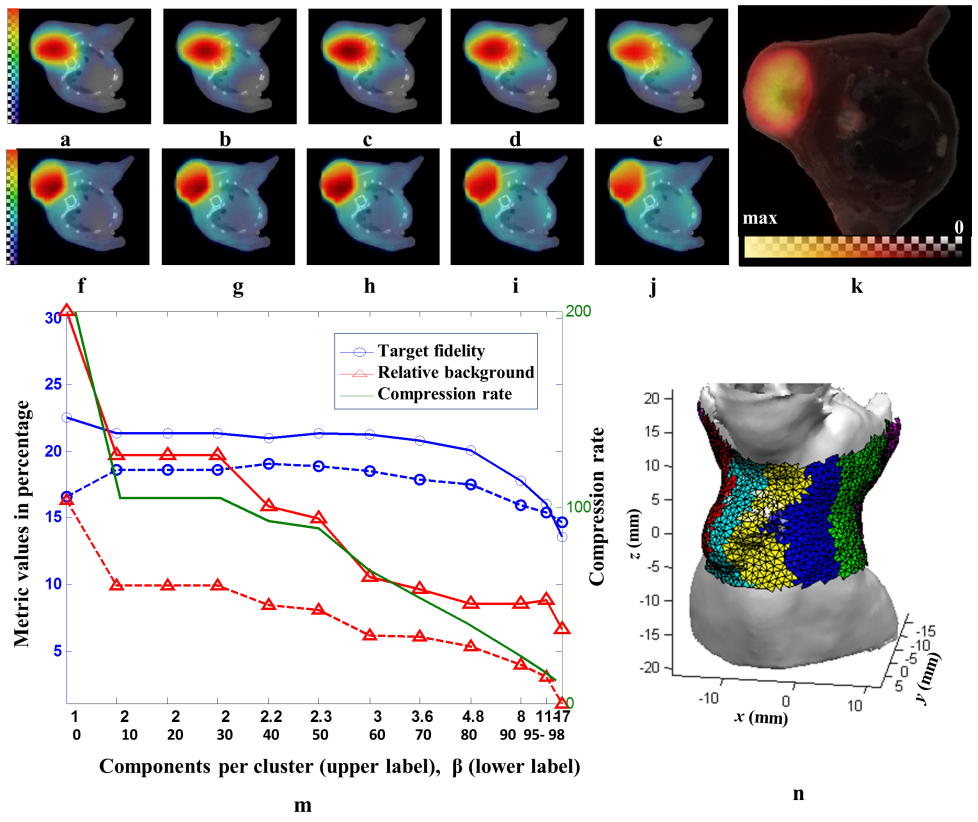

Figure 5.7: Compression results for the *in vivo* case; (a) an axial slice of the original reconstruction, (b-e) slices for $\beta = 90$, 80, 20 and 0 (compression rates of 25, 41, 104 and 209), (f) and (g-j) corresponding results using anatomical priors; (k) *ex vivo* validation; (m) $h_t(X)$, $h_b(X)$ and the compression rate vs. average number of retained components per cluster and vs. β (dotted curves correspond to reconstructions using anatomical priors). (n) Clusters on the animal surface.

background metrics defined in Equation 5.26 for this experiment. The detectors were partitioned into 10 clusters for this dataset, as depicted by different colors in Figure 5.7(n). The *in vivo* reconstructions were further validated *ex vivo* as shown in Figure 5.7(k) using cryo-sectioning, where the fluorescence image is imposed over the grayscale image of the axial cut of the sample. Both target fidelity and relative background metrics, respectively $h_t(X)$ and $h_b(X)$, showed a generally descending trend for increasing cumulative energy threshold β (corresponding to decreasing compression rate). Also for this case, the distortion is visually minimal for $\beta \geq 20$ (compression rate of around 100) and increases significantly at $\beta = 0$. For reconstructions done with the help of the anatomical informa-

tion, seen in Figure 5.7(g-h), the distortion is more due to the increased reconstructed signal in the background. It should be noted that within each figure, all the axial slices are on the same location on the z-axis and are rendered using the same colormap.

5.6 Discussion

In this chapter an algorithm was presented for reducing the size of the FMT-XCT inverse problem, while retaining much of the information. The performance was validated for phantom, *ex vivo* and *in vivo* measurements. These datasets represent fluorescence distributions of different natures (subcutaneous to deep-seated). It was observed that up to 100 times reduction in the measurement space are possible without losing image quality. It should be noted that this compression cannot be achieved trivially by, for instance, picking every 100^{th} source position. The proposed method results in a relatively small weight matrix, manageable in explicit form and faster reconstruction. Also, the possibility to express the weight matrix in explicit form affords direct inversion methods and approaches based on SVD.

It should be noted that for full-rotation FMT-XCT, the numerical complexity of solving the forward problem is independent of the compression scheme and, to some extent, from number of source positions or projection angles. The forward problem should be solved for all surface mesh nodes regardless if compression is used. In short, for the average tetrahedral mesh edge length of ≈ 1.3 mm, there are 1000-2500 surface mesh nodes of which only a portion are in the FOV. However, for an average setting, there are 20 gantry locations, each with 20 source positions and 400 detector points; resulting in around 8000 source or detector points. Therefore it is numerically faster to solve the forward problem for all surface nodes rather than for all source and detector locations for all gantry locations, as explained in Section 4.2.3. The number of forward problems to be solved (1000-2500) is likely to be much smaller than the total number of retained coefficients for any compression method that does not cause severe information loss. Therefore, the forward problem time is not likely to be affected by compression. However, the inversion time is significantly reduced by the compression method. The total inversion time and total number of measurements for the three experiments

Table 5.1: Reduction of FMT-XCT inversion time with compression. The results are shown for three datasets, where the first numbers in parentheses show the total numbers of measurements and the second numbers the reconstruction times. The reconstruction times include all processing steps involved.

	Original (time, size)	With compression (time, number of measurements) $\beta = 80$	$\beta = 60$	$\beta = 20$	$\beta = 0$
Phantom	(48s, 227087)	(7.0s, 3531)	(3.7s, 2450)	(3.4s, 2332)	(2.6s, 1166)
Ex vivo	(60s, 401506)	(7.1s, 5532)	(5.1s, 2908)	(5.1s,2908)	(3.6s,1454)
In vivo	(58s, 364040)	(6.6s, 8634)	(4.9s, 5193)	(3.9s, 3382)	(2.8s, 1691)

without and with different degrees of compression are presented in Table 5.1. The processing times with compression include all the processing steps involved. As seen, the processing times and the system sizes are reduced by one and two orders of magnitude, respectively. Processing was performed in MATLAB on a computer with an Intel Core™ i7 CPU @ 3.4 GHz and 16 GB RAM. [3]

5.7 Conclusion

An algorithm was proposed to significantly reduce the size of the weight matrix by compressing the spatially clustered Born data acquired by full-rotation FMT-XCT. The proposed approach takes advantage of the redundancy among different source positions and adjacent gantry angles. The *ex vivo* and *in vivo* experiments validated the algorithm's performance for fluorescence emanating from shallow as well as deep regions. Up to 100-fold compression was demonstrated with minimal reconstruction distortion. The reduced model size speeds up the reconstructions and affords inversion methods which require, for instance, singular value decomposition of the weight matrix. The combination of the inter-source compression method, presented here, and the 2-D transform-based intra-source compression approaches is possible and a topic of ongoing research.

[3] The processing times reported in P. Mohajerani and V. Ntziachristos, "Compression of Born ratio for fluorescence molecular tomography/x-ray computed tomography hybrid imaging: methodology and *in vivo* validation", Opt. Lett. 38, No. 13 (2013), differ from those in Table 5.1, as the processing was done on different machines.

While compression as proposed here reduced the system size without distorting the solution, robust and accurate inversion based on anatomical priors is also an important topic and is discussed in the next chapter.

6 Inversion based on weighted least squares

6.1 Introduction[1]

Hybrid FMT and anatomical imaging systems, such as the FMT-XCT modality discussed previously in this work, aim at mitigating the ill-posed nature of the FMT inverse problem through structured regularization of the solution (i.e. the fluorophore concentration vector). Conventional regularization schemes, such as the well-known Tikhonov regularization based on minimization of the L_2 norm of the solution, can result in reconstructions with low spatial correlation with anatomical description of the tissue. Structured regularization methods, on the other hand, essentially enforce different penalization methods or levels on different parts of the solution vector, depending on the organ they geometrically correspond to. For instance, the knowledge that a given specific probe has a high uptake ratio (relative to general background) in a specific organ affected by cancer, can be employed to enforce a lower level of penalization in that organ compared to the background, as discussed in Section 4.3.

Several penalization methods have been proposed for constructing structured regularization matrices. Weighted-segments methods [32] aim to minimize the L_2 solution norm to different degrees in different segments, while Laplace-type approaches [32,73,74] enforce smoothness within each segment. Edge-preserving methods have been proposed as well based on application of the anisotropic diffusion function [94].

[1] The material presented here will be also partly presented (at places with modifications and improvements) in P. Mohajerani and V. Ntziachristos, "Weighted least squares inversion for fluorescence molecular tomography", to be submitted.

The accuracy of FMT-XCT reconstructions largely depends on the performance of structured regularization methods. Two major factors determine the performance of a structured regularization approach by directing the inversion to the correct fluorophore distribution. The first factor is the level of modeling error, which in general affects the quality of reconstruction for any inversion approach. Although Born normalization is known to mitigate the adverse impact of incomplete knowledge about the optical map of the tissue [95], a certain level of modeling mismatch is unavoidable due to inaccuracies of the light propagation model involved (such as in areas with high concentration of transparent liquid or air) and large fluctuations in optical properties of tissue. Moreover, the penalization methods used to shape regularization matrices are often parameterized. For instance, in the weighted-segments method, different parameters (weights) are used to weight the solution norm in anatomical segments during the reconstruction process. The correct setting of the regularization parameters constitutes the second factor affecting the performance of FMT-XCT.

Estimation of the penalization parameters (such the segment weights) is achieved using a two-step inversion process, where in the first step an initial estimation of the distribution is obtained. The results of the first step are often in the form of estimations of the average concentration values in different organs. The penalization parameters are then calculated as a descending function of the estimated averages. In the next section, we analyze this approach and demonstrate potential problems which can adversely affect the reconstruction accuracy due to the aforementioned issues.

In this chapter we propose a method to address the above issues to improve the accuracy of structured regularization methods. The key idea in the proposed approach is the following. When we are mainly interested in learning about the fluorophore distribution in one anatomical segment or a group of segments (for instance, by the way of finding initial estimates for the average concentration values in the segment or segments), certain data points play a more critical role in our decision making process than others. The proposed method preferentially suppresses the residual values associated with these values to improve the reconstruction accuracy within one or several anatomical segments (or organs). This way the reconstruction is not required to suppress all residuals equally; a require-

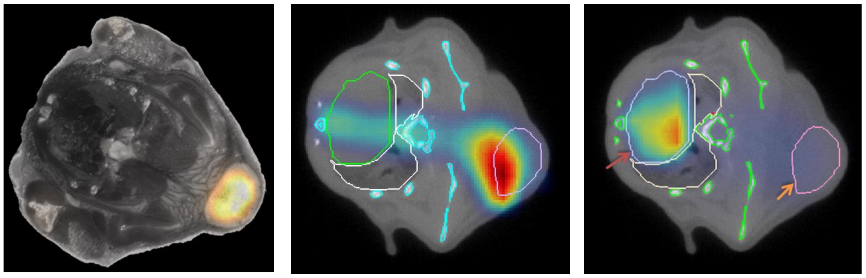

Figure 6.1: Demonstration of possible shortcomings of structured regularization-based inversion for a 4T1 subcutaneous tumor model; (a) the actual distribution of fluorescence (yellow signal) imposed over grayscale cryo-section, obtained by cryo-sectioning *ex vivo*, (b) FMT-XCT reconstruction without use of anatomical priors and (c) reconstruction where the first inversion estimates the average distribution in the heart region and the background, demonstrating reconstruction bias.

ment which due to inherently large modeling errors can sometimes lead to large reconstruction errors in the anatomical segments of interest.

A Mamdani-type fuzzy inference system (FIS) is designed and employed to assign different weights to different residual values toward preferential suppression using the method of weighted least squares (WLS). The fuzzy rules are designed based on an information-theoretic analysis of the system behavior. The presented approach can be used to either derive a more accurate initial estimation of the concentration averages (as is done here) or, otherwise, through direct incorporation in other inversion schemes with or without structured regularization. The proposed method is demonstrated and validated in this chapter for several studies including two phantom studies, one *ex vivo* study and two *in vivo* studies. These case studies cover a large span of modeling imperfections and characteristics of fluorophore distribution.

6.2 Problem statement

The accuracy of FMT reconstructions are significantly improved by incorporation of the anatomical priors in the inversion process. These priors are often used to design structured regularization which enforces preferential penalization of a measure (most often L_2 norm) of fluorophore concentration or its spatial derivatives in segments of interest in contrast

to other segments or background. The parameters associated with the structured regularization are either set heuristically or are adjusted using data-driven methods. In the later approach a first inversion is performed, for instance on a lower resolution inversion grid or on an otherwise lower-dimensional model, to achieve an initial estimation of the fluorophore distribution. This initial estimation, often in form of estimated concentration averages in different segments or organs, is then used to adjust the regularization parameters, which are in turn used to further refine the reconstruction using parameterized structured regularization in the second inversion [25, 72]. It should be noted here that in this work, the terms segment and organ are used interchangeably to refer to anatomically delineated subvolumes of the tissue. In context of phantom studies, in particular, the term segment is obviously the more proper choice.
The data-specific (or data-driven) approach [72] can be described as followed. For a group of segments T_i, $i = 1 \dots n$ an initial estimation of the fluorophore distribution can be obtained by estimating the average concentration in each segment, defined by μ_i, $i = 1 \dots n$ using the following lower-dimensional version of the FMT problem

$$\mu = \arg\min \left(\|W_o \mu - M\| \right) \quad \texttt{subject to} \quad \mu > 0, \tag{6.1}$$

where μ is a column vector of $n + 1$ elements, with the first n entries denoting the average fluorophore concentration values in the n segments T_i and the $(n+1)^{\text{th}}$ value denoting the average concentration in the background. The set of segments T_i, $i = 1 \dots n$ which in general can be a subset of all available anatomical segments, is referred to in this work as the "target set". The initial average estimations are then used to assign lower weights to segments with larger estimated average concentration in the second inversion [72]. Other variations, such as directly calculating the concentration averages from on an initial Tikhonov-based reconstruction, are also possible [25]; however, we found the approach described in Equation 6.1 to have superior performance as it reduces ill-posedness in the first inversion by handling a lower-dimensional problem.
The heuristic approaches assume that the fluorophores are indeed concentrated in the targeted region, while the data-driven approaches assume that the initial estimation obtained from the first inversion, is already a good approximation of the actual distribution. These assumptions, however, do not always hold. For instance, consider the following hypothetical experiment. We are interested to learn if a newly developed probe

targets a known subcutaneous tumor model or, vice versa, to find out if a particular enzyme or macromolecule targetable using a known probe is indeed expressed in a new tumor model - both of these situations being of significant practical relevance in preclinical research. It is not known *a priori* if the injected probe will accumulate in the target region; in fact, this is the very question which molecular imaging using FMT-XCT seeks to answer. Heuristically adjusted preferential penalization of the solution norm outside the investigated organ or tumor can lead to reconstruction bias and, hence, false alarm in case the probe is actually not accumulated in the tumor (due to lack of the targeted enzyme, for instance). Furthermore, conventionally regularized FMT or its lower-dimensional variations (such as solving for signal averages in segments instead of the entire distribution [72]) can lead to significantly inaccurate solutions, with large deviation from the actual solution.

Examples of these two situations are demonstrated in Figure 6.1 for an *in vivo* study of a nude mouse injected with 1 million 4T1 cells subcutaneously. IntegriSense 750 was injected through the tail vein 24 hours prior to imaging and accumulated exclusively in the subcutaneous tumor, as also seen in the *ex vivo* validation based on cryo-sectioning illustrated in Figure 6.1(a). FMT-XCT reconstruction without use of anatomical priors in the inversion is shown Figure 6.1(b), where the reconstructed concentration drifts toward the region deeper than the tumor instead of being contained within the tumor volume. Note that this example is not to demonstrate the necessity of utilization of anatomical priors in inversion, but to show that the initial reconstruction (later used in adjusting the structured regularization term) can be highly inaccurate. The second scenario, namely the reconstruction bias, is demonstrated in Figure 6.1(c) where the tissue is divided into heart and background. The interest of imaging has been to find out there is considerable concentration in the segment of interest (here heart) where, as seen, the inversion has erroneously reconstructed high concentration in the heart.

6.3 Weighted least squares (WLS)

Weighted least squares (WLS) is a powerful tool for directing reconstruction accuracy into a given subset of measurements. We briefly review this method in this section. Suppose $F(x;\theta)$ is a parameterized system

model where θ is a vector denoting the system parameters, x is the input vector and $y = F(x;\theta)$ constitutes the output vector. The method of least squares itself is an approach for estimating the set of system parameters given a set of input and output data vectors X and Y by solving the following minimization problem

$$\theta_0 = \arg\min_{\theta} \|R\|_2 \,,\; R = y - F(x;\theta), \tag{6.2}$$

where the vector R is called the residual vector and $\|R\|_2 = \sqrt{\sum_i R(i)^2}$. Minimization of the derivative of the residual norm in general case can be achieved using various numerical methods, such as the Gauss-Newton method.

A particularly interesting case occurs when the model function is linear. Through differentiation it can be shown that the optimal least square solution to the linear problem of $M = \mathbf{W}X$ is given as

$$X_0 = \left(\mathbf{W}^\top \mathbf{W}\right)^{-1} \mathbf{W}^\top M. \tag{6.3}$$

If measurement noise (or error) are uncorrelated random variables with zero mean and equal variance and also uncorrelated with X, then the least square solution is an unbiased estimator with minimum energy of error (Gauss-Markov theorem). This solution is also the maximum-likelihood estimation (MLE) when the measurements are corrupted by uncorrelated Gaussian noise. If the measurement noise variables are uncorrelated but have different variances, then an unbiased best linear estimator is constructed by weighting the residual in the linear least squares formulation as

$$X_0 = \arg\min_{X} \left(\sum_i \omega_i |R(i)|^2 \right), \tag{6.4}$$

where residual vector is $R = \mathbf{W}\,X - M$ and the weights ω_i are real positive numbers equal to reciprocal of the variances the measurement noises [96]. ω_i's are referred herein as "residual weights" or simply gains.

The optimization problem of Equation 6.4 is referred to as weighted least square (WLS) as the residual terms are weighted differently. The weights ω_i in Equation 6.4 formulation of WLS are optimally set to the reciprocals of the noise variances [96]. In other words, the larger the noise associated with a given measurement point, the less we care about the corresponding residual value and, accordingly, the smaller the corresponding weight ω_i.

Accurate knowledge about the noise characteristics in the FMT-XCT problem is not available in animal imaging scenarios, where the noise is often caused more dominantly by modeling errors than the additive, relatively small, camera noise.

WLS has the capability to "focus the accuracy" of the inversion to certain portions of the measurement as well as "discounting imprecision" due to large measurement noise or modeling error [96] (terms in double quotation marks introduced in [96]). As a result, WLS is a suitable tool for enforcing lower residual energy for the measurements which have a higher impact on the reconstruction in the segments of interest (i.e. the target set). Assignment of residual weight ω_i to a given measurement according to the corresponding intrinsic and fluorescence values as well as the spatial relationship to the target set, is a fairly complex problem which hardly lends itself to comprehensive quantitative formulation. In this next section, we present an information-theoretic analysis which paves the way for designing a fuzzy inference system for weight adjustment.

6.4 Analysis based on information theory

Consider a given source-detector data pair (i, m), where i and m denote, respectively, the intrinsic and fluorescence measurements (normalized by the corresponding laser powers and exposure times). For simplicity, we assume that each segment in a group of segments $T_1, \ldots, T_n$ is limited to only one voxel and that the fluorescence concentration in background has a constant value. Then, the fluorescence measurement can be written as

$$m = \sum_{i=1}^{n} g_{s,i}\, g_{i,d}\, \mu_i + \sum_{i \neq 1 \ldots n} g_{s,i}\, g_{i,d}\, \mu_b + \nu, \tag{6.5}$$

where $g_{s,i}$ and $g_{d,i}$ are the modeled (in contrast to the actual) Green's function between source s and detector d and the voxel i, μ_i's denote the concentration on voxel i corresponding to the segment T_i and μ_b is the background concentration. In the more general case, μ_i's denote average concentration values in different segments. The noise term is denoted as ν and contains in reality the measurement noise as well as terms arising from inaccurate values of the Green's function due to modeling mismatch (difference between modeled and actual values). We further simplify the

analysis by assuming the target fluorescence has a homogenous value of μ_t within all target regions and μ_b outside the target regions. These assumptions are only to make the analysis tractable and are not later enforced when processing FMT-XCT datasets. Then, Equation 6.5 can be written as

$$m = \alpha\mu_t + \beta\mu_b + \nu, \tag{6.6}$$

where

$$\begin{aligned} \alpha &= \sum_{i=1}^{n} g_{s,i}\, g_{i,d} \\ \beta &= \sum_{j\neq 1\ldots n} g_{s,j}\, g_{j,d}. \end{aligned} \tag{6.7}$$

To quantify the information gained regarding the value of μ_t after having observed the measurement pair (m, i), we employ the Kullback-Leibler (K-L) divergence [97]. For two probability distributions $f_P(x)$ and $f_Q(x)$ over a random variable X, the K-L divergence is defined as

$$D_{KL}(P||Q) = \int_{-\infty}^{+\infty} f_P(x) \log\left(\frac{f_P(x)}{f_Q(x)}\right) dx. \tag{6.8}$$

K-L divergence has been used in several medical imaging applications and primarily for image registration [98, 99]. The information gained regarding target segment T having observed (m, i) is given as

$$IG_T(m, i) = D_{KL}(f(\mu_t|m, i)||f(\mu_t)). \tag{6.9}$$

The conditional probability distribution $f(\mu_t|m, i)$ can be written using Bayes' rule as

$$f(\mu_t|m, i) = \frac{f(m, i|\mu_t)f(\mu_t)}{f(m, i)}. \tag{6.10}$$

The subscript indices designating the corresponding random variables are implied in the context and not displayed here for simplicity of notations. Furthermore $f(m, i|\mu_t)$ can be expanded as

$$f(m, i|\mu_t) = f(m|i, \mu_t)f(i|\mu_t). \tag{6.11}$$

Ignoring the increase of optical absorption causes by the higher fluorophore concentration (a common approximation in FMT methodology),

it can be safely assumed that the value of the intrinsic signal and the fluorophore concentration are independent. That is,

$$f(i|\mu_t) = f(i). \tag{6.12}$$

By combining equations Equation 6.10, Equation 6.11 and Equation 6.12, and using $f(m,i) = f(m|i)\, f(i)$ we get

$$f(\mu_t|m,i) = \frac{f(m|i,\mu_t)f(\mu_t)}{f(m|i)}. \tag{6.13}$$

The conditional probability distributions $f(m|\mu_t, i)$ and $f(m|i)$ can be easily shown to be proportional to the respective distributions for the Born ratio. That is

$$\begin{aligned} f_M(m|i,\mu_t) &= \frac{f_B(\frac{m}{i}|i,\mu_t)}{i} \\ f_M(m|i) &= \frac{f_B(\frac{m}{i}|i)}{i}, \end{aligned} \tag{6.14}$$

where M and B are random variables associated with fluorescence and Born signals. Denoting the Born ratio $b = \frac{m}{i}$, the information gain $IG_T(m,i)$ can be written then as

$$IG_T(m,i) = \int_{-\infty}^{+\infty} \frac{f(m|i,\mu_t)f(\mu_t)}{f(m|i)} \ln\left(\frac{f(m|i,\mu_t)}{f(m|i)}\right) d\mu_t, \tag{6.15}$$

where $f(\mu_t)$ has been cancelled out in the numerator and the denominator of the fraction of the natural logarithm term.

Furthermore, the Born signal can be written as

$$b := \frac{m}{i} = \frac{\alpha}{i}\mu_t + \frac{\beta}{i}\mu_b + \frac{\nu}{i}. \tag{6.16}$$

The Green's function values $g_{s,d}, g_{i,d}$ and $g_{s,i}$ are not known *a priori* - otherwise, there would be very small or no modeling mismatch and the reconstructed results would have been actual maximum likelihood solutions due to independence of the measurement noise. We assume the intrinsic measurement i is a good approximation of the modeled (using FEM) Green's function between the respective source and detector pair and, hence, $\frac{\alpha}{i}$ and $\frac{\beta}{i}$ can be properly approximated using the correspond-

ing conventional FMT weight matrix vector. That is, we assume

$$\begin{aligned} W_t &:= \frac{\sum_{i=1}^{n} g_{s,i}\, g_{d,i}}{g_{s,d}} \approx \frac{\alpha}{i} \\ W_b &:= \frac{\sum_{i \neq 1 \ldots n} g_{s,i}\, g_{d,i}}{g_{s,d}} \approx \frac{\beta}{i}. \end{aligned} \tag{6.17}$$

In reality, the intrinsic measurement is not equal to the modeled Green's function $g_{s,d}$; however, this assumption makes the analysis tractable and leads to conclusions which are intuitively justifiable as well.

To solve Equation 6.15, the distributions of the Born data given μ_t and i can be easily found based on Equation 6.16 as follows. It should be noted that given two independent random variables, the distribution of their summation $Z = X + Y$ is given by the convolution of the two distributions as

$$f_{Z=X+Y}(z) = \int_{-\infty}^{+\infty} f_X(x)\, f_Y(z - x)\, dx. \tag{6.18}$$

The information gain $IG_T(m, i)$ can be found by solving the integrals in Equation 6.15. The integrals are readily numerically calculated for given distributions of noise, μ_t and μ_b.

It is critical to take positivity of concentrations into account in the respective probability distributions of these variables; otherwise, the calculations would reduce to trivial conclusions. To facilitate numerical calculations, the values of μ_t and μ_b are assumed to be instances of random variables with uniform distributions between 0 and μ_0, i.e. $\mu_t\,, \mu_b \sim U(0, \mu_0)$. The fluorescence noise term is further assumed to be uniformly distributed, that is $\nu \sim U(0, \sigma)$. As described above, the noise value contains terms due to modeling mismatch and is, hence, in practice not independent from the fluorophore concentration values μ_t, μ_b. However, in the analysis presented here we assume independence of the noise term from the measurements and μ_t and μ_b.

Toward numerical calcluation of the integrals in Equation 6.15, it should be noted that when X and Y are uniformly distributed as $X \sim U(a, b)$

and $Y \sim U(c,d)$, then $f_{X+Y}(z)$ is given by

$$f_{Z=X+Y}(z) = \begin{cases} \frac{h(z-a-c)}{z_1-a-c} & a+c < z < z_1 \\ h & z_1 \leq z \leq z_2 \\ \frac{h(b+d-z)}{b+d-z_2} & z_2 < z < b+d \\ 0 & z \geq b+d \text{ or } z \leq a+c, \end{cases} \tag{6.19}$$

where $z_1 = a + c + \min(b-a, d-c)$ and $z_2 = b + d - \min(b-a, d-c)$ and $h = \frac{1}{\max(b-a,d-c)}$. The results of the numerical calculations of the information gain are presented in Figure 6.2, where we have used $\beta = 1$, $\mu_0 = 1$ and $\sigma = 0.1$. IG has been calculated and shown in Figure 6.2(a) for a fixed value of fluorescence $m = 0.2$, which can be considered as a "low" value for the specified probabilistic settings, versus α defined as relative weight and the intrinsic signal. Results for fixed intrinsic = 1 ("medium" value), fixed relative weight $\alpha = 1$ ("medium value") and fixed fluorescence = 2.5 ("high value") are shown, respectively, in Figure 6.2(b-d). Here, we present an analysis of the results shown in Figure 6.2. This analysis helps us in the next section to design a fuzzy-based approach for adjusting residual weights in the WLS method. In the following analysis we refer to signal values by qualitative adjectives such as low, medium and high. While the respective signal ranges justify these descriptive terms, they are not quantified in this section and serve to facilitate qualitative discussion.

Figure 6.2(a) indicates that the information gain decreases with decreasing intrinsic signal for a fixed, low fluorescence signal. This can be justified as low intrinsic values correspond to larger noise energy (as the Born signal noise is given by $\frac{\nu}{i}$ in Equation 6.16). The larger noise range means that less information can be drawn from the measurements regarding μ_t. In other words, a Born value of $\frac{0.2}{i}$ could have been contributed to by either of the α, μ_t, μ_b or noise ($\frac{\nu}{i}$) terms and, given the signal ranges, none of these options can be reliably excluded. Furthermore, it can be observed that IG increases with increasing α. This is justified as follows. Given the low value of the fluorescence, the Born signal has low values for medium and high intrinsic signals. For higher values of the relative weight α, we can be more certain that the value of μ_t is small; otherwise, it would have resulted in a large Born signal. This is new information drawn from the measurement regarding μ_t, which results in higher IG.

Figure 6.2(b) when examined vertically, for instance along the depicted

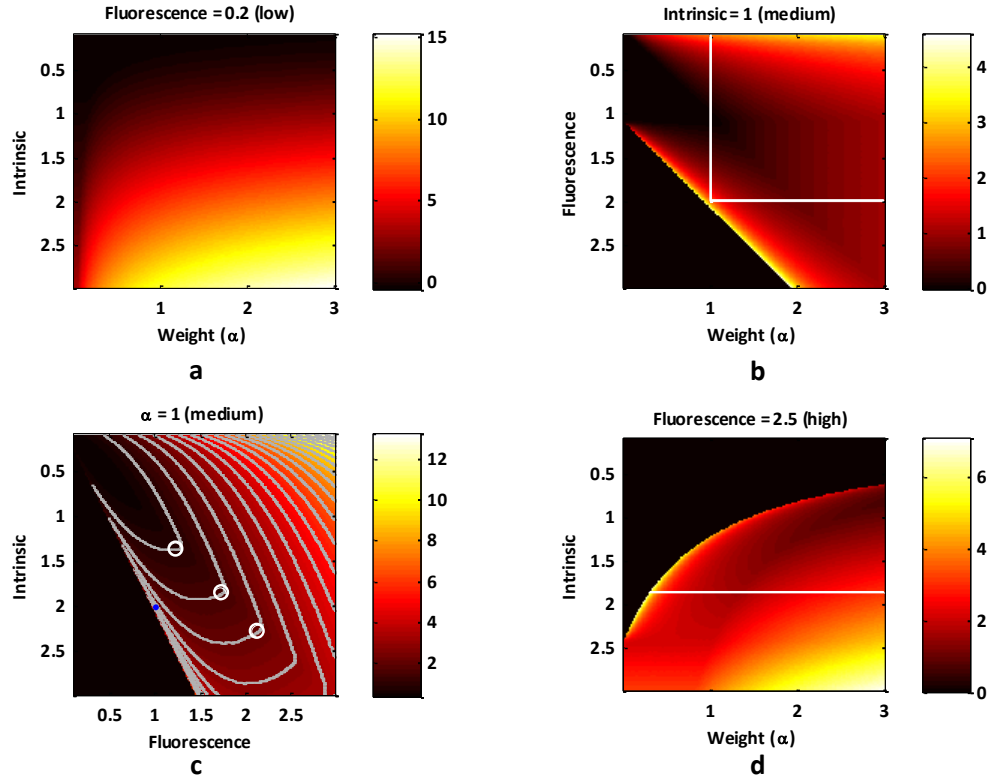

Figure 6.2: Information gain (Kullback-Leibler divergence between *a priori* and *a posteriori* distributions of target fluorescence) versus normalized intrinsic and fluorescence signals and relative weight α; (a) for fluorescence equal to 0.2 ("low"), (b) for intrinsic equal to 1 ("medium"), (c) for relative weight of 1 ("medium") and (d) for "high" fluorescence of 2.5. The information gain profiles along the lines in (b) and (d) and the contours in (c) are analyzed in the text.

white vertical line segment, indicates that IG first decreases and then increases with increasing fluorescence. For low fluorescence IG is high, as given intrinsic = 1, μ_t should have been low (otherwise, the Born signal would have been large). With increasing fluorescence, this conclusion, however, does not hold anymore; resulting in lower IG. However, for higher fluorescence (e.g. 2), IG is high again as large Born signal could not be accounted for solely from the sum of $\mu_b + \nu < 1.2$. Therefore μ_t should be large. A similar argument holds along the horizontal white line Figure 6.2(b). The three white contours (marked with circles) in Figure 6.2(c) indicates that when the intrinsic and fluorescence values have comparable values (both low, both medium or both large) then IG

is low. This is shown in Figure 6.2(c) for $\alpha = 1$, but holds generally in other cases as well. This is justified as these values correspond to medium Born values, which could have been contributed to by any of the three terms in Equation 6.16.

Figure 6.2(d), when studied along the horizontal white line, indicates that the first decreasing and then increasing trend in IG for fixed intrinsic values and fixed high fluorescence vs. increasing α. This is justifiable using a similar line of reasoning as for Figure 6.2(b). The dark regions in Figure 6.2(b-d) indicate non-realizable values, given the above parameter-settings.

In the next section, we build upon the heuristic knowledge afforded by this analysis to construct a fuzzy inference system (FIS) to estimate the residual weights given the optical measurements and the anatomical priors. Approaches based on using conditional entropy or the concept of "observed information" presented above can be used to quantify the amount of information (or uncertainty) that a given measurement pair adds to the information (or removes from the uncertainty) associated with one or a group of segments. Accordingly, the measurements with more relevant information are assigned larger residual weights. However, the formulations are highly parameterized and make strong assumptions. We have found that these issues severely limit the applicability of information-theoretic approaches to improve the accuracy of FMT-XCT inversion in targeted segments in a robust manner. As a result, we propose a robust fuzzy inference system in the next section for optimization of the residual weights in WLS.

6.5 Fuzzy-based algorithm optimization of WLS

In this section we use heuristic knowledge about behavior of measured signals with respect to geometrical relationship to target segments, to design a fuzzy inference system (FIS) to robustly adjust the residual weights. FIS systems are well-suited to system design applications where robust and complete quantitative description of input-output relationships are not readily available [100]. The input and outputs in our case consists of, respectively, the measurements plus the anatomical information and

the residual weights (or, alternatively, the residual weights and the reconstruction accuracy in the targeted region). The fuzzy-based WLS method is also referred to herein as FWLS.

Specifically let $i_{s,d}$, $f_{s,d}$, $p^f_{s,d}$, $p^i_{s,d}$, $\tau^f_{s,d}$ and $\tau^i_{s,d}$ represent, respectively, the measured intrinsic and fluorescence intensities read out from the CCD and the laser powers at fluorescence and intrinsic measurements and the exposure times for source s and detector d. Also, let σ denote the average value of the CCD dark image. Toward fuzzification of $i_{s,d}$ and $f_{s,d}$, we normalize these measurements in the domain of the respective gantry angle θ as

$$\begin{aligned} F_{s,d} &= \min\left(\frac{f^{'}_{s,d}}{F_m}, 1\right) \\ I_{s,d} &= \min\left(\frac{i^{'}_{s,d}}{I_m}, 1\right), \end{aligned} \tag{6.20}$$

where

$$\begin{aligned} f^{'}_{s,d} &= \frac{\max(f_{s,d} - \sigma, 0)}{p^f_{s,d}\,\tau^f_{s,d}} \\ i^{'}_{s,d} &= \frac{\max(i_{s,d} - \sigma, 0)}{p^i_{s,d}\,\tau^i_{s,d}}, \end{aligned} \tag{6.21}$$

and

$$\begin{aligned} F_m &= \mathcal{P}_\alpha\left(f^{'}_{s,d} | (s,d) \in P_s\right) \\ I_m &= \mathcal{P}_\alpha\left(i^{'}_{s,d} | (s,d) \in P_s\right), \end{aligned} \tag{6.22}$$

where P_s denotes the set of all detectors in projection angle θ for source s and $\mathcal{P}_\alpha(S)$ denotes the α^{th} percentile of the set S, defined as the smallest number which is greater that α percent of elements of S ($\alpha = 94$).

Furthermore, for a group of anatomical segments $T_1, \ldots, T_n$ defined as subsets of the set of all reconstruction voxels, the relative weight is defined for the FIS system as

$$\zeta(s,d) = \min\left(\frac{\rho(s,d)}{\max(\rho(s,d))}, \frac{\gamma(s,d)}{\max(\gamma(s,d))}\right), \tag{6.23}$$

where

$$\begin{aligned}\gamma(s,d) &= \frac{\sum_{v\in\bigcup T_i} g_{s,v}g_{v,d}}{\sum_{v\notin\bigcup T_i} g_{s,v}g_{v,d}} \\ &= \frac{\|\mathbf{W}((s,d),\bigcup T_i)\|_1}{\|\mathbf{W}\|_1 - \|\mathbf{W}((s,d),\bigcup T_i)\|_1},\end{aligned} \tag{6.24}$$

and

$$\rho(s,d) = \sum_{v\in\bigcup T_i} g_{v,d}, \tag{6.25}$$

where $\mathbf{W}((s,d),\bigcup T_i)$ in Equation 6.24 denotes entries of the weight matrix $\mathbf{W}$ corresponding the row of the measurement pair (s,d) and voxels located in the segment set $\{T_1,\ldots,T_n\}$ and the maxima in Equation 6.23 are taken over (s,d), i.e. all measurements.

The definitions of $\rho(s,d)$ and $\gamma(s,d)$ given above, can be interpreted as follows. For a given group of segments, $\gamma(s,d)$ is equal to ratio of the fluorescence (or, equally, the Born) signal measured (at detector d when tissue is illuminated by source s) when the distribution is 1 inside $\bigcup T_i$ and 0, outside relative to when the distribution is 0 inside $\bigcup T_i$ and 1 outside. Furthermore, the value of $\rho(s,d)$ is equal to the fluorescence signal measured at detector d, when the distribution is 1 inside $\bigcup T_i$ and 0 outside, assuming homogenous distribution of excitation fluence. That is, $\rho(s,d)$ is equal to the fluorescence emanating from $\bigcup T_i$ if the entire volume of $\bigcup T_i$ was excited equally.

The value of $\gamma(s,d)$ is relatively large if $\bigcup T_i$ has a considerable overlap with the "banana shape" between s and d. The banana shape consists of a cluster of voxels to which the measurement has a high sensitivity and arises in fluorescence and not fluorescence diffuse optical tomography, where the sensitivity is defined with respect to changes in optical properties [8]. Also, The value of $\rho(s,d)$ is relatively large if $\bigcup T_i$ is relatively close to the detector d, in comparison with other detectors. Therefore, roughly speaking, $\zeta(s,d)$ as defined in Equation 6.23 has a large value if and only if $\bigcup T_i$ has a considerable overlap with the one half of the banana shape which is closer to the detector side. Both terms in Equation 6.23 are normalized with corresponding maximum values across all source and detector pairs in any given projection.

The variables $I_{s,d}$, $F_{s,d}$ and $\zeta(s,d)$ defined above, are referred to as normalized intrinsic (`INT`), normalized fluorescence (`FLUO`) and relative weight (`ALPHA`), respectively. These variables are fuzzified using the fuzzy sets

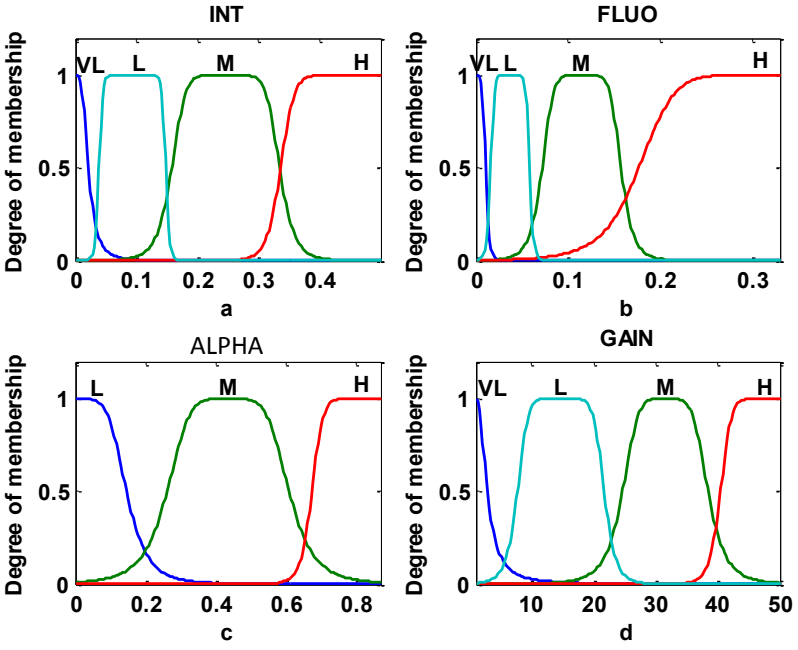

Figure 6.3: Input and output membership functions of the fuzzy inference system (FIS) for optimization of weighted least squares (WLS); (a) normalized intrinsic signal `INT`, (b) normalized fluorescence signal `FLUO`, (c) normalized weight `ALPHA` and (d), the output variable `GAIN`.

depicted in Figure 6.3. Four sets for very low (VL), low (L), medium (M) and high (H) values are defined for each of normalized intrinsic and fluorescence variables. The relative weight `ALPHA` is fuzzified using the three L, M and H fuzzy sets as shown in Figure 6.3(c). Figure 6.3(d) shows 4 fuzzy output sets for the residual weight, defined as `GAIN`. The membership functions of all the fuzzy sets are designed using generalized bell-shaped membership functions. The fuzzy rules of the FIS system are presented in Table 6.1. Residual values corresponding to measurements with very low normalized intensity or very low relative weight, as well as measurements with comparable normalized fluorescence and intrinsic values are assigned a "very low" gain (the fuzzy set VL for `GAIN` has a maximum value at 1, which corresponds to conventional suppression of residuals in LS). The Mamdani-type [101] FIS system employed in this work used multiplication for (fuzzy) logical `AND` operation and maximum for `OR` operation. Aggregation was done through summation and the final gain was achieved by defuzzifying the aggregated fuzzy output using "middle of maximum".

Table 6.1: Fuzzy inference system rules for assigning residual weights driven by data and anatomical priors. The fuzzy variables `INT`, `FLUO` and `ALPHA` are normalized intrinsic, fluorescence and relative weight (as described in the text) and `GAIN` represents the residual weighting gain. Also VL, L, M and H represent the fuzzy sets "very low", "low", "medium" and "high", respectively.

	Antecedent							Consequent
1	if	(`INT` is VL)	or	(`ALPHA` is L)			then	(`GAIN` is VL)
2	if	(`INT` is L)	and	(`FLUO` is L)			then	(`GAIN` is VL)
3	if	(`INT` is M)	and	(`FLUO` is M)			then	(`GAIN` is VL)
4	if	(`INT` is H)	and	(`FLUO` is H)			then	(`GAIN` is VL)
5	if	(`INT` is L)	and	(`FLUO` is M)	and	(`ALPHA` is L)	then	(`GAIN` is L)
6	if	(`INT` is H)	and	(`FLUO` is L)	and	(`ALPHA` is M)	then	(`GAIN` is L)
7	if	(`INT` is L)	and	(`FLUO` is H)	and	(`ALPHA` is M)	then	(`GAIN` is M)
8	if	(`INT` is L)	and	(`FLUO` is M)	and	(`ALPHA` is M)	then	(`GAIN` is M)
9	if	(`INT` is L)	and	(`FLUO` is H)	and	(`ALPHA` is H)	then	(`GAIN` is H)
10	if	(`INT` is M)	and	(`FLUO` is VL)	and	(`ALPHA` is H)	then	(`GAIN` is H)
11	if	(`INT` is H)	and	(`FLUO` is VL)	and	(`ALPHA` is H)	then	(`GAIN` is H)

The WLS approach can be used with or without structured regularization. However, using the WLS approach along with structured regularization, takes full advantage of the anatomical priors by first improving the accuracy of the initial estimation of segment averages in few targeted segments and then, using this improved initial estimation to penalized the reconstruction in low-value segments. Specifically, this combination of the two methods can be written as:

$$\begin{aligned}
&\text{a.} \quad G = \mathrm{FIS}(M, I, \bigcup T_i) \\
&\text{b.} \quad \mu_0 = \arg\min \left(\|\mathrm{diag}(G)(W_o \mu - M)\| \right) \ \texttt{subject to} \ \mu > 0 \\
&\text{c.} \quad \lambda_0 = \Gamma(\mu_0) \\
&\text{d.} \quad X = \arg\min \left(\|\mathbf{W}X - M\| + \|\mathrm{diag}(\lambda_0) X\| \right),
\end{aligned} \tag{6.26}$$

where Γ is a decreasing function of the vector μ, which maps the segment averages to segment weights (for the weighted segment approach of part (c)). Also, $G = \mathrm{FIS}(M, I, \bigcup T_i)$ denotes residual weights calculated by the FIS system for fluorescence and intrinsic measurement vectors M and I and the segments $\bigcup_i T_i$.

Table 6.2: Optical (reduced) scattering and absorption coefficients for various tissues (extracted from [49]) and for the phantom material.

	Tissue	Bone	Lung	Heart	Phantom
μ_a (cm^{-1})	0.3	0.1	0.25	0.35	0.2
μ_s (cm^{-1})	10	20	30	23	15

As a reminder, the "data-specific priors" method referred to as DS herein, is defined as

$$\begin{aligned} &\text{a.} \quad \mu_0 = \arg\min \left(\|W_o \mu - M\| \right) \ \texttt{subject to} \ \mu > 0 \\ &\text{b.} \quad \lambda_0 = \Gamma(\mu_0) \\ &\text{c.} \quad X = \arg\min \left(\|\mathbf{W} X - M\| + \|\mathrm{diag}(\lambda_0) X\| \right). \end{aligned} \tag{6.27}$$

In this work, we have used the following mapping [32]

$$\Gamma(\mu_i) = \frac{(1+a)\max_i(\mu_i)}{\mu_i + a \max_i(\mu_i)}, \tag{6.28}$$

where a was set to 0.06 herein.

Obviously, the combination of the fuzzy-based WLS approach with other penalization approaches in various orders is also possible.

6.6 Results

The proposed method, as shown in Equation 6.26, has been verified using a large number of phantom and animal studies. In this section, we demonstrate the results for two phantom studies, one *ex vivo* study and two *in vivo* studies. These cases cover a large range of modeling imperfections and fluorophore distributions. The optical scattering and absorption coefficients used for all cases are presented in Table 6.2. Measured intrinsic values (prior to power and exposure time normalization and after subtraction of the average readout noise level of 620 counts) smaller than 100 counts were not used in the processing and reconstruction using any of the methods.

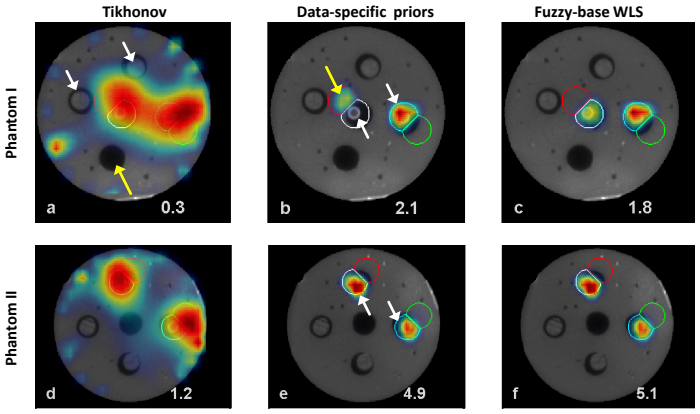

Figure 6.4: Fuzzy-based WLS verified using two phantom studies. Reconstructions based on Tikhonov regularization, data-specific priors and the proposed fuzzy-based WLS are shown for phantom I (phantom II) in (a),(b) and (c) ((d), (e) and (f)), respectively. In both phantoms, two absorbing, carbon rods are placed inside 2 (white arrows in (a)) of the 5 holes in an agar-based phantom and one hole is left empty (yellow arrow (a)). Two fluorescent tubes are placed in 2 other holes in locations marked with white arrows in (b), for phantom I, and (e), for phantom II. Each slice is normalized to its own maximum (denoted by the numbers in right, bottom corners).

6.6.1 FWLS inversion of phantom and *ex vivo* data

Figure 6.4 present the results for two phantom studies performed using a silicon-based cylindrical phantom with a diameter of 19 mm. To introduce optical perturbation and increase modeling mismatch, two absorbing, carbon rods were placed inside the phantom and one hole was left empty (filled with air), as shown in Figure 6.4. Two fluorescent tubes filled (as explained in Appendix C) with Alexa 750 (Invitrogen, Grand Island, NY, USA) were inserted into two of the holes. In phantom I case, one tube was inserted in the center and one in an off-center hole while in the phantom II case both tubes were inserted in two off-center holes. In both cases, 4 segments were created; two containing the inserted tubes and two segments adjacent to the tubes containing no fluorophores.

The Tikhonov-based reconstruction for both cases, Figure 6.4(a) and (d), do give an indication of approximate tube locations. However, the results, especially for phantom I, are relatively inaccurate. The results based on data-specific priors (DS), as demonstrated in Equation 6.1, are presented

Table 6.3: Relative concentration values in different segments for phantom and *ex vivo* studies; DS and FWLS denote, respectively, data-specific priors and fuzzy-based weighted least squares. Numbers in brackets correspond to segments containing the fluorescent tubes. Last column shows the L_2 norm of the entire reconstructed vector. The second row shows segment volumes normalized to the volume of the first segment "Tube 1".

	Segment	Tube 1	Cylinder 1	Tube 2	Cylinder 2	$\|X\|$
	Volume	1	1	1	1	
Phantom I	DS	[59]	3	[0]	37	19.2
	FWLS	[61]	0	[38]	1	17.9
Phantom II	DS	[41]	4	[55]	0	43.2
	FWLS	[41]	2	[56]	0	43.5
Ex vivo	DS	[0]	100			17.1
	FWLS	[63]	37			11.2

in Figure 6.4(b) and (e) and reconstruction using the fuzzy-based WLS are shown in Figure 6.4(c) and (f), for phantoms I and II, respectively. The "target set" consisted here of all four segments. While for phantom II, both approaches reconstruct the tubes in the correct segments, the DS-based method failed to reconstruct the middle tube in phantom I correctly, as seen in Figure 6.4(b). This is because of erroneous first estimation of segment averages, which is likely due to large modeling mismatch and large depth of the middle tube. However, the fuzzy-based WLS approach has correctly reconstructed the middle tube in phantom I as well.

For quantification and comparison purposes we use the following measure. For a given anatomical segment (organ) within a group of segments (organs), its "relative concentration" is defined as

$$r_i = 100 \times \frac{\mu_i}{\sum_i \mu_i}, \tag{6.29}$$

where μ_i is the average value of the reconstructed signal within the volume of the i^{th} segment. A value of, say, 70% for the relative concentration defined as such for a given segment, however, does not mean that 70% of the reconstructed signal is contained within the respective segment. But in general the higher the value of relative concentration, the more pronounced the segment appears in the reconstructions in comparison to other segments and background. The reconstruction results are quantified for different segments and the results are presented in Table 6.3

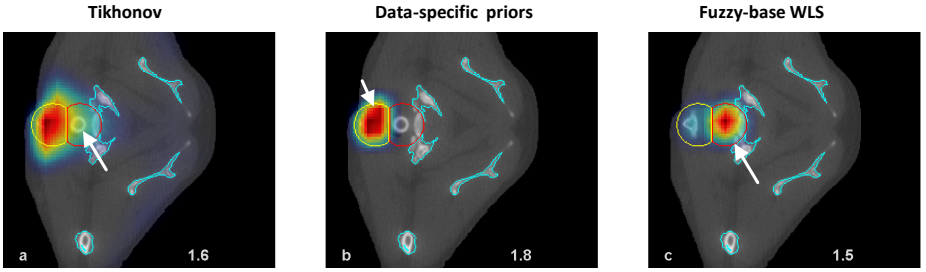

Figure 6.5: Fuzzy-based WLS verified using an *ex vivo* study. Two anatomical segmented are specified: red curve, containing the fluorescent tube (pointed to in (a)), and an additional segment shown by the yellow curve. Reconstructions based on Tikhonov regularization, data-specific priors and the proposed fuzzy-based WLS are shown in (a), (b) and (c), respectively. Numbers in bottom right corners denote maximum fluorescence intensities within respective slices.

using the "relative concentration" for the two tubes and the two other segments (cylinder 1 and cylinder 2). Furthermore, Figure 6.5 demonstrates reconstruction results for an *ex vivo* study, where a fluorescent tube filled with Alexa 750 was inserted through the esophagus in a CD1 mouse post-mortem. Two segments were created; one containing the tube and one adjacent to it, containing no fluorophores. Both Tikhonov-based and DS-based approaches (Figure 6.5(a) and (b), respectively) have erroneously reconstructed the fluorophores in the cylinder segment while the fuzzy-based approach has correctly reconstructed the solution in the tube segment. The "target set" consisted here of both segments. The quantification results for this case are also presented in Table 6.3.

6.6.2 FWLS inversion of subcutaneous distributions

The proposed method is further verified using an *in vivo* study for a subcutaneous fluorophore distribution. A nude mouse developed a subcutaneous tumor through injection of one million 4T1 breast tumor cells subcutaneously behind the thorax. The 4T1 model was injected with 2 nmol of IntegriSense 750 (PerkinElmer, Waltham, MA, USA) in the tail vein 24 hours prior to imaging (same mouse was used in Section 7.3.2)

Figure 6.6 shows the verification results for the 4T1 model. The reconstructions were performed once using the optical properties presented in Table 6.2 for the respective organs (Figure 6.6(a-c)) and once using

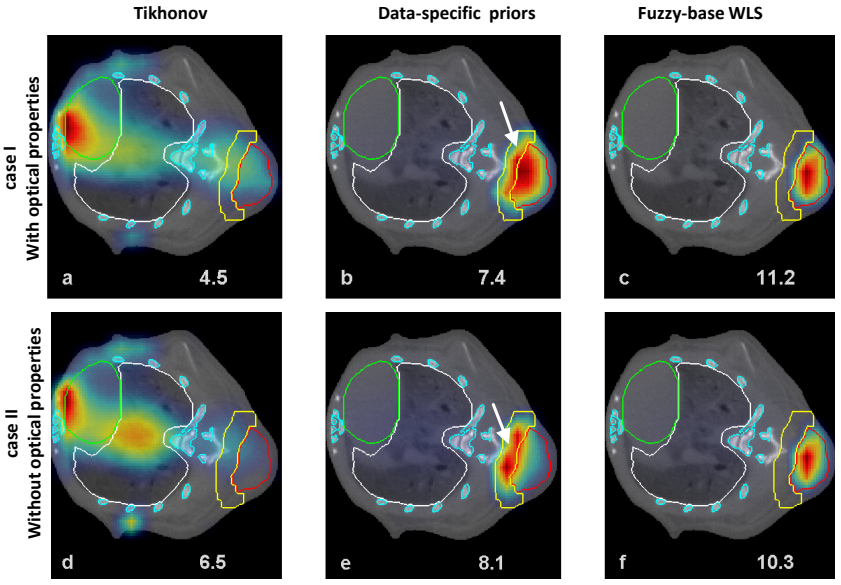

Figure 6.6: Fuzzy-based WLS verified using an *in vivo* study of a nude mouse with a subcutaneous 4T1 tumor. Five anatomical segmented are specified: bones (blue), lung (white), heart (green), tumor periphery (yellow) and tumor (red). Reconstructions based on Tikhonov regularization, data-specific priors and the proposed fuzzy-based WLS are shown with (without) inclusion of different optical properties denoted as case I (case II) in (a), (b) and (c) ((d), (e) and (f)), respectively. *Ex vivo* validation for this case is shown in Figure 6.1(a). Numbers in bottom right corners denote maximum fluorescence intensities within respective slices.

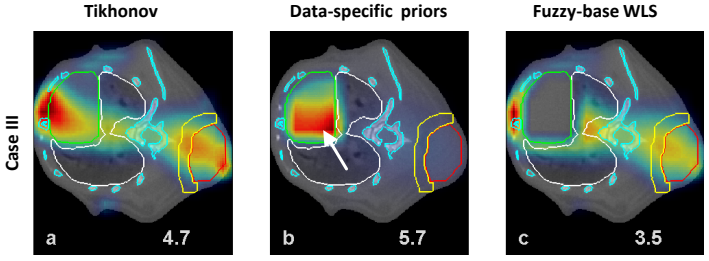

Figure 6.7: Fuzzy-based WLS reconstruction - a bias study; (a-c) denote, respectively, reconstructions based on Tikhonov regularization, data-specific priors and the proposed fuzzy-based WLS, the target set is "Heart".

homogenous optical properties for all organs (Figure 6.6(b-e)). The proposed approach focuses the reconstruction accuracy in the target segment set; however, it does not create reconstruction bias. In fact by the virtue of higher reconstruction focus, the typical bias behavior of conventional weighted-segment approaches is largely avoided using the

Table 6.4: Relative concentration values in different segments for the 4T1 *in vivo* study; DS and FWLS denote, respectively, data-specific priors and fuzzy-based weighted least squares. Numbers in brackets correspond to reconstructions in the subcutaneous tumor. Case I (case II) denote reconstructions for target set {tumor, periphery} with inclusion of organ-specific (homogenous) optical properties and case III is where the target set is {heart}. Cases I and II and the case III are graphically demonstrated in, respectively, Figure 6.6 and Figure 6.7. *Italic* numbers signify that the corresponding segment (column) was not in the target set for the corresponding row. Last column shows the L_2 norm of the entire reconstructed vector. The second row shows segment volumes normalized to the volume of the first segment "Tumor".

	Organ	Tumor	Periphery	Heart	$\|X\|$
	Volume	1	0.98	2.81	
Case I	DS	[39]	45	*5*	73.5
	FWLS	[84]	0	*4*	87.1
Case II	DS	[19]	56	*9*	62.7
	FWLS	[73]	1	*9*	66.7
Case III	DS	*[15]*	*16*	47	68.9
	FWLS	*[29]*	*28*	0	87.8

proposed approach. To demonstrate this fact, we have reprocessed the 4T1 study, while setting the target segment to the heart segment only. It is know that heart contains almost no concentration of IntegriSense, as also seen from the *ex vivo* validation in Figure 6.1(a). The results are presented in Figure 6.7, where the DS-based approach has resulted in large concentration in the heart, as seen in Figure 6.7(b). This is typical of weighted-segment based approaches. This issue is, however, mitigated by using the fuzzy-based approach, as seen in Figure 6.7(c). In fact, using the proposed method, not only no fluorescence was reconstructed in the heart, but also the signal was largely reconstructed in the tumor region. The quantitative results for case I, Figure 6.6(a-c), as well as this bias study denoted as case II are presented in Table 6.4

6.6.3 FWLS inversion of FMT—phase-contrast CT

An interesting case is presented in this section using a model of pancreatic ductal adenocarcinoma (PDAC). The study was performed on a 63 day old $Ptf1a^{+/Cre}$, $Kras^{+/LSL\text{-}G12D}$, $p53^{LoxP/LoxP}$ (CKP) [102–104]

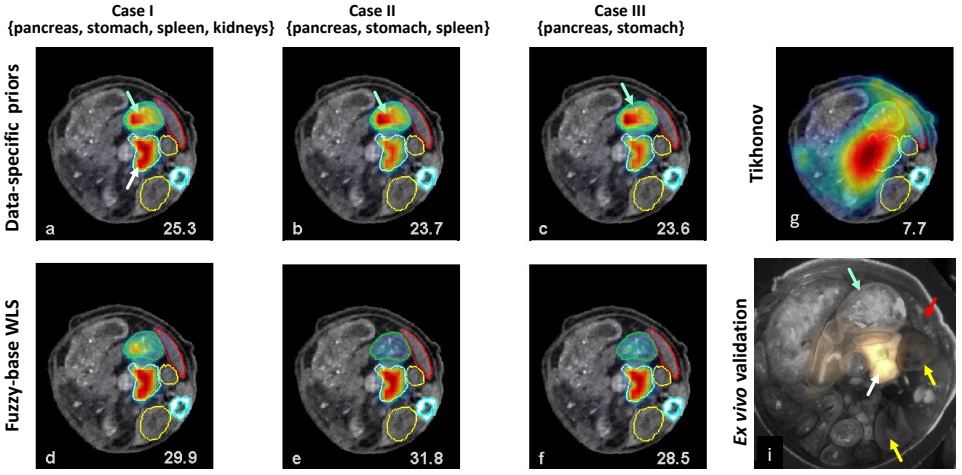

Figure 6.8: Fuzzy-based WLS verified using an *in vivo* study of a PDAC mouse with pancreatic tumor. Five anatomical segmented are specified: bones (cyan), pancreas (white), kidneys (yellow), stomach (green) and spleen (red). (a-c) Reconstructions using data-specific priors when the targeted segment sets are {pancreas, stomach, spleen, kidneys}, {pancreas, stomach, spleen} and {pancreas, stomach}, respectively. Corresponding results using the proposed fuzzy-based WLS approach are shown in (d-f). Tikhonov- based reconstruction is shown in (b). (i) *Ex vivo* validation depicting fluorescence in yellow transparency over the gray-scale cryo-section (green, white, yellow and red arrows point to stomach, pancreas, kidneys and spleen, respectively). Numbers in bottom right corners denote maximum fluorescence intensities within respective slices.

model of pancreatic ductal adenocarcinoma (PDAC), injected with IntegriSense 680, 24 hours prior to injection.[2] This animal was imaged using new hybrid modality approach consisting of FMT and phase-contrast X-ray computed tomography (PCCT). Briefly, PCCT is a novel anatomical modality which enables imaging organs with much higher soft tissue contrast than conventional CT. This hybrid approach is called FMT-PCCT and is presented and discussed later in detail in Section 7.3.

Figure 6.8 presents the reconstruct results using Tikhonov-based and DS-based approaches as well as the proposed fuzzy-based approach for the PDAC model. In addition to bones, 4 organs were segmented from the PCCT images as well. These segments include the pancreas (white contour), stomach (green contour), spleen (red contour) and kidneys (yellow

[2] Animal and its strain specification were provided by Dr. M. Trajkovic-Arsic, as part of a collaboration project with Priv.-Doz. Dr. Jens Siveke's research group from II. Medizinische Klinik, Klinikum rechts der Isar.

Table 6.5: Relative concentration values in different segments for the PDAC *in vivo* study. DS and FWLS denote, respectively, data-specific priors and fuzzy-based weighted least squares. Numbers in brackets correspond reconstructions in the subcutaneous tumor. Cases I, II and III correspond to target sets {pancreas, stomach, spleen, kidneys}, {pancreas, stomach, spleen} and {pancreas, stomach}, respectively. *Italic* numbers signify that the corresponding segment (column) was not in the target set for the corresponding case (row). Last column shows the L_2 norm of the entire reconstructed vector. The second row shows segment volumes normalized to the volume of the first segment "Pancreas".

	Organ	Pancreas	Stomach	Spleen	Kidneys	$\|X\|$
	Volume	1	2.18	0.43	1.90	
Case I	DS	[65]	31	1	0	73.5
	FWLS	[70]	25	3	0	87.1
Case II	DS	[62]	35	0	*1*	62.7
	FWLS	[81]	17	0	*0*	66.7
Case III	DS	[62]	35	1	1	68.9
	FWLS	[76]	21	*1*	*1*	87.8

contour) are all located geometrically close to each other on the left side of the animal. The results presented for three cases; case I, II and III correspond to target sets {pancreas, stomach, spleen, kidneys}, {pancreas, stomach, spleen} and {pancreas, stomach}, respectively. As explained in Section 6.2, the "target set" include the anatomical segment for which the average concentrations are estimated using either the DS-based approach or the proposed approach. All other segmented and non-segmented organs are referred to as "tissue".

As can be seen in all cases, the DS-based method reconstructed the signal in both the pancreatic tumor and the stomach, while the fuzzy-based method has correctly reconstructed the fluorescence in the pancreas in all three cases. The quantification results based on Equation 6.29 are presented for all cases in Table 6.5.

Finally, it should be noted that the entire execution of the fuzzy inference system along with projection-based normalization of the intrinsic and fluorescence values lasted around 1 second in MATLAB on a computer with an Intel Core^{TM} i7 CPU @ 3.4 GHz and 16 GB RAM.

6.7 Discussion

Given a linear model of FMT and set a of measurements, under certain assumptions, the maximum likelihood solution is obtained by minimizing the residual norm. However, it was observed that the FMT solution without anatomical priors may be inaccurate due to modeling imperfection. In this direction, the major step toward improving the solution has been inclusion of anatomical priors in the structure of the regularization term. Efficiently using anatomical priors necessitates sensible settings of penalization parameters; otherwise, the solution can become biased. Optimization methods of these parameters rely on solving a lower-dimensional version of the FMT problem, with or without priors, to form initial estimations of distribution intensity in each segment. However, this approach is also limited by the accuracy of the first solution, which may have large spatial offset from the actual distribution - a situation an example of which was illustrated in Figure 6.1(b). To mitigate these problems, the accuracy of the first estimations should be improved. Once an initial estimation with correct spatial relation between segments has been established, the penalization terms can be reliably optimized.

A reevaluation of the imaging standpoint is at this stage in order. In many molecular tomographic imaging applications, such as probe or animal model development or therapy monitoring, the primarily interest of using imaging is to learn about the concentration of a particular fluorophore, or the lack thereof, in a particular lesion. Hence, simply put, the reconstruction accuracy in a given organ or lesion matters more than the accuracy of reconstruction in the rest of the tissue. One underlying assumption in conventional FMT-XCT reconstruction schemes, is the independence and uniform variance of the errors associated with different measurements. This assumption then leads to the conventional least-squares reconstructions, which as seen can result in erroneous reconstructions.

In this chapter we proposed a fuzzy inference system for optimizing the residual weights. The proposed fuzzy-based WLS system, also called FWLS, was employed to improve initial concentration average estimation for the two-step inversion process using the weighed segments approach. However, combinations with other inversion schemes and in different orders are also possible. The optimal combination of FWLS with other penalization schemes is an interesting topic for further investigation.

The proposed fuzzy-based weighted least squares approach was verified using two phantom studies and one *ex vivo* study for reconstruction of fluorescent tubes. The phantom results presented in Figure 6.4 demonstrate more accurate reconstruction using FWLS than without (i.e. using DS) in reconstructing the middle tube in phantom I. For phantom II, both methods were equally accurate with comparable signal intensities, as shown in Table 6.3. For the *ex vivo* study, DS erroneously reconstructed the tube in the empty segment, due to the erroneous initial estimation of concentration, while FWLS resulted in a more accurate reconstruction.

The proposed method was also verified using *in vivo* studies; a nude mouse injected with 4T1 cells subcutaneously (referred to here as the 4T1 model) and a model of PDAC. These two models represent two important classes of fluorophore distributions in small animal imaging. The distribution in the 4T1 model was confined to the small volume of the subcutaneously tumor and was, therefore, on average only few millimeters under the skin. The PDAC model, on the other hand, represents a case where the tumor spans a volumetric domain (the oblong shape of pancreas) which extends from around 3 mm up to 10 mm under the skin.

The 4T1 model was reconstructed with heterogeneous optical properties (as described in Table 6.2), denoted as case I, and homogenous optical properties (all organs set to "Tissue" values of Table 6.2), denoted as case II. The results were presented in Figure 6.6. It is known and expected that the reconstructions are generally more accurate with the inclusion of organ-specific optical properties in the forward modeling. Nevertheless, the two cases were included to investigate different levels of modeling imperfection. As can be seen from Figure 6.6, the solutions with inclusions of *a priori* information in the inversion solution are better than Tikhonov-based regularization - a fact which is also expected. However, data-specific based (DS) approach generates a large portion of the reconstructed signal in the segment labeled tumor's periphery. It is clear from the *ex vivo* validations that no significant signal existed in this periphery region. The DS results, however, have a larger signal average in the periphery region than in the tumor region in both case I and case II, as can also be seen in Table 6.4. This is due to fact that initial estimation of fluorophore distribution was partly erroneous. The situation is worse for case II, where almost all of the signal is reconstructed in the periphery. On the other hand, FWLS has correctly reconstructed the concentration

in the tumor, where it in reality exists. The FWLS solutions are almost equally accurate for both case I and case II.

Interestingly, although FWLS uses gains as high as 50 to preferentially minimize certain residual values, the high gains do not translate to artificially increased signal concentrations. This can be observed in all of the cases presented in the previous section. For the 4T1 study, as can be seen in Table 6.4, the FWLS reconstructions have an L_2 norm (last column) comparable to the other solutions. In fact, the FWLS have slightly a smaller than other reconstructions, as the correct solution (accumulated in the tumor) has on average a lower depth than erroneous ones (e.g. accumulation in periphery). It was further observed for all cases presented that FWLS does not necessarily create reconstruction bias by reconstructing artificially high or low values in regions subject to reconstruction focus, i.e. the "target set".

The processing results for the PDAC model, imaged using a novel FMT-based hybrid modality called FMT-PCCT (refer to Section 7.3), demonstrate superior performance for reconstruction with a group of anatomically neighboring segments. As observed in Table 6.5, DS resulted in signal accumulation in the stomach segment with an average value of 48-56 % of the average in pancreatic tumor. The corresponding range for using the proposed approach was 21-35%; a difference also clearly visually visible from the reconstructions illustrated in Figure 6.8.

Reconstruction bias is a typical behavior of structured regularization approaches and, in particular, the weighted segments approach. An example is presented in the bias study of Figure 6.7, where the heart was set as the target segment in both DS and FWLS algorithms. It is known from *ex vivo* validation (Figure 6.1(a)) that there is no conspicuous accumulation of IntegriSense in the heart. Nevertheless, DS reconstructed almost the entire distribution in the heart while FWLS reconstructed almost no signal in the heart, as seen in Figure 6.7. By improving the accuracy of the initial estimation in the heart region, FWLS has assigned a very low weight to the heart for the second inversion using weighted-segments.

The regularization parameter λ was set to $0.023\|\mathbf{W}\|$ and $0.051\|\mathbf{W}\|$ for phantom and animal studies, respectively. Both of these values are less than the point of the maximum curvature of the L-curve of the respective Tikhonov reconstructions. The point of maximum curvature was found in the studies presented here to result in over-regularization. Moreover,

a smaller λ is generally applied to phantom studies due to lower level of modeling error.

The fuzzy rules presented in Table 6.1 were designed heuristically with the help of insight driven from the analysis of the results afforded by the information-theoretic treatment presented in Section 6.4. The information gain (IG) was defined as the Kullback-Leibler distance between *a priori* probability distribution of the concentration (in a target set of segments) and the conditional probability distribution given a pair of intrinsic and fluorescence measurements. This measure can be potentially used itself to optimize the residual weights (or gains, as defined here). However, determination of the residual weights as a direct function of the information gain defined using the statistical settings presented in Section 6.4, was hindered due to the difficulty of robust settings of the model parameters and incompleteness of the statistical model itself in fully representing the FMT-XCT system. These shortcomings were overcome by the fuzzy inference system, which made construction of a robust weight optimization framework possible. Optimization of the current statistical framework and application of other measures such the Fisher information, defined as the negative of the Hessian of the log-likelihood function, for direct adjustment of the residual weights is an interesting topic for further investigation.

An important issue regarding the data-specific approach and similar approaches based on obtaining an initial estimation of the concentration average in one or more segments is the following. For convenience of discussion let us consider the case of the *ex vivo* case presented in Figure 6.5. If the initial estimation was to be made for the concentration in the segment containing the fluorescent tube, while ignoring other anatomical segments, the initial estimation (through the DS approach, for instance) would have correctly estimated a high concentration in the tube. However, the same occurs if the estimation is performed for the empty cylindrical segment - that is, DS reconstructs mainly in the empty cylinder. The reason for this phenomenon is partly due to the very small volume of the targeted segment with respect to the background. In other words, even a small amount of fluorophore erroneously reconstructed in a small segment, results in a large average value. While, a large segment containing small tumors with high fluorophore concentrations (typical in lung models, for instance), will be assigned a small average concentration. This way, the smaller segments are in general assigned larger concentration

values, which could lead to inaccurate reconstructions. While this issue does not directly affect the proposed WLS-based approach (as, per se, it does not entail estimation of average values), it does pose a problem for approaches relying on initial estimation of segment averages (such the combination of the FWLS and DS proposed above, or DS alone). Estimation of other statistical moments for different segment might mitigate this problem.

6.8 Conclusion

In this chapter we proposed a method for robust inversion of FMT-XCT through weighted residual minimization. The weights applied to the residual vector were optimized for each measurement pair using a fuzzy inference system consisting of three inputs, one output and 11 rules. The inputs consisted of normalized intrinsic and fluorescence values as well as a relative weight assigned to the set of target segments (or organs). The rules were designed with the insight afforded through an information-theoretic analysis of the FMT-XCT problem using the Kullback-Leibler divergence. The fuzzy system then creates fuzzy gains, which when defuzzified can be applied to preferentially suppress the corresponding residual values. As such, the accuracy of the weighted least square can be focused within the target segments. The proposed approach can be applied with structured regularization approaches in many configurations to optimize the inversion of FMT-XCT. The proposed method was verified using several phantom, *ex vivo* and *in vivo* studies. The results demonstrated significant improvement in reconstruction accuracy for all cases and especially in animal studies.

Building upon the system potential and the flexibility and accuracy of the XFMT code equipped with FEM modeling of light propagation and other algorithmic developments, we have further explored and developed several preclinical applications, as presented in the next chapter.

7 Hybrid tomographic imaging of animal models

7.1 Introduction

The processing framework developed so far has been verified with and applied to several *in vivo* experiments targeting regions in various organs for small animal studies performed using the FMT-XCT systems at HMGU and Klinikum rechts der Isar. In this chapter we present one example, consisting of imaging a pancreatic tumor. While FMT has been proposed for imaging in the pancreas region in stand-alone mode [105] and in conjunction with MRI [106], the results presented here constitute, to our knowledge, the first three-dimensional quantitative imaging of a pancreatic tumor using FMT-XCT. As aforementioned, other animal studies have been processed using the developed XFMT processing framework as well and are presented briefly in Appendix C. We furthermore present here for the first time, hybrid imaging using FMT and phase-contrast CT, called FMT-PCCT, for small animal imaging. Phase-contrast computed tomography (PCCT) is an emerging technology which aims at anatomical imaging using the phase-shift experienced by X-ray photons traveling through the tissue [107]. PCCT has a much higher soft tissue contrast than the conventional absorption-based CT. We demonstrating hybrid imaging using FMT-PCCT via *in vivo* animal studies, where the high contrast PCCT images were used to generate *a priori* information for FMT inversion, in regions where the conventional CT has low or no contrast. The FMT-PCCT images presented in this chapter are the first demonstration of this hybrid approach, which we believe, as will be discussed, will play an important role in the future wider-scale deployment of FMT.

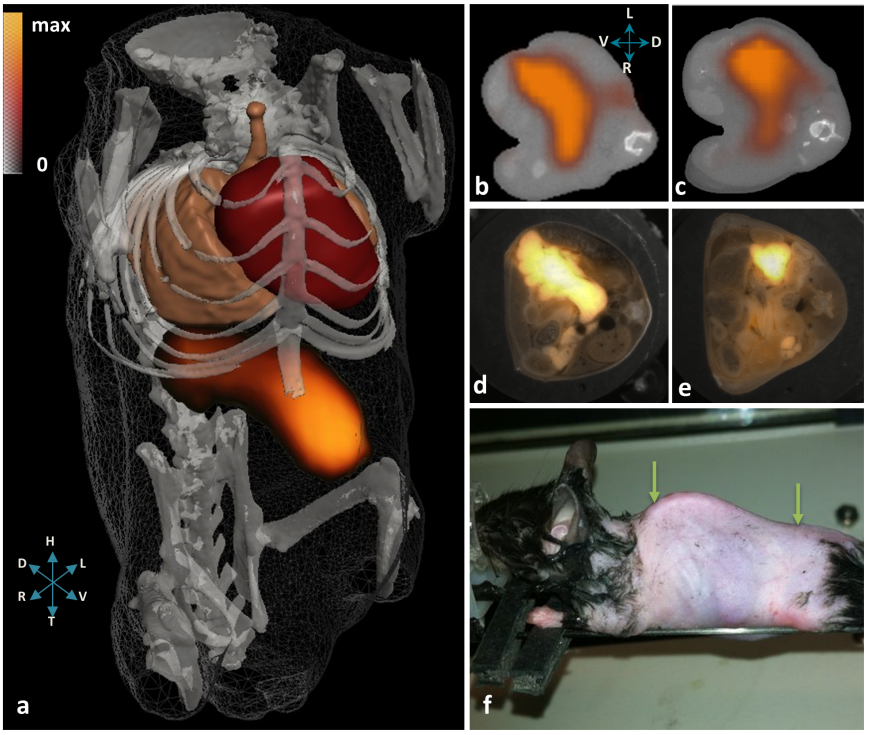

Figure 7.1: Tomographic imaging of integrin expression in a pancreatic cancer model *in vivo*; (a) 3-D demonstrations of the reconstructed fluorescence signal along with skeleton, lungs and heart (red and brown isosurfaces), (b,c) FMT reconstructed as transparency overlays on CT slices through the abdomen, (d,e) corresponding *ex vivo* validations using cryo-sectioning as fluorescence signal imposed over grayscale cryo-sections and (f) animal positioning on the bed with red arrows pointing to the scanned field of view. Coordinate system is designated by D (dorsal), V (ventral), H (head), T(tail), L(left) and R(right).

7.2 Imaging of a pancreatic cancer model[1]

FMT-XCT was applied toward tomographic, *in vivo* imaging and characterization of tumors in $Ptf1a^{+/Cre}$, $Kras^{+/LSL\text{-}G12D}$, $p53^{LoxP/LoxP}$ (CKP)

[1] The imaging results here are presented also in M. Trajkovic-Arsic, et.al. "Molecular imaging of integrin $\alpha_v\beta_3$ for *in vivo* detection of precursor lesions and pancreatic cancer", Journal of Nuclear Medicine, vol. 55, 2014 (see Publications overview at the end of the dissertation for full author list). The imaging and processing were performed by the author at HMGU. Xiaopeng Ma from IBMI and Dr. Neal C. Burton from iThera Medical helped with cryo-sectioning. Dr. Neal. C. Burton also helped with animal positioning on imaging bed. Animal and its strain specification were provided by Dr. M. Trajkovic-Arsic, as part of a collaboration project with Priv.-Doz. Dr. Jens Siveke's research group at from II. Medizinische Klinik, Klinikum rechts der Isar. Results are reproduced with permission from Dr. M. Trajkovic-Arsic.

[102–104] model of pancreatic ductal adenocarcinoma (PDAC). The PDAC model was injected with IntegriSense 680 and imaged 24 hours later *in vivo* by the FMT-XCT system. The imaging results are presented in Figure 7.1. To our knowledge, this is the first demonstration of imaging pancreatic tumors using FMT-XCT. The reconstructed signal closely resembles the known topography of the pancreas itself and the *ex vivo* cryo-sections. The mouse was imaged in the shaved region pointed to in Figure 7.1(f). No anatomical priors were used in the processing, as micro-CT has negligible soft tissue contrast in this region; an issue which sets the stage for the development presented in the next section.

7.3 Hybrid FMT—phase-contrast CT (FMT-PCCT)[2]

The performance of FMT as a molecular imaging modality is generally limited due to strong scattering of NIR photons in tissue and modeling imperfections arising from lack of complete optical description of the sample and light propagation modeling inaccuracies. The performance of FMT can also be improved by efficient synergy of anatomical information in light propagation modeling and inverse solution. FMT-XCT as a hybrid modality enabled *in vivo* imaging of several animal models, as demonstrated in the previous section.

While offering high spatial resolution at low cost and short imaging time, conventional absorption-based CT (also referred to as micro-CT) - without enhancement of contrast agents - suffers from low soft tissue contrast. In a typical CT scan of a mouse, for instance, only the bones and lungs have significant contrast with respect to the general tissue. This issue

[2] The results presented here will also be presented (at places with minimal or no changes) in P. Mohajerani, et al., "FMT-PCCT: Hybrid fluorescence molecular tomography - X-ray phase-contrast CT imaging of mouse models *in vivo*", IEEE Trans. Medical Imaging, vol. 33, 2014 (see Publications overview at the end of the dissertation for full author list). All phase-contrast imaging and reconstructions were performed by Alexander Hipp, Marian Willner and Mathias Marschner at Professor Franz Pfeiffer's research group at Garching Forschungszentrum. Animal preparation, FMT imaging, FMT-PCCT coregistration and processing, generation of FMT-PCCT results and reconstructions as well as *ex vivo* validations were performed by the author at HMGU. Xiaopeng Ma at IBMI contributed to segmentation of PCCT images. Karin Rardich, Dr. Neal C. Burton, Uwe Klemm and Dr. Vladimir Ermolayev helped with animal experiments.

hinders the realization of the full potential of FMT-XCT by posing a challenge in delineation of target lesions which are often surrounded by soft tissue.

Phase-contrast X-ray imaging methods have rapidly evolved lately. Among them is grating interferometry which functions with common X-ray tubes [107]. *In vivo* small animal imaging has been potentially made possible recently through integration of an X-ray phase-contrast computed tomography (PCCT) system into a rotating gantry [108, 109]. High resolution and low cost, as advantages of conventional micro-CT over other methods such as MRI, are also afforded by PCCT. Moreover, PCCT also information regarding electron density [110] as well as scattering caused by features on the micrometer length scale [111]. However, the PCCT requires longer acquisition times and exposures doses as several images are recorded per projection. Nevertheless, the improved contrast is maintained for doses compatible with *in vivo* experiments [112].[3]

Herein, we demonstrate for the first time hybrid FMT-PCCT imaging of mice. Two animal models, one with a subcutaneously injected 4T1 breast cancer cells and a model of pancreatic ductal adenocarcinoma (PDAC), were imaged *in vivo* by a full-rotation FMT system and then *ex vivo* by a grating-based PCCT system. The results substantiate the potential of FMT-PCCT in imaging specific uptake of fluorescent probes in lesions where there is low or no contrast with surrounding tissue in micro-CT.

The animals were imaged with the FMT systems *in vivo*. A 93 day old nude mouse was injected with one million 4T1 breast tumor cells subcutaneously behind the thorax 10 days before imaging. Furthermore, a 63 day old $Ptf1a^{+/Cre}$, $Kras^{+/LSL\text{-}G12D}$, $p53^{LoxP/LoxP}$ (CKP) [102–104] model of pancreatic ductal adenocarcinoma (PDAC) was imaged using FMT as well.[4] The 4T1 model and the PDAC model were injected with 2 nmol of IntegriSense 750 and IntegriSense 680 (PerkinElmer, Waltham, MA, USA) in the tail vein 24 hours prior to imaging, respectively. IntegriSense targets integrin $\alpha_v\beta_3$ which is known to be expressed in both models [25, 113]. The mice were imaged by the FMT system [32] at HMGU *in vivo* under Isoflurane anesthesia.

[3] Dr. Martin Bech at Professor Franz Pfeiffer's group at TUM's department of physics in Garching Forschungszentrum significantly contributed to this paragraph.

[4] Animal and its strain specification were provided and by Dr. M. Trajkovic-Arsic, as part of a collaboration project with Priv.-Doz. Dr. Jens Siveke's research group from II. Medizinische Klinik, Klinikum rechts der Isar.

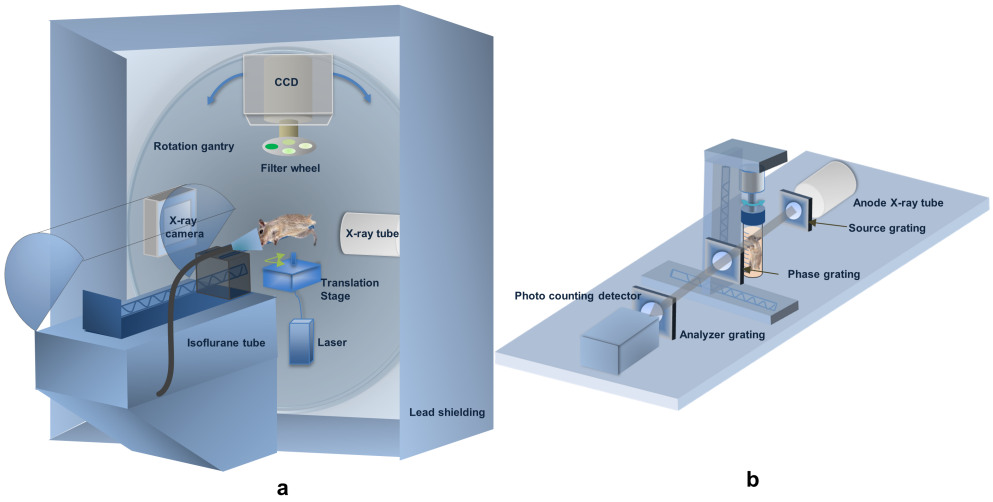

Figure 7.2: FMT-PCCT system components; (a) the fluorescence molecular tomography (FMT) system and the complementary conventional computed tomography (micro-CT) subsystem and (b) the X-ray phase-contrast computed tomography system (PCCT) based on a Talbot-Lau interferometer consisting of three gratings. The sample was imaged *in vivo* under Isoflurane anesthesia in the FMT and *ex vivo* in a falcon tube immersed in a transparent water container (not shown) in the PCCT system.[5]

The FMT system was discussed previously in this work; however, a schematic diagram of this system is shown in Figure 7.2(a) for completeness of discussion. Optical imaging was performed within a field of view centered on the region of interest at 24 equispaced gantry angles. The 680 nm and 750 nm lasers scanned the sample at, on average, 26 source locations per gantry angle, where at each location intrinsic and fluorescence images were obtained using the cooled CCD [32]. The *in vivo* FMT imaging lasted a total of on average 45 minutes for each mouse. Conventional micro-CT scans were also acquired after the FMT acquisition for volumetric coregistration and comparison purposes and lasted 20 minutes. The animals were sacrificed after the FMT imaging through intraperitoneal overdose injection of Ketamin and Xylazin. Afterwards, the 4T1 and PDAC mice were preserved in a 4% paraformaldehyde (PFA) fixation solution for 2 weeks and 4 weeks, respectively. A longer fixation time was required for the PDAC model to ensure most of the air bubbles mainly arising in colon are dissolved away in PFA. The air bubbles

[5] Xiaopeng Ma at IBMI contributed to graphic designs. Figure 7.2(b) was designed using a photograph provided by Alexander Hipp, at Garching Forschungszentrum.

can cause significant artifacts in PCCT images due to high scattering. X-ray phase-contrast computed tomography (PCCT) was carried out for both mice using a Talbot-Lau interferometer [110] located at the chair for biomedical physics of TUM, as demonstrated in Figure 7.2(b), equipped with a photon counting detector and a rotating anode X-ray tube source. The interferometer consisted of source, phase and analyzer gratings [107]. The sample was placed directly in front of the phase grating to maximize sensitivity [114].[6] The mice were transported back to HMGU for *ex vivo* validation after PCCT imaging. *Ex vivo* validation was achieved using a cryostat (CM1950, Leica Microsystems GmbH, Wetzlar, Germany), retrofitted with a fluorescence imaging system [115]. A maximum 30 second exposure time was applied for acquiring fluorescence cryo-sections, as the fluorescence is strongly weakened after several weeks of immersion in PFA 4%.

7.3.1 FMT-PCCT processing

To reconstruct the phase-contrast CT images, filtered back-projections using Hilbert filter were applied to the recorded differential phase-contrast projections and the effective pixel size was 100 $\mu m \times$ 100 μm.[7] The PCCT slices were then manually segmented to extract the animal volume from the surrounding PFA solution and container and organs. A mouse atlas [116] as well as cryo-section photographs obtained *ex vivo* were consulted during the segmentation to help with recognition and localization of different organs. The animal volume extracted from the PCCT was coregistered with the CT volume (obtained after the FMT acquisition *in vivo* using the conventional CT subsystem of Figure 7.2(a)), employed as the volumetric reference for coregistration, by achieving a maximum overlap between the skeletons in both scans using an rigid transformation.[8] Different optical absorption and scattering coefficients as reported in [49],

[6] Technical details, citations and text regarding phase-contrast imaging hardware and reconstruction were provided and corrected by Alexander Hipp, Marian Willner and Dr. Martin Bech at Professor Franz Pfeiffer's research group at Garching Forschungszentrum and reproduced here with their permission.

[7] Further technical details regarding PCCT system, imaging and reconstruction to be presented in P. Mohajerani, et al., "FMT-PCCT: Hybrid fluorescence molecular tomography - X-ray phase-contrast CT imaging of mouse models *in vivo*", IEEE Trans. Medical Imaging, vol. 33, 2014 (see Publications overview at the end of the dissertation for full author list).

[8] Coregistration was done using D-J. Kroon's "demon registration version 8f" toolbox based on a method described in [117]. Functions LineNormals2D.m and LineCurvature2D.m from same author were used for line curvature calculations.

reported in Table 6.2, were assigned to general tissue, bone, lungs and heart for solving the forward problem. The tissue volume was discretized for each mouse using a tetrahedral mesh with an average edge length of 1.3 mm. The mesh was generated using the methods described in [43,44]. The light propagation in mouse tissue was then modeled using a finite element method (FEM) approach based on the method described in [33], as described in detail in Chapter 2. The inverse problem was solved over a rectilinear grid with 1 mm resolution using LSQR with 50 iterations [69]. The segmented organs containing the cancerous lesions were used as *a priori* anatomical information shaping the regularizer using the weighted-segmented approach in the inverse problem [32]. The segment weights for the structured regularization were set using a two-step inversion approach, where in the first step the average concentration values in different anatomical segments are estimated and in the second step these initial estimations are used to penalize reconstructions in different segments [32, 72]. To set the regularization parameter, the L-curve was calculated and the point with maximum curvature was found. The regularization parameter was set to the point of maximum curvature, which means the solutions are not over-regularized.

7.3.2 Results

Figure 7.3 demonstrates FMT-PCCT imaging of the nude mouse with a subcutaneous 4T1 tumor. Figure 7.3(a) shows the 3-D representation of FMT reconstruction results along with skeleton, lungs, heart and parts of adipose tissue segmented from PCCT images. Figure 7.3(b) illustrates one transverse slice of the FMT-PCCT reconstruction overlaid as transparency on the corresponding PCCT slice. *Ex vivo* validation was achieved using cryo-sectioning, as shown in Figure 7.3(c) where the contrast-enhanced fluorescence image of the cryo-section is overlaid on the grayscale cryo-section; showing specific uptake of IntegriSense 750 in the subcutaneous tumor. Representative corresponding PCCT and conventional micro-CT transverse slices are illustrated in Figure 7.3(d) and (e). As seen, the tumor has a much higher soft tissue contrast in the PCCT image than the conventional CT image. Specifically, soft tissue contrasts (ratio of intensity difference intensity in target region, in percentage) of 15% and 85% were observed for a point inside the tumor, red marks in Figure 7.3(d) and (e), relative to the adjacent background (blue

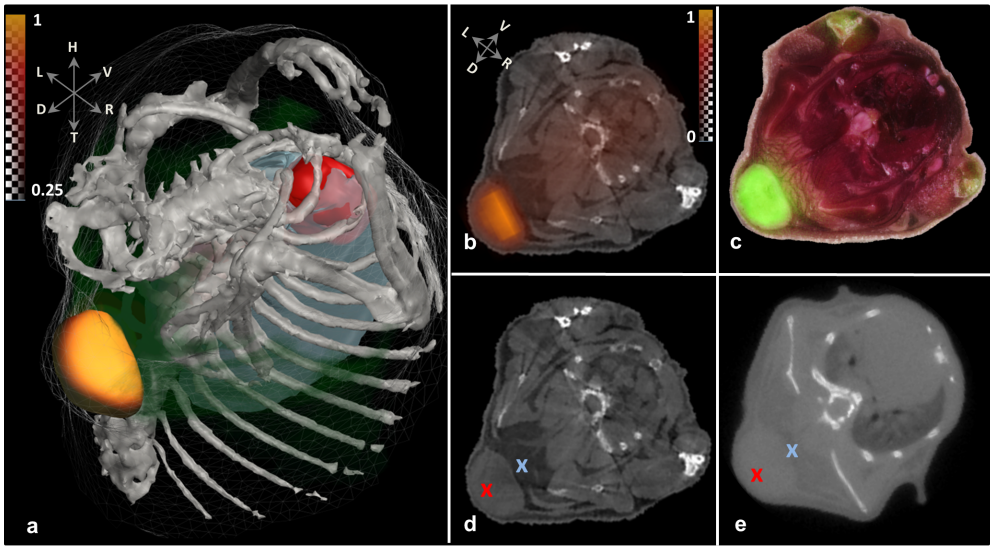

Figure 7.3: Hybrid FMT-PCCT imaging for a subcutaneous 4T1 tumor model; (a) 3-D FMT-PCCT reconstruction showing the high concentration of IntegriSense 750 in the tumor - heart, lungs and adipose tissue are shown in red, light brown and green, respectively, (b) FMT-PCCT reconstruction imposed over a PCCT transverse slice, (c) *ex vivo* validation using cryo-sectioning where the fluorescence cryo-section is contrast-enhanced superimposed as transparency over the cryo photograph, (d) PCCT slice and (e) the corresponding CT slice. The relative soft tissue contrast between the tumor and surrounding tissue (red and blue marks in (d) and (e), respectively) were 85% and 15% for the PCCT slice (d) and the CT slice (e), respectively. Coordinate system is designated by D (dorsal), V (ventral), H (head), T(tail), L(left) and R(right). The brightness of images (a,b,d) was slightly increased for print clarity.

marks), for the CT and PCCT slices, respectively. The pixel intensities in the PCCT grayscale slice images represent the phase shift induced to the X-rays by the tissue in each voxel and are proportional to the refractive index decrement. Figure 7.4 further illustrates the potential of FMT-PCCT hybrid imaging for the PDAC model. Specifically, Figure 7.4(a) and (b) demonstrate the FMT reconstruction coregistered with the 3-D PCCT scan from the two view angles denoted by arrows in Figure 7.4(c), which shows the animal volume obtained from the micro-CT (shown here due its slightly larger FOV). First-level estimations were performed for the pancreatic tumor, kidneys, spleen and the rest of the tissue.

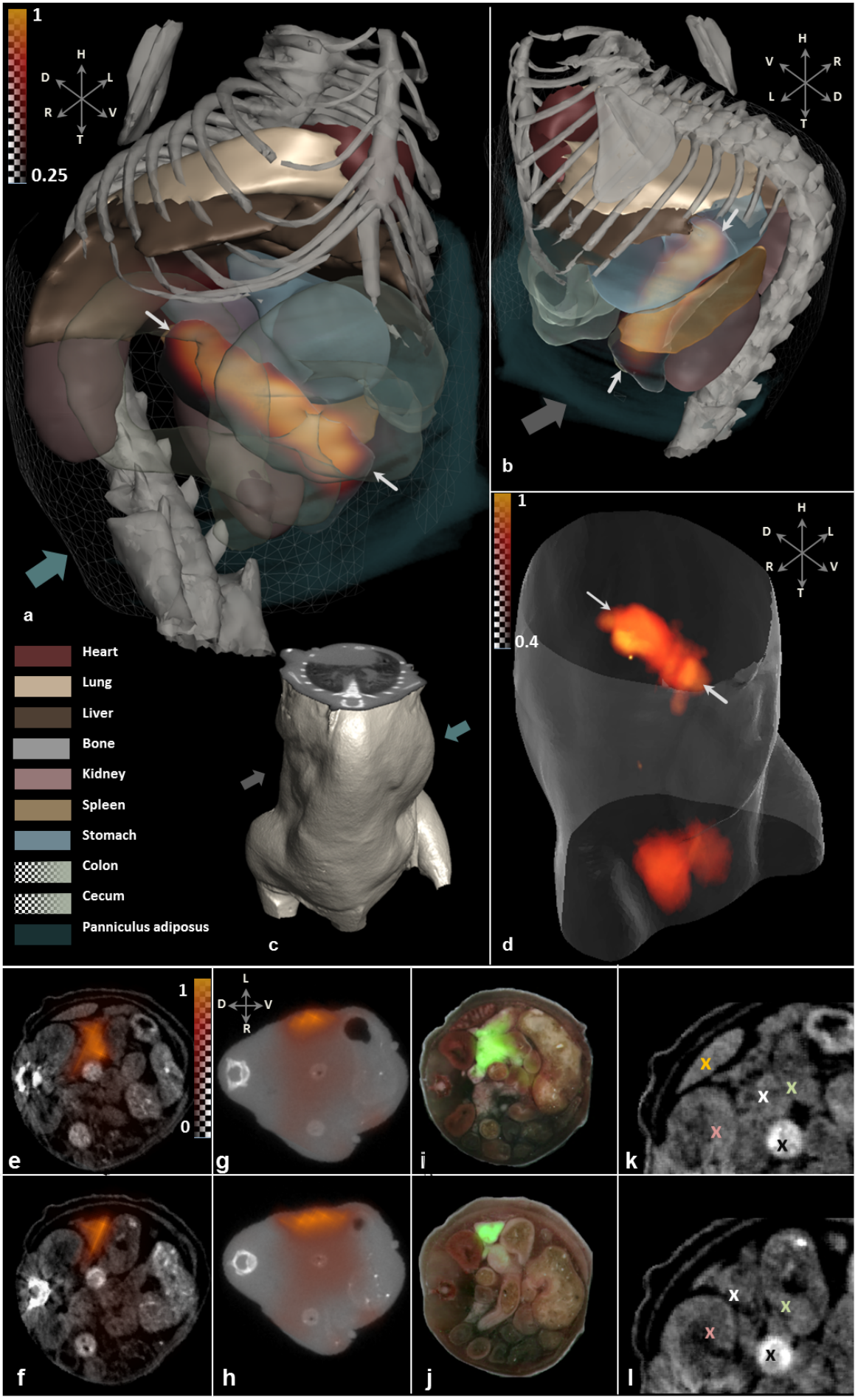

Figure 7.4: FMT-PCCT imaging of a PDAC model; (a, b) 3-D FMT-PCCT reconstructions showing specific accumulation of IntegriSense in the pancreatic tumor (both tumor ends marked with white arrows). Organs are segmented from PCCT, while micro-CT skeleton is shown in (a,b) due to its slightly larger FOV. View angles of (a, b) are shown with, respectively, dark green and gray arrows on the micro-CT volume in (c). (d) 3-D *ex vivo* validation, (e, f) FMT-PCCT reconstruction imposed over transverse PCCT slices, (g, h) corresponding FMT-XCT reconstruction, (i-j) fluorescence cryo-sections (pseudo-green, contrast enhanced) over cryo photograph, (k-l) enlarged views of the PCCT slices.)

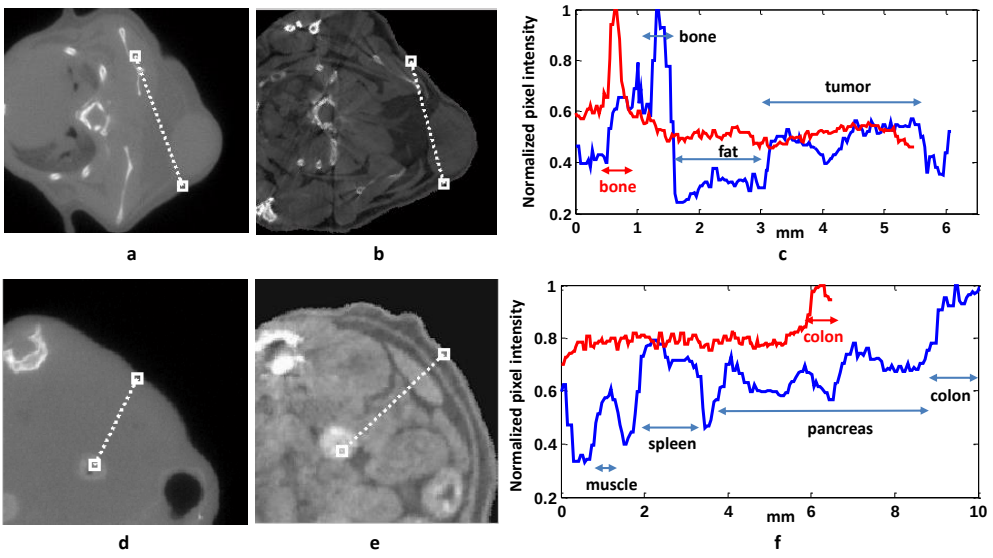

Figure 7.5: Intensity profiles of phase-contrast and micro-CT images; (a) micro-CT slice of the 4T1 model, (b) the corresponding PCCT slice and (c) the intensity profiles of the micro-CT image (red curve) and the PCCT image (blue curve) along the white dotted lines. Corresponding results for the PDAC model are shown in (d-f). Parts of the intensity curves corresponding to different tissues are labeled in (c) and (f), where the labels in black (red) fonts correspond to PCCT (micro-CT) intensity profiles. The x-axis in (c) and (f) denote distance in mm along the line segments, where distance 0 corresponds to the upper white squares in all four cases. No enhancement was applied for brightness or contrast to the raw images.

Lung, heart, pancreas, stomach, spleen, kidneys, colon, cecum as well as panniculus adiposus are segmented from the PCCT images using a semi-automatic method. Although the bones are clearly visible in the PCCT scan, the skeleton segmented from the micro-CT scan is shown in Figures 7.4(a) and (b) for better demonstration due to the larger FOV of the micro-CT. *Ex vivo* validation based on cryo-sectioning is illustrated in Figure 7.4(d), where the accumulation of the probe in the pancreatic tumor can be readily distinguished (the lower hyperintensity shows probe accumulation in the bladder and peritoneal cavity). Two transverse slices of the FMT-PCCT reconstruction overlaid as transparency on the corresponding PCCT slices are shown in Figure 7.4(e) and (f) and corresponding FMT-XCT reconstructions are presented in Figure 7.4(g) and (h), respectively.

Corresponding *ex vivo* validation images are shown in Figure 7.4(i) and (j) where the fluorescence image of the cryo-section is overlaid in pseudo-green on the color cryo-section photographs. Enlarged portions of the PCCT slices are shown in Figure 7.4(k) and (l), where the spleen, pancreas, stomach, left kidney and colon are marked with orange, white, green, pink and black, respectively.

The body of the mouse bloated slightly post-mortem, as can be recognized from different cross-sectional areas between PCCT and PC scans (e.g. between Figure 7.4(e) and (g)). Coordinate systems are designated by D (dorsal), V (ventral), H (head), T (tail), L (left) and R (right). The brightness of parts (a-d) was slightly increased for print clarity. The intensity of the micro-CT and PCCT images along sample line segments for the two *in vivo* studies are presented in Figure 7.5. Figure 7.5(a) and (b) show corresponding transverse micro-CT and PCCT images, without processing for contrast or brightness enhancements, for the 4T1 model. The pixel intensity profiles along the dotted white lines are shown in Figure 7.5(c), where the red and blue curves correspond to, respectively, micro-CT and PCCT images. Different tissues are marked as intervals on the intensity profile curves Figure 7.5(c). As seen, there are significant gaps between tumor, fat and bone tissue in the PCCT intensity profile (blue curve), while only bone tissue has conspicuous contrast relative to background in the micro-CT intensity profile (red curve).

The 15% contrast in micro-CT intensity between fat and tumor tissue (blue and red marks in Figure 7.3(e)) is barely distinguishable in the red curve in Figure 7.5(c). Both intensity profiles are normalized to the respective maxima. The corresponding results for the PDAC model are given in Figure 7.5(d-f). The line segment in Figure 7.5(e) starts (from the upper white square) in skin and crosses, respectively, fat, muscle, fat, spleen and pancreas and ends at the lower white square in the colon. Different intervals corresponding to these tissues can be readily distinguished in the PCCT intensity profile (blue curve) in Figure 7.5(f). Micro-CT had noticeable contrast only in colon.

7.4 Discussion

We proposed and demonstrated for the first time hybrid herein fluorescence molecular tomography-X-ray phase-contrast computed tomography (FMT-PCCT) for non-invasive three-dimensional molecular imaging of small animals. FMT-PCCT combines the sensitive molecular imaging capability of FMT with the high resolution, high contrast anatomical imaging of PCCT to deliver improved quantitative tomographic images of biodistribution of fluorophores *in vivo*. FMT-PCCT was demonstrated for two animal experiments; a nude mouse with subcutaneously injected 4T1 tumor cells and a model of pancreatic ductal adenocarcinoma (PDAC). The FMT measurements were performed *in vivo* followed by *ex vivo* PCCT imaging. Conventional CT scans were also obtained *in vivo* after FMT imaging for comparison and volumetric coregistration purposes. The PCCT images showed a much higher soft tissue contrast than the conventional CT images. This capability of PCCT afforded accurate reconstruction of cancerous lesions in both models through incorporation of anatomical information segmented from the PCCT in the FMT reconstruction process. A current drawback of PCCT is the long acquisition time, which is mainly due to the quantum efficiency of the detectors, the need to acquire multiple radiographic projections and the imperfect grating structures.[9] The reduction of the phase-contrast imaging acquisition time toward *in vivo* phase-contrast imaging is possible and a topic of ongoing research [108, 109, 118–120].

While sustaining the high resolution and low cost of conventional CT, PCCT improves the soft tissue contrast. We believe this feature will play a critical role in future evolvement of FMT-PCCT as a preclinical whole body *in vivo* imaging modality. An important current issue toward wider deployment of FMT-XCT is the difficulty associated with segmentation of organs from the CT images due to the low contrast of target lesions relative to the background or the complete lack thereof (as observed in our demonstration of the PDAC model in Figure 7.4). This issue

[9] Author appreciates insight provided by Alexander Hipp at Garching Forschungszentrum for this sentence.

specially poses problems for the end users of current FMT systems, as the segmentation of conventional CT segments are mostly based on semi-automatic methods which require user interference. This issue will likely play a smaller role in FMT-PCCT, as the higher soft tissue contrast will make possible or improve segmentation automation.

7.5 Conclusion

Building upon the flexibility, efficiency and accuracy of the processing framework presented in the previous chapters, we presented in this chapter *in vivo* experiments for studying tumor development in various models (one case presented in this chapter and more cases presented in Appendix C). Some of the results were first-time imaging demonstrations using FMT-XCT. Furthermore, FMT-PCCT was developed and demonstrated here for the first time for imaging animal models. The FMT and PCCT imaging were performed *in vivo* and *ex vivo*, respectively, and the imaging results were cross validated with *ex vivo* cryo-sectioning. FMT-PCCT demonstrates the ability to effectively reconstruct the target fluorescence signal through incorporation of anatomical information afforded by PCCT in lesions, where low or no contrast relative to surrounding tissue is observed in conventional CT images. Due to low cost, high sensitivity and ability to tomographically image fluorescence in soft tissue lesions, we believe FMT-PCCT equipped with better segmentation methods afforded by high soft tissue contrast of PCCT will be an important tool for preclinical molecular imaging in future.

The developments presented until this point in this work addressed solely preclinical applications. We have further expanded the scope of fluorescence-enhanced molecular imaging to the clinic to develop novel algorithms and applications for imaging of inflammation in human hand joints, made possible by the insight and accuracy afforded by the tools developed so far.

8 Spatiotemporal analysis for imaging rheumatoid arthritis

8.1 Introduction[1]

Imaging can play a significant role in the early diagnosis of rheumatoid arthritis (RA) and monitoring the effectiveness of a corresponding treatment [121,122]. As most common chronic form of arthritis [123] RA is an autoimmune disease which typically affects the synovial joint linings, triggering buildup of synovitis in joints and resulting in cartilage and bone damage. Conventionally, X-ray imaging has been employed for imaging RA features, such as bone and joint destruction as a result of inflammation. However, this approach is limited to imaging effects due to relatively advanced inflammation with visible bone damage [124]. MRI and ultrasound imaging are also employed as alternatives to X-ray imaging for

[1] The materials presented in this chapter are also presented (mostly with minimal or no changes) in P. Mohajerani, et al., "Spatiotemporal analysis for ICG-aided imaging of rheumatoid arthritis in hand joints", Journal of Biomedical Optics 18(9), 097004, September 2013 (see Publications overview at the end of the dissertation for full author list). Material reproduced with permission from the Society of Photo Optical Instrumentation Engineering (SPIE).
Dr. Peter B. Nöel and Priv.-Doz. Dr. Reinhard Meier from Professor Ernst J. Rummeny's group at the department of radiology, Klinikum rechts der Isar performed optical and MR imaging of hands, examined the patients, assisted with clinical details and provided clinical insight, information and findings (such as MR scans, inflammation severity and location as well as other information from patients) used in this chapter.

early RA imaging. Promising results have been shown to make early diagnosis possible. Limitations include the high cost and long examination time (for MRI) or the operator dependency (for ultrasound) [125].

Optical imaging has been considered as an alternative RA imaging method, since it offers fast non-invasive imaging [126–134]. Transillumination planar imaging using a 675 nm laser was considered to assess the progress of disease by observing human proximal interphalangeal (PIP) finger joints and evaluating features of the optical images collected using image classification algorithms [128]. This approach was able to resolve inflammation in PIP joints in a group of 72 joints with 80% sensitivity and 89% specificity, and was shown better in assessing inflammatory variations in the synovium. Optical tomography approaches have also been considered to three-dimensionally resolve diffusion coefficient changes between rheumatoid synovial tissue in rheumatoid PIP joints in comparison to healthy PIP joints [127] [131, 133, 135, 136]. These methods aim at reconstructing the optical absorption and scattering coefficients in two-dimensional planes or three-dimensionally in finger joints and rely on the increase in the optical absorption and scattering due to "clouding of the synovial fluid or membrane inflammation" [128, 131] or measurement of water concentration and tissue oxygen saturation levels [137] to differentiate between osteoarthritic and healthy joints. It was reported in [131] that the optical absorption and scattering of synovial tissue can increase up to an order of magnitude with inflammation and the frequency-domain diffuse optical tomography was shown to differentiate between healthy and arthritic joints with more than 85% sensitivity and specificity in a group of 99 PIP joints with rheumatoid arthritis and 120 healthy PIP joints [135]. Diagnosis of osteoarthritis in distal interphalangeal (DIP) joints of 22 patients and 18 volunteers with 91% sensitivity and 100% specificity was demonstrated in [137] using an X-ray guided multispectral technique. It should be noted that optoacoustic methods have also been proposed for imaging inflammatory arthritis and osteoarthritis in small animal and human joints [138, 139]. The aforementioned optical and optoacoustic planar or tomographic optical imaging methods have been limited to interphalangeal human finger joints. Laser

Doppler imaging has further been proposed for imaging perfusion maps of microvasculature in PIP and metacarpophalangeal MCP human hand joints [140, 141].

In addition to intrinsic contrast, the use of fluorescent dyes and probes has been also proposed to offer diagnostic information on the inflamed synovial tissue based on planar and tomographic molecular imaging techniques [142, 143]. Optical imaging employing Indocyanine Green (ICG) has been considered in particular for visualizing RA in preclinical and clinical applications [23, 129, 132, 144, 145]. Indocyanine Green is a synthetic organic fluorescent dye that has been considered in a variety of clinical applications, including hepatic clearance studies, retinal angiography as well as intraoperative applications such as brain surgery and gastroenterological surgery [146–150]. Studies for the detection of breast cancer [151] and the identification of atherosclerosis [152] have been also considered. Upon intravenous administration, ICG distributes into the vascular system, typically binding to plasma proteins. ICG has a half-life of 3-4 minutes after injection and clears though the hepatobiliary tract. ICG has peak optical absorption at around 780 nm and peak fluorescence at 830 nm in blood [153].

A common method to clinically visualize ICG using optical imaging is epi-illumination fluorescence imaging (EFI), i.e. a photographic approach, whereby the illumination and the detection are placed on the same side of tissue [21, 134, 154, 155]. Trans-illumination and optical tomography imaging have, however, also been demonstrated [2, 156]. When performing EFI, the sample is typically subjected to plane illumination and the fluorescence signal is measured using a CCD at the corresponding wavelength using appropriate optical filters that reject the excitation light and only allow the emission light to be detected. Such cameras can operate at video rates allowing dynamic measurement of fluorophore biodistribution. This approach is "surface weighted" which means that fluorescence coming from the surface of the tissue is collected more efficiently than deeper seated fluorescence which is instead attenuated as a function of depth. It should be noted that ICG-based EFI imaging as proposed in [144] is, to our knowledge, to date the only fluorescence-based clinical

tool for imaging synovitis in human hand joints and at the same time the only technique for simultaneously imaging synovitis in all carpal, metacarpophalangeal and interphalangeal joints of the human hand. ICG-aided diagnosis of rheumatoid arthritis in carpal, MCP, PIP and DIP joints of human hands was reported in [27] to have a sensitivity of 39.6% and specificity of 85.2% in a group of 45 patients. Another study reported 76% sensitivity and 54% specificity for 252 patients [23].

The output of EFI imaging is a number of fluorescence frames obtained at sequential time points. The visual inspection of this information and derivation of diagnostic information is not straight-forward due to the large amount of the data collected and perhaps the presence of subtle spatiotemporal changes that are not easily captured by human perception. In order to quantitatively examine the ICG spatiotemporal profile obtained from clinical measurements following an intravenous bolus injection of ICG to patients, we employed principal component analysis (PCA) [87]. PCA analysis is commonly applied in studying dynamic events and has been used in such applications as differentiating internal organs in mice [155], spectral unmixing applications [157] and multispectral optoacoustic tomography real-time imaging [158]. PCA was applied herein to decompose the complex temporal and spatial dependencies of fluorescence signals following ICG administration and investigate whether we could identify dynamic or spatial patterns associated with RA. A secondary objective of this work was to further gain insights on the effects of depth on the signals recorded. The purpose of the spatiotemporal processing was to investigate whether ICG of higher concentration or different time-kinetics was delivered at the synovial lining compared to the surrounding tissue; as this could be employed as a marker of RA characterization. A numerical phantom model built using a manually segmented MR scan of a metacarpophalangeal joint has been used to simulate the fluorescence image sequences based on the finite element method (FEM). The performance of the proposed method has been demonstrated using this phantom as well as for individual joints from 10 patients diagnosed with RA and 5 healthy volunteers. Detailed case-studies are presented as well for 8 joints with various degree of synovitis severity.

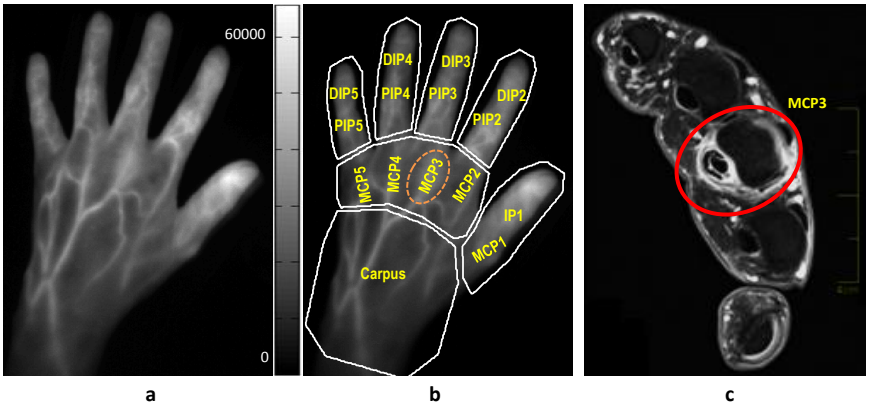

Figure 8.1: Sample clinical images of a patient's hand after ICG injection; (a) sample epi-illumination fluorescence image of the left hand 40 seconds after injection of ICG. The patient has mild synovitis in the 3rd metacarpophalangeal joint of the left hand, as seen by relative signal increase in the delineated region, (b) the joint names indicated on the fluorescence image (MCP = metacarpophalangeal, PIP = proximal interphalangeal and DIP = distal interphalangeal). White curves depict regions of interest (ROI) specified for processing purposes, (c) the corresponding contrast enhanced, fat saturated, T1-weighted MR image of the metacarpophalangeal region where the inflammation in the 3rd MCP joint is highlighted due to a higher relative concentration of the MR contrast agent.

8.2 Clinical imaging of rheumatoid arthritis

The methodology and analysis performed in this chapter have been developed in the context of a recent study conducted at the Klinikum rechts der Isar, Munich, Germany, with the purpose of evaluating ICG-aided diagnosis of RA [27]. Patients with more than one tender and/or swollen joint among carpal, metacarpophalangeal, proximal interphalangeal or distal interphalangeal joints were recruited, when the symptom duration exceeded 6 weeks for up to 24 months. The patients were examined by two rheumatologists via bimanual palpation and then underwent imaging using a 3T MR machine (Verio, Siemens Erlangen, Germany). The MR scanning was performed on both hands simultaneously with patients in a prone position and hands stretched out in praying posture. Gadopentetatedime glumine (Magnograf, Schering, Berlin, Germany) was injected

as contrast agent at a dose of 0.02 ml per kg body weight. Non-enhanced proton density fat saturated images and post-contrast T1-weighted fat saturated scans were obtained in axial and coronal planes. The contrast agent shows a higher relative concentration in inflamed than healthy synovial joint linings [27]. Three radiologists scored the degree of inflammation in a total of 30 joints of both hands using the MR scans. Synovitis scores on a 4-point-ordinate scale (0: no inflammation, 1: mild, 2: moderate, 3: severe) were assigned to each joint according to the semi-quantitative assessment system suggested by the OMERACT MRI group. These MR scores constitute the diagnostic information for our work.

Figure 8.1 shows characteristic images for a patient with mild (MR score of 1) arthritis in the third metacarpophalangeal (MCP) joint of the left hand. The bright area around the 3rd MCP joint region, marked in Figure 8.1(b) indicates relatively high accumulation of ICG in the synovial membrane of this joint. The corresponding axial MR image is shown in Figure 8.1(c), where the inflammation is visible as hyper-intense signal alteration on T1 weighted, fat saturated, contrast enhanced MR images due to the higher concentration of the MR contrast agent. The regions of interest delineated with white lines in Figure 8.1(c) are manually specified for each patient and are used in the proposed method, presented in the Section 8.3.

Fluorescence imaging was performed with a near-infrared fluorescence imaging system (Xiralite X4, Mivenion GmbH, Berlin, Germany), which allows for real-time image acquisition at the fluorescence wavelength of ICG from the human hands after epi-illumination excitation [23, 27, 144]. The device employs a cooled CCD camera, equipped with an 800 nm long-pass optical filter, which captured images at a frame rate of one image per second for a total duration of 360 seconds. For optical imaging, the patient placed the hands inside the device, on a template designed to keep the fingers apart. Continuous illumination with LEDs at 740 nm was applied to both hands. The patients received a bolus injection at a dosage of 0.1 mg per kg body weight. ICG was injected intravenously 10 seconds after the beginning of the imaging acquisition so that pre-ICG administration baseline measurements were always available.

8.3 Spatiotemporal analysis

To analyze the fluorescence data collected, principal component analysis (PCA) was employed to decouple the fluorescence image sequence into different temporal and spatial components. As reviewed in Section 5.3, PCA is a transformation for converting a group of random variable realizations to set a of numbers, which can be considered as realizations of uncorrelated random variables [87]. PCA was applied to a temporally and spatially-windowed subsequence of the original raw fluorescence image sequence, measured from patients' hands as described in Section 8.2. The resulting principal components in each subsequence were then combined to form another sequence. This new sequence was efficiently rendered as a sequence of color images, where each color corresponds to a principal component. The signal due to inflammation is likely to appear as one of such components if it had a dynamic behavior that differs from this of regular tissue.

The proposed processing method achieves signal separation through multiple levels of localization in time and space. In the first pre-processing step, the hand image is divided into various regions of interest (ROI) as shown in Figure 8.1(b). There are 7 ROIs considered for different regions of the hand. This step is necessary as the signals have different temporal and spatial characteristics in various hand regions due to different vascular and anatomical structures and, therefore, hemodynamic. For example, there is a denser dorsal venous network in the digital (consisting of proximal interphalangeal (PIP) and distal interphalangeal (DIP) ROIs) compared to the carpal joints, contributing to more signal interference in interphalangeal joints. Similarly, the synovial tissue regions in the metacarpophalangeal (MCP) joints are shallower and smaller than the carpal synovium and, therefore, appear as better defined yet smaller spots in the fluorescence images compared to the signal coming from inflamed carpal joints. These observations necessitate spatially localized processing, as the processing method seeks component separation through minimization of spatial and temporal correlations. The processing is best focused on regions with similar signal dynamics. Hence, joints

with similar signal behavior are processed in one ROI. The 7 ROIs used herein were shown to result in adequately homogenous spatiotemporal dynamics within each ROI, without losing spatiotemporal features. A second pre-processing step was used to localize the processing also in the time domain. This step is explained in the next paragraph.

To briefly explain the application of PCA herein, we can assume $\{I_p\}$, $p = 1 \dots P$, as a set of P fluorescence images of $M_1 \times M_2$ pixel size, obtained correspondingly at P time points after the injection of ICG. In our study P was equal to 360, corresponding to 360 images acquired over 360 seconds. Then for a given joint, let $\{J_p\}$, $p = 1 \dots P$ denote the sequence of cropped images at the corresponding ROI, as shown in Figure 8.1. The average intensity within each ROI was subtracted from this image sequence, such as each $\{J_p\}$ had a mean value of zero. Just as the spatial windowing through the application of the ROI windows is conducive to better performance, the windowing across the time domain also leads to better signal separation, due to changes in hemodynamic characteristics post injection. For instance, signals undergo rapid changes in the first seconds after injections, while they tend to have an exponential decay in the last few minutes of imaging. Specifically, L successive images were taken from the subsequence $\{J_p\}$ and weighted using a time window. Assuming that this subsequence is H_i^k, where i ranges from 1 to L and k ranges from 1 to $P - L$, we then write

$$H_i^k = W(i) J_{k+i}, \tag{8.1}$$

where W denotes the window sequence. The windows length L was empirically adjusted such as the L images within the time window W have a stationary spatiotemporal behavior, that is, can be well approximated as linear combinations of few spatial components.

For the work presented here, a rectangular window of varying length was employed. The length of the window W was shorter at the beginning of the sequence, where the temporal dynamism was stronger and became longer as signal later stabilized. The sequence H_i^k was the image sequence that was finally processed by PCA.

To implement the PCA on H_i^k, every image in the sequence H_i^k was first vectorized by tagging along all the columns, i.e.

$$h_i^k = \left(H_i^k(1,1)\dots H_i^k(M_1,1)\dots H_i^k(1,M_2)\dots H_i^k(M_1,M_2)\right), \tag{8.2}$$

where $H_i^k(n,m)$ is the n^{th} row, m^{th} column element of the matrix H_i^k. For a given k all the images in the sequence H_i^k were vectorized and stacked on top of each other to form a $L \times M_1\, M_2$ matrix $\mathbf{X}_k$ as

$$\mathbf{X}_k = \begin{pmatrix} h_1^k \\ \vdots \\ h_L^k. \end{pmatrix}. \tag{8.3}$$

The PCA transformation on this matrix relied on the singular value analysis of the $L \times L$ correlation matrix $\mathbf{C}_k$ defined as

$$\mathbf{C}_k := \mathbf{X}_k^\top \mathbf{X}_k = \mathbf{T}_k^\top \mathbf{D} \mathbf{T}_k, \tag{8.4}$$

where the $L \times L$ unitary matrix $\mathbf{T}_k$ is the matrix of eigenvectors of $\mathbf{C}_k$ and $^\top$ is the transpose operator. The diagonal matrix $\mathbf{D}$ contains the eigenvalues of $\mathbf{C}_k$, i.e. the singular values of $\mathbf{X}_k$, sorted in decreasing order. The PCA transformation of matrix $\mathbf{X}_i$ is then given by

$$\mathbf{S}_k = \mathbf{T}_k^\top \mathbf{X}_k, \tag{8.5}$$

where $\mathbf{T}_k$ and $\mathbf{S}_k$ are $L \times L$ and $L \times M_1\, M_2$ respectively. It was observed that only the first three components had significant energy and the components beyond the third one could be ignored. In other words,

$$\mathbf{X}_k \approx \widehat{\mathbf{T}}_k \widehat{\mathbf{S}}_k, \tag{8.6}$$

where $\widehat{\mathbf{T}}_k$ and $\widehat{\mathbf{S}}_k$ are matrices containing the first 3, respectively, columns and rows of matrices $\mathbf{T}_k$ and $\mathbf{S}_k$. The values of the time profile and the spatial components, in $\widehat{\mathbf{T}}_k$ and $\widehat{\mathbf{S}}_k$ matrices respectively, may become negative, as the PCA transformation does not enforce positivity. The negative values pose a problem for result interpretation. For this reason

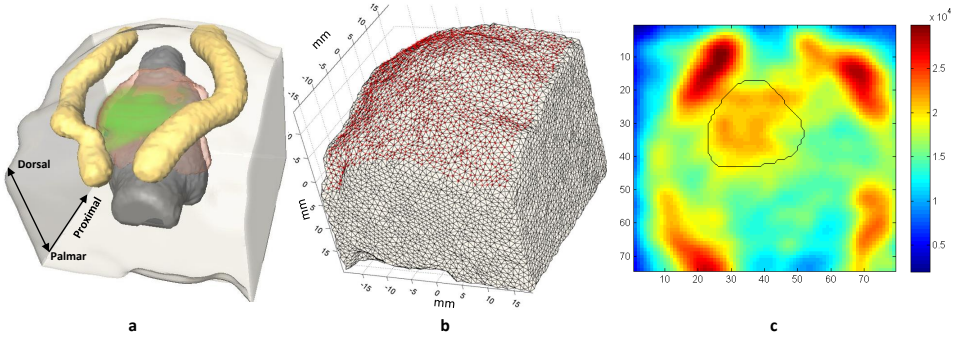

Figure 8.2: Numerical tissue phantom built using segmentation of axial MRI slices of a metacarpophalangeal finger joint; (a) the phantom contains general tissue, two dorsal veins (yellow isosurfaces), bones (gray isosurface) and synovium (red isosurface) and ICG accumulated in the synovium shown by the green shade; (b) tetrahedral mesh generated for the numerical phantom with the red dots designating the illumination on the surface; (c) a sample simulated fluorescence image (as seen by a camera located above the hand and seeing the dorsal side) for synovium located at the depth of 2 mm with an uptake ratio of 3 relative to general tissue, with the black curve delineating the joint region. The units in (c) are pixel intensity counts.

the three imaging components were weighed by the corresponding values of the temporal vectors and thresholds were applied using preset positive numbers. The corresponding three PCA components sequences are called $\{C_i^1\}$, $\{C_i^2\}$ and $\{C_i^3\}$. For each window position the three components from the middle frame weighed as such are then mapped into the blue, red and green transparency channels of a colored image, in decreasing order of the amplitude of their corresponding singular values. The resulting color image is considered as a single frame in a video sequence, which is finally presented to the reader. It should be noted also that all frames are normalized across the entire sequence for a more meaningful depiction.

8.4 FEM-based analysis

To justify the use of superficial measurements for recovering diagnostic information from deeper seated activity as well as studying the performance of the proposed PCA method, we simulated the fluorescence signals recorded as a function of assumed physical and geometrical factors

that relate to the imaging problem studied herein. The simulated factors include the depth and estimates of the relative ICG uptake ratio of the synovial linings. We have furthermore investigated the visibility of the targeted fluorescence signal in various time stages as the ICG is distributed through the hand and joint area.

Figure 8.2 demonstrates the numerical phantom model that was developed and used for the above purposes. The phantom geometry was developed using manual segmentation of axial MR images of a MCP joint of patient with severe inflammation in the 2^{nd} MCP joint. Three elements were identified in the segmentation; bone, veins and synovium as shown by different colors on Figure 8.2(a). The ICG was assumed to accumulate in both the background tissue (volume outside of bones) and in the synovium at different concentrations. In particular, it was assumed that the concentration of the fluorophores in the inclusion and the background, i.e. the rest of the slab, constitute an uptake ratio of $N : 1$. To estimate the dynamic range of the uptake ratio N, we measured intensity of fluorescence observed in several inflamed joints relative to signal in adjacent non-joint tissue. In the measured samples, the joint to non-joint fluorescence ratios ranged between 2.5 and 6.0. While these measured ratios depend on many physical factors such as the imaging time point or the location, the extracted dynamic range serve as an estimate of the underlying uptake ratio. Because of higher attenuation of deep-seated inflammation signal due to depth effects, this estimate is likely to be a conservative one. Interestingly, intensity of the inflamed synovium was observed in MR images to be, depending on severity of inflammation, 2 to 7 times larger than surrounding tissue. This is justifiable, as the Gadolinium-based MR contrast agent and ICG are both blood pooling agents and the respective signal intensities are expected to correlate with blood concentration; even though having different distribution patterns due to their different molecular weights. This effect has also been observed in ICG-based mammography [159].

The ICG that accumulated in the synovium is shown by green shade on Figure 8.2(a) and corresponded N-fold increased fluorophore concentration in the target tissue (synovium), with regard to background, as

described above. A finite-element method (FEM) was employed to simulate the propagation of the incident light and calculate the intensity emitted by fluorophores for a given ICG distribution. The mesh consisted of 48880 nodes and 278832 elements, with an average edge length of 1.3 mm and was generated using the methods described in [43, 44]. The light propagation in tissue was modeled using FEM-based discretization of the diffusion equation (DE) [33]. The DE, as a first order approximation of the more general radiative transfer equation (RTE), is valid for modeling light propagation in turbid tissue where the scattering coefficient is much larger than the absorption coefficient. In tissues, this optical condition does not generally hold in regions containing clear fluid such as the synovial or air such as in the lungs, or in regions with very high absorption such as within large blood vessels. Nevertheless, light modeling based on the diffusion approximation is widely used for preclinical applications (such as tumor localization in murine models of lung cancer [25]) and clinical applications, including tomographic imaging of human interphalangeal finger joints [137, 160, 161] as well as for simulation of light propagation in joints [127]. RTE and its higher order approximations are employed as well as a more accurate model for tomographic imaging of finger joints but computational particulars also impose a number of approximations and assumptions [135]. A recent study showed that, given *a priori* anatomical information, the DA-based modeling of light propagation results in less than 4% error tomographic reconstruction for in human joints, in comparison with higher order approximations of RTE; however, the error was higher without knowledge of accurate optical properties [35]. The tissue's optical absorption and scattering coefficients were set to typical values of 0.05 mm^{-1} of 1.0 mm^{-1}, typical for tissue. Figure 8.2(b) shows the tetrahedral mesh generated for the phantom and the red dots mark the illumination. Figure 8.2(c) depicts a sample fluorescence image obtained via FEM modeling.

Dynamic fluorescence images were simulated over 360 seconds by assigning time-dependent ICG concentrations to different tissue segments. Specifically, the blood flow was mimicked by weighting the ICG concentration in the background, veins and synovium according to time courses

experimentally obtained from fluorescence measurements from the patient whose MR scan was used for the phantom construction. Three time-curves were measured from three different locations, i.e. the dorsal vein, general tissue and inflamed joint locations. The final simulated image sequence contains the fluorescence signal emanating from different entities in the phantom and an added Gaussian measurement noise with 1.5% of the fluorescence signal energy.

8.5 A localization metric

In this section, we establish a framework for quantitative evaluation of the results and comparison of raw and processed component image sequences. This framework is then used to evaluate the performance of the proposed method in localizing desirable signal components in both FEM-based simulated and clinical fluorescence image sequences. The idea behind such framework is to quantify the presence of a component in an image which can be potentially attributed to the target fluorescence source, i.e. in our case, the inflammation signal. This is achieved by segmentation of the image and then evaluation of the binary segments against a reference binary image. The reference binary image is manually set to a region where the joint is expected (for clinical images, this region was set with the help of MR coronal images). If an image segment is localized to the region denoted by the reference binary image, it can be potentially associated with the fluorescence signal emanating from joint inflammation. Specifically, given an image sequence, raw or processed, and a region of interest where a joint is expected to be located, a localization metric was designed whose value indicates if the image sequence suggests the existence of a localized signal component in the joint region. This metric has a value between 0 and 100, where a value of 100 indicates suggests existence of a signal component confined within and spanning the joint region and 0 suggest no localized signal component in the joint region. This metric is applied on every image in the sequence and the metric associated with the image sequence is defined as the maximum of all metrics for the images in the sequence. Hence, the image with

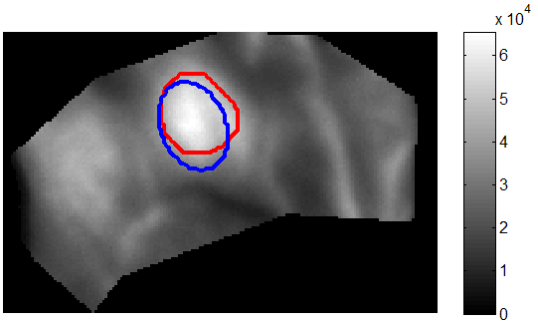

Figure 8.3: Fluorescence image in the MCP area of a patient with moderate inflammation in the 2nd right MCP joint. The blue ellipse shows the region the joint is located, i.e. the reference joint region, and the red curve designates the segmented region that best overlaps with the reference joint region.

the maximum metric value is regarded as the one containing the best candidate signal component. For clarification purposes, an example is presented in Figure 8.3. The blue ellipse delineated in Figure 8.3 denotes the approximated location of the 2nd MCP joint, defined as the "joint ROI". The fluorescence signal emanating from the ICG accumulated in the inflamed synovial lining is expected to appear as a distinguishable and localized signal component at least partly within the joint ROI. The fluorescence image in Figure 8.3 contains such component, delineated by the red curve. This component has been segmented using the segmentation approach metric framework proposed in the section.

Specifically, let R denote a binary image which is 1 inside the joint region and 0 outside. For a given image I of size $N \times M$, a binary image J is constructed as follows.

$$J = I > \beta I_0, \tag{8.7}$$

where I_0 indicates the average intensity of I and the coefficient was heuristically set to 1.5 for the fluorescence images I obtained from patients hands as described in Section 8.2. The binary image J is further processed using morphological operations. Finally, a connected component, also called a binary label, of the resulting binary image that has the largest overlap with R is kept as the candidate signal component. Let K be the binary image containing this segment.

The similarity between the reference binary images R and the segmented

binary image K renders a measure of the likelihood of the signal component designated by the binary region in K, to have been originated from fluorescence within the region designated by R. To quantify the similarity between R and K, we employ the Jaccard distance [162] as an overlap-based measure and the Hausdorff distance [163] as a boundary-based measure and the signal energy. The application of Hausdorff and Jaccard distances as typical boundary-based and overlap-based localization metrics is a common approach for segmentation and image retrieval evaluation purposes [164–168]. A survey and comparison of several localization metrics for the purpose of evaluation of image interpretation systems is presented in [169].

Specifically, for two sets A and B in a metric space, the Jaccard distance is given as

$$J_\delta(A,B) = 1 - \frac{A \bigcap B}{A \bigcup B}. \tag{8.8}$$

Also, the Hausdorff distance is defined as

$$d_H(A,B) = \max\{d_A(b), d_B(a) | a \in A, b \in B\}, \tag{8.9}$$

where for a set S

$$d_S(a) = \min\{d(a,s) | s \in S\}, \tag{8.10}$$

with $d(a,s)$ denoting the Euclidean distance between points a and s. For two binary images, the metrics above are then defined for the sets of non-zero pixels.

In this work the localization metric for a binary image K, a given reference binary image R and the original grayscale image I, is defined as

$$S(K,R) = 100 \times \left(1 - \max\left(\frac{\max\left(d_H(K,R), r\right)}{r}, J_\delta(K,R), 1 - E(K)\right)\right), \tag{8.11}$$

where $d_H(K,R)$ and $J_\delta(K,R)$ denote respectively the Hausdorff distance and the Jaccard distance between K and R and $E(K)$ is the energy of the image I within the label in K normalized by the energy of the image I. The number r denotes the major radius of an ellipse that envelopes R.

$S(K, R)$ ranges between 0 and 100. The configuration of Equation 8.11 ensures that a high value of $S(K, R)$ means small Hausdorff and Jaccard distances and a high energy concentration within the segmented region. Specifically, $S(K, R) = 100$ means that the K and R are identical and that the entire signal energy is confined to K, i.e. perfect localization. On the other hand, a value of 0 for $S(K, R)$ indicates no overlap or a large Hausdorff distance between K and R or no signal energy contained within the area defined by K.

The metric for a given image sequence I_i is defined as

$$S(\{I_i\}, R) = \max_i S(I_i, R). \tag{8.12}$$

The metric proposed here is used later for two purposes. First, it is employed to compare the processed component sequences against the draw image sequence for various joints with different degrees of inflammation severity. Secondly, the metric is used to study the performance of the method vs. different physical factors such as lesion depth and uptake ratio using the numerical phantom presented above in Section 8.4.

8.6 Processing of simulated data and impact of physical factors

In this section we investigate the impact of physical and geometrical parameters, such as the synovium depth or the concentration of the ICG in the synovium on the fluorescence signal obtained for the geometrical arrangement presented in Section 8.2. Figure 8.4(a) demonstrates results from the numerical phantom study. The FEM-based model discussed in Chapter 2 was used to simulate the propagation of incident planar illumination in the tissue and the resulting fluorescence signal emanating from the synovial inclusion, the background tissue and the veins. The z-axis in Figure 8.4(a) denotes the relative contrast between the fluorescence signal in the joint region, as shown in Figure 8.2(c), and the background signal in the simulated images for different depths between 2 and 7 mm and

uptake ratios between 1 and 10, whereby "uptake ratio" denotes ratio of ICG concentration in synovium over the background. Figure 8.4(b) illustrates the results obtained from a simulated longitudinal measurement. Specifically, for each depth and uptake ratio the proposed PCA-based method was applied to the raw fluorescence image sequence generated using the numerical phantom, where different frames denote the simulated fluorescence signal intensity images over 360 seconds, as elaborated in Section 8.3. Next, localization metric values for the simulated raw image sequences as well as the corresponding processed sequences were found, as shown in Equation 8.12. The localization metric was calculated for the individual simulated images based on the approach described in Section 8.5. The z-axis in Figure 8.4(b) denotes the value of the localization metric calculated for different depths and uptake ratios for both the raw image sequences (surface marked with solid lines) and the processed sequences (surface marked with dotted lines). A high value for the localization metric indicates presence of a signal component attributable to the synovium fluorescence. The results suggest that fluorescence signals can be retrieved for depths where synovitis can occurs for different joints. In addition the PCA analysis shows the presence of a signal component localized in the joint region for larger range of uptake ratios and a given a depth and vice versa. The fluorescence signal in finger joints is also affected by the impact of the blood flow on the ICG distribution. After the intravenous injection, the ICG circulates to the hands though the radial and ulnar arteries and then flows back through palmar and venous veins, resulting in fluorescence signal emanating from dorsal veins and general tissue interfering with the synovitis signal. The FEM simulations presented in Figure 8.4(a) suggest that even for synovitis up to 3 mm under skin, interference occurring for uptake ratios less than 3 can complicate signal detection. However, as seen in Figure 8.4(b), the PCA-based method could decouple the fluorescence signals from the vein and background signal for the FEM-based time-series simulations for lesions up to 5 mm deep for uptake ratios less than 5, while the target signal could be distinguished in the raw fluorescence images only up to 2 mm of depth.

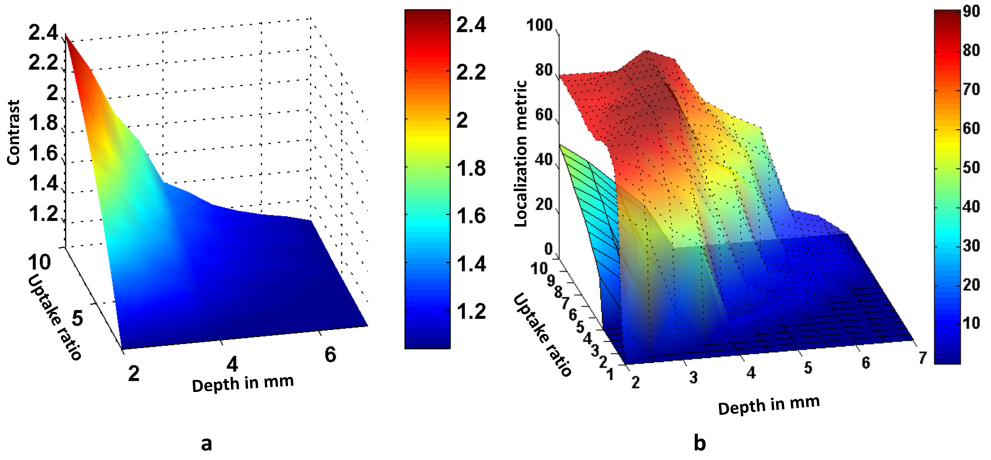

Figure 8.4: Simulation and processing results for the numerical phantom presented in Figure 8.2, Section 8.4; (a) the ratio between the signal intensities in the joint ROI and in the background for various depths of the synovium and ICG uptake ratio in the synovium, calculated for the simulated raw fluorescence image sequence (contrast denotes the maximum of this ratio over the entire sequence); (b) localization metric for the raw simulated fluorescence sequences (surface marked with solid lines) and for the 3 processed image sequences corresponding to the three components (surface marked with dotted lines) vs. depths and uptake ratios. A higher value for the localization metric indicates presence of a localized component in the joint region in the corresponding image sequence.

8.7 Results

8.7.1 Spatiotemporal analysis of arthritic joint images

Following the analysis of simulated data, we applied the PCA method in the study of RA patients. Figure 8.5 shows raw and processed results for a fluorescence image sequence obtained from a 64 year old female patient with severe arthritis in the left carpus and moderate and severe synovitis in, respectively, left 4^{th} and 2^{nd} PIP joints. The ROI of these three joints of the left hand are delineated in Figure 8.5(a). Transverse T1-weighted contrast-enhanced fat-saturated MR images verifying the synovitis severity of left carpus and 2^{nd} and 4^{th} PIP joints for this patient are also shown in Figure 8.5(r-t), respectively. The raw fluorescence

images measured at time points 37, 43, 53 and 89 seconds are shown in, respectively, Figure 8.5(b-e) within the ROI corresponding to the carpus joint. Figure 8.5(f-i) show the corresponding processed images at these time points, where the three components are mapped, accordingly to increasing magnitude of the corresponding singular values, to the green, red and blue channels of depicted color images. The color values in processed images range between 0 and 1. A prominent fluorescence signal appears on the raw images of the carpus, in particular at time point 37 seconds. Accordingly a strong first PCA component (mapped to the blue channel) appears image in Figure 8.5(f-i), congruent to the location where the fluorescence signal appears in the raw data. Interestingly, component number 1 appears in all time points of the sequence, in contrast to the raw fluorescence signal that virtually disappeared at later time points as shown in Figure 8.5(d, e). The raw and processed image frames for the left 2^{nd} PIP joint are shown in Figure 8.5(j,k) and (n,o), respectively, and Figure 8.5(l,m) and (p,q) present corresponding results for the left 4^{th} PIP joint, for time points 30 and 42 seconds post injection. Similar to the carpus, a strongly localized signal component appears in the first component, visible in the two time points displays for both joints.

The severe synovitis of the left carpal and 2^{nd} PIP joints as well as the moderate synovitis of 4^{th} PIP joint can be easily seen in the blue channel of the processed images. This example demonstrates the virtue of the proposed method in temporal and spatial decoupling of the various signal components contributing to the fluorescence image. Specifically, the signal from the veins and the synovitis are clearly decoupled into the three color channels (corresponding to the three principal components) in Figure 8.5(g) for the carpus, at the time point 24 seconds. The synovitis signal is the most temporally persistent component (in comparison with the vein signals, for instance). It is therefore transformed into the blue channel, which is the most dominant channel; i.e. with the largest singular value. On the other hand, the vein signal passes through the green and red channels at different time points. Some of the synovitis signal has leaked as well into the red channel, as seen in Figure 8.5(f). The localization metric calculated for raw and processed image sequences were

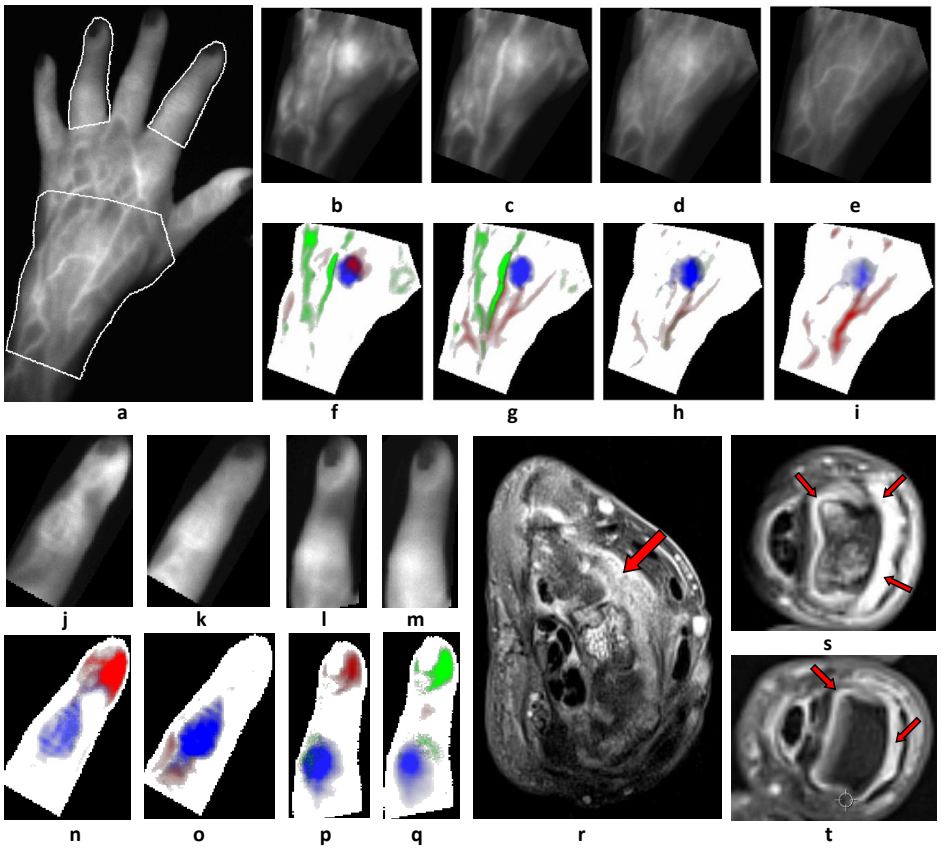

Figure 8.5: Case study of a 64 year old female patient with severe synovitis in the left carpus and severe and moderate synovitis in, respectively, left 2nd and 4th PIP and joints; (a) sample fluorescence image at 100 seconds with corresponding three regions of interest (ROI) delineated by white curves; (b-e) raw fluorescence images (0-65535 intensity counts with black indicating 0) corresponding to time points 37, 43, 53 and 89 seconds post injection, respectively; (f-i) corresponding processed colored images at the same four time points. Moreover, (j-k) and (n,o) are raw and processed images for the left 2nd PIP and (l,m) and (p,q) correspond to the results for the left 4th PIP joint for time points 30 and 42 (seconds post injection). The inflamed synovial linings characterized by higher relative accumulation of MR contrast agent are marked on transverse contrast-enhanced T1-weighted MR images in (r-t) for left carpus and 2nd and 4th PIP joints, respectively. The three principal components are mapped to red, green and blue channels in (f-i) and (n-q). In all cases and time points shown, the signal in the blue channel signifies synovitis, while green and red channel signals can be mainly attributed to fluorescence emanating from dorsal veins in (f-i) and the dense vascular network of fingertips in (n-q).

calculated according to Equation 8.12. The reference ROIs for the three joint in this and next cases were set using the fluorescence images and

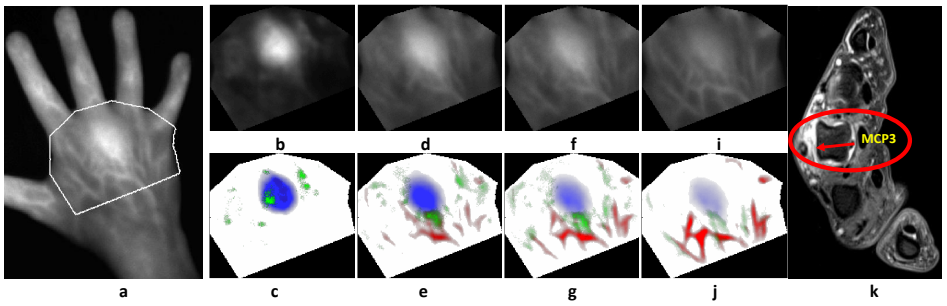

Figure 8.6: Case study of a 46 year old female patient with severe synovitis in the third right metacarpophalangeal (MCP) joint; (a) sample fluorescence image at 100 seconds with metacarpophalangeal ROI delineated by white line; (b-e) Raw fluorescence images corresponding to time points 35, 57, 67 and 91 seconds post injection, respectively; (f-i) corresponding processed colored images at the same four time points; (j) a transverse contrast-enhanced T1-weighted fat-saturated MR image of the MCP joints with the red arrow depicting the inflamed synovial lining characterized by higher relative accumulation of MR contrast agent. The three principal components are mapped to red, green and blue channels in (f-i). The signal in the blue channel signifies synovitis in the 3rd MCP at all 4 time points. The green and red channel signals can be attributed to background and vein signal, respectively.

the corresponding MR coronal images, as the anatomical reference. The metric values for these joints and other joints studied in this section are presented in Table 8.1. The metric for the processed sequence represent the maximum of the 3 sequences, corresponding to the 3 components. As can be seen the 1st component (mapped to blue channel) in the processed sequence achieves a maximum metric of 83 for the carpus, while the corresponding value for the raw sequences is 35. For the 2nd and 4th PIP joints of the left hand, metric values of, respectively, 66 and 46 were calculated for the processed sequences, while no localized components were found in the raw images, leading to a metric value of 0. This is likely due to the strong coupling of synovitis signal with the signal from non-specific background and dorsal venous networks of fingers. Another presentation for a severely arthritic joint presented in Figure 8.6, further demonstrates the decoupling ability of the proposed method. In this case a 46 year old female patient with severe synovitis in the 3rd right MCP joint. The raw fluorescence images in the MCP region, as delineated in Figure 8.6(a), are shown in Figure 8.6(b-e) at time points 35, 57, 67 and

91 seconds after ICG injection. The corresponding processed images are shown in Figure 8.6(f-i). As in the previous case, a strong fluorescence signal appeared in this case as well in the raw fluorescence images at the MCP 2nd region. This signal is stronger at earlier time points and later weakens. Correspondingly, the first PCA component showed a strong signal that similarly diminished with time due to mechanical movements or instability. A transverse MR image of the right metacarpophalangeal joints of this patient is shown in Figure 8.6(j), which verifies an area with apparent severe synovitis at the 3rd right MCP joint. Due to its strength and temporal persistence, the synovitis signal also shows up in the blue channel here and the vein signal mostly in the red channel. There is very little contribution in the green channel. Similar to the previous case, the inflammation signal is well decoupled from the background in the last time point, while fairly unclear in the raw fluorescence image. The metric values for this case, as seen from Table 8.1, are 31 and 60 for, respectively, the raw and the blue channel of the processed sequence.

The cases presented in Figure 8.5 and Figure 8.6 corresponded to carpal, MCP and PIP joints with moderate to severe synovitis. The proposed method is also applied to joints with mild to moderate synovitis. As described in Section 8.2 the joints with mild and moderate synovitis correspond to MR-assigned synovitis scores of 1 and 2, respectively.

The processing results for a 49 year old female patient with mild to moderate joint synovitis are presented in Figure 8.7. The processing results are shown for two regions of interest (ROI); the carpus ROI in the MCP ROI as shown in Figure 8.7(a). Transverse images of the metacarpophalangeal region and image of the carpus, as shown in Figure 8.7(h-i) and (r-s) respectively, present the MR findings for this patient with the red arrows depicting synovitis. The patient suffers moderate synovitis in the 3rd right MCP and the left carpal joints and mild synovitis in the 2nd right MCP joint.

Figure 8.7(b-d) and Figure 8.7(e-g) demonstrate the raw fluorescence images and the processed images corresponding to the time points 37, 52 and 99 for the MCP region. The results of the analysis for the MCP

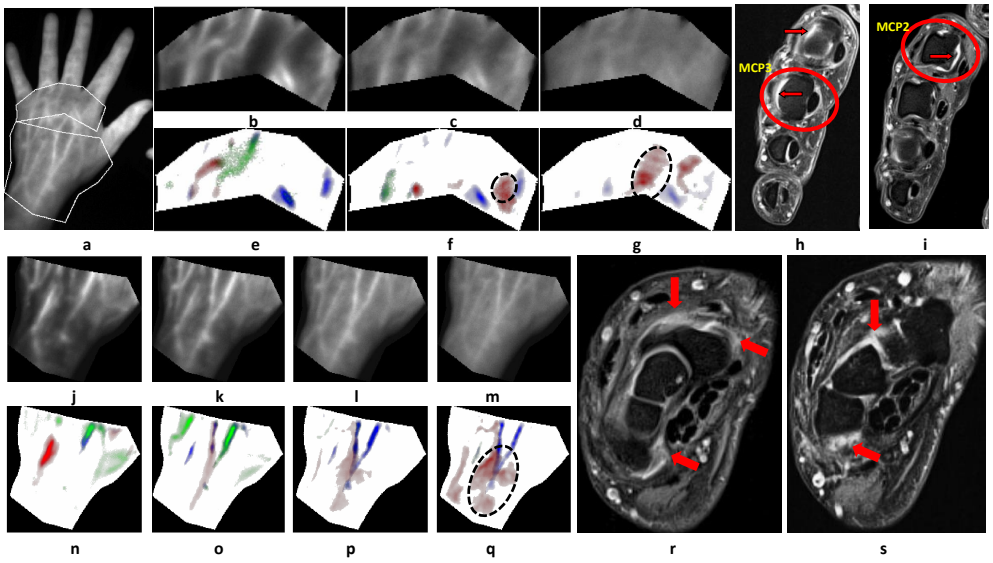

Figure 8.7: Case study for a 49 year old female patient with moderate synovitis in the left carpal and second metacarpophalangeal (MCP) joints and mild synovitis in the 3rd left MCP joint; (a) sample fluorescence image at 100 seconds with metacarpophalangeal and carpal ROIs delineated by white lines; (b-d) raw fluorescence images corresponding to time points 37, 52 and 99 seconds, respectively; (e-g) corresponding processed colored images at the same three time points in the left MCP region; (h-i) transverse contrast-enhanced T1-weighted MR images of the MCP joints with the red arrows depicting the inflamed synovial lining in 2nd and 3rd MCP joints. The signal in the red channel specified by the dashed ellipses in (f) and (g) can be attributed to synovitis. Images (j-m) and (n-q) corresponding to, respectively, raw and processed images of the carpus at time points 37, 48, 72 and 99 seconds; (r-s) two transverse MR images of the carpus. The red channel signal in (q) delineated by the dashed ellipse can be associated with the moderate carpus synovitis.

region are presented in. This patient had mild synovitis in the 3rd MCP joint and moderate synovitis in the 2nd, 4th and 5th MCP joints. While almost invisible and indistinguishable in the raw fluorescence images, the synovitis signals are clearly seen in the marked locations in Figure 8.7(f) and (g). Furthermore, the raw fluorescence images for time points 37, 48, 72 and 99 are and the corresponding processed images for the carpus are shown in Figure 8.7(j-m) and (n-q) respectively. The signal from carpus synovitis is almost invisible in the raw fluorescence images, i.e. Figure 8.7(j-m). However, the red channel shows a transient signal component in Figure 8.7(q) inside the marked region, which can be potentially

attributed to the inflammation in the carpus. The vein signal appears in the red and green channels transiently in Figure 8.7(n-q) and persistently in the blue channel across all 4 time points. As seen in Table 8.1, the localization metric values for the 2^{nd} and 3^{rd} MCP joints reach a maximum of, respectively, 54 and 48 in the red channel and 0 in the raw sequence. The corresponding metric values for the carpus are 32 and 0 for the red channel of the processed sequence and the raw sequence, respectively. It should be mentioned that although the patient was diagnosed based on MR to have moderate synovitis in both 4^{th} and 5^{th} left MCP joints, both raw and processed sequences achieve very low (0 and 8, respectively) metric values, which means the inflammation was not detectable in either sequence.

8.7.2 Spatiotemporal analysis of healthy joint images

Figure 8.8 demonstrates a control case of a 43 year old male patient with no inflammation in the right carpus. The raw fluorescence and processed images are shown in Figure 8.8 for the carpus ROI, delineated in Figure 8.8(a) for a sample fluorescence image at time point 100 seconds. Specifically, images Figure 8.8(b-d) depict the cropped raw fluorescence images obtained at time points 36, 42 and 61 seconds post injection and Figure 8.8(e-g) shows the corresponding processed images consisting of the 3 PCA components mapped to red, green and blue channels. Moreover, Figure 8.8(h) presents the T1-weighted MR findings for this patient as a coronal image of the carpus. No significant contrast due to a higher uptake of MRI contrast agent can be observed in Figure 8.8(h) and an synovitis score of 0 was subsequently assigned by the radiologists group (see Section 8.2 for explanation). The signal components appearing in the three color channels, corresponding to the 3 PCA components, of Figure 8.8(b-d) are uncharacteristic of carpus inflammation and can be attributable to veins or artifacts. In this case, neither the raw fluorescence sequence nor the processed color images show any signal components typical of carpus inflammation. As observed in Table 8.1 the metric

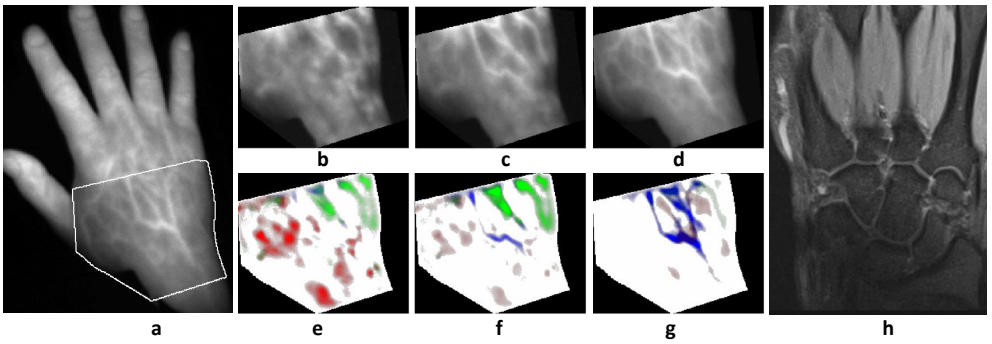

Figure 8.8: Control case study of a 43 year old male patient with healthy right carpal joint (a) Sample fluorescence image at 100 seconds with carpal ROI delineated by white line; (b-d) raw fluorescence images corresponding to time points 36, 42 and 61 seconds respectively; (e-g) corresponding processed colored images at the same four time points; (h) a coronal contrast-enhanced T1-weighted MR image of the carpus joints. The signal appearing in the red, blue and green channels in (e-g) are due to veins or otherwise isolated spots, as in (e), and are uncharacteristic of carpus inflammation signal.

Table 8.1: Localization metric values calculated for raw and processed image sequences for cases presented in Figure 8.5-Figure 8.8. Columns 1 through 5 indicate, respectively, the joint name and location, the MR-based synovitis score, the localization metric values for raw and processed sequences and the channel where the frame with the maximum metric occurs.

	Score	Metric values		Channel with
		raw	processed	maximum score
Left carpus, Fig. 8.5	3	35	83	1 (blue)
Left 2nd PIP, Fig. 8.5	3	0	66	1 (blue)
Left 4th PIP, Fig. 8.5	2	0	46	1 (blue)
Right 3rd MCP, Fig. 8.6	3	31	60	1 (blue)
Left carpus, Fig. 8.7	2	0	32	2 (red)
Left 2nd MCP, Fig. 8.7	2	0	54	2 (red)
Left 3rd MCP, Fig. 8.7	1	0	48	2 (red)
Left 4th MCP, Fig. 8.7	2	0	8	3 (green)
Left 5th MCP, Fig. 8.7	2	0	9	3 (green)
Right carpus, Fig. 8.8	0	0	0	-

values for both processed and raw sequences are 0 for this case; that is, no localized component in the joint ROI was detected. The data processing and simulations presented here were performed in MATLAB on a Windows-based PC with a 2:3 GHz Intel CPU and 3.25 GB of RAM. The mesh generation, FEM modeling and forward problem solution lasted, re-

Table 8.2: Distribution of synovitis severity among the 450 hand joints of 10 patients and 5 healthy volunteers.

	Healthy (score 0)	Mild (score 1)	Moderate (score 2)	Severe (score 3)
Carpal	10	11	5	2
Metacarpophalangeal	59	73	17	1
Interphalangeal	235	28	6	1

spectively, 60, 127 and 460 seconds. The processing of a given dataset consisting of 360 images took 110 seconds for all of 30 hand joints.

8.7.3 Analysis results for 450 joints

The PCA-based processing method proposed in Section 8.3. was applied to fluorescence image sequences obtained from a group of 10 patients (7 females, aged 49±15) and 5 healthy volunteers (4 females, aged 24±2). The patients and volunteers were selected, examined and imaged with contrast-enhanced MRI and MR-based synovitis scores of 0 to 3 (healthy to severe) were assigned to each of the 450 joints, as explained in Section 8.2. The distribution of synovitis severity among different joint groups (carpal, metacarpophalangeal and interphalangeal) are shown in Table 8.2. For each of the 450 joints, the localization metric was calculated for both the raw sequence and the processed sequences, as defined in Section 8.5. As a reminder, the metric has values in the range of 0 to 100, where a higher metric value indicates presence of a signal component in the corresponding sequence localized around the respective joint. Figure 8.9 presents a box-and-whisker plot of metric values for all joints grouped according to synovitis severity for both raw and processed sequences. A threshold can be applied to the localization metric to make a decision about synovitis severity of a given joint and the results can be illustrated using the so-called receiver operating characteristic (ROC) curves. In a typical classification method, the ROC curve denotes the true positive rate (TPR) vs. the false positive rate (FPR). TPR denotes the percentage of positives classified as such and is also called sensitivity. The FPR is the percentage of negatives classified as positive. The

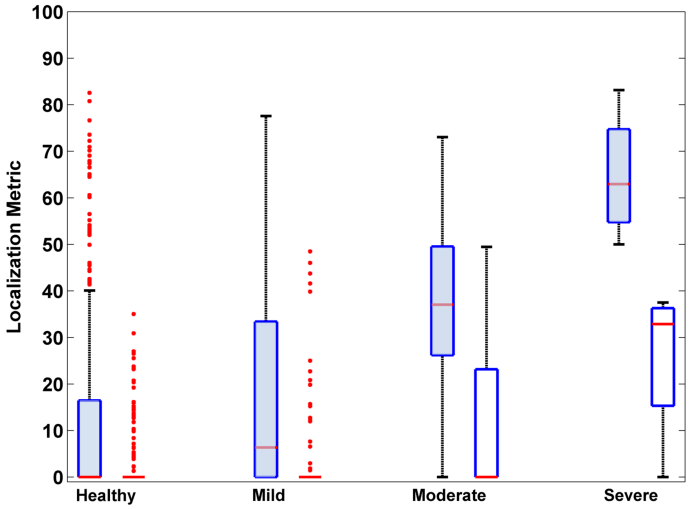

Figure 8.9: Box plot of localization metric values assigned to raw and processed sequences for individual 450 joints of 10 patients and 5 healthy volunteers. The joints are grouped according to the severity of synovitis, where the left, blue boxes in each of the 4 groups correspond to processed sequences and the right boxes to raw sequences. Outliers are denoted by red points, the red line segment indicates the median and box lower and upper edges are 25^{th} and 75^{th} percentile. In groups "healthy", "mild", "moderate" and "severe" there were 285, 121, 40 and 4 joints, respectively.

rate of negatives detected as such equals specificity, hence, FPR in one minus specificity. Therefore, ROC can be seen as well as sensitivity vs. specificity.

The ROC curves for the analysis of 450 joint imaging results are presented in Figure 8.10 for both raw (blue solid and dotted curves) as well as processed (red solid and dotted curves). The solid ROC curves denote sensitivity vs. specificity when the threshold is applied to the metric to make a decision between "healthy" and "mild, moderate or severe synovitis", denoted here as classification I. The dotted ROC curves present sensitivity vs. specificity when the decision is made between "healthy or mild synovitis" and "moderate or severe synovitis", denoted here as classification II.

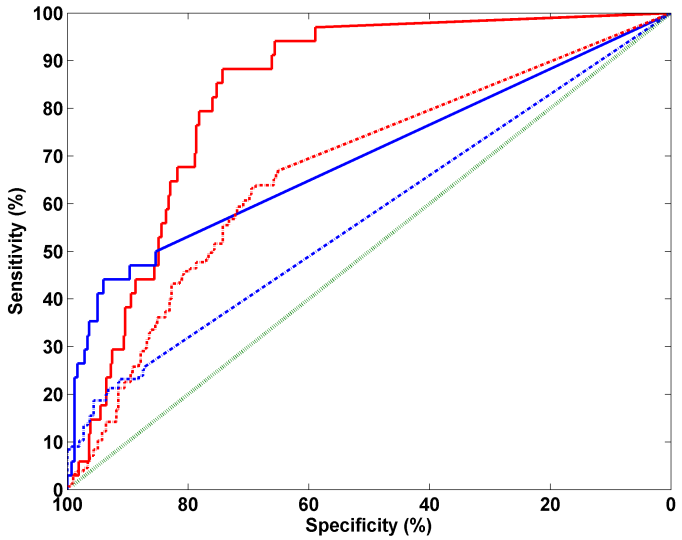

Figure 8.10: Receiver operator characteristic (ROC) curves for localization metric values assigned to raw (blue curves) and processed (red curves) sequences for 450 joints of 10 patients and 5 healthy volunteers. The solid and dotted curves show classification performance for differentiating, respectively, between (healthy) vs. (mild, moderate or severe synovitis), denoted as classification I, and (healthy or mild synovitis) vs. (moderate and severe synovitis), denoted as classification II. The green dotted line represents random classification line of (sensitivity = 1 - specificity).

8.8 Discussion

Fluorescence images from RA patients and a healthy volunteer were analyzed for their intensity and their spatiotemporal characteristics also against MR images. It was found that PCA analysis applied in time-series fluorescence images of the hand captured following intravenous ICG administration can decouple fluorescence signals associated with inflammation from the background and vein interference signals simulated. Case studies were presented for 8 carpal, metacarpophalangeal and interphalangeal joints from 4 patients with varying degrees of synovitis (healthy to severe) were presented in sections 8.7.1 and 8.7.2. Two patients had severe synovitis (MR-assigned synovitis score of 3) and one had mild to moderate synovitis (respective MR scores of 1 and 2) in carpal and metacarpophalangeal joints. One of the patients had moderate and mild synovitis in the 2^{nd} and 4^{th} proximal interphalangeal joints of the left hand. One patient with healthy carpal joint, as verified by

MRI, was shown to visually establish a control case study. The processing result along with the corresponding transverse or coronal images of contrast-enhanced T1-weighted MR images where presented in Figure 8.5-Figure 8.8.

These findings were corroborated with numerical simulations based on a numerical phantom built using a segmented MR scan and were used to better understand the clinical findings. As expected, the contrast between the target and background fluorescence quickly falls with increasing depth and uptake ration, as shown in Figure 8.4(a). This reduces the detection sensitivity as was also observed by the localization metric surface in Figure 8.4(b), which suggests lack of a localized signal component distinguishable as desirable fluorescence in the raw fluorescence measurements. It was found that a localized signal component appears in the joint region in at least one of the PCA components for lower depth and uptake ratios than in the original images, as shown in the dotted surface in Figure 8.4(b), in a wider area in depth-uptake plane.

The impact of physical factors on the fluorescence signal was studied in Section 8.6. Observations of MR images of different patients revealed a synovial lining depth of 2-5 mm, 3-8 mm and 7-16 mm for interphalangeal, metacarpophalangeal and carpal joints, respectively. It can be seen from Figure 8.4(a) that, even for relatively large uptake ratios, it is difficult to detect the desirable signal at locations deeper than around 5 mm, due to the low relative contrast. These observations suggest low detectability of the targeted fluorescence signal in the raw fluorescence images for joints located deeper than 5 mm under skin, which can apply to some MCP and carpal joints. However, this conclusion does not necessarily mean that the fluorescence emanating from the inflammation of such joints cannot be distinguished in the raw images. The reason is that the numerical phantom presented in Section 8.4 does not render a full description of the *in vivo* situation. Factors such as heterogeneous and time-variant background fluorescence or non-uniform optical properties in tissue can degrade or improve the signal quality in comparison to predictions by the numerical model.

As noted, a low value of localization metric suggests presence of a signal component localized to the joint region and hence potentially attributable to the inflammation signal. While a higher metric value generally suggests improved performance in terms of signal visibility, the metric value cannot be interpreted as an indicator of the statistical sensitivity or specificity values. This observation means that the manifestation of a localized signal component in the joint regions, attributable the synovitis signal, has been more frequent in the processed sequences. However, the proposed method has a higher localization metric value for the healthy interphalangeal joints. This can be attributed to the dense dorsal vein network in the fingers; a fact that contributes to false positives and lowers sensitivity for the interphalangeal joints.

Corresponding analysis of the clinical data demonstrated that the contrast between synovial tissue and background tissue generally scaled with the severity of the disease; however it diminished with time due to background non-specific fluorescence signals. Subcutaneous dorsal veins demonstrated particularly high non-specific signals, however the entire tissue non-specifically uptakes ICG and offer strong background signals. This reduction of contrast may lead to false positives or negatives; thus, adversely affecting sensitivity. Similarly, fluorescence obtained from ICG circulating in the relatively dense subcutaneous venous network in interphalangeal joints further complicates the reading of raw images and may lead to reduced sensitivity and specificity.

Conversely the PCA analysis revealed components linked to time-dependencies of the ICG circulation. Three components were identified to reveal clinically relevant time relationships. In particular, the first component demonstrated congruence with the appearance of increased fluorescence signals in joints. In other words, the first PCA component (i.e. the blue channel in the processed images) demonstrates consistent fluorescence signal increase in given joints. This was the case for fluorescence signals emanating from joints with moderate to severe synovitis demonstrated in Figure 8.5 and Figure 8.6. Signals from veins are also mapped to the first component for the same reason in Figure 8.7. The 2nd

and 3rd PCA components mapped respectively to the red and green channels in the processed images generally represent signal of transient nature. This temporally variable signal can arise from several sources. The fluorescence emanating from deep seated lesions such as synovial lining, due to transitory accumulation of ICG, or the fluorescence carried quickly through veins can contribute to the 2nd and 3rd components. The transient, yet strong, signal emanating from dense vascular of fingertips also often contributes to red and green components, as seen in Figure 8.5(n-q). Since the 3rd component, represented by the green channel, corresponds to the lowest singular value and, hence, signal with lowest temporal correlation, it is generally expected to represent highly transient signals. The transient nature and, therefore, the level of information in the three PCA components are more pronounced at early time points, e.g. 20 seconds to 100 seconds, after the injection. At later time points, such as after 120 seconds post injection, the signal is mainly composed of the 1st PCA component and there is very little contribution from the 2nd and 3rd components, as the ICG has reached a relatively stable distribution in the hands and the signal experiences merely an exponential decay.

As explained, the temporal characteristics of the fluorescence signal in a given location in tissue impact the association of the fluorescence to a given PCA component. These temporal characteristics are mainly determined by the distribution of the ICG by the blood, as explained in Section 8.6, and other physiological factors such as tissue capillary permeability. However, it is not possible to attribute the fluorescence due to ICG presence in a certain tissue to a given PCA component.

The performance of the proposed approach is also limited by the physical factors of depth and uptake ratio. As with the raw fluorescence images, the interpretation of the processing results is user dependent. Characterization of certain signal components localized around the joint areas should be performed carefully so as not to lower diagnostic specificity. Furthermore, the presence of a strong transient or persistent signal component in a given joint might deteriorate the decoupling of the targeted fluorescence signals emanating from other joints. An example can be seen in the case study demonstrated in Figure 8.7. The patient was diagnosed

based on the MR images with moderate synovitis in the 4^{th} and 5^{th} left MCP joints. However, neither the raw data nor the processed sequence can indicate synovitis in these joints. This might be due to poor accumulation of ICG in the joint linings, or interference from background tissue. In Section 8.7.3 we presented imaging results for 450 joints of 5 healthy volunteers and 10 patients. The box plot demonstration of the localization metrics calculated for raw and processed sequences was presented in Figure 8.9. As seen, the metric values calculated for the processed sequences generally correlate with severity of synovitis and are much higher than the corresponding values for calculated using raw data for arthritis joints. The metric values for processed data from healthy joints are also lower for healthy joints than arthritic joints. A more rigorous performance analysis was achieved using the ROC curves presented in Figure 8.10. It can be seen that when differentiating between "healthy" and "mild, moderate or severe synovitis", denoted as "classification I" and corresponding to solid ROC curves in Figure 8.10, classification using raw data is relatively close to random line (specificity = sensitivity). This is due to fact that the target inflammation signal is almost always corrupted by interference from veins and other tissue; hence, complicating observation of a localized signal component in the joint regions. The situation is better when differentiating between "healthy or mild synovitis" and "moderate or severe synovitis", denoted as "classification II", using raw data (corresponding to the dotted blue curves in Figure 8.10). In fact for classification II, a specificity of 90% and a sensitivity of 44% can be achieved using the raw data. This is in accordance with the results of the clinical study presented in [27], which reports relatively low sensitivity (around 39%) for a relatively high specificity (around 85%) when differentiating between healthy and inflamed joints (classification I). It should be noted for specificity values larger than 90%, the sensitivity values when using the raw data are slightly larger than when using the processed data, in both classifications I and II; though in all cases sensitivity is smaller than 45%. This is due to the fact that for healthy joints, more localized components have been detected in processed sequences than in raw data, as also seen in Figure 8.9.

The area under curve (AUC) values found for the ROC curves presented in Figure 8.10. For a given classifier ranking positive samples higher than negative ones, Ref. [170] reports, "the AUC of a classifier is equivalent to the probability that the classifier will rank a randomly chosen positive instance higher than a randomly chosen negative instance". Hence, AUC a measure of classifier's quality [170]. For classification I, AUC values of 0.57 and 0.67 were found when using, respectively, raw (dotted blue ROC curve) and processed sequences (dotted red ROC curve). For classification II, AUC values of 0.69 and 0.83 were calculated when using, respectively, raw data (solid blue ROC curve) and processed data (solid red ROC curve). For the current dataset and specificity $> 60\%$, the sensitivity achievable for any threshold when using the raw data is limited to 25% and 50% for classifications I and II, respectively. However, when using the processed data, the sensitivity is limited to 65% and 94% for classifications I and II, respectively. These observations suggest using the proposed PCA-based method results in superior clinical performance than relying on raw data for diagnosis.

It is important to note that the fluorescence image sequenauthor = Abdoulaevces are in practice analyzed and interpreted for diagnosis by specially trained human readers [23, 27]. The specificity and sensitivity values inferred from ROC curves of Figure 8.10 serve to compare diagnostic value between raw and processed data. While the results demonstrate performance improvement when using the proposed method, the sensitivity and specificity of diagnosis performed by an expert human reader is expected to be higher than the values inferable from the ROC curves presented here. Furthermore, a cross-examination of both raw and processed sequences is likely to improve performance over using either sequence alone. A more complete clinical assessment of the proposed method requires examination of processed sequences by trained human readers for a clinically significant group of patients and is a subject of ongoing research.

8.9 Conclusion

The proposed method has the capability of differentiating between signal components which have different temporal behavior. This capability potentially enables separation of fluorescence emanating from tissue parts with different temporal and spatial profiles of ICG uptake. The interference from fluorescence in veins and the general tissue can be particularly mitigated rendering the time-series analysis potentially as highly relevant to improve detection of inflamed joints compared to observing intensity images. The resulting color image sequences, when examined along with the original raw dataset, can help better localize the signal components due to the inflammation; hence, improving diagnostic performance as shown by analysis of results of processing imaging data for 450 joints. The results of this work can also be employed to design next generation optical systems and methods for imaging and detection of joint inflammation using exogenous fluorescence. Understanding the impact of physical and physiological factors on the detectability of the desirable fluorescence signal and the proposed numerical model can be employed to optimize the hand and finger posture during imaging. Moreover, the FEM-based time-series simulation framework can be employed to analyze the performance of other post-processing approaches. The imaging approach considered in this chapter was a planar imaging method. In this chapter we propose and study three-dimensional imaging of synovitis in human finger joints using tomography.

9 Tomographic imaging of synovitis

9.1 Introduction[1]

In this chapter, we report optical imaging of synovitis in human finger joint using contrast-enhanced fluorescence molecular tomography (FMT). The proposed methods and imaging results are the, to our knowledge, the first demonstration of fluorescence-based imaging of inflammation in human joints.

The process of detection and assessment of disease progression of inflammatory arthritis disorders is often based on a combination of clinical, laboratory and imaging data. Early initiation of effective therapy prevents destruction, preserves function and is able to induce lasting remission. Therefore, there is a growing demand for sensitive and specific tools for early detection of inflammatory arthritis [121]. Current clinical imaging approaches include X-ray radiography, ultrasound and magnetic resonance imaging (MRI). As detailed in Section 8.1, optical imaging

[1] The materials in this chapter are presented (at places with minimal or no changes and with slightly different processing parameters) in P. Mohajerani, et al., "Fluorescence-aided tomographic imaging of synovitis in the human finger", Radiology, vol. 272, 2014 (see Publications overview at the end of the dissertation for full author list). Priv.-Doz. Dr. Reinhard Meier (department of radiology) and Dr. med. Klaus Thürmel (department of rheumatology) at Klinikum rechts der Isar performed MR imaging of hands, examined the patients, assisted with clinical details and provided clinical insight, information and findings (such as MRI scans, inflammation severity and location as well as other information from patients) used in this chapter. Maximilian Koch at IBMI performed FMT imaging for one of the patients.

methods have been proposed as well for imaging inflammation in joints, and in particular, hand joints, as inexpensive and sensitive alternatives.

These methods often rely on changes in optical characteristic of affected joints to provide quantitative 2-D or 3-D images of the underlying joint, synovium, or synovial fluid. As mentioned, recently Indocyanine Green (ICG), a nonspecific, clinically-approved synthetic organic near-infrared fluorescent dye, has been employed for detecting inflammatory lesions in hand joints [27, 144]. Current fluorescence-based approaches rely on planar methods and allow for fast two-dimensional imaging of biodistribution of ICG.

However, planar imaging methods do not resolve information in depth and deliver a weighted projection of the underlying three-dimensional (3-D) fluorophore distribution [11]; limiting sensitive and quantitative detection of synovitis [27]. A more complete survey of current optical methods for imaging arthritis in hand joints was presented in Section 8.1.

We report the first clinical fluorescence-based tomography for 3-D optical imaging of synovitis in the human finger joint. Synovitis is an inflammation of the synovial membrane lining the joint capsule and typically marks the onset of rheumatoid arthritis. Our approach relies on the higher local concentration of intravenously injected ICG in hyperperfused synovium - a fact substantiated by the results presented in the previous chapter. The FMT system at HMGU was optimized for imaging finger proximal interphalangeal (PIP) joints of the 2^{nd} and 3^{rd} fingers.

A study was conducted in collaboration with the department of radiology and the department of rheumatology of TUM and Klinikum rechts der Isar, wherein a group of 4 healthy volunteers and 5 patients with rheumatoid arthritis (and not other forms of arthritis) were examined and imaged using the proposed method. *In vivo* results are presented here and validated and fused with contrast enhanced 3T MR images.

9.2 Image acquisition

The 360 degree rotation FMT system located at HMGU [32] was optimized and used for imaging the proximal interphalangeal (PIP) joint, as

shown in Figure 9.1. The imaging protocol was optimized to allow acquisition over several hundred source positions, at reasonable signal quality and imaging time, as explained later.

FMT imaging was planned 20 minutes after intravenous bolus injection of 1 mg ICG per kg of body weight(actual imaging times were 22.7 ± 6.0 minutes, see Table 9.2).[2] Patients placed the hand inside the FMT device on a hand holder in prone position and the imaging lasted on average 12 minutes (12.0 ± 2.4 minutes) in an average field of view of 15 mm in the axial direction of finger over 17 gantry projections.

The individual imaging times and starting points are given in minutes in Table 9.2. The tip of the finger was placed in a thimble, which serves as a reference pivotal point. The 750 nm laser (B&W Tek, Newark, DE, USA) scanned the sample at on average 14 source locations per gantry angle, where at each location intrinsic and fluorescence images were obtained using the cooled CCD (Pixis 512B, Princeton Instruments, Trenton, NJ, USA) [32].

Fixed laser powers of 97 and 184 mW and exposure times of 100 and 200 ms were used for intrinsic and fluorescence acquisitions, respectively. These values were observed consistently to result in intrinsic and fluorescence signal in counts of tens of thousands, without saturation. A analysis of the acquisition time is given in Table 9.1. The imaging consisted of acquisition of front-illumination images at every 10 degrees (used for volume reconstruction) during the first minute of imaging. Intrinsic-fluorescence image pairs were afterwards acquired every 20 degrees. A front-illumination image was acquired at every gantry angle prior to laser scanning to manually indicate the scanning FOV using MATLAB's `ginput` - devised to prevent erroneous source positioning due to finger movement.

In the beginning of the project, the axial span of the joint was extracted automatically by marking the joint area with two black tapes wrapped on the middle and based knuckles. For the two female volunteers this

[2] Injections performed at HMGU by Priv.-Doz. Dr. Reinhard Meier and Claudio von Schacky from the department of radiology, Klinikum rechts der Isar.

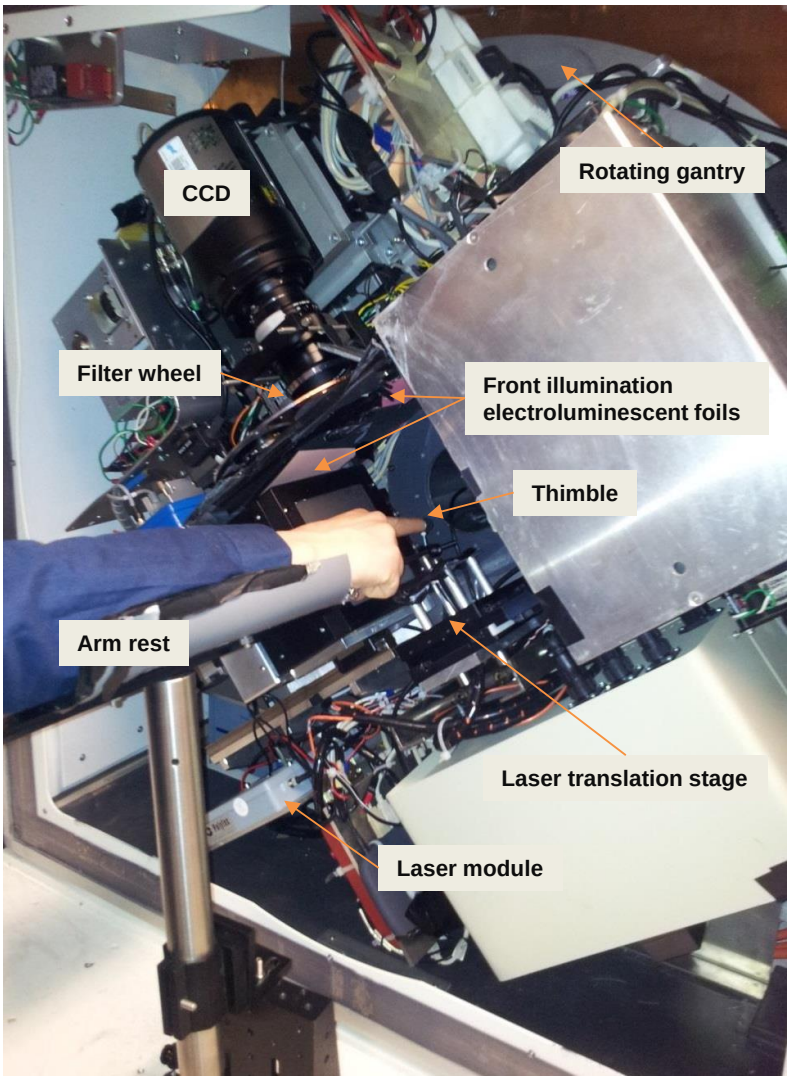

Figure 9.1: Hardware for imaging finger joint using FMT; the patient places the forearm on the holder in prone position and stretches the middle or index finger out, placing the fingertip in a thimble. The CT modules are not turned on during acquisition and a lead plate covers the front face.

initial method was used which resulted in relatively lower imaging time of 8 minutes for these two cases. For one patient (9^{th} row of Table 9.2) the black tape was used in conjunction with the manual method (the tape can be seen in Figure D.2). The tape was later removed and replaced with the manual indication of FOV toward further convenience.

Table 9.1: Acquisition time analysis for tomographic joint imaging; the total imaging time of 13 minutes consists of approximately 100 seconds attributable to optical exposure times shown below and around 620 seconds overhead. The overhead consists of mechanical overhead (due to gantry and filter wheel movement) and CCD readout time. The intimal acquisition of 34 front-illumination images lasts approximately 1 minute. The information below is presented for an average of 320 source positions.

	Intrinsic acquisition	Fluorescence acquisition	1st Front illum. acquisition	2nd Front illum. acquisition
Frequency	320	320	34	17
Exposure (s)	0.1	0.2	0.1	0.1
Total (s)	32	64	3.4	1.7

9.3 Clinical imaging and examination[3]

Five patients with rheumatoid arthritis (all female, mean age 64.8 ± 13.2), and four healthy volunteers (2 female, mean age 28.8 ± 3.5) were imaged in this study. The patients underwent 3T MRI imaging (Verio, Siemens, Erlangen, Germany) using a flexible surface coil. T1 weighted fat-saturated contrast-enhanced MR images were obtained with patients in prone position with for both hands simultaneously in praying form. The protocol presented in [27] was used toward MR imaging. Briefly, the protocol consists of coronal fat-saturated and T1-weighted turbo spin echo imaging, followed by injection of 0.02 ml/kg of gadopentetate dimeglumine (Magnograf, Schering, Berlin, Germany). Transverse and coronal fat-saturated T1-weighted turbo-spin echo imaging were performed post-injection [27].

Synovitis scores on a 4-point-ordinate scale (0: no inflammation, 1: mild, 2: moderate, 3: severe) were assigned to each joint according to the assessment system designed by the OMERACT MRI group. The patients and volunteers were recruited from March 2012 to March 2013 through the Department of Rheumatology at Klinikum rechts der Isar.

Patients with affected proximal interphalangeal joints of the hand with certain exclusion criteria as mentioned in [27] were included in this study.

[3] Clinical information and protocol were provided by Priv.-Doz. Dr. Reinhard Meier, Klinikum rechts der Isar.

This study was approved by the local ethics committee at our institutions and was conducted according to the principles of the Declaration of Helsinki.[4]

9.4 FMT processing of finger joints

Since, unlike FMT-XCT, the acquisition of CT images was not a possibility in this study, front illumination images were used to reconstruct a 3-D volume of the imaged tissue. This volume was required for modeling the light propagation and as a geometrical reference for motion compensation. The light propagation in the finger tissue was modeled using finite element method (FEM) based discretization of the diffusion equation [33], as described in Chapter 2. A background subtraction method was applied to Born normalized data to compensate for non-specific uptake of ICG. Reconstructions were performed at 1 mm^3 resolution using the LSQR method. The impact of ICG temporal decay was compensated during reconstructions as explained in Section 9.4.2. The fluorescence signal was observed to drop about 47% after the 12 minute acquisition, as discussed in Section 9.4.2.

The 3-D volume designating the tissue's volume was reconstructed using the 34 front-illumination images by back-projection of the image boundaries based on the camera's geometrical description, as discussed in Section 9.4.1. Homogenous optical absorption and scattering of 0.1 and 1.5 cm^{-1}, typical for human tissue, were used in the FEM-based modeling of light propagation in finger. The FEM tetrahedral mesh (generated using the `CGAL` library [44]) consisted of on average 10000 nodes and 58000 tetrahedral elements.

Performance of the FEM-based propagation modeling for one source position is examined in Figure 9.3 for clinical data obtained from a finger at intrinsic wavelength (this level of conformance does not hold for all source positions, due to unaccounted-for geometrical irregularities and

[4] "Ethical Principles for Medical Research Involving Human Subjects" `http://www.who.int/bulletin/archives/79(4)373.pdf`.

tissue heterogeneity). Finger motion in the transverse plane was corrected by finding the offset between the acquired intrinsic images and the projection of the 3-D volume for the given gantry angle. The intrinsic and fluorescence images were shifted to match the projected image of the volume and source position locations were corrected accordingly. This scheme can compensate translational motion in the transverse plane, but not motion in the axial direction or rotation of the finger. The fluorescence signal was observed for to drop exponentially at with a half time of 13 minutes.

The measured fluorescence images were correspondingly weighted prior to reconstruction based on their acquisition time point (with 20 minutes post-injection time point taken as '0' time point). This operation also compensated for differences between the actual imaging times and the planned 20-minute point-injection time point. These time differences were unavoidable due to logistical limitations, such as system crash and restarting, measurement interruption due to large motion of the finger or the subject's preference toward speedier completion of the imaging. LSQR with 50 iterations was used to solve the following regularized problem

$$x = \arg\min \left(\|\mathbf{W}\, x - M\|_2^2 + \lambda^2 \|x\|_2^2 \right), \tag{9.1}$$

where $\mathbf{W}$, x and M are weight matrix, fluorophore concentration vector and measurement vectors, respectively. The regularization parameter λ was set to $0.03\|\mathbf{W}\|_2$ for all cases. The reconstruction voxels located 2 mm or less under the skin were attributed to surface artifacts and removed from all reconstructions. Born data larger than 1.7, corresponding to intrinsic values less than 100 or with corresponding source-detector Euclidean distance of less than 10 mm were discarded. The performance of this method, including volume reconstruction and motion compensation schemes, was verified using a phantom study containing a fluorescent tube with simulated motion applied during acquisition. The results are shown in Figure 9.2.

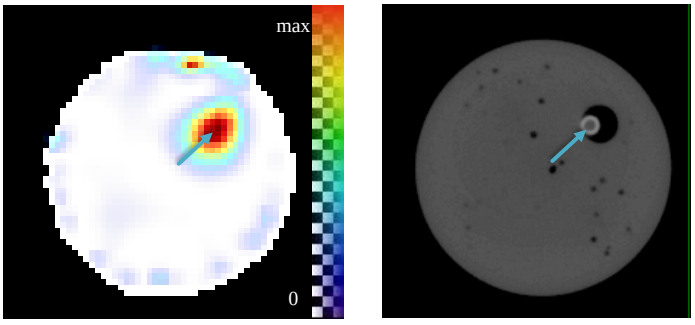

Figure 9.2: Compensation of simulated motion for phantom data; the compensation approach was verified by manually moving the phantom during the reconstructions. The reconstructed tube shown in the FMT slice in (a) is observed to be in the correct location, pointed to by the blue arrow in the CT transverse image shown in (b).

9.4.1 Volume reconstruction

The volume of the finger is required for (1) modeling the light propagation in the tissue (2) motion compensation after the acquisition. Here we describe the reconstruction of tissue volume from the front-illumination images. At every gantry angle θ in the first acquisition stage one photograph is in reflection mode obtained using the front-illumination electroluminescent foils. There are 34 such angles spanning -10 to 320 degrees. Let I_i denote the photograph at the i^{th} gantry position.

The image I_i contains skin as well as background and is segmented to a binary image J_i which contains only the pixels representing the skin. Furthermore, at every gantry angle the camera is modeled using a 3×4 camera matrix C_i such that point (X, Y, Z) in the 3-D coordinate system corresponds to a pixel (x, y) in the binary mask J_i according to the following equation [52]:

$$\begin{pmatrix} xw \\ yw \\ w \end{pmatrix} = C_i \begin{pmatrix} X \\ Y \\ Z \\ 1, \end{pmatrix}, \tag{9.2}$$

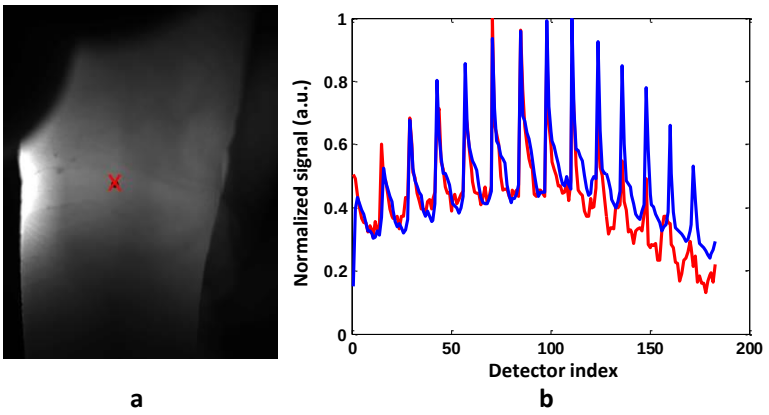

Figure 9.3: Light propagation modeling in finger tissue - experimental intrinsic signal measurements vs. FEM simulations; (a) trans-illumination image (with 20% brightness enhancement) of a finger joint, seen from the palmar side, at the intrinsic wavelength of 750 nm with the red marker showing the source location; (b) measured intrinsic signal (blue) vs. the FEM-based simulated signal (red) over different detector indices. Both signals are normalized to 1.

where the left side is the representation of the pixel location in homogenous coordinates. We define then the projection operator P_i

$$(x, y) = P_i(X, Y, Z). \tag{9.3}$$

The reconstruction volume is define of all 3-D points (X, Y, Z) such that

$$\sum_i J_i \left(P_i(X, Y, Z)\right) > N. \tag{9.4}$$

In other words, all 3-D points whose projections fall inside at least N image masks. N was set to a value less than 34, depending on the number of obstructers in each case (such as the holder's bar attached to the thimble or other fingers).

9.4.2 ICG decay compensation

After the injection, ICG is gradually washed out of the blood mainly through the hepatobiliary tract and is known to have a half-time of 2-3 minutes in human blood [153]. The temporal decay of fluorescence

signal due to ICG's washout should be taken into account in the FMT reconstruction process.

To characterize the temporal decay of the fluorescence signal measured using the trans-illumination geometry of the FMT system in the finger joint region, we performed the following experiment. After the FMT imaging of the finger joint, a second set of the measurements using the same imaging settings were obtained for 2 patients and 2 healthy volunteers. For one volunteer a 3$^{\text{rd}}$ set was obtained as well for the same joint and imaging parameters. Then for each case the average value of the fluorescence signal within a region of interest (ROI) on the skin was found for different source locations for both the first and the second acquisitions. The ROIs were the same between the consecutive acquisitions for a given joint. For one volunteer these values were also found for the 3$^{\text{rd}}$ acquisition.

Let v_1 and v_2 denote the corresponding average values within the same ROIs for a given joint and source location at times t_1 and t_2 in seconds. We assume $t_2 > t_1$, which results in $v_1 > v_2$. Assuming exponential decay of form $e^{(-\alpha t)}$ for the fluorescence signal (a valid assumption as acquisitions occur several minutes post injection), the exponential decay coefficient α for measurement pair (v_1, v_2) is given as

$$\alpha = \frac{(\ln v_1 - \ln v_2)}{(t_2 - t_1)}. \tag{9.5}$$

Correspondingly, signal reduction in percentage after 12 minutes of acquisition time, given as $100 \times (v_1 - v_2)/v_1$ for $t_2 = t_1 + 720s$, is estimated as $e^{-\alpha \times 720}$. A histogram of these estimations of the fluorescence signal fall in percentage for all the 4 joints and source locations is presented in Figure 9.4. The time difference between samples, i.e. $t_2 - t_1$, ranged from 720 seconds to 2700 seconds. To compensate for the effect of the temporal decay of the ICG's fluorescence signal in the FMT measurements, based on the results presented in Section 9.4.2, an exponential decay coefficient $\alpha = 8.83 \times 10^{-4}\, s^{-1}$ was selected, which corresponds to 47% reduction of fluorescence signal in 12 minutes (typically between

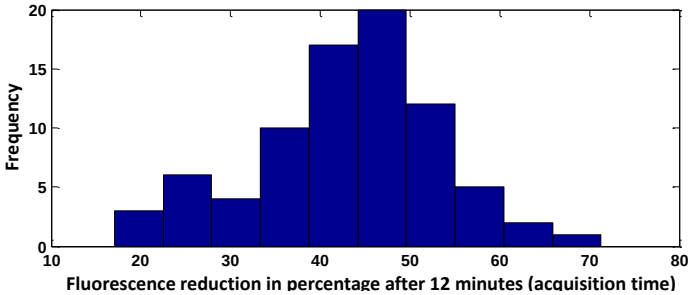

Figure 9.4: Reduction of fluorescence signal after 12 minute imaging time; the histogram shows signal reduction in percentage after 12 minutes calculated using consecutive imaging of 2 patients and 2 volunteers. The signal values corresponding to the same regions were calculated between same source locations in the first and second acquisitions and the difference was calculated in percentage as the ratio between the signal reduction and the first value.

20 and 32 minutes after injection) and a half-time of around 13 minutes for the fluorescence intensity. The fluorescence measurements were then compensated for the decay according to their acquisition time point. Specifically, for a study lasting a total N minutes and P projections, the fluorescence measurements acquired at the p^{th} projection are then multiplied by $e^{+\left(\alpha\times 60\times \frac{(p-1)(N-20)}{P-1}\right)}$, where $p = 1 \ldots P$.

9.4.3 Background fluorescence correction

ICG shows higher accumulation in the inflamed synovium due to synovial hyperplasia with neoangiogenesis and subsequent local hyperperfusion. However, as a blood pooling agent, ICG has also non-negligible concentration in vascular bed present in other tissue. This non-specific distribution of ICG contributed to significant background fluorescence emanating from the rest of the joint and interfering with the target signal originating at the inflamed synovial tissue. Here, we describe our implementation of an approach presented in [61] for compensation of background fluorescence.

Specifically, for the i^{th} source-detector pair, let $M(i)$ and $D(i)$ denote, respectively, the normalized Born value (after compensation of temporal decay as described above) and the Euclidean distance between the corresponding source and detector points. The background fluorescence can

be approximated by a linear function of the source-detector distance [61]. Accordingly, the measurement vector corrected for background fluorescence, defined as $\tilde{M}$, is estimated herein as

$$\tilde{M}(i) = M(i) - \max(\beta\, D(i) + \delta, 0). \tag{9.6}$$

The parameter δ is as $\delta = -\frac{\sigma}{\beta}$, where σ is the 1^{st} percentile of the vector D (smallest number larger than 1% of all elements of D, selected to remove outliers) and the slope β is adjusted so that the 99.9% of Born values in M lie above the line $\beta\, d + \delta$, with d denoting the source-detector distance variable. This way the line presents a linear lower bound of the Born data within the source-detector distance span. Values of M falling below this line were set to zero. Parameters heuristically optimized as such, achieve reasonable performance for all subjects. Imaging prior to ICG injection revealed small (< 50 counts) signal due to autofluorescence. Background subtraction is an important step to achieve imaging accuracy, which in some cases was relatively sensitive to parameters of Equation 9.6.

9.4.4 FMT and MRI coregistration

The FMT reconstructions were performed within the volume reconstructed from the front-illumination photos. The reconstruction results were coregistered with MRI for validation and comparison purposes, using the following approach. Given an transverse MR image of the joint, the problem of coregistration consist of two steps; (1) finding a corresponding transverse representation of the FMT reconstruction and (2) finding the proper orientation in the transverse plane between the FMT and MR transverse images. To solve the first problem, an MR transverse image indicative of the joint inflammation was selected. These slices have a slice spacing of 2.7 mm and slice thickness of 2 mm. In most cases, the inflammation is visible in 1 or 2 such MR images through the joint split or right underneath it. A corresponding group of FMT slices was selected using the following approach. It is known that palmar joint creases of PIP joints present a good approximation of the anatomical location of the underlying joint split. A distance of 2-3 mm between the palmar PIP crease and joint

location has been reported in [171] for a group of 48 patients. We have used these surface anatomical markers to approximately locate the underlying joint location. Specifically, for every finger joint studied, one or two salient transversal creases on the palmar side of the joint were delineated. The "crease location" was set to with the help of these crease lines. A group of 5 FMT slices with 2 mm above the crease location and 3 mm below it were selected and believed to span the area of interest in the joint. For one patient, the inflammation was approximately 7-9 mm below the PIP joint split, and the ROI was set accordingly for the FMT. The transverse FMT images shown in results below are the maximum intensity projections (MIP) of FMT in this ROI, after proper orientation performed as follows.

The orientation of a MIP projection of FMT signal should be properly adjusted such that the polar coordinate system in the FMT image and the MR image are the same. That is, the dorsal and palmar sides in both images should be oriented in the same angles; for instance, with the sagittal planes in both modalities to be vertical in the transverse planes. This was again achieved using anatomical markers. For the FMT, the sagittal plane was found by seeking the gantry angle where the front-illumination photograph shows the palmar side, again based on palmar creases. For the MRI the accurate sagittal plane was found using the orientation of the flexion tendons with respect to proximal phalanx. Although the patients were asked to place the hand in prone position on the arm rest Figure 9.1, the sagittal plane in the imaged finger was found to have a deviation of up to 30 degrees in some cases from the expected vertical orientation, which results from involuntary twisting of the hand.

After proper orientation of both transverse MR image and MIP image of FMT, the MR image was scaled to match the resolution of the FMT volume (voxel side length of 0.095 mm). Then a 2-D translation was optimally found using correlation to superimpose the transverse image of the FMT volume and the MR image.

Table 9.2: Details for individual volunteers and patients; the 2nd and 3rd joints denote, respectively, the proximal interphalangeal joints of the index and middle fingers of the respective side. The image time point designates the start of the FMT acquisition after intravenous ICG administration and imaging length is the acquisition time (both numbers given in minutes). The signal mean, maximum and root mean square (RMS) values are presented for the reconstructed fluorescence signal with a field of view of 5 mm in the axial direction (along the finger) centered on the respective joint using the palmar joint crease lines (abbreviations: male (M), female (F), healthy volunteer (Vol.) and patient (Pat.)).

	Age	Gender	Joint	MR score	Imaging point	Imaging length	Signal mean	Signal max	Signal RMS
Vol.	28	M	2nd, Right	0	23	11	1.67	3.83	1.77
Vol.	33	M	3rd, Left	0	14	12	0.70	1.48	0.74
Vol.	28	F	2nd, Right	0	16	8	1.40	2.84	1.48
Vol.	25	F	2nd, Right	0	27	8	1.44	3.39	1.51
Pat.	67	F	2nd, Right	2	33	12	2.37	5.09	2.50
Pat.	42	F	3rd, Left	2	24	13	4.25	8.68	4.50
Pat.	73	F	3rd, Left	3	20	13	2.42	5.40	2.56
Pat.	67	F	3rd, Right	3	20	13	3.00	8.36	3.13
Pat.	75	F	3rd, Right	3	28	13	3.59	7.77	3.78

9.5 Results

To validate the FMT acquisition and reconstruction approaches described herein along with the volume reconstruction and motion compensation approaches, a phantom experiment was performed as follows. A silicon-based cylindrical phantom with containing a fluorescent tube filled with around 400 picomoles of Alexa 750 was imaged in the FMT system.

Finger motion was simulated by moving the phantom arbitrarily in the transverse plane during the acquisition. The phantom volume was reconstructed from the front-illumination images and motion compensation approach was applied to the acquired dataset. The reconstruction result showing the reconstructed tube in transverse slices is presented in Figure 9.2(a) and an transverse slice of the corresponding CT scan imaged using the built-in micro-CT module, is shown in Figure 9.2(b). This example verifies the operation of the volume reconstruction and motion compensation operations.

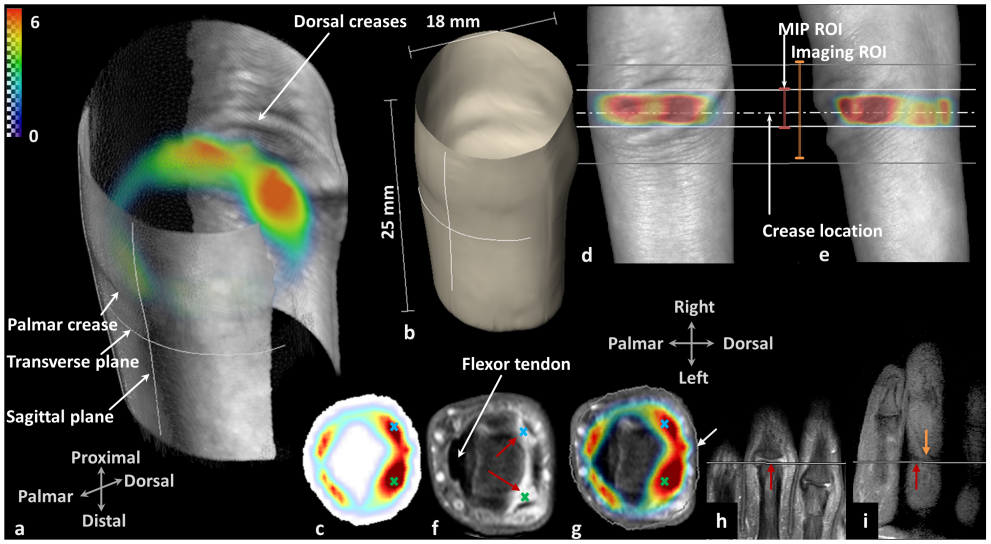

Figure 9.5: FMT imaging results of the 3rd left PIP joint (with MR synovitis score of 2) of a 42 year old female patient; (a) 3-D representation of the reconstruction fluorescence, where the skin on the palmar and dorsal side is wrapped on the volume surface (b) isosurface of the reconstructed volume, (c) MIP projection of the FMT signal in the transverse plane as a transparency color image with jet colormap on a white volume slice. (d) and (e) MIP projections in the coronal and sagittal planes. The 5 mm axial ROI of the MIP projection of (c) is shown in (d) and (e). (f) The corresponding transverse MR image, where the red arrows point to the inflammations and (g) coregistered image between the FMT MIP image and the MR transverse image, with the white arrow pointing to the boundary of the coregistered FMT volume. (h) and (i) MR images in two coronal planes, with the location of the transverse image of (f) pointed to by red arrows and the orange arrow points to the palmar creases. Imaging ROI denotes the detector range.

Below we present the imaging results for one patient and one healthy volunteer. Further processing results for the other 4 patients and one volunteer are presented in Appendix D.

9.5.1 FMT imaging of an inflamed joint

FMT imaging results for a patient with moderate synovitis in the left 3rd PIP joint are shown in Figure 9.5(a). Palmar creases were employed as anatomical surface markers indicative of underlying joint location [171] The reconstruction fluorescence signal was limited to a region 2 mm distal

from the distal palmar joint crease and 3 mm proximal to it, as shown in Figure 9.5(d, e). A maximum intensity projection (MIP) of the FMT signal within this region of interest (ROI) in the axial direction is shown in Figure 9.5(c). MIP projections in sagittal and coronal planes (seen from the palmar side) are demonstrated in Figure 9.5(d, e), respectively. An T1-weighted post-contrast MR transverse image of the joint is shown in Figure 9.5(f), where the bright spots designated inflammation marked by higher uptake of gadolinium [27]. The FMT MIP image was coregistered with the MR transverse image (as explained in Section 9.4.4) and shown in Figure 9.5(g). The MR image is collocated with the palmar creases; partly visible in the coronal MR images Figure 9.5(h) and (i). The FMT reconstruction demonstrated a signal profile similar to the MR image. It shows higher ICG uptake on the dorsal side 3 mm below the skin with the left side (blue ×) stronger than the right side (green ×); profile features that are also observed in the MR image and are therefore indicative of signal uptake in the underlying inflamed synovium.

9.5.2 FMT imaging of a healthy joint

Imaging results for the 2nd right PIP joint of a 28 year old male healthy volunteer is presented in Figure 9.6. The MIP images shown in this figure showing the same colormap (and same maximum value) as in the previous case.

9.5.3 Processing results for 9 joints[5]

Figure 9.7 shows signal maximum and average values within respective MIP ROIs for 4 volunteers and 5 patients with moderate to severe inflammation. Signal characteristics between the healthy and inflamed joints varied significantly (signal average for volunteers 1.55±0.15; patients 3.12±0.80). A double-sided T-test [172] between average values rejected the null hypothesis (both groups having the same average signal)

[5] The results are extended to 12 joints in P. Mohajerani, et al., "Fluorescence-aided tomographic imaging of synovitis in the human finger", Radiology, vol. 272, 2014.

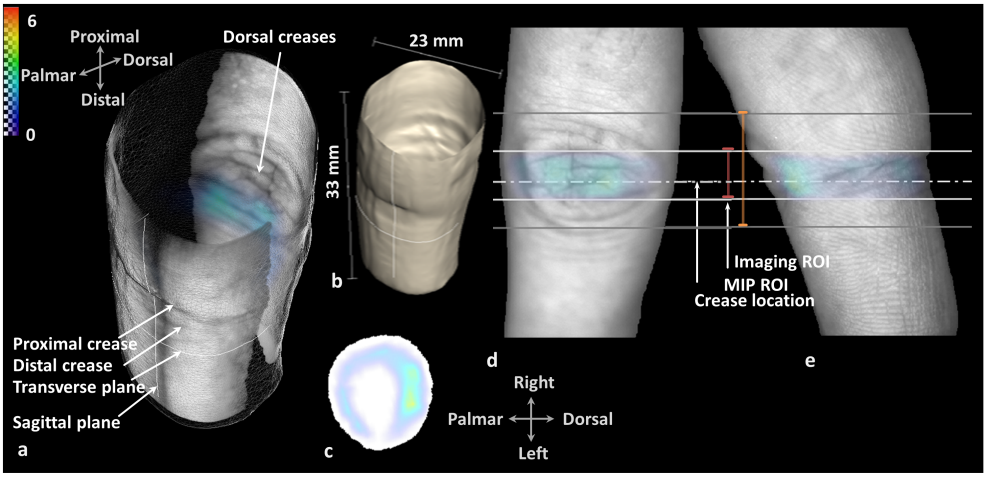

Figure 9.6: FMT imaging results of the 2nd right PIP joint of a 28 year old male healthy volunteer; (a) 3-D representation of the reconstruction fluorescence, where the skin on the palmar and dorsal side is wrapped on the volume surface and two salient dorsal and proximal palmar crease lines are visible, (b) isosurface of the reconstructed volume, (c) MIP projection of the FMT signal in the transverse plane as a transparency color image with jet colormap on a white volume slice. (d) and (e) MIP projections in the coronal and sagittal planes. The 5 mm axial ROI of the MIP projection of (c) is shown in (d) and (e). This joint showed largest reconstructed signal among all healthy subjects.

at significance level of 0.0047 (less than the conventional limit of 0.05). Although the ICG concentration in blood is believed to be comparable in all cases (1.7 μM assuming 75 kg body weight and 5 liters of blood), the controls showed weaker signal intensity than the patients. This can be explained as the ICG in healthy joints does not concentrate in any specific lesion and therefore contributes mainly to the background fluorescence, which is significantly reduced after the background subtraction approach-leaving only weak signal components. Moreover, the FMT reconstruction results can be scored from 0 to 3 according to their in a fashion similar to MRI. One way to achieve this is by assigning semi-quantitative synovitis scores according to the average intensity. We assign synovitis scores of 0, 2 and 3 to the joints within the span of the blue, orange and red squares shown in Figure 9.7, respectively. This way all volunteers are given a score of 0 and all joints with RA are given a score of 3, except number 5 and 7 which are given a score of 2. The correlation between the semi-

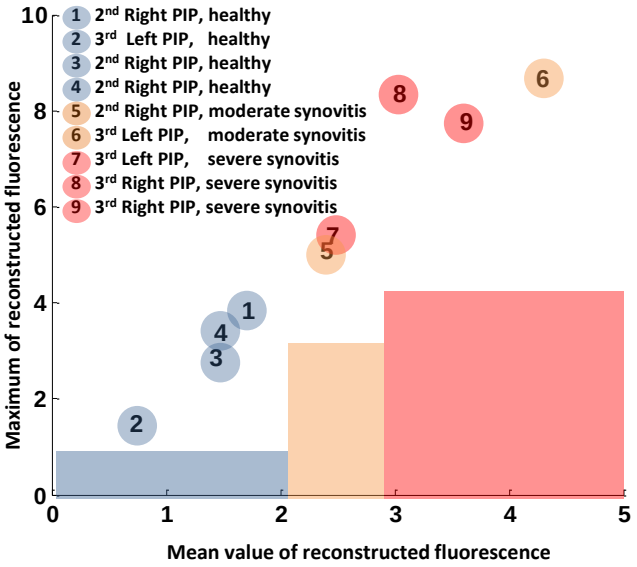

Figure 9.7: Comparison of signal characteristics for healthy joints of 4 healthy volunteers and arthritic joints of 5 patients; average and maximum of reconstructed fluorescence signal intensity in a region of 5 mm in the axial direction around respective proximal interphalangeal (PIP) joints. The same processing parameters were applied to all cases. Two patients had moderate synovitis (MR synovitis score of 2) in their left PIP joints and 3 patients had severe synovitis (MR synovitis score of 3) in one left and two right PIP joints. The blue, orange and red squares show average signal intervals used for semi-quantitative scoring of the FMT results.

quantitative scoring between FMT (achieved as described here) and MRI can be evaluated using, for instance, Spearman's rank correlation coefficient.[6] The Spearman's coefficient calculated as such for the 9 subjects presented herein has a value of 0.88.

9.6 Discussion

Application of FMT to imaging synovitis was presented in this chapter. Imaging was performed for a group of 4 healthy volunteers and 5 patients. The results for a patient and a healthy volunteer were presented in Figure 9.5 and Figure 9.6, respectively. Signal metrics and imaging details

[6]The Spearman's coefficient was calculated using MATLAB's `corr.m`, where a value of 1 indicates maximum correlation.

were presented for all patients in Table 9.2. The imaging results for another healthy volunteer and all other patients are presented in Section D, Figure D.1, Figure D.2, Figure D.3, Figure D.4 and Figure D.5. Based on the MR findings, three of the patients had inflamed synovium just under (proximal) the joint split on the dorsal side. One patient had synovitis several millimeters under the joint split (Figure D.4).

The FMT reconstructions in form of the maximum intensity projection (MIP) images, closely resemble the MR findings for all 5 patients in terms of relative signal distribution in the transverse plane. The conspicuous signal components in most cases appear in almost the same locations (with respect to anatomical markers) in the transverse plan for both MR and FMT reconstructions. There are, however, some differences. Specifically, while the high ICG accumulation seen in Figure D.3(c) and (g) (located toward the anatomical right side) does correspond to the hyperintensity in the MR image shown in Figure D.3(f) with the red arrow, the FMT signal has a slightly lower depth than the MR signal. Furthermore, the left-side FMT signal (located at the lower half of Figure D.3(c) and (g)) remotely corresponds to the lower (or anatomically left-most) part of the MR signal and can be, perhaps, considered as an artifact. Another imperfection can be seen in Figure D.5(c) and (g), where the FMT signal does not span the entire stretch of the MR signal and additionally presents an artifact on the palmar side. It should be noted that such artifacts and reconstruction imperfections are common and understandable in fluorescence tomography and occur even in controlled experiments with homogenous phantoms. Therefore, the spatial correlation between MR and FMT signal profiles for the results presented here can be reasonably deemed as satisfactory and is relatively accurate given the ill-posed nature of the FMT problem and high levels of modeling imperfection due to lack of complete optical description of *in vivo* joint tissue. The application of anatomical priors obtained from MRI in conjunction with optical measurements can potentially improve the imaging accuracy.

The mean, maximum and RMS values of the reconstructed fluorescence within a FOV of 5 mm span in the axial direction were presented in Table 9.2. Based on the results presented in Figure 9.7 and Table 9.2, the

healthy joints all had a lower signal value (both in terms of mean and maximum intensity) than the ones affected with RA. Furthermore, the joint number 5 which had moderate synovitis had a lower signal value than the three joints with severe synovitis; namely joints 7-9. However, the joint number 6 with moderate synovitis had the strongest signal among all joints. This could be due to the difference distribution patterns of ICG and MR contrast agent (as the mild-severe semi-quantitative scoring has been obtained from the MRI findings) or due to experimental variabilities which are unaccounted for. Nevertheless, the proposed method achieves significant signal characteristics between healthy and inflamed joints. This was shown by the two-sided T-test performed on the average values of reconstructed signal. The null hypothesis states that the group of patients and the group of volunteers have the same signal average. The T-test rejected this hypothesis at 0.0047 - well below the customary 0.05 level. Similarly low significance values were observed when the hypothesis is constructed for signal maximum and RMS. As can be seen in Figure 9.7, the points 7, 8 and 9 (corresponding to joints with severe inflammation) lay above the points 1-4 (healthy) and 5 (moderate inflammation) but under point 6 (severe inflammation) in the mean-maximum plane. However, the same statistical claim made above regarding differentiation between healthy and inflamed joints cannot be made regarding differentiating between moderate and severe inflammation using the T-test applied to either of signal metrics (p-value of 0.0047). The statistical evaluation of our method is limited by the number of subjects ($n = 9$) in our study. While a larger scale study is needed to fully characterize the method, the initial results here are promising and demonstrating potential of imaging RA using FMT.

An injection dose of 1 mg per kg of body weight was carried out approximately 20 minutes before the imaging. Assuming a body weight of 75 kg and 5 liters of blood in body, this dose translates an ICG concentration of around 20 μM. The fluorescence was observed to have a significant value even up to 1 hour after injection. This fact suggests that it is possible to reduce ICG injection dose - perhaps down to 0.1 mg per kg as used in the planar rheumatoid arthritis imaging studies of the previous

chapter. While reducing the injection cost, currently several hundred euros per dose, the reduction of injection dose is likely to necessitate certain adjustments in the acquisition protocol and the processing, as the signal levels would be reduced and the ICG temporal decay characteristics might change. Several improvements to the current methodology are possible, as delineated in Chapter 10.

9.7 Conclusion

By providing a 3-D quantitative map of fluorescence throughout the joint, FMT was shown to have the potential to be employed in clinic for detecting synovitis. Patients with synovitis could be discriminated from healthy volunteers. MRI was used in this study as the gold standard, and the FMT images were found to have intensity characteristics that are generally stronger for severe synovitis. Also, the spatial profile of the reconstructed signal was observed to resemble closely that of the contrast-enhanced transverse MR images. It is not foreseen that FMT will replace the MRI in the clinic - however, due to its low cost and high sensitivity it is a potential complementary tool for early inflammation detection and therapy monitoring. Coregistration of FMT data with MRI or XCT allow for precise anatomic orientation and additional information of bony erosions. Further optimization of system hardware and software toward faster imaging of all finger joints at lower injection doses are possible and topic of ongoing research.

10 Conclusions and recommendations for future work

Molecular imaging using optical technology powered by specific and non-specific fluorescent probes has vast preclinical and clinical applications. Several of these applications have only emerged in the recent years and seek to provide new tools for new demands or to replace or complement established imaging technology. The emerging applications and the increasingly powerful imaging systems pose several numerical and algorithmic challenges. Full realization of imaging potential for recent and upcoming preclinical and clinical applications demands highly optimized processing and novel algorithms capable of accurate modeling of light propagation in tissue and data processing in a timely and memory-efficient fashion as well as inversion and analysis algorithms for robust extraction of underlying physical quantities from the large quantities of measured signal.

In this thesis we addressed some of the main challenges associated with fluorescence-enhanced imaging using planar and tomographic technologies. We developed a comprehensive framework for processing data acquired by hybrid FMT-X-ray CT systems. The code builds upon optimized processing, accurate FEM-based modeling of light propagation in tissue, geometrical calibration as well as optimization of the acquisition protocol to facilitate efficient processing of FMT-XCT measurements. Several technical issues were handled toward achieving an optimized processing framework capable of fully capturing the wealth of information made available by the FMT-XCT hardware. As an example, the mesh

size and quality used for discretization of the tissue volume for solving the forward problem using the FEM method was analysed using numerical and tissue phantoms and it was concluded that a tetrahedral mesh with uniform resolution and an average edge length of 1.3 mm or smaller results in a maximum 5% error in forward modeling, which suffices for our application. Accurate geometrical calibration between optical and CT domains is another issue which was thoroughly addressed in this work using a two-step camera and laser calibration process. The MATLAB-based code, implementable in 32 bit environment, is equipped with a highly efficient and versatile GUI which is critical in tailoring the several functionalities of the code to each specific application. A short manual of the code operation is given in Appendix B and the processing time for a typical animal study takes a total of about 5-10 minutes.

We further proposed a novel compression method to address the issue of measurement space size in FMT-XCT. Rapid acquisitions using CCD technology and rotational geometries, afford large amount of data, resulting in up to millions of measurement points. In such sizes, the representation of the weight matrix is often only possible in implicit form; a fact which limits the inversion algorithm to methods requiring only matrix-vector multiplication, such as the conjugate gradient methods. Moreover, large measurement space size reduces the processing speed by, for instance, slowing down the inversion process. While previous methods for reducing the measurement size have relied on compression based on the redundancy in the domain of acquired images, in Chapter 5 we proposed a new method for compression of Born data in FMT-XCT based upon data redundancy and correlation between different source positions. The method was verified using phantom as well as mice measurements. Besides the novelty of the method itself, we demonstrated for the first time to our knowledge, compression of *in vivo* FMT measurements.

A new method based on weighted least squares was proposed in Chapter 6 toward robust inversion of FMT-XCT. The proposed method is driven by the measurements and the anatomical priors and uses a fuzzy inference system to optimize the residual weights. The fuzzy system was designed with the help of an analysis of the tomographic system using the concept

of Kullback-Leibler divergence from the information theory. The proposed method was applied in conjunction with structured regularization to estimate the signal averages in different anatomical segments; used in turn to design the regularizer matrix. The proposed algorithm was verified using several phantom and animal studies. It was observed that the reconstruction accuracy is significantly improved, while the conventional problem of reconstruction bias is alleviated.

The developed processing framework was further verified using several *in vivo* animal studies. In particular, we demonstrated for the first time hybrid imaging using FMT and phase-contrast CT; a hybrid imaging approach called FMT-PCCT. FMT-PCCT draws upon the large soft tissue contrast afforded by phase-contrast imaging to further improve the quality of molecular imaging. Animals were imaged *in vivo* in the FMT machine at HMGU and later *ex vivo* in the phase-contrast imaging system located at Garching research center. The results demonstrate the superior performance of FMT-PCCT relative to FMT-XCT where micro-CT has low or no contrast. FMT-PCCT is expected to be a future trend in fluorescence tomography, as the enhanced soft tissue contrast makes specific reconstruction in various organs possible. The increased contrast also makes automatic segmentation of tumors possible; a factor of critical importance for wider adaptation of hybrid FMT in preclinical research.

We further expanded the utility of the developed framework and presented further methods for clinical applications. Drawing upon the flexibility and accuracy of the XFMT code and the insight affordable by the FEM modeling of light propagation in tissue, we analyzed and proposed methods for two clinical applications for fluorescence-enhanced imaging and characterization of arthritis in human hand joints. A spatiotemporal analysis method was proposed and applied to fluorescence image sequences acquired by a planar imaging system, which has recently entered the clinic for diagnosis and monitoring the therapy of rheumatoid arthritis in human hand joints. The method proposed in this work aimed at decoupling various signal components in fluorescence images obtained in epi-illumination geometry post intravenous injection of ICG in patients.

The proposed method was extensively analyzed using FEM-based simulations of a phantom build from segmentation of a MR scan as well as clinical data. Localized signal components in the locations of joints could be attributed to inflammation signal, which is some cases were indistinguishable in the original sequence due to interference from the background. Processing results for 450 joints of patients and healthy volunteers quantified using the developed localization metric suggested improved diagnostic performance when the proposed spatiotemporal analysis is used.

We further proposed and performed for the first time fluorescence molecular tomographic imaging of synovitis in human finger joints through several acquisition and algorithmic optimizations carried out to make the imaging possible. The FMT system located at HMGU was optimized for imaging human finger joints *in vivo* after intravenous injection of ICG. Previous optical methods for imaging arthritis to human joints have been limited to planar or diffuse optical tomography methods without fluorescence. The results were demonstrated for a group of 4 healthy volunteers and 5 patients with moderate to severe inflammation. The patients were examined by clinicians at Klinikum rechts der Isar. The FMT imaging results as well as the results of the spatiotemporal analysis were compared against T1 weighted post-contrast MR images as the gold standard. The tomographically reconstructed fluorescence had a consistently higher value in the inflamed than in the healthy joints and showed high correlation of spatial profile with the MR findings.

Future development is possible in many aspects of this work, both in optimization and algorithmic developments as well as hardware improvement.

10.1 Numerical and algorithmic developments

There are several opportunities for algorithmic developments to improve the performance of FMT-XCT. Concurrent reconstruction of the optical parameters and the fluorophore concentration has been previously

researched [173]. This optimization approach can minimize the error due to modeling imperfection. It has also been shown that using different optical properties for heart, lung and bone regions as well as background tissue results in improved performance [25,49]. However, these methods use preset optical properties which are not necessarily accurate. Combining DOT and FMT techniques using anatomical priors can further improve imaging performance by optimizing the estimated optical map. Possible implementations are a topic for future research in this direction.

The segmentation of the CT images is a function of critical importance in FMT-XCT. So far, the segmentation implemented in FMT-XCT is mainly limited to bones, lungs and heart and is often semi-automatic methods requiring expert interference from the user [59]. This limits the availability of the technology to end-users, who are oftentimes biologists. Moreover, tumors can arise in other locations which do not lend themselves to current segmentation methodologies. For instance, subcutaneous tumor models are widely used by biologists to research and develop new probes. However, segmentation of these tumors is currently done manually. It seems that segmentation frameworks based on anatomical atlases of mice can facilitate automatic segmentation of known organs as well as deformities arising from abnormal lesions, such as the subcutaneous tumors. We believe atlas-driven segmentation approaches will play an important role in future deployment of FMT-XCT. This issue will have even more significance in FMT-PCCT, where the wealth of anatomical information in the phase-contrast CT scans can evoke a breakthrough in the FMT technology - yet, only when automatic, rapid and reliable extraction of these anatomical priors is made possible.

In this work we presented a compression approach for reducing the size of the FMT problem. It was shown that it is possible to compress the Born data up to two orders of magnitude without losing information. This fact makes explicit representation of the weight matrix possible. The ability to keep the entire weight matrix in memory in a manageable fashion can potentially open the door to other reconstruction approaches than the conventional conjugate-gradient based methods (such as LSQR), as it might be possible to devise more intelligent inversion schemes using, for

instance, SVD decomposition of the weight matrix. Full exploitation of this smaller weight matrix size, is an attractive opportunity for future research. Furthermore, the combination of intra-source, transformation-based approaches with the proposed inter-source method is possible and can potentially result in higher compression rates while maintaining a minimal information loss.

The fuzzy-based weighted least squares method proposed in Chapter 6 can be further expanded in several ways. Neuro-fuzzy systems can be used to further optimize the fuzzy rules using several phantom and animal studies. Furthermore, it is possible to directly optimize the residual weights using information-theoretic measures such as the proposed Kullback-Leibler divergence-based information gain or other measures such as Fisher information. However, successful approaches for direct weight adjustment based on information-theoretic measures require adequately accurate statistical modeling of the underlying system behavior. Finally, tomographic imaging of synovitis using FMT can be potentially improved using higher order approximations of RTE instead of DE for modeling light propagation in joint tissue as well as by application of anatomical priors (e.g. extracted from post-contrast or non-contrasted MR scans) in the inversion process.

10.2 Hardware developments

From the hardware point of view, we have shown that the bottleneck in acquisition time was the overhead due to mechanical movement, CCD readout time and LabView overhead time. The acquisition protocol can be optimized to significantly reduce the acquisition time. This entails more intelligent algorithms for setting the laser power and exposure times, as was accomplished to a certain extent in this work for the finger imaging project presented in Chapter 9. Furthermore, more intelligent source positioning algorithms relying on *a priori* knowledge about the target lesion location can result in reduction of measurement time. Patterned source illumination achievable, for instance, using micro-mirrors will expedite the acquisition. As an alternative, it is possible to mimic diffusive

source patterns using curvilinear scan of the laser beam. Given the new CT technology which has enabled us at IBMI to acquire full CT scans at less than 2 minutes along with the aforementioned developments, it is believed to be possible to achieve a full-rotation FMT-XCT scan within a nominal axial field of view of 20 mm in about 10 minutes or less.

Fluorescence-enhanced planar and tomographic imaging of joint inflammation also lends itself to further hardware optimization and development. Specifically, the spatiotemporal treatment and the FEM-based analysis of the fluorescence image sequences acquired by the ICG-enhanced planar imaging system, paves the way for optimization of the illumination and imaging configuration. As the hand and finger positioning can affect the local blood flow, other hand formations (such as the clenched formation, for instance) can be examined and analyzed to further reduced the interfering signal specially emanating from the dorsal veins, toward improved diagnostic capability.

Tomographic imaging of synovitis as presented in Chapter 9, can especially benefit from hardware optimization. To achieve the full potential of this method it is necessary to design a custom FMT system for this application, with provisions for fixed positioning of the finger and minimization of imaging time and discomfort for the patients, who are often among the elderly. We have performed the experiment with the relatively high ICG dose of 1 mg per kg of body weight. Such high dose is relatively expensive (several hundred euros per injection) and, in our experience, unnecessary. Acceptable signal levels were observed even 40-60 minutes after injection - suggesting possibility of using much lower doses. Due to mechanical difficulties, it was not possible with the current FMT system and holder to image distal interphalangeal (DIP) joints. Imaging these joints and other joints of the hand are possible with FMT from the imaging point of view, and are an attractive topic for future research. We believe with a custom designed FMT system for imaging interphalangeal joint, it can be possible to acquire a full dataset in 3-5 minutes or less.

Further, it is foreseeable that the combination of FMT and phase-contrast CT, presented in this work as FMT-PCCT, will be a future direction of

fluorescence tomography. However, the full *in vivo* realization of this technology is perhaps a few years away, as the phase-contrast imaging technology is still in the development phase and is too time consuming.

In conclusion, we developed a framework for efficient processing of FMT or FMT-XCT measurements based on accurate modeling of light propagation in tissue, processing and system calibration, while addressing several numerical challenges. We presented a novel method for compression of FMT data verified, for the first time to our knowledge, to *in vivo* data, thereby significantly reducing the complexity of the system. The fuzzy-based weighted least squares method is a novel approach toward robust inversion of FMT-XCT, which when combined with structured regularization methods, largely improves the reconstruction accuracy, beyond the current state of the art, as verified using several studies. The developed framework enabled several preclinical cancer studies in various organs *in vivo*. Drawing upon the flexibility and potential of the developed processing and algorithmic framework, we presented for the first time hybrid imaging using FMT and phase-contrast CT - a hybrid approach we believe to have a critical role in the future of preclinical molecular imaging. The developed technology and insight allowed us to further expand the scope to clinical applications. We presented signal analysis algorithms for planar ICG-aided imaging of rheumatoid arthritis, enabling significantly improved visibility of target inflammation fluorescence signal and better understanding of signal behavior in human tissue. We further developed hardware and processing methods and algorithms for the first molecular tomographic imaging of synovitis in human finger joints. The clinical results for several patients were corroborated with MRI findings and demonstrated accurate localization of inflammation in finger joints *in vivo* as well as reliable differentiation between healthy and inflamed joints. We believe the presented methods and algorithms further pave the way for wider adaptation of fluorescence imaging and tomography in preclinical as well as clinical scenarios toward better understanding of cancer, drug development, monitoring of personalized therapy and more accurate and earlier clinical diagnosis.

Appendix A

Finite-element integral calculations

As explained in Section 2.3, FEM modeling of light propagation of light in turbid media involves solving several integrals as shown in Equation 2.11-Equation 2.13. Consider a given voxel υ consisting of 4 nodes p_1, p_2, p_3 and p_4. Within this voxel, a spatial basis function ψ_i is assigned to each node p_i, such that for every point in space $\mathbf{r}$, we have

$$\psi_i(\mathbf{r}) = \begin{cases} 1 - \frac{\|\mathbf{r}-p_i\|}{\|q-p_i\|} & \text{if } \mathbf{r} \in \upsilon \\ 0 & \text{else,} \end{cases} \tag{A.1}$$

where q is the intersection of the line formed by points $(\mathbf{r}, p_i)$ and the plane formed by the other three nodes of the voxel.

To solve the FEM problem, it is necessary to find the following integrals within this voxel

$$\begin{aligned} I_1 &= \int_{\upsilon} \psi_j(\mathbf{r})\psi_i(\mathbf{r})\, d\upsilon \\ I_2 &= \int_{\delta} \psi_j(\mathbf{r})\psi_i(\mathbf{r})\, d\delta \\ I_3 &= \int_{\upsilon} \nabla\psi_j(\mathbf{r}).\nabla\psi_i(\mathbf{r})\, d\upsilon, \end{aligned} \tag{A.2}$$

where the second integral is performed over a surface triangle of the voxel shown by δ, and $\nabla\psi_j(\mathbf{r})$ shows the gradient of the spatial basis function $\psi_j(\mathbf{r})$.

A relatively easy way to solve these integrals is to find an affine transform $f(\mathbf{r})$

$$f(\mathbf{r}) = \mathcal{A}\,\mathbf{r} + b, \tag{A.3}$$

such that under this transformation, the voxel v becomes a "unit" tetrahedron v_0 with vertices $(0,0,0)$, $(1,0,0)$, $(0,1,0)$, $(0,0,1)$. The volume of the original voxel is then given as $\frac{1}{6\det\mathcal{A}}$.

The integrals in Equation A.2 can be then rewritten for $f(\mathbf{r})$ instead of for $\mathbf{r}$ and solved instead over this unit tetrahedron. It can be easily shown that the following integrals hold for the unit tetrahedron v_0

$$\int_{v_0} \psi_j(\mathbf{r})\,\psi_i(\mathbf{r})\,dv = \begin{cases} \frac{V_0}{10} & \text{if } i = j \\ \frac{V_0}{20} & \text{if } i \neq j. \end{cases} \tag{A.4}$$

Similarly, for a "unit triangle" τ_0 with vertices $(0,0,0),(1,0,0),(0,1,0)$ we have

$$\int_{\tau_0} \psi_j(\mathbf{r})\psi_i(\mathbf{r})\,d\delta = \begin{cases} \frac{A_0}{6} & \text{if } i = j \\ \frac{A_0}{12} & \text{if } i \neq j. \end{cases} \tag{A.5}$$

A_0 and V_0 represent area and volume of τ_0 and v_0, respectively. These integrals for an arbitrary tetrahedron or triangle are then given as the corresponding value for the unit elements multiplied by the tetrahedron's volume or triangle's area.

The last integral in Equation A.2 can be solved as follows. Under transformation of Equation A.3, we have $\mathbf{r}_0 = \mathcal{A}\,\mathbf{r} + b$ which maps the tetrahedral v to the unit tetrahedral v_0. It can be shown that the basis functions for v_0 denoted by $\psi_i^0(\mathbf{r_0})$ are given as

$$\begin{aligned} \psi_1^0(\mathbf{r_0}) &= 1 - x - y - z \\ \psi_2^0(\mathbf{r_0}) &= x \\ \psi_3^0(\mathbf{r_0}) &= y \\ \psi_4^0(\mathbf{r_0}) &= z, \end{aligned} \tag{A.6}$$

where is it assumed the 1^{st}, 2^{nd}, 3^{rd} and 4^{th} vertices of the tetrahedral falls on $(0,0,0)$, $(1,0,0)$, $(0,1,0)$, $(0,0,1)$, respectively. Since the transformation retains distance ratios and straight lines, $\psi_i(\mathbf{r}) = \psi_i^0(\mathbf{r_0})$. Fur-

thermore, $\nabla\psi_i(\mathbf{r}) = \frac{\delta\,\psi_i(\mathbf{r})}{\delta\,x} + \frac{\delta\,\psi_i(\mathbf{r})}{\delta\,y} + \frac{\delta\,\psi_i(\mathbf{r})}{\delta\,z}$. For a given coordinate x we have

$$\frac{\delta\,\psi_i(\mathbf{r})}{\delta\,x} = \frac{\delta\,\psi_i^0(\mathbf{r_0})}{\delta\,x}. \tag{A.7}$$

By combining Equation A.7 and A.6, we have

$$\begin{aligned}
\frac{\delta\,\psi_1(\mathbf{r})}{\delta\,x} &= \frac{\delta}{\delta\,x}\left(1 - \begin{bmatrix}1 & 1 & 1\end{bmatrix}\mathcal{A}\begin{bmatrix}x\\y\\z\end{bmatrix}\right) = -\underbrace{(\mathcal{A}_1 + \mathcal{A}_2 + \mathcal{A}_3)}_{\mathcal{A}_s} \\
\frac{\delta\,\psi_2(\mathbf{r})}{\delta\,x} &= \frac{\delta}{\delta\,x}\left(\mathcal{A}_1\begin{bmatrix}x & 0 & 0\end{bmatrix}^\top\right) = \mathcal{A}_1(1) \\
\frac{\delta\,\psi_3(\mathbf{r})}{\delta\,x} &= \frac{\delta}{\delta\,x}\left(\mathcal{A}_2\begin{bmatrix}0 & y & 0\end{bmatrix}^\top\right) = 0 \\
\frac{\delta\,\psi_4(\mathbf{r})}{\delta\,x} &= \frac{\delta}{\delta\,x}\left(\mathcal{A}_3\begin{bmatrix}0 & 0 & z\end{bmatrix}^\top\right) = 0,
\end{aligned} \tag{A.8}$$

where $\mathcal{A}_i$ is the i^{th} row of $\mathcal{A}$. The derivatives can be similarly calculated versus y and z. Therefore, Therefore for an arbitrary tetrahedron υ we have

$$\int_{\upsilon} \nabla\psi_j(\mathbf{r}).\nabla\,\psi_i(\mathbf{r})\,d\upsilon = V\,\mathbf{F}(i,j), \tag{A.9}$$

where ∇ denotes the divergence operator, V is the volume of the voxel υ and

$$\mathbf{F} = \begin{bmatrix}\mathcal{A}_s\\\mathcal{A}_1\\\mathcal{A}_2\\\mathcal{A}_3\end{bmatrix}^\top \begin{bmatrix}\mathcal{A}_s\\\mathcal{A}_1\\\mathcal{A}_2\\\mathcal{A}_3\end{bmatrix}. \tag{A.10}$$

Based on these closed-form representations, the integrals for all voxels in are easily calculated, based on which an efficient MATLAB-based implementation of FEM modeling was presented in Section 2.4.

Appendix B

Workflow of the XFMT code

This appendix serves a short manual for working with the XFMT code. The code can be run from within the code folder by invoking the GUI, using the command `XFMT_GUI.m`. The GUI sets up the path. The code is capable of processing datasets acquired the FMT system located at HMGU and the FMT system located at the Klinikum rechts der Isar, as well as the FMT 2500 system. Here we focus on processing data obtained the first two systems; PerkinElmer's data is processed similarly.

Note - *To eliminate the need to redo certain operations, the code saves internal variables at several instances in* `MAT` *files (described below). If one needs to redo these operations, the corresponding* `MAT` *files should be deleted.*

Loading a new dataset – In `load` a new dataset can be loaded by clicking on the corresponding `FMT` file. The code reads all the `FMT` files in the corresponding folder and combines files into a single dataset - it is assumed that the different `FMT` files corresponding to separate gantry angles, as the imaging operation might have been interrupted and resumed. Therefore, the obsolete `FMT` files should be removed. After automatically resolving gantry jitter, the code reads the optical data from `SPE` and `EPI` files and normalizes for laser power and exposure times using the meta-data read from the `FMT` file. The CT dataset is read from the `VFF` file and the user is asked to set the air-tissue threshold and locate the bed bars, if any, using a GUI. The entire combined dataset is then normalized for

laser power and exposure times and saved in a `unifedimport.mat` file. Next, CT preview images are generated (and stored in a `MAT` file), which are maximum intensity projection (MIP) images of the CT volume seen through the CCD camera. The comparison between these CT preview images and the front-illumination images also helps detect calibration problems, if any. A copy of the parameters file, `XFMT_GUI.m` is copied to the folder of the running study. This file can be edited in the next stage, which makes customized processing for a given dataset possible.

Adjusting ROIs – The user now sets several ROIs as seen in Figure B.1: the reconstruction ROI (the red line segment), the light propagation modeling ROI (the yellow line segment) and the detector placement ROI (the cyan line segment). The ROIs can be moved separately or together. Generally, changing the smallest ROI (the reconstruction ROI), changes all other ones accordingly. It is necessary to remove detectors located in undesirable regions; such as over the bars, the bed strings or ears. This is possible using the `Remove detectors` button. Upon `Save detectors` the removed regions are saved in a `MAT` file and applied to future processing of the same dataset as well, at any detector pitch. Any changes made to the `XFMT_Param.m` file should be made at this stage. The segmentation can also be carried out here using the segmentation buttons or in MATLAB using the variable `Geo.Volume`.

Processing – By pressing `Processing` several operations are performed. First, the mesh is generated at the target edge size for the forward modeling ROI and then the forward problem is solved for all surface nodes within the FOV. The inverse problem is solved and the results are shown in the transverse slice panel of the GUI.

Further processing – A useful feature of this code is that it allows reprocessing with modifications of the setting parameters at minimally required effort. Such postprocessing steps, include background subtraction (using the lower right panel), changing the reconstruction resolution, using prior information with different algorithms and parameters, etc.

Viewing, saving and retrieving the results – The results can be viewed in the transverse plane, or in separate MATLAB figures within

a given ROI (purple line segment) for several transverse slices, for any given lambda. The lambda can be set according to the L-curve displayed in the L-curve panel. Upon calling `globals.m`, all structures relevant to the working dataset are made global. The GUI should be closed and the variables saved in a `MAT` file. The `MAT` file can be later loaded into MATLAB and into the GUI, using `Import from workspace`. All specific details and settings of the past processing are loaded and applied to the GUI.

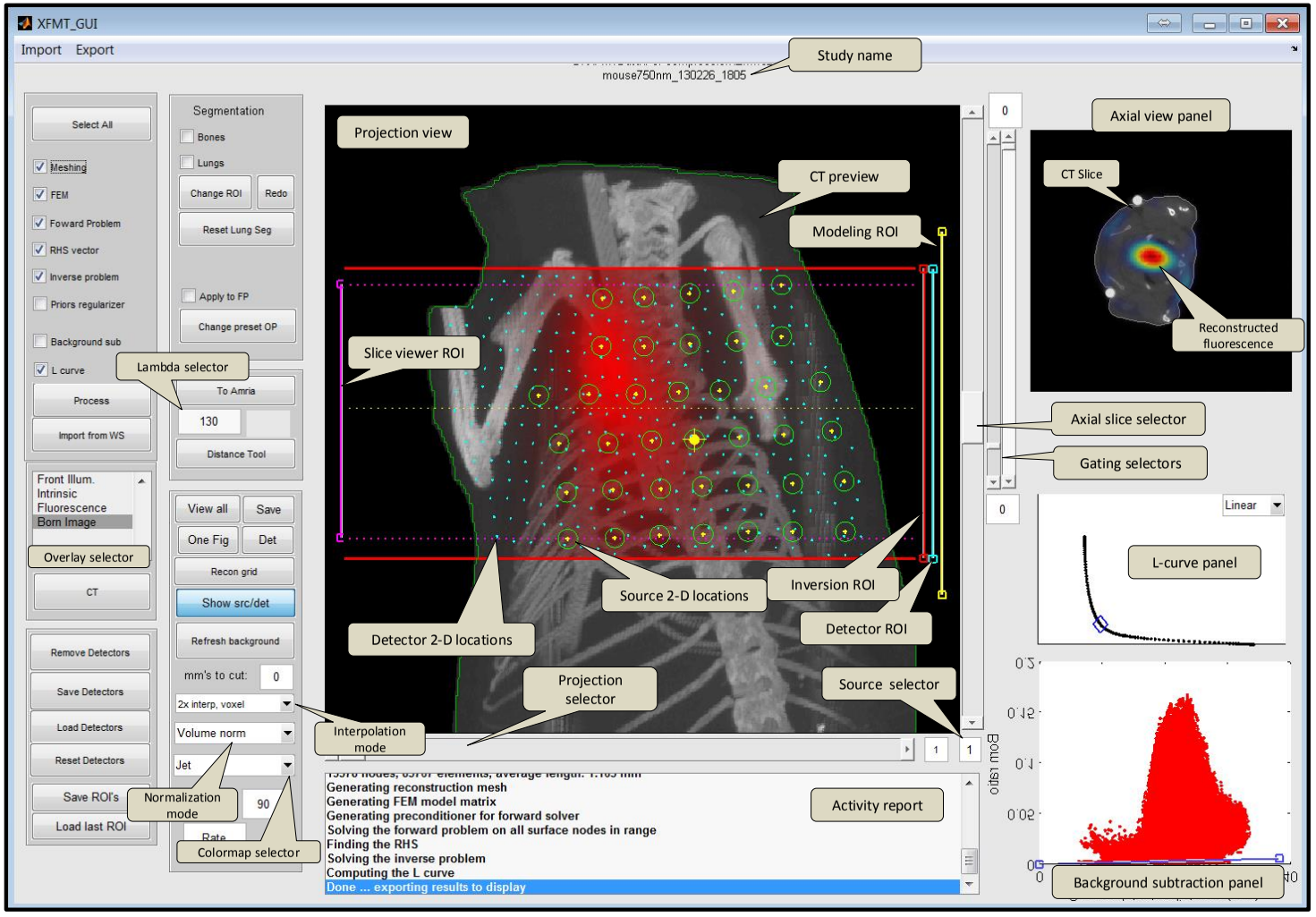

Figure B.1: The graphical user interface (GUI) of the XFMT code; the results are shown for an *ex vivo* dataset containing a fluorescent tube inserted through the esophagus. Various processing units are labeled on the GUI.

Appendix C

Further FMT-XCT processing results

An *in vivo* small animal study involving FMT often consists of the following steps. Animals are normally injected with a nonspecific or specific fluorescent probe targeting specific receptors believed to be expressed in the target lesion or tumor. Every probe has a certain half-life time in tissue which determines an optimal imaging time point. For instance, imaging with ProSense, AngioSense and IntegriSense (PerkinElmer, Waltham MA, USA) should be done 24 hours post injection, while MMPSense 750 Fast (PerkinElmer, Waltham MA, USA) requires an imaging time point of 6 hours post injection. *In vivo* imaging using FMT is carried out under Isoflurane anesthesia. The animals are often sacrificed after one or several imaging sessions and deep frozen in a -80 C freezer for *ex vivo* validation via cryo-sectioning [115] or histological staining.

Furthermore, in many phantom and *ex vivo* experiments it is helpful or necessary to insert a glass tube filled with fluorescent solution in the phantom or in the animal. This can be achieved as follows. A fluorescent solution is produced with desirable concentration solved in a 2% solution of Intralipid. Then a capillary plastic tube is inserted inside a capillary glass tube and the fluorescent solution is inject using a syringe of appropriately thin size at the bottom of the glass tube through the plastic tube. When approximately at desirable length, the plastic tube is pulled out and the liquid at the bottom of the glass tube is forced

to accumulate all at the bottom using a centrifuge device. The same process is followed by using a new plastic tube to seal off the top of the fluorescent solution with a thin drop of oil (such microscope oil) and the same process is repeated to fill the rest of the tube with 2% Intralipid (with no fluorescence). To insert the tube through the esophagus of a mouse post-mortem, the mouse is placed in supine position before rigor mortis and the tongue is pulled out using a pair of tweezers and the glass tube is inserted with the closed end first. For an adult CD1 mouse, the tube is expected to penetrate up to 3 cm inside the body.[1]

In Section 7.2 we demonstrated tomographic imaging of specific uptake of IntegriSense 680 in the pancreas of a PDAC model. In this appendix, we demonstrate further tomographic imaging results for other *in vivo* studies, processed using the proposed numerical and algorithmic framework. Here we demonstrate three other processing case studies to substantiate the potential of the developed framework.

– **Tomographic imaging of scVEGF\Cy in tumor xenografts**[2]

Vascular endothelial growth factor (VEGF) is a signaling protein which plays an important role in angiogenesis, i.e. the process of blood vessels formation. By binding to VEGF receptors, VEGF leads to expansion of tumor vasculature by promoting angiogenic signaling [174]. Several therapeutic approaches aim at inhibition of VEGF signaling. Success of these approaches often relies on ability to extract information about vascularization processes *in vivo* by using VEGF as an imaging target. Here we present the results of imaging the biodistribution of a single-chain Cys-tagged VEGF, labeled with Cy5.5 (scVEGF\Cy), as the fluorescent probe binding to cell-surface receptors of VEGF. Figure C.1 demonstrates *in vivo* imaging of scVEGF\Cy distribution in a CD1 nude mouse injected subcutaneously on the dorsal side with HT-29 human colorectal

[1] The author appreciates Dr. Nikolaos Deliolanis for instructions.

[2] The imaging results are presented in V. Ermolayev, et al. "Non-invasive *in vivo* and *ex vivo* imaging and quantification of scVEGF\Cy distribution in tumor xenografts", to be submitted. Further technical details regarding the biology, model and probe can be found there. The FMT imaging, animal preparation and cryo-sectioning were carried out by Dr. Vladimir Ermolayev and Dr. Angelique Ale and FMT-XCT processing and image generation was carried out by the author at HMGU using the XFMT code. Results are reproduced with permission from Dr. Vladimir Ermolayev.

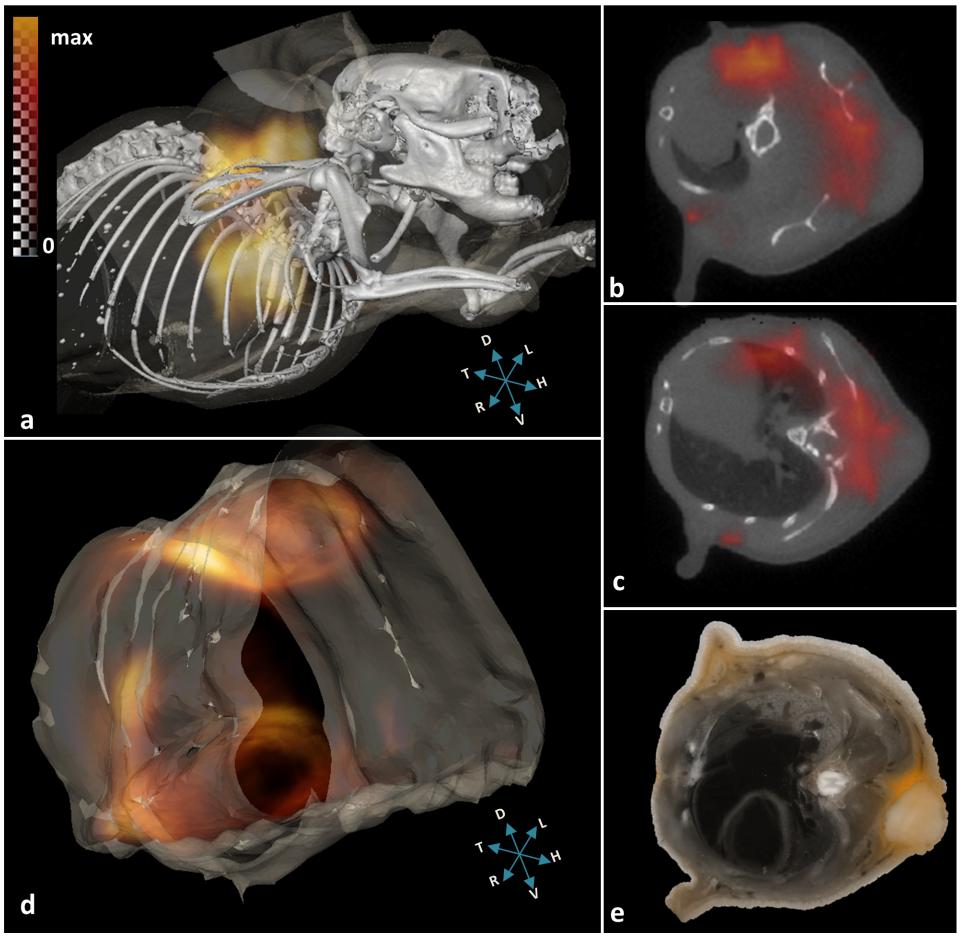

Figure C.1: Tomographic imaging of scVEGF\Cy accumulation in tumor xenograft; (a) 3-D reconstruction of scVEGF\Cy fluorescence, (b, c) FMT-XCT slices showing fluorescence accumulation just underneath the tumor, (d) 3-D demonstration of fluorescence signal measured *ex vivo* via cryo-sectioning and (e) *ex vivo* validation as fluorescence image over grayscale cryo-section.

carcinoma cells. FMT-XCT reconstructions, corroborated with *ex vivo* validations, demonstrate specific distribution of scVEGF\Cy inside and on the periphery of the subcutaneous tumor xenograft. No anatomical priors were used in the inversion.

– **Tomographic imaging of internal hemorrhages in Aga2\+ mutant mice**[3]

[3] The imaging results are presented in V. Ermolayev, et al., "*Ex vivo* assessment and non-invasive *in vivo* imaging of internal hemorrhages in Aga2\+ mutant mice", Biochem Biophys Res Commun, 2013. 432(2). The FMT imaging, animal preparation and cryo-sectioning were carried out by Dr. Vladimir Ermolayev and Dr.

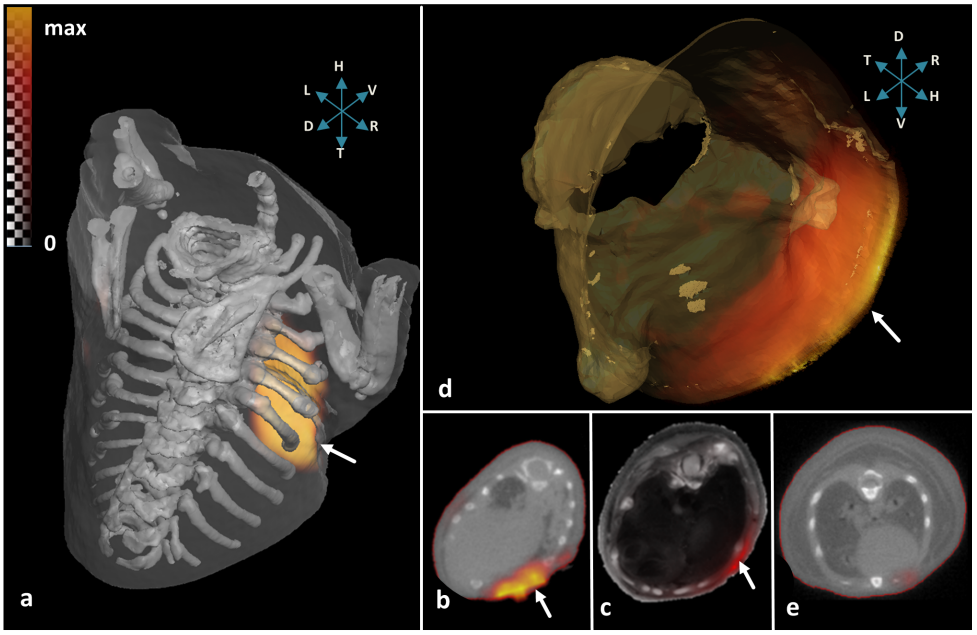

Figure C.2: Tomographic imaging of internal hemorrhages in a Aga2\+ mutant mouse; (a) 3-D demonstration showing high fluorophore concentration (pointed to by arrows) indicating active bleeding sites reconstructed in the periphery of thorax area of a 9 day old severely affected Aga2\+ mouse, (b) 2-D demonstration as fluorescence over CT slice (c) *ex vivo* validation via cryo-sectioning where the red signal shows strong fluorescence, (d) 3-D reconstruction of fluorescence cryo-sections and (e) FMT reconstruction for a 9-day wild type, where the reconstructed signal is negligible.

As a part of a study to understand the development of osteogenesis imperfecta [79], Aga2\+ mouse models of osteogenesis imperfecta [175] were imaged using FMT. Wild types and Aga\+ mice of different ages were intraperitoneally injected with AngioSense (a blood pooling agent, PerkinElmer, M.A.) and imaged with FMT-XCT 1.5-2 hours post injection. Hemorrhages in the thorax area of wild type mice as well as Aga2/+ were studied by imaging the fluorescence emanating from AngioSense accumulation in affected sites. The results for a 9 day old Aga2\+ mutant mouse presented in Figure C.2, demonstrated active internal bleeding only in the periphery of thorax.

Angelique Ale and FMT-XCT processing and image generation were carried out by the author at HMGU using the XFMT code. Results are reproduced with permission from Dr. Vladimir Ermolayev.

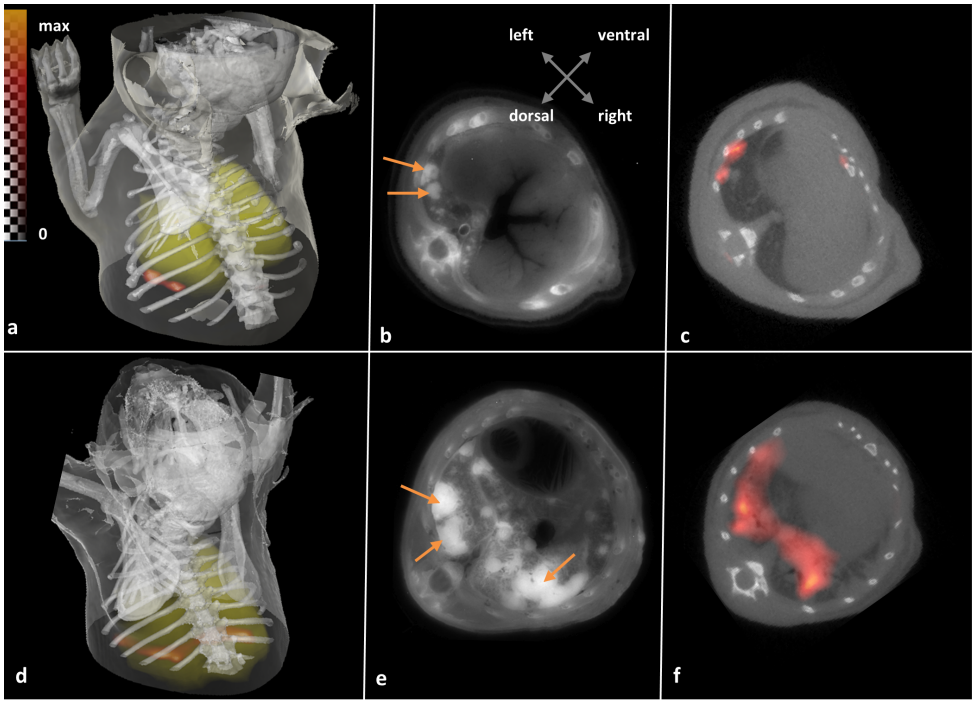

Figure C.3: Detection of lung tumors in KRAS mice; (a) 3-D representation of FMT-XCT imaging results of a 4 week old KRAS mouse, (b) *ex vivo* validation as a fluorescence image of the cryo-section with the arrows pointing to the tumors, (c) an FMT-XCT slice as fluorescence signal laid over the CT slice, (d-f) corresponding results for an 18 week old KRAS with larger tumors. The lungs are shown in (a) and (d) by green color.

– **Tomographic lung imaging in transgenic KRAS mice**[4]

FMT-XCT was employed toward *in vivo* detection early malignant lung tumors by targeting integrins as early cancer markers. Integrin $\alpha_v\beta_3$ is in particular expressed in transgenic KRAS models of lung cancer [176]. Figure C.3 presents the result of imaging a 4 week and an 18 week old mouse injected with IntegriSense 680 as the fluorescent probe. IntegriSense 680 (PerkinElmer, Waltham MA, USA) is a fluorescent probe with peak excitation at 675 nm and peak fluorescence at 700 nm and specifically targets integrin $\alpha_v\beta_3$. The *in vivo* imaging results along with the *ex vivo* valida-

[4] The imaging results are presented in V. Ermolayev, et al., "Early recognition of lung cancer by integrin targeted imaging in KRAS mouse model", submitted. The FMT imaging, animal preparation and cryo-sectioning were carried out by Dr. Vladimir Ermolayev and Dr. Angelique Ale and FMT-XCT processing and image generation were carried out by the author at HMGU using the XFMT code. Results are reproduced with permission from Dr. Vladimir Ermolayev.

tions demonstrate the imaging potential for very small tumors as well as metastasized lesions. Anatomical priors were employed in the reconstruction.

Appendix D

Tomographic imaging of synovitis - further case studies

Tomographic imaging of synovitis in human finger joints *in vivo* was presented in Chapter 9. The results were shown for 1 patient and 1 healthy volunteer. In this appendix we present imaging results for one other healthy volunteer (the results from the two other volunteer equally present no conspicuous signal as quantified in Table 9.2 and are hence not shown here) and the other 4 patients. In the figures below, the FMT reconstructions are shown both in 3-D form as 2-D projections. The 2-D projections consist of maximum intensity projections (MIP) in transverse, coronal and sagittal planes, superimposed as transparency color images (using MATLAB's "jet colormap") over, respectively, the corresponding transverse volume slice, the front-illumination photograph of the dorsal side and the front-illumination photograph of the left or right sagittal side. The transverse MIP is taken within a 5 mm span around the "crease location", denotes as the MIP ROI. For patients the FMT transverse MIP slices are coregistered with corresponding transverse MR images, as described in Section 9.4.4. The locations of the MR transverse images in the coronal planes are also shown. The notations and markers otherwise follow those depicted in Figure 9.5 and are not repeated for brevity.

Further processing details are also provided here for completeness. As mentioned in Section 9.2, the acquisition method was slightly different for the first two female volunteers. Specifically, for these volunteers there

was only one front-illumination acquisition performed during the imaging (i.e. using the older acquisition method described in Section 3.4). The compensation of the temporal decay of ICG was performed for all subjects accordingly to the respective fluorescence-intrinsic total acquisition times (i.e. ignoring the first illumination set). Moreover, for these subjects there fluorescence exposure time was 150 ms (instead of 200 ms for the other subjects) and the laser powers were also slightly different (i.e. 86 and 241 mW instead of 97 and 184 mW). These differences between laser powers and exposure times were taken into account for equal scaling the reconstructions across all subjects. All reconstruction were further clipped at 0.25 of their respective maxima. For the patient presented in Figure D.4, 14 projections were used due to mechanical blocking of the gantry movement by the hand. Lastly, the MIP demonstrations in figures below and Figure 9.5 and Figure 9.6 were performed after interpolating the reconstructed values of the rectilinear reconstruction grid voxels from the grid nodes in the transverse plane using the 2×2 kernel of $\begin{pmatrix} 0.25 & 0.25 \\ 0.25 & 0.25 \end{pmatrix}$.

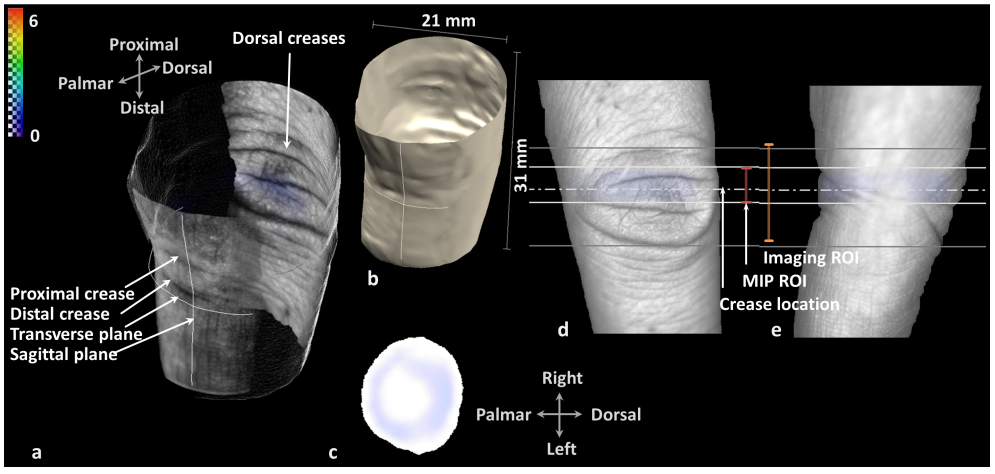

Figure D.1: FMT imaging results of the 3rd left PIP joint of a 33 year old male healthy volunteer; (a) 3-D representation of the reconstruction fluorescence (b) isosurface of the reconstructed volume, (c) MIP projection of the FMT signal in the transverse plane as a transparency color image with jet colormap on a white volume slice, (d) and (e) MIP projections in the coronal and sagittal planes.

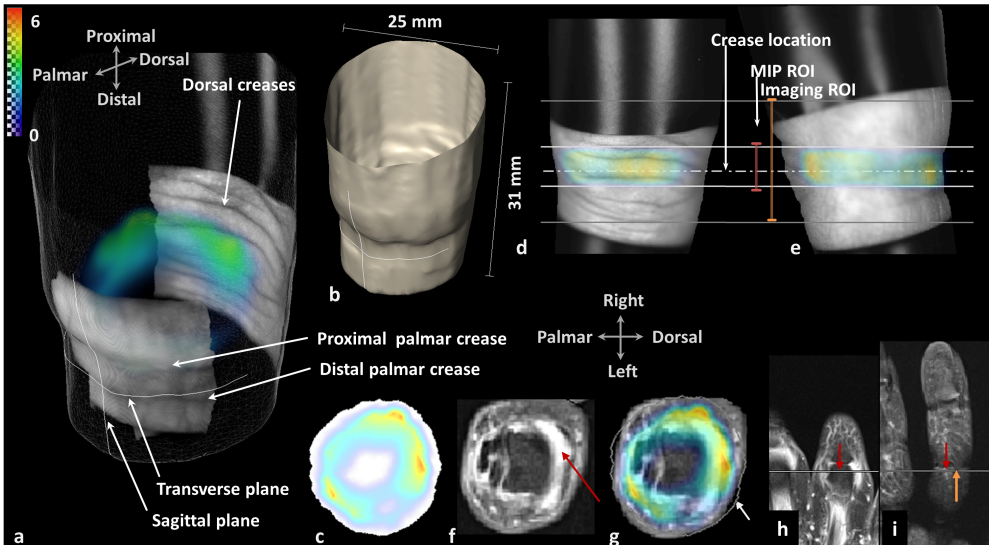

Figure D.2: FMT imaging results of the 2nd right PIP joint (with MR synovitis score of 2) of a 67 year old female patient; (a) 3-D fluorescence reconstruction, (b) isosurface of the reconstructed volume, (c) FMT MIP projection, (d) and (e) coronal and sagittal MIP projections, (f) the corresponding transverse MR image, where the red arrow point to the inflammations, (g) coregistered image between the FMT MIP image and the MR transverse image, (h) and (i) MR images in two coronal planes.

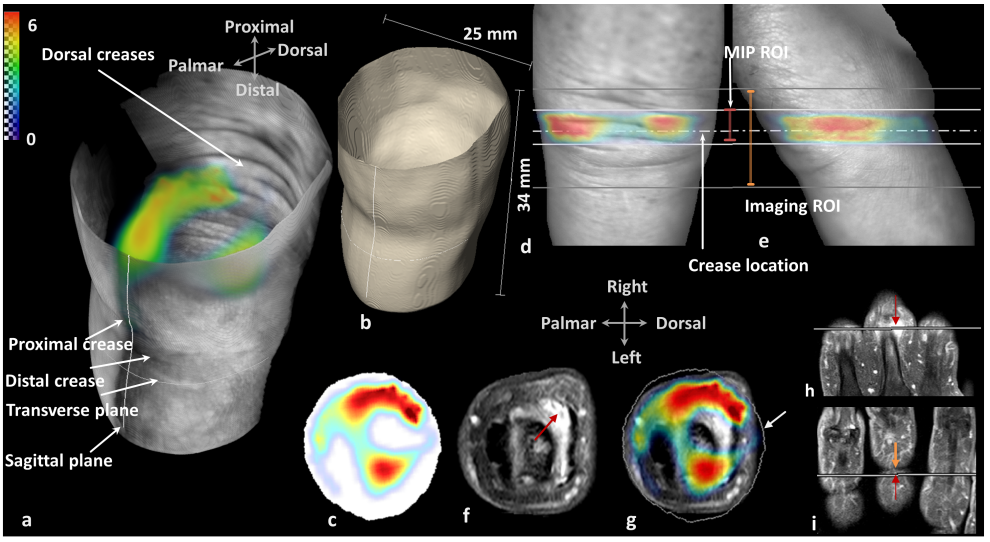

Figure D.3: FMT imaging results of the 3rd right PIP joint (with MR synovitis score of 3) of a 75 year old female patient; (a) 3-D fluorescence reconstruction, (b) reconstructed volume, (c) transverse MIP projection, (d) and (e) coronal and sagittal MIP projections, (f) transverse MR image, (g) coregistered image between the FMT MIP image and the MR transverse image, (h) and (i) MR images in two coronal planes.

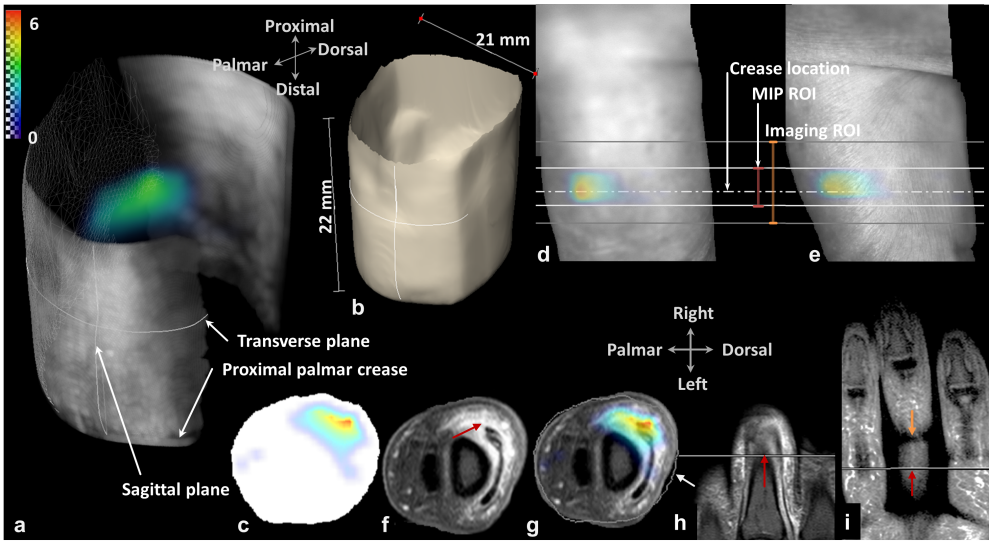

Figure D.4: FMT imaging results of the 3rd left PIP joint (with MR synovitis score of 3) of a 73 year old female patient; (a) 3-D fluorescence reconstruction, (b) reconstructed volume, (c) transverse MIP projection, (d) and (e) coronal and sagittal MIP projections, (f) transverse MR image, where the red arrow points to the inflammations, (g) coregistered image between the FMT MIP image and the MR transverse image, (h) and (i) MR images in two coronal planes.

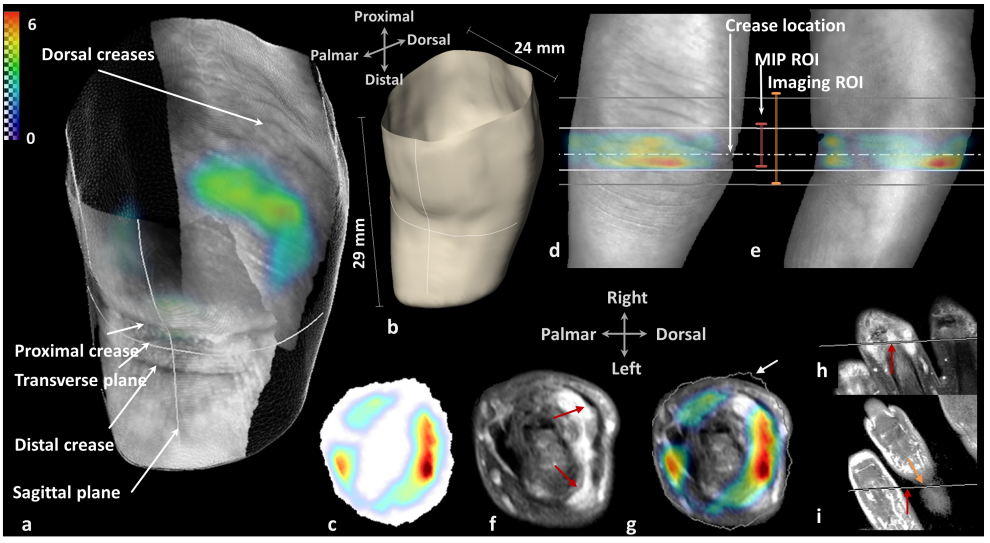

Figure D.5: FMT imaging results of the 3rd right PIP joint (MR score of 3) of a 67 year old female patient; (a) 3-D fluorescence reconstruction, (b) reconstructed volume, (c) transverse MIP projection, (d) and (e) coronal and sagittal MIP projections, (f) transverse MR image, (g) coregistered image between the FMT MIP image and the MR transverse image, (h) and (i) MR images in two coronal planes.

Publications overview

(journal papers since 2010 at TUM, pertaining to this work)

- **P. Mohajerani**, M. Koch, K. Thürmel, E. J. Rummeny, V. Ntziachristos, R. Meier, "*Fluorescence-aided tomographic imaging of synovitis in the human finger*", Radiology, vol. 272, 2014.
- **P. Mohajerani**, A. Hipp, M. Willner, M. Marschner, X. Ma, M. Trajkovic-Arsic, M. Koch, K. Radrich, N. C. Burton, A. Ale, V. Ermolayev, J. T. Siveke, M. Bech, F. Pfeiffer, V. Ntziachristos,"*FMT-PCCT: Hybrid fluorescence molecular tomography- X-ray phase-contrast CT imaging of mouse models*", IEEE Transactions of Medical Imaging, vol. 33, 2014.
- **P. Mohajerani** and V. Ntziachristos, "*Compression of Born ratio for fluorescence molecular tomography/x-ray computed tomography hybrid imaging: methodology and in vivo validation*", Optics Letters, vol. 38, num. 13, p. 2324-2326, 2013.
- **P. Mohajerani**, R. Meier, P. B. Noël, E. J. Rummeny and V. Ntziachristos, "*Spatiotemporal analysis for ICG-aided imaging of rheumatoid arthritis in hand joints*", Journal of Biomedical Optics 18(9), 097004, 2013.
- **P. Mohajerani**, Stratis Tzoumas, Amir Rosenthal and V. Ntziachristos,"*Optical and optoacoustic model-based tomography of tissue biomarkers*", submitted 2014.
- **P. Mohajerani** and V. Ntziachristos,"*Weighted least squares inversion for fluorescence molecular tomography*", to be submitted 2014.

- K. Radrich, **P. Mohajerani**, J. Bussemer, M. Schwaiger, A. Beer, V. Ntziachristos, "*Hybrid fluorescence molecular tomography of multiple molecules*", Journal of Biomedical Optics, vol. 19, issue 4, 2014.
- M. Trajkovic-Arsic, **P. Mohajerani**, A. Sarantopoulos, E. Kalideris, K. Steiger, I. Esposito, X. Ma, G. Themelis, N. C. Burton, C. W. Michalski, J. Kleeff, S. Stangl, A. J. Beer, K. Pohle, H. J. Wester, R. M. Schmid, R. Braren, V. Ntziachristos and J. T. Siveke, "*Molecular imaging of integrin $\alpha_v\beta_3$ for in vivo detection of precursor lesions and pancreatic cancer*", Journal of Nuclear Medicine, vol. 55, 2014.
- V. Ermolayev, Christian M. Cohrs, **P. Mohajerani**, A. Ale, M. Hrabé de Angelis, V. Ntziachristos, "*Ex-vivo assessment and non-invasive in vivo imaging of internal hemorrhages in Aga2/+ mutant mice*", Biochem. Biophys. Res. Comm. 432, p. 389-393, 2013.
- V. Ermolayev, **P. Mohajerani**, A. Ale, N. Deliolanis, S. K. Sarkar, M. Backer, J. M. Backer and V. Ntziachristos, "*Non-invasive in vivo and ex vivo imaging and quantification of scVEGF/Cy distribution in tumor xenografts*", to be submitted.
- V. Ermolayev, **P. Mohajerani**, A. Ale, A. Sarantopoulos, M. Aichler, G. Kayser, A. Walch and V. Ntziachristos, "*Early recognition of lung cancer by integrin targeted imaging in K-ras mouse model*", submitted.

Abbreviations and acronyms

2-D	Two-dimensional
3-D	Three-dimensional
CCD	Charge-coupled device
CG	Conjugate gradient
CT	Computed tomography
CW	Continuous wave
DA	Diffusion approximation
DE	Diffusion equation
DS	Data-specific
DIP	Distal interphalangeal
DOT	Diffuse optical tomography
EFI	Epi-illumination fluorescence imaging
FEM	Finite element methods
FIS	Fuzzy inference system
FWLS	Fuzzy-based weighted least squares
FMT	Fluorescence molecular tomography
FOV	Field of view
GF	Green's function
GUI	Graphical user interface

HMGU Helmholtz Zentrum München – Deutsches Forschungszentrum für Gesundheit und Umwel

IBMI Institute for biological and medical imaging

ICG Indocyanine green

IG Information gain

K-L Kullback-Leibler

LSQR Least squares method

MCP Metacarpophalangeal

MIP Maximum intensity projection

MRI Magnetic resonance imaging

NIR Near-infrared

PCA Principal component analysis

PCCT Phase-contrast X-ray computed tomography

PDAC Pancreatic ductal adenocarcinoma

PIP Proximal interphalangeal

RA Rheumatoid arthritis

RMS Root mean square

ROC Receiver operator characteristic curve

ROI Region of interest

RTE Radiative transfer equation

SVD Singular value decomposition

TUM Technische Universität München

WLS Weighted least squares

XCT X-ray computed tomography

XFMT Fluorescence molecular tomography/X-ray CT, used to refer to the processing framework developed and presented here

List of Figures

List of Tables

Bibliography

[1] V. Ntziachristos. Going deeper than microscopy: the optical imaging frontier in biology. Nature Methods, 7(8):603–614, 2010.

[2] V. Ntziachristos, C. Bremer, E. E. Graves, J. Ripoll, and R. Weissleder. In vivo tomographic imaging of near-infrared fluorescent probes. Molecular Imaging, 1(2):82–88, 2002.

[3] J. C. Hebden, S. R. Arridge, and D. T Delpy. Optical imaging in medicine: I. experimental techniques. Physics in medicine and biology, 42(5):825, 1997.

[4] S. R. Arridge and J. C. Hebden. Optical imaging in medicine: Ii. modelling and reconstruction. Physics in Medicine and Biology, 42(5):841, 1997.

[5] M. S Patterson, B. Chance, B. C. Wilson, et al. Time resolved reflectance and transmittance for the non-invasive measurement of tissue optical properties. Appl. Opt, 28(12):2331–2336, 1989.

[6] S. R. Arridge. Optical tomography in medical imaging. Inverse Problems, 15(2):41–93, 1999.

[7] V. Ntziachristos, J. Ripoll, L. V. Wang, and R. Weissleder. Looking and listening to light: The evolution of whole-body photonic imaging. Nature Biotechnology, 23(3):313–320, 2005.

[8] A. P. Gibson, J. C. Hebden, and S. R. Arridge. Recent advances in diffuse optical imaging. Physics in Medicine and Biology, 50(4):1–43, 2005.

[9] S. A. Hilderbrand and R. Weissleder. Near-infrared fluorescence: application to in vivo molecular imaging. Curr Opin Chem Biol, 14(1):71–9, 2010.

[10] R. Weissleder and V. Ntziachristos. Shedding light onto live molecular targets. Nature Medicine, 9(1):123–128, 2003.

[11] V. Ntziachristos. Going deeper than microscopy: the optical imaging frontier in biology. Nat Methods, 7(8):603–14, 2010.

[12] K. Licha. Contrast agents for optical imaging. Topics in Current Chemistry, 222:1–29, 2002.

[13] Andreas H. Hielscher. Optical tomographic imaging of small animals. Current Opinion in Biotechnology, 16(1 SPEC ISS):79–88, 2005.

[14] Gratzer W. B. and Kollias N. Personal communication. Technical report, Med. Res. Council Labs.

[15] N. Kollias. Personal communication. Technical report, Wellman Laboratories, Harvard Medical School.

[16] G. M. Hale and M. R. Querry. Optical constants of water in the 200-nm to 200-µm wavelength region. Appl. Opt., 12(3):555–563, Mar 1973.

[17] Vasilis Ntziachristos. Fluorescence molecular imaging. Annual Review of Biomedical Engineering, 8:1–33, 2006.

[18] R. Weissleder. A clearer vision for in vivo imaging. Nature Biotechnology, 19:316–317, 2001.

[19] C. Bremer, C. H. Tung, and R. Weissleder. In vivo molecular target assessment of matrix metalloproteinase inhibition. Nature Medicine, 7:743–748, 2001.

[20] R. Weissleder. Molecular imaging in cancer. Science, 312(5777):1168–1171, 2006.

[21] V. Ntziachristos, G. Turner, J. Dunham, Stephen W., A. Soubret, J. Ripoll, and H. A. Shih. Planar fluorescence imaging using normalized data. Journal of Biomedical Optics, 10(6):064007, 2005.

[22] C. Kim, K. H. Song, F. Gao, and L. V. Wang. Sentinel lymph nodes and lymphatic vessels: Noninvasive dual - modality in vivo mapping by using indocyanine green in rats - volumetric spectroscopic photoacoustic imaging and planar fluorescence imaging 1. Radiology, 255(2):442–450, 2010.

[23] S. G. Werner, H. E. Langer, S. Ohrndorf, M. Bahner, P. Schott, C. Schwenke, M. Schirner, H. Bastian, G. Lind-Albrecht, B. Kurtz, G. R. Burmester, and M. Backhaus. Inflammation assessment in patients with arthritis using a novel in vivo fluorescence optical imaging technology. Annals of the Rheumatic Diseases, 71(4):504–510, 2012.

[24] E. M. Sevick-Muraca and J. C. Rasmussen. Molecular imaging with optics: primer and case for near-infrared fluorescence techniques in personalized medicine. Journal of biomedical optics, 13(4):041303–041303, 2008.

[25] A. Ale, V. Ermolayev, E. Herzog, C. Cohrs, M. H. de Angelis, and V. Ntziachristos. FMT-XCT: in vivo animal studies with hybrid fluorescence molecular tomography-x-ray computed tomography. Nat Methods, 9(6):615–20, 2012.

[26] A. Corlu, R. Choe, T. Durduran, M. A. Rosen, M. Schweiger, S. R. Arridge, M. D. Schnall, and A. G. Yodh. Three-dimensional in vivo fluorescence diffuse optical tomography of breast cancer in humans. Optics Express, 15(11):6696–6716, 2007.

[27] R. Meier, K. Thuermel, P. Moog, P. Noel, C. Ahari, M. Sievert, F. Dorn, S. Waldt, C. Schaeffeler, D. Golovko, B. Haller, C. Ganter, S. Weckbach, K. Woertler, and E. J. Rummeny. Detection of synovitis in the hands of patients with rheumatologic disorders: Diagnostic performance of optical imaging in comparison with magnetic resonance imaging. Arthritis & Rheumatism, 64(8):2489–2498, 2012.

[28] V. Ntziachristos, A. Yodh, M. Schnall, X. Ma, and B. Chance. Calculation of local optical properties in highly scattering media using a-priori structural information for application to simultaneous nir-mr breast examination. Proceedings of SPIE - The International Society for Optical Engineering, 3566:200–206, 1999.

[29] M. Guven, B. Yazici, X. Intes, and B. Chance. Diffuse optical tomography with a priori anatomical information. Physics in Medicine and Biology, 50(12):2837–2858, 2005.

[30] A. Da Silva, M. Leabad, T. Bordy, J. M. Dinten, P. Peltie, and P. Rizo. X-ray and optical multimodality tomographer for small animal examination. volume 6431 of Progress in Biomedical Optics and Imaging - Proceedings of SPIE, page 64310. SPIE - International Society for Optical Engineering, Bellingham WA, WA 98227-0010, United States.

[31] F. Stuker, C. Baltes, K. Dikaiou, D. Vats, L. Carrara, E. Charbon, J. Ripoll, and M. Rudin. Hybrid small animal imaging system combining magnetic resonance imaging with fluorescence tomography using single photon avalanche diode detectors. IEEE Trans Med Imaging, 30(6):1265–73, 2011.

[32] R. B. Schulz, A. Ale, A. Sarantopoulos, M. Freyer, E. Soehngen, M. Zientkowska, and V. Ntziachristos. Hybrid system for simultaneous fluorescence and x-ray computed tomography. IEEE Transactions on Medical Imaging, 29(2):465–473, 2010.

[33] S. R. Arridge, M. Schweiger, M. Hiraoka, and D. T. Delpy. A finite element approach for modeling photon transport in tissue. Medical Physics, 20:299, 1993.

[34] Huabei Jiang. Optical image reconstruction based on the third-order diffusion equations. Optics Express, 4(8):241–246, 1999.

[35] Z. Yuan, Q. Zhang, E. Sobel, and H. Jiang. Comparison of diffusion approximation and higher order diffusion equations for optical tomography of osteoarthritis. J Biomed Opt, 14(5):054013, 2009.

[36] Edgar Scherleitner and Bernhard G. Zagar. Optical tomography imaging based on higher order born approximation of diffuse photon density waves. IEEE Transactions on Instrumentation and Measurement, 54(4):1607–1611, 2005.

[37] M. Schweiger, S. R. Arridge, M. Hiraoka, and D. T. Delpy. The finite element method for the propagation of light in scattering media: Boundary and source conditions. Medical Physics, 22:1779, 1995.

[38] S. R. Arridge, M. Cope, and D. T. Delpy. The theoretical basis for the determination of optical pathlengths in tissue: temporal and frequency analysis. Phys Med Biol, 37(7):1531–60, 1992.

[39] J. Ripoll, V. Ntziachristos, R. Carminati, and M. Nieto-Vesperinas. Kirchhoff approximation for diffusive waves. Physical Review E. Statistical Physics, Plasmas, Fluids, and Related Interdisciplinary Topics, 64(5 I):051917–1, 2001.

[40] B. C. Wilson and G. Adam. A monte-carlo model for the absorption and flux distributions of light in tissue. Medical Physics, 10(6):824–830, 1983.

[41] M. R. Hestenes and E. Stiefel. Methods of Conjugate Gradients for Solving Linear Systems. Journal of Research of the National Bureau of Standards, 49:409–436, December 1952.

[42] Douglas N Arnold. A concise introduction to numerical analysis. Institute for Mathematics and its Applications, Minneapolis, 2001.

[43] P. Alliez, L. Rineau, S. Tayeb, J. Tournois, and M. Yvinec. 3d mesh generation. 2012.

[44] Q. Q. Fang and D. A. Boas. Tetrahedral mesh generation from volumetric binary and gray-scale images. 2009 IEEE International Symposium on Biomedical Imaging: From Nano to Macro, Vols 1 and 2, pages 1142–1145, 2009.

[45] Jorge Ripoll. Light diffusion in turbid media with biomedical application. PhD thesis, PhD Thesis, University of Madrid, 2000.

[46] G. Strang P. O. Persson. A simple mesh generator in matlab. SIAM Rev., 46(2), 2004.

[47] P. Mohajerani, A. A. Eftekhar, J. Huang, and A Adibi. Optimal sparse solution for fluorescent diffuse optical tomography: Theory and phantom experimental results. Applied Optics, 46(10):1679–1685, 2007.

[48] Huabei Jiang. Frequency-domain fluorescent diffusion tomography: a finite-element-based algorithm and simulations. Applied Optics, 37(22):5337, 1998.

[49] D. Hyde, R. Schulz, D. Brooks, E. Miller, and V. Ntziachristos. Performance dependence of hybrid x-ray computed tomography/fluorescence molecular tomography on the optical forward problem. Journal of the Optical Society of America a-Optics Image Science and Vision, 26(4):919–923, 2009.

[50] V. Ntziachristos and R. Weissleder. Experimental three-dimensional fluorescence reconstruction of diffuse media by use of a normalized born approximation. Optics Letters, 26(12):893–895, 2001.

[51] A. Soubret, J. Ripoll, and V. Ntziachristos. Accuracy of fluorescent tomography in the presence of heterogeneities: study of the normalized born ratio. Medical Imaging, IEEE Transactions on, 24(10):1377–1386, 2005.

[52] T. A. Clarke and J. G. Fryer. The development of camera calibration methods and models. Photogrammetric Record, 16(91):51–66, 1998.

[53] Tatjana Wunderlich. Optimization, calibration and noise reduction in a hybrid system for fluorescence and x-ray tomography[diploma thesis]. 2009.

[54] M. Grant and S. Boyd. Cvx: Matlab software for disciplined convex programming, version 2.0 beta, 2012.

[55] M. Grant and S. Boyd. Graph implementations for nonsmooth convex programs, Recent Advances in Learning and Control (a tribute to M. Vidyasagar), chapter 95-110. Springer, 2008.

[56] B. W. Pogue, T. O. McBride, C. Nwaigwe, U. L. Osterberg, J. F. Dunn, and K. D. Paulsen. Near-infrared diffuse tomography with a priori mri structural information: testing a hybrid image reconstruction methodology with functional imaging of the rat cranium. Proceedings of SPIE - The International Society for Optical Engineering, 3597:484–492, 1999.

[57] R. B. Schulz, A. Ale, A. Sarantopoulos, M. Freyer, E. Sohngen, M. Zientkowska, and V. Ntziachristos. Hybrid fluorescence tomography/x-ray tomography improves reconstruction quality. Molecular Imaging Ii, 7370, 2009.

[58] A. Ale, R. B. Schulz, A. Sarantopoulos, and V. Ntziachristos. Imaging performance of a hybrid x-ray computed tomography-fluorescence molecular tomography system using priors. Medical Physics, 37(5):1976–1986, 2010.

[59] R. B. Schulz M. Zientkowska K. H. Englmeier M. Freyer, A. Ale and V. Ntziachristos. Fast automatic segmentation of anatomical structures in x-ray computed tomography images to improve uorescence molecular tomography reconstruction. Journal of Biomedical Optics, 15(3), 2010.

[60] E. F. Kaasschieter. Preconditioned conjugate gradients for solving singular systems. Journal of Computational and Applied Mathematics, 24(1):265–275, 1988.

[61] A. Soubret and V. Ntziachristos. Fluorescence molecular tomography in the presence of background fluorescence. Physics in Medicine and Biology, 51(16):3983–4001, 2006.

[62] M. Gao, G. Lewis, G. M. Turner, A. Soubret, and V. Ntziachristos. Effects of background fluorescence in fluorescence molecular tomography. Applied Optics, 44(26):5468–5474, 2005.

[63] A. Ale, V. Ermolayev, N. C. Deliolanis, and V. Ntziachristos. Fluorescence background subtraction technique for hybrid fluorescence molecular tomography/x-ray computed tomography imaging of a mouse model of early stage lung cancer. J Biomed Opt, 18(5):56006, 2013.

[64] S. R Arridge and W. R. B. Lionheart. Nonuniqueness in diffusion-based optical tomography. Optics Letters, 23(11):882–884, 1998.

[65] E. E. Graves, J. Ripoll, R. Weissleder, and V. Ntziachristos. A submillimeter resolution fluorescence molecular imaging system for small animal imaging. Medical Physics, 30(5):901–11, 2003.

[66] P. Mohajerani, A. A. Eftekhar, J. Huang, and A. Adibi. Sparse soluton for fluorescent diffuse optical tomography systems: Phantom results. In Lasers & Electro-Optics Society, IEEE, pages 166–167.

[67] J. Dutta, S. Ahn, C. Li, S. R. Cherry, and R. M. Leahy. Joint l1 and total variation regularization for fluorescence molecular tomography. Phys Med Biol, 57(6):1459–76, 2012.

[68] G. H. Golub, P. C. Hansen, and D. P. O'Leary. Tikhonov regularization and total least squares. SIAM J. Matrix Anal. Appl., 21:185–194, 1999.

[69] C.C. Paige and M.A. Saunders. Lsqr: An algorithm for sparse linear equations and sparse least squares. TOMS, 8(1):43–71, 1982.

[70] G. Boverman, Q. Fang, S. A. Carp, E. L. Miller, D. H. Brooks, J. Selb, R. H. Moore, D. B. Kopans, and D. A. Boas. Spatio-temporal imaging of the hemoglobin in the compressed breast with diffuse optical tomography. Physics in Medicine and Biology, 52(12):3619–3641, 2007.

[71] J. C. Baritaux, K. Hassler, and M. Unser. An efficient numerical method for general l(p) regularization in fluorescence molecular tomography. IEEE Trans Med Imaging, 29(4):1075–87, 2010.

[72] D. Hyde, E. L. Miller, D. H. Brooks, and V. Ntziachristos. Data specific spatially varying regularization for multimodal fluorescence molecular tomography. IEEE Transactions on Medical Imaging, 29(2):365–374, 2010.

[73] D. Hyde, E. Miller, D. Brooks, and V. Ntziachristos. New techniques for data fusion in multimodal fmt-ct imaging. 2008 IEEE International Symposium on Biomedical Imaging: From Nano to Macro, Vols 1-4, pages 1597–1600, 2008.

[74] S. C. Davis, H. Dehghani, J. Wang, S. Jiang, B. W. Pogue, and K. D. Paulsen. Image-guided diffuse optical fluorescence tomography implemented with laplacian-type regularization. Optics Express, 15(7):4066–4082, 2007.

[75] P. C. Hansen. Rank-deficient and discrete ill-posed problems: numerical aspects of linear inversion. Society for Industrial and Applied Mathematics, Philadelphia, PA, USA, 1998.

[76] M. Freyer, A. Ale, R. B. Schulz, M. Zientkowska, V. Ntziachristos, and K. H. Englmeier. Fast automatic segmentation of anatomical structures in x-ray computed tomography images to improve fluorescence molecular tomography reconstruction. Journal of Biomedical Optics, 15(3), 2010.

[77] D. Hyde, E. Miller, D. H. Brooks, and V. Ntziachristos. A statistical approach to inverting the born ratio. IEEE Transactions on Medical Imaging, 26(7):893–905, 2007.

[78] D. Hyde, E. Miller, D. Brooks, and V. Ntziachristos. differential equation-driven regularization for joint fmt-ct imaging, 2009.

[79] V. Ermolayev, C. M. Cohrs, P. Mohajerani, A. Ale, M. Hrabe de Angelis, and V. Ntziachristos. Ex-vivo assessment and non-invasive in vivo imaging of internal hemorrhages in aga2/+ mutant mice. Biochem Biophys Res Commun, 432(2):389–93, 2013.

[80] N. Ducros, A. Bassi, G. Valentini, G. Canti, S. Arridge, and C. D'Andrea. Fluorescence molecular tomography of an animal model using structured light rotating view acquisition. J Biomed Opt, 18(2):20503, 2013.

[81] Karin Radrich, Angelique Ale, Vladimir Ermolayev, and Vasilis Ntziachristos. Improving limited-projection-angle fluorescence molecular tomography using a co-registered x-ray computed tomography scan. Journal of biomedical optics, 17(12):126011–126011, 2012.

[82] E. E. Graves, J. P. Culver, J. Ripoll, R. Weissleder, and V. Ntziachristos. Singular-value analysis and optimization of experimental parameters in fluorescence molecular tomography. J. Opt. Soc. Am. A, 21(2):231–241, Feb 2004.

[83] V. Klema and A. J. Laub. The singular value decomposition: Its computation and some applications. Automatic Control, IEEE Transactions on, 25(2):164–176, 1980.

[84] N. Ducros, A. Bassi, G. Valentini, M. Schweiger, S. Arridge, and C. D'Andrea. Multiple-view fluorescence optical tomography reconstruction using compression of experimental data. Optics Letters, 36(8):1377–1379, 2011.

[85] N. Ducros, C. D'andrea, G. Valentini, T. Rudge, S. Arridge, and A. Bassi. Full-wavelet approach for fluorescence diffuse optical tomography with structured illumination. Optics Letters, 35(21):3676–3678, 2010.

[86] J. Ripoll. Hybrid fourier-real space method for diffuse optical tomography. Optics Letters, 35(5):688–690, 2010.

[87] I.T. Jolliffe. Principal Component Analysis. Springer Series in Statistics. Springer, 2nd edition, 2002.

[88] A. Jin, B. Yazici, A. Ale, and V. Ntziachristos. Preconditioning of the fluorescence diffuse optical tomography sensing matrix based on compressive sensing. Optics Letters, 37(20):4326–4328, 2012.

[89] T. J. Rudge, V. Y. Soloviev, and S. R. Arridge. Fast image reconstruction in fluoresence optical tomography using data compression. Optics Letters, 35(5):763–765, 2010.

[90] A. Landragin-Frassati, J. M. Dinten, D. Georges, and A. Da Silva. Model reduction using wavelet multiresolution technique applied to fluorescence diffuse optical tomography. Applied Optics, 48(36):6878–6892, 2009.

[91] X. Cao, X. Wang, B. Zhang, F. Liu, J. W. Luo, and J. Bai. Accelerated image reconstruction in fluorescence molecular tomography using dimension reduction. Biomedical Optics Express, 4(1):1–14, 2013.

[92] X. Liu, B. Zhang, J. Luo, and J. Bai. Principal component analysis of dynamic fluorescence tomography in measurement space. Phys Med Biol, 57(9):2727–42, 2012.

[93] J.A. Hartigan. Clustering algorithms. John Wiley & Sons, Inc., 1975.

[94] T. Correia, J. Aguirre, A. Sisniega, J. Chamorro-Servent, J. Abascal, J. J. Vaquero, M. Desco, V. Kolehmainen, and S. Arridge. Split operator method for fluorescence diffuse optical tomography using anisotropic diffusion regularisation with prior anatomical information. Biomed Opt Express, 2(9):2632–48, 2011.

[95] A. Soubret, J. Ripoll, and V. Ntziachristos. Accuracy of fluorescent tomography in the presence of heterogeneities: Study of thenormalized born ratio. IEEE Transactions on Medical Imaging, 24(10):1377–1386, 2005.

[96] C. Shalizi. Advanced Data Analysis from an Elementary Point of View. Cambridge University Press, 2014-2015.

[97] S. Kullback. Information theory and statistics. John Wiley and Sons, 1959.

[98] A. Gholipour, N. Kehtamavaz, R. W. Briggs, and K. S. Gopinath. Kullback-leibler distance optimization for non-rigid registration of echo-planar to structural magnetic resonance brain images. 2007 IEEE International Conference on Image Processing, Vols 1-7, pages 3017–3020, 2007.

[99] R. Gan, J. Wu, A. C. S. Chung, S. C. H. Yu, and W. M. Wells. Multiresolution image registration based on kullback-leibler distance. Medical Image Computing and Computer-Assisted Intervention - Miccai 2004, Pt 1, Proceedings, 3216:599–606, 2004.

[100] C. C. Lee. Fuzzy-logic in control-systems - fuzzy-logic controller .1. IEEE Transactions on Systems Man and Cybernetics, 20(2):404–418, 1990.

[101] E. H. Mamdani and S. Assilian. An experiment in linguistic synthesis with a fuzzy logic controller. International Journal of Man-Machine Studies, 7(1), 1975.

[102] H. Nakhai, S. Sel, J. Favor, L. Mendoza-Torres, F. Paulsen, G. I. Duncker, and R. M. Schmid. Ptf1a is essential for the differentiation of gabaergic and glycinergic amacrine cells and horizontal cells in the mouse retina. Development, 134(6):1151–60, 2007.

[103] S. R. Hingorani, E. F. Petricoin, A. Maitra, V. Rajapakse, C. King, M. A. Jacobetz, S. Ross, T. P. Conrads, T. D. Veenstra, B. A. Hitt, Y. Kawaguchi, D. Johann, L. A. Liotta, H. C. Crawford, M. E. Putt, T. Jacks, C. V. Wright, R. H. Hruban, A. M. Lowy, and D. A. Tuveson. Preinvasive and invasive ductal pancreatic cancer and its early detection in the mouse. Cancer Cell, 4(6):437–50, 2003.

[104] S. Marino, M. Vooijs, H. van Der Gulden, J. Jonkers, and A. Berns. Induction of medulloblastomas in p53-null mutant mice by somatic inactivation of rb in the external granular layer cells of the cerebellum. Genes Dev, 14(8):994–1004, 2000.

[105] A. Neesse, A. Hahnenkamp, H. Griesmann, M. Buchholz, S. A Hahn, A. Maghnouj, V. Fendrich, J. Ring, B. Sipos, D. A Tuveson, et al. Claudin-4-targeted optical imaging detects pancreatic cancer and its precursor lesions. Gut, 62(7):1034–1043, 2013.

[106] K. S. Samkoe, S. C. Davis, S. Srinivasan, J. A. O'Hara, T. Hasan, and B. W. Pogue. A study of mri-guided diffuse fluorescence molecular tomography for monitoring pdt effects in pancreas cancer. pages 73803M–73803M–8, 2009.

[107] F. Pfeiffer, T. Weitkamp, O. Bunk, and C. David. Phase retrieval and differential phase-contrast imaging with low-brilliance x-ray sources. Nature Physics, 2(4):258–261, 2006.

[108] A. Tapfer, M. Bech, B. Pauwels, X. Liu, P. Bruyndonckx, A. Sasov, J. Kenntner, J. Mohr, M. Walter, J. Schulz, and F. Pfeiffer. Development of a prototype gantry system for preclinical x-ray phase-contrast computed tomography. Medical Physics, 38(11):5910–5915, 2011.

[109] A. Tapfer, M. Bech, A. Velroyen, J. Meiser, J. Mohr, M. Walter, J. Schulz, B. Pauwels, P. Bruyndonckx, X. Liu, A. Sasov, and F. Pfeiffer. Experimental results from a preclinical x-ray phase-contrast ct scanner. Proceedings of the National Academy of Sciences of the United States of America, 109(39):15691–15696, 2012.

[110] T. Weitkamp, A. Diaz, C. David, F. Pfeiffer, M. Stampanoni, P. Cloetens, and E. Ziegler. X-ray phase imaging with a grating interferometer. Opt Express, 13(16):6296–304, 2005.

[111] F. Pfeiffer, M. Bech, O. Bunk, P. Kraft, E. F. Eikenberry, C. Bronnimann, C. Grunzweig, and C. David. Hard-x-ray dark-field imaging using a grating interferometer. Nature Materials, 7(2):134–137, 2008.

[112] A. Tapfer, R. Braren, M. Bech, M. Willner, I. Zanette, T. Weitkamp, M. Trajkovic-Arsic, J. T. Siveke, M. Settles, M. Aichler, A. Walch, and F. Pfeiffer. X-ray phase-contrast ct of a pancreatic ductal adenocarcinoma mouse model. PLoS One, 8(3):e58439, 2013.

[113] A. Sarantopoulos E. Kalideris K. Steiger I. Esposito X. Ma G. Themelis N. C. Burton C. W. Michalski J. Kleeff S. Stangl A. J. Beer K. Pohle H. J. Wester R. M. Schmid R. Braren V. Ntziachristos M. Trajkovic-Arsic, P. Mohajerani and J. T. Siveke. Molecular imaging of integrin $\alpha_v\beta_3$ for in vivo detection of precursor lesions and pancreatic cancer. submitted, 2013.

[114] T. Donath, M. Chabior, F. Pfeiffer, O. Bunk, E. Reznikova, J. Mohr, E. Hempel, S. Popescu, M. Hoheisel, M. Schuster, J. Baumann, and C. David. Inverse geometry for grating-based x-ray phase-contrast imaging. Journal of Applied Physics, 106(5), 2009.

[115] A. Sarantopoulos, G. Themelis, and V. Ntziachristos. Imaging the bio-distribution of fluorescent probes using multispectral epi-illumination cryoslicing imaging. Molecular Imaging and Biology, 13(5):874–885, 2011.

[116] Takamasa Iwaki, Hiroshi Yamashita, and Toshiyuki Hayakawa. Color atlas of sectional anatomy of the mouse. Adosuri, 2005.

[117] D-J. Kroon and C. H Slump. Mri modalitiy transformation in demon registration. pages 963–966, 2009.

[118] P. P. Zhu, K. Zhang, Z. L. Wang, Y. J. Liu, X. S. Liu, Z. Y. Wu, S. A. McDonald, F. Marone, and M. Stampanoni. Low-dose, simple, and fast grating-based x-ray phase-contrast imaging. Proceedings of the National Academy of Sciences of the United States of America, 107(31):13576–13581, 2010.

[119] A. Bravin, P. Coan, and P. Suortti. X-ray phase-contrast imaging: from pre-clinical applications towards clinics. Physics in Medicine and Biology, 58(1):R1–R35, 2013.

[120] A. Yaroshenko, F. G. Meinel, M. Bech, A. Tapfer, A. Velroyen, S. Schleede, S. Auweter, A. Bohla, A. O. Yildirim, K. Nikolaou, F. Bamberg, O. Eickelberg, M. F. Reiser, and F. Pfeiffer. Pulmonary emphysema diagnosis with a preclinical small-animal x-ray dark-field scatter-contrast scanner. Radiology, 2013.

[121] P. Emery and M. A. Quinn. Window of opportunity in early rheumatoid arthritis: Possibility of altering the disease process with early intervention. Clinical and Experimental Rheumatology, 21(5):S154–S157, 2003.

[122] M. Ostergaard, B. Ejbjerg, and M. Szkudlarek. Imaging in early rheumatoid arthritis: roles of magnetic resonance imaging, ultrasonography, conventional radiography and computed tomography. Best Practice & Research in Clinical Rheumatology, 19(1):91–116, 2005.

[123] S. E. Gabriel. The epidemiology of rheumatoid arthritis. Rheumatic Disease Clinics of North America, 27(2):269–281, 2001.

[124] M. Backhaus, T. Kamradt, D. Sandrock, D. Loreck, J. Fritz, K. J. Wolf, H. Raber, B. Hamm, G. R. Burmester, and M. Bollow. Arthritis of the finger joints: a comprehensive approach comparing conventional radiography, scintigraphy, ultrasound, and contrast-enhanced magnetic resonance imaging. Arthritis Rheum, 42(6):1232–45, 1999.

[125] P. Emery, R. J. Wakefield, P. J. O'Connor, P. G. Conaghan, D. McGonagle, E. M. A. Hensor, W. W. Gibbon, and C. Brown. Finger tendon disease in untreated early rheumatoid arthritis: A comparison of ultrasound and magnetic resonance imaging. Arthritis & Rheumatism-Arthritis Care & Research, 57(7):1158–1164, 2007.

[126] W. T. Chen, U. Mahmood, R. Weissleder, and C. H. Tung. Arthritis imaging using a near-infrared fluorescence folate-targeted probe. Arthritis Research & Therapy, 7(2):R310–R317, 2005.

[127] A. D. Klose, A. H. Hielscher, K. M. Hanson, and J. Beuthan. Two- and three-dimensional optical tomography of finger joints for diagnostics of rheumatoid arthritis. Proceedings of SPIE, 3566:151–160, 1999.

[128] A. K. Scheel, A. Krause, I. Mesecke-von Rheinbaben, G. Metzger, H. Rost, V. Tresp, P. Mayer, M. Reuss-Borst, and G. A. Muller. Assessment of proximal finger joint inflammation in patients with rheumatoid arthritis, using a novel laser-based imaging technique. Arthritis and Rheumatism, 46(5):1177–1184, 2002.

[129] T. Fischer, I. Gemeinhardt, S. Wagner, D. von Stieglitz, J. Schnorr, K. G. A. Hermann, B. Ebert, D. Petzelt, R. MacDonald, K. Licha, M. Schirner, V. Krenn, T. Kamradt, and M. Taupitz. Assessment of unspecific near-infrared dyes in laser-induced fluorescence imaging of experimental arthritis. Academic Radiology, 13(1):4–13, 2006.

[130] A. Hansch, O. Frey, D. Sauner, I. Hilger, M. Haas, A. Malich, R. Brauer, and W. A. Kaiser. In vivo imaging of experimental arthritis with near-infrared fluorescence. Arthritis and Rheumatism, 50(3):961–967, 2004.

[131] A. H. Hielscher, A. D. Klose, A. K. Scheel, B. Moa-Anderson, M. Backhaus, U. Netz, and J. Beuthan. Sagittal laser optical tomography for imaging of rheumatoid finger joints. Physics in Medicine and Biology, 49(7):1147–1163, 2004.

[132] T. Dziekan, C. Weissbach, J. Voigt, B. Ebert, R. Macdonald, M. L. Bahner, M. Mahler, M. Schirner, M. Berliner, B. Berliner, J. Osel, and I. Osel. Detection of rheumatoid arthritis by evaluation of normalized variances of fluorescence time correlation functions. Journal of Biomedical Optics, 16:076015, 2011.

[133] Y. Xu, N. Iftimia, H. B. Jiang, L. L. Key, and M. B. Bolster. Imaging of in vitro and in vivo bones and joints with continuous-wave diffuse optical tomography. Optics Express, 8(7):447–451, 2001.

[134] T. Fischer, B. Ebert, J. Voigt, R. Macdonald, U. Schneider, A. Thomas, B. Hamm, and K. G. Hermann. Detection of rheumatoid arthritis using non-specific contrast enhanced fluorescence imaging. Acad Radiol, 17(3):375–81, 2010.

[135] A. H. Hielscher, H. K. Kim, L. D. Montejo, S. Blaschke, U. J. Netz, P. A. Zwaka, G. Illing, G. A. Muller, and J. Beuthan. Frequency-domain optical tomographic imaging of arthritic finger joints. IEEE Trans Med Imaging, 30(10):1725–36, 2011.

[136] J. M. Lasker, C. J. Fong, D. T. Ginat, E. Dwyer, and A. H. Hielscher. Dynamic optical imaging of vascular and metabolic reactivity in rheumatoid joints. J Biomed Opt, 12(5):052001, 2007.

[137] Z. Yuan, Q. Zhang, E. S. Sobel, and H. Jiang. Image-guided optical spectroscopy in diagnosis of osteoarthritis: a clinical study. Biomed Opt Express, 1(1):74–86, 2010.

[138] Y. Sun, E. S. Sobel, and H. Jiang. First assessment of three-dimensional quantitative photoacoustic tomography for in vivo detection of osteoarthritis in the finger joints. Med Phys, 38(7):4009–17, 2011.

[139] J. R. Rajian, G. Girish, and X. Wang. Photoacoustic tomography to identify inflammatory arthritis. J Biomed Opt, 17(9):96013–1, 2012.

[140] E. Y. Ng and T. J. How. Laser-doppler imaging of osteoarthritis in proximal interphalangeal joints. Microvasc Res, 65(1):65–8, 2003.

[141] W. R. Ferrell, P. V. Balint, C. G. Egan, J. C. Lockhart, and R. D. Sturrock. Metacarpophalangeal joints in rheumatoid arthritis: laser doppler imaging–initial experience. Radiology, 220(1):257–62, 2001.

[142] D. Chamberland, Y. Jiang, and X. Wang. Optical imaging: new tools for arthritis. Integr Biol (Camb), 2(10):496–509, 2010.

[143] L. L. Gompels, N. H. Lim, T. Vincent, and E. M. Paleolog. In vivo optical imaging in arthritis–an enlightening future? Rheumatology (Oxford), 49(8):1436–46, 2010.

[144] B. Christoph, L. Hans-Eckhard, and Stephanie W. Assessing activity of rheumatic arthritis with fluorescence optical imaging. European Musculoskeletal Review, 4(2):96–100, 2009.

[145] R. Meier, C. Krug, D. Golovko, S. Boddington, G. Piontek, M. Rudelius, E. J. Sutton, A. Baur-Melnyk, E. F. Jones, and H. E. Daldrup-Link. Indocyanine green-enhanced imaging of antigen-induced arthritis with an integrated optical imaging/radiography system. Arthritis & Rheumatism, 62(8):2322–2327, 2010.

[146] J. S. Slakter, A. Giovannini, L. A. Yannuzzi, B. Scassellati-Sforzolini, D. R. Guyer, J. A. Sorenson, R. F. Spaide, and D. Orlock. Indocyanine green angiography of multifocal choroiditis. Ophthalmology, 104(11):1813–1819, 1997.

[147] E. H. Kim, J. M. Cho, J. H. Chang, S. H. Kim, and K. S. Lee. Application of intraoperative indocyanine green video angiography to brain tumor surgery. Acta Neurochir (Wien), 153(7):1487–95, 2011.

[148] J. Caesar, S. Shaldon, L. Chiandussi, L. Guevara, and S. Sherlock. The use of indocyanine green in the measurement of hepatic blood flow and as a test of hepatic function. Clin Sci, 21:43–57, 1961.

[149] B. Ebert, B. Riefke, U. Sukowski, and L. C. Kai. Cyanine dyes as contrast agents for near-infrared imaging in vivo: acute tolerance, pharmacokinetics, and fluorescence imaging. Journal of Biomedical Optics, 16(6), 2011.

[150] A. Raabe, J. Beck, R. Gerlach, M. Zimmermann, and V. Seifert. Near-infrared indocyanine green video angiography: a new method for intraoperative assessment of vascular flow. Neurosurgery, 52(1):132–9, 2003.

[151] G. C. Wishart, S. W. Loh, L. Jones, and J. R. Benson. A feasibility study (icg-10) of indocyanine green (icg) fluorescence mapping for sentinel lymph node detection in early breast cancer. Ejso, 38(8):651–656, 2012.

[152] C. Vinegoni, I. Botnaru, E. Aikawa, M. A. Calfon, Y. Iwamoto, E. J. Folco, V. Ntziachristos, R. Weissleder, P. Libby, and F. A. Jaffer. Indocyanine green enables near-infrared fluorescence imaging of lipid-rich, inflamed atherosclerotic plaques. Science Translational Medicine, 3(84), 2011.

[153] R. C. Benson and A. H. Kues. Fluorescence properties of indocyanine green as related to angiography. Phys. Med. Biol., 23(1):159–163, 1978.

[154] V. Ntziachristos, C. Bremer, and R. Weissleder. Fluorescence imaging with near-infrared light: new technological advances that enable in vivo molecular imaging. European Radiology, 13(1):195–208, 2003.

[155] E. M. C. Hillman and A. Moore. All-optical anatomical co-registration for molecular imaging of small animals using dynamic contrast. Nature Photonics, 1(9):526–530, 2007.

[156] X. Intes, J. Ripoll, Chen Yu, S. Nioka, A. G. Yodh, and B. Chance. In vivo continuous-wave optical breast imaging enhanced with indocyanine green. Medical Physics, 30(6):1039–47, 2003.

[157] A. S. Montcuquet, L. Herve, F. Navarro, J. M. Dinten, and J. I. Mars. Nonnegative matrix factorization: a blind spectra separation method for in vivo fluorescent optical imaging. Journal of Biomedical Optics, 15(5), 2010.

[158] J. Glatz, N. C. Deliolanis, A. Buehler, D. Razansky, and V. Ntziachristos. Blind source unmixing in multi-spectral optoacoustic tomography. Optics Express, 19(4):3175–3184, 2011.

[159] V. Ntziachristos, A. G. Yodh, M. Schnall, and B. Chance. Concurrent mri and diffuse optical tomography of breast after indocyanine green enhancement. Proceedings of the National Academy of Sciences of the United States of America, 97(6):2767–2772, 2000.

[160] Q. Zhang, Z. Yuan, E. Sobel, and H. Jiang. X-ray guided three-dimensional diffuse optical tomography: In vivo study of osteoarthritis in the finger joints. volume 6431 of Progress in Biomedical Optics and Imaging - Proceedings of SPIE, page 643112. SPIE -International Society for Optical Engineering, Bellingham WA, WA 98227-0010, United States.

[161] Y. Xu, N. Iftimia, H. Jiang, L. L. Key, and M. B. Bolster. Three-dimensional diffuse optical tomography of bones and joints. J Biomed Opt, 7(1):88–92, 2002.

[162] L. Michael and D. Winter. Distances between sets. Nature, 234:34–35, 1971.

[163] D. P. Huttenlocher, G. A. Klanderman, and W. J. Rucklidge. Comparing images using the hausdorff distance. IEEE Transactions on Pattern Analysis and Machine Intelligence, 15(9):850–863, 1993.

[164] R. Cérdenes, M. Bach, and R.D. Luis. A multimodal evaluation method for medical image segmentation. Computerized Medical Imaging and Graphics, 96(2):108–124, 2009.

[165] K. H. Zou, S. K. Warfield, A. Bharatha, C. M. C. Tempany, M. R. Kaus, S. J. Haker, W. M. Wells, F. A. Jolesz, and R. Kikinis. Statistical validation of image segmentation quality based on a spatial overlap index - scientific reports. Academic Radiology, 11(2):178–189, 2004.

[166] W. R. Crum, O. Camara, and D. L. G. Hill. Generalized overlap measures for evaluation and validation in medical image analysis. IEEE Transactions on Medical Imaging, 25(11):1451–1461, 2006.

[167] K. Popuri, D. Cobzas, A. Murtha, and M. Jagersand. 3d variational brain tumor segmentation using dirichlet priors on a clustered feature set. International Journal of Computer Assisted Radiology and Surgery, 7(4):493–506, 2012.

[168] M. Basseville. Distance measures for signal-processing and pattern-recognition. Signal Processing, 18(4):349–369, 1989.

[169] B. Hemery, H. Laurent, B. Emile, and C. Rosenberger. Comparative study of localization metrics for the evaluation of image interpretation systems. Journal of Electronic Imaging, 19(2), 2010.

[170] T. Fawcett. An introduction to roc analysis. Pattern Recognition Letters, 27:861–874, 2006.

[171] W. D. Bugbee and M. J. Botte. Surface anatomy of the hand. the relationships between palmar skin creases and osseous anatomy. Clin Orthop Relat Res, (296):122–6, 1993.

[172] K. Gauvreau and M. Pagano. Student's t test. Nutrition, 9(4):386, 1993.

[173] A. B. Milstein, Q. Zhang, S. Oh, K. J. Webb, C. A. Bouman, R. P. Millane, and D. A. Boas. Fluorescence imaging in optical diffusion tomography. 2002 IEEE International Symposium on Biomedical Imaging, page 4 pp. IEEE.

[174] N. Ferrara and R. S. Kerbel. Angiogenesis as a therapeutic target. Nature, 438(7070):967–74, 2005.

[175] T. S. Lisse, F. Thiele, H. Fuchs, W. Hans, G. K. Przemeck, K. Abe, B. Rathkolb, L. Quintanilla-Martinez, G. Hoelzlwimmer, M. Helfrich, E. Wolf, S. H. Ralston, and M. Hrabe de Angelis. Er stress-mediated apoptosis in a new mouse model of osteogenesis imperfecta. PLoS Genet, 4(2):e7, 2008.

[176] G. J. Riely, J. Marks, and W. Pao. Kras mutations in non-small cell lung cancer. Proc Am Thorac Soc, 6(2):201–5, 2009.